UNIVERSITÉ DE GRENOBLE

THÈSE

Pour obtenir le grade de

DOCTEUR DE L'UNIVERSITÉ DE GRENOBLE

Spécialité : **Physique/Physique subatomique & Astroparticules**

Arrêté ministérial :

Présentée par

Yaxian Mao

Thèse dirigée par **Pr. Christophe Furget**
et codirigée par **Pr. Daicui Zhou**

préparée au sein du **Laboratoire de Physique Subatomique et de Cosmologie**

Mesures des corrélations γ-hadron dans les collisions p-p avec l'expérience ALICE au LHC

Thèse soutenue publiquement le **3 juin 2011**,
devant le jury composé de :

.
Pr Yugang Ma, président du jury, SINAP Shanghai (China)

Pr. Nu Xu, rapporteur, LBNL Berkeley (USA)

Pr. Xu Cai, examinateur, CCNU Wuhan (China)

Pr. Daicui Zhou, co-directeur de thèse, CCNU Wuhan (China)

Dr. Christelle Roy, rapporteur, IPHC Strasbourg (France)

Dr. Yves Schutz, examinateur, CERN Geneva (Suisse)

Dr. Serge Kox, examinateur, LPSC Grenoble (France)

Pr. Christophe Furget, directeur de thèse, LPSC Grenoble (France)

博士学位论文

&   中 的 双 粒 子 关 联 测 量 及 介 质 效 应 的 研 究

论文作者：　　　毛　亚　显

指导教师：　周代翠, Christophe Furget 教授

学科专业：粒子物理与原子核物理

研究方向：高能重离子碰撞实验

华中师范大学物理科学与技术学院

&

法国格勒诺布尔理工大学物理学院

2011年5月

Two Particle Correlations with Photon Triggers to Study Hot QCD Medium in ALICE at LHC

A Dissertation Presented

BY

Yaxian Mao

to

The Doctoral School in partial fulfillment of the requirements

For the Degree of Doctor of Philosophy in Physics

of

Huazhong Normal University

and

Université de Grenoble

Supervisors: Daicui Zhou,   Christophe Furget,   Yves Schutz

Academic Titles: Professor, Professor, Directeur de Recherches

May   2011

Résumé

Depuis le démarrage du LHC (the Large Hadron Collider), le complexe accélérateurs du CERN (Organisation Européenne pour la Recherche Nucléaire) réalise des collisions entre protons et entre ions lourds à des énergies jamais atteintes auparavant. ALICE (A Large Ion Collider Experiment), l'une des expériences principales installées auprès du LHC, est dédiée à l'étude de la matière nucléaire soumise à des conditions extrêmes de température et d'énergie. L'objectif de l'expérience est de vérifier l'existence d'un nouvel état de la matière, le QGP (Quark Gluon Plasma) et d'en étudier les propriétés. Cette étude permettra d'explorer les aspects fondamentaux de l'interaction forte, l'une de 4 interactions fondamentales de l'univers responsable de la cohésion de la matière ainsi que du vide qui lui est associé.

Pour mener à bien cet ambitieux programme scientifique, il est essentiel de choisir des observables pertinentes porteuses d'informations utiles pour la compréhension de la nature de la matière créée dans les collisions d'ions lourds aux énergies ultra relativistes. Les informations extraites de nombreuses observables permettront, à partir de modelisations des principes fondamentaux mis en jeu, de concevoir une interprétation cohérente des phénomènes observés. Après une mise en contexte de ce programme de recherche, les principaux aspects des collisions entre ions-lourds et un bref état des lieux des résultats obtenus à ce jour dans ce domaine sont présentés dans une première partie de ce document.

Parmi les observables, la production de jets de hadrons est particulièrement intéressante. Les jets résultent du processus de hadronisation de partons de grande impulsion transverse et apparaissent dans les détecteurs comme un faisceau collimaté de hadrons. Les partons de grande impulsion transverse quant à eux sont créés dans les interactions dures entre partons (de type $2 \rightarrow 2$) constituant les projectiles en collision. La mesure de la structure des jets, telle la distribution des hadrons en fonction de la fraction d'énergie du parton initial emporté par chacun d'eux, est l'observable de prédilection. En effet, dans les collisions entre ions lourds les partons de grande impulsion transverse sont créés simultanément avec le milieu chaud et dense, objet de notre étude, et voient leurs propriétés cinématiques modifiées lorsqu'ils traversent ce même milieu. Lors du processus de hadronisation, les hadrons gardent la mémoire des modifications subies par le parton de façon à modifier la structure du jet. Ces modifications sont révélées en comparant la structure du jet lorsque le parton de grande impulsion transverse est produit dans des collisions proton–proton (on parle de structure du jet dans le vide) avec la structure du jet lorsque le parton est produit dans

des collisions noyaux-noyaux (on parle de structure du jet dans le milieu). Reste un problème technique: alors que les jets sont aisément identifiés et mesurés dans les collisions proton–proton, dans les collisions entre ions lourds, le fond sous jacent de hadrons dans l'état final rend la mesure des jets particulièrement ardue. De plus il est impossible de connaître quelle était l'impulsion du parton lors de sa création, seule l'impulsion finale après interaction avec le milieu est mesurable, ce qui complique l'interprétation de la mesure.

Pour pallier à ces problèmes techniques, j'ai choisi d'étudier un type de processus dur particulier, celui qui met un en jeu dans l'état final un photon (il s'agit des photons directs par opposition aux photons de décroissance des mésons neutres). L'impulsion ($\vec{p_\gamma}$) du photon, qui n'interagit pas fortement avec le milieu, permet de calibrer l'impulsion du parton ($\vec{p_p} = -\vec{p_\gamma}$) tel qu'il a été créé dans le processus dur. Ainsi l'impulsion du photon nous donne l'impulsion du parton avant interaction avec le milieu et la mesure de l'impulsion du jet nous donne l'impulsion du parton après interaction avec le milieu. De plus la mesure du photon permet de s'affranchir de l'identification des jets, puisqu'il suffira de mesurer la corrélation azimutale entre le photon et l'ensemble des hadrons générés dans la collision. Cependant, les faibles section efficace du processus photon–jet rend cette mesure relativement difficile. Les éléments nécessaires à l'étude des corrélations et les équipements expérimentaux sont décrits dans la deuxième partie de ce document.

La stratégie d'un telle étude commence par la validation de la mesure, qui consiste à étudier à l'aide de simulations Monte Carlo d'une part quelle est la sensisibilité de l'observable choisie pour révéler le phénomène recherché et d'en quantifier les effets et d'autre part si le signal est mesurable avec les systèmes de détection de l'expérience. Cette étude est décrite dans la troisième partie de ce document. Je décris les performances attendues pour l'étude des corrélations azimutales entre photons et hadrons chargés mesurés avec l'expérience ALICE. Deux quantité sont extraites de cette étude à partir des simulations de collisions proton–proton: la valeur moyenne du moment transverse total au niveau partonique ($< k_T >$) et la distribution de la fraction (x_E) d'énergie du jet emportée par les hadrons produits en coincidence avec un photon (fonction de corrélation). Les mêmes quantités sont extraites à partir de simulations de collisions d'ions lourds et les modifications subies par le mileu sont analysées: la distribution des valeurs de k_T est élargie d'une quantité qui peut être directement reliée au coefficient de transport du milieu et la fonction de corrélation est modifiée de façon à supprimer les hadrons de grande valeur de x_E (jet quenching) et à augmenter le nombre de hadrons à petites valeurs de x_E (production radiative de gluons). L'amplitude de cette dernière modification est proportionnelle au coefficient de transport et à la distance parcourue

dans le milieu. Je termine cette partie consacrée aux simulations (et à laquelle j'ai consacré la plus grande partie de mon temps) par une étude détaillée qui devrait permettre, théoriquement, de réaliser une étude tomographique du milieu formé dans les collisions d'ions lourds. La procédure repose sur une idée suggérée par X.N Wang et consiste à localiser le processus dur dans le milieu (grande valeur de x_E pour une production du photon et du jet en surface et petite valeur de x_E pour une production profondeur) et ainsi sonder le milieu de la partie la plus dense jusqu'à la partie la moins dense en surface. Je conclus que la mesure relève du défi expérimental !

La quatrième partie de ce document est consacrée à l'analyse des données collectées en 2010 pour des collisions proton–proton à une énergie dans le centre de masse de $\sqrt{s} = 7$ TeV. Pour cette première longue campagne de mesure au LHC, l'expérience ALICE n'était pas encore dans les conditions optimales pour la mesure des corrélations photon–jet. En effet, les calorimètres électromagnétiques n'offraient qu'une acceptance réduite et l'expérience ne disposait pas encore d'un déclenchement sélectif pour enrichir les données enregistrées en événements photon – jet. Il en a résulté un nombre d'événements insuffisant pour une étude concluante. En particulier la statistique disponible a limité l'étude au domaine d'énergie inférieur à 10 GeV, domaine très défavorable pour l'identification des photons directs du fait de leur rareté dans le bruit de fond prédominant des photons de décroissance. S'est ajouté à ce handicap, le peu de temps disponible pour compléter une analyse très délicate. Des résultats préliminaires sont présentés pour les corrélations entre photons inclusifs et hadrons chargés et photons isolés et hadrons chargés: les structures 2 jets et mono jet sont bien identifiées, une valeur de $\langle k_T \rangle$ a été déterminée et les distributions en x_E ont été construites.

Cette première analyse est un premier pas vers une analyse complète de l'observable photon – jet à partir des données plus riches (calorimètre complet, et déclenchement sélectif) qui seront collectées en 2011 pour les collisions proton–proton et Pb–Pb.

Dans la dernière partie de ce document, je décris ma contribution au contrôle qualité des calorimètres électromagnétiques pendant la prise de données.

摘　　要

在现代自然科学研究中，一项极具挑战性的研究目标是在最小尺度上探索物质的构成。 一种描述基本粒子与作用力的理论–标准模型，假定物质的基本结构是由夸克和轻子通过规范粒子的相互作用而组成的，认为组成物质结构的最小单元是夸克（u, d；c, s；t, b）、轻子(e, ν_e；μ, ν_μ；τ, ν_τ)，以及传递相互作用力的媒介子，即玻色子($W^\pm$和Z^0)、胶子(g)和光子(γ)。基本作用力根据规范粒子的不同划分为电磁相互作用，弱相互作用和强相互作用。 正是这些基本粒子和相互作用力构建了亚原子世界。然而，这个理论并不十分完备，因为它依然无法解释某些基本的问题，比如：基本粒子质量的起源、宇宙的真实真空、以及宇宙中物质远比反物质多的问题...。

人们普遍认为，强相互作用由量子色动力学(Quantum Chromodynamics, QCD)描述。量子色动力学的重要特性是渐近自由性质，即随着相互作用的动量标度的变大，强相互作用的耦合常数(α_s)趋于零。 在渐近自由状态下，部分子间的相互作用是微扰的。 QCD预言，在相对论重离子碰撞下，部分子可以达到这种状态，形成夸克胶子等离子体(QGP)。 美国布鲁海文国家实验室(BNL)利用相对论重离子对撞机(RHIC)来寻找这种新的物质形态。 位于欧洲核子研究中心(CERN)的大型强子对撞机(LHC)于2009年正式启动运行，实现了前所未有的TeV能区的高能重离子碰撞，LHC上的大型重离子对撞机实验(ALICE)合作组专门致力于高温高能量密度的极端条件下强相互作用的基本性质及其物理真空的研究。

基于量子色动力学(QCD)，利用格点计算方法，人们成功地预言了夸克从禁闭的普通强子物质中退禁闭到QGP相的临界温度。 实验上，该临界温度首先在CERN$\sqrt{s_{NN}} = 17.2$ GeV下的SPS重离子碰撞实验中达到。进而在美国布鲁海文国家实验室(BNL)运行的质心能量$\sqrt{s_{NN}} = 60 - 200$ GeV下的相对论重离子对撞机(RHIC)实验中，证实了从强子物质到夸克物质的相变能在高温高密条件下发生。 位于欧洲核子研究中心(CERN)的大型强子对撞机LHC实现了质心能量$\sqrt{s_{NN}} = 2.76$ TeV下的铅-铅碰撞，该能量高于RHIC碰撞能量的~14倍，使其在更高温度下形成的热密QCD物质持续更长时间。 另外，LHC能区的重离子碰撞诱导产生的硬散射过程更加丰富，这些敏锐的硬探针将提供TeV能区下细致研究QGP性质的机会。比如，在核–核中心碰撞中高横动量强子产额的压低和背对背喷注之间的关联消失。 ALICE探测器就是为了更加系统的测量核–核碰撞中产生的末态粒子，由此反映碰撞初期出现的热密物质相的性质。特别是，通过测量相空间中强子谱的改变，可以研究硬散射部分子在穿越密度物质时的能量损失效应及碎裂函数性质。 在重离子碰撞中，由于喷注淬火效应，硬散射过程产生的大横动量部分子穿越密度物质时会因为多重散射而损失能量，导致高横动量的强子产额减少，低动量强子数目会增多，引起强子谱在相空间中的重新分布。 因此，通过测量核环境下部分子的碎裂函数(FF)，即测量部分子喷注

产生的强子携带喷注动量份额 $z = p_{T_h}/E_T^{jet}$ 的分布函数,将真空中的碎裂函数(质子–质子碰撞或核–核边沿碰撞中的碎裂函数)与被介质修正后的碎裂函数(核–核中心碰撞下的碎裂函数)分布进行比较,就可以推断核–核碰撞中的密度物质及其性质。

本论文主要目的是利用光子–强子的关联测量来研究部分子的碎裂函数,即通过测量高能直接光子与散射到光子背面强子之间的关联来研究喷注的碎裂函数。 高能直接光子在碰撞初期的硬散射过程中直接产生,主要来自康普顿散射($qg \rightarrow \gamma q$)和湮灭过程($q\bar{q} \rightarrow \gamma g$)。 由于光子的平均自由程很大,在碰撞区域内与其他粒子只有电磁相互作用,因此光子携带了它们初始产生时刻的信息。 而与该光子产生于同一硬散射过程的部分子会碎裂为末态强子,通过对强子的测量,就能获得部分子在穿越密度物质后的信息。 将产生于同一事件中的光子和强子关联,我们就能得到密度物质作用于部分子喷注上的效应。 我选择了高横动量的喷注作为对介质作断层扫描的探针:观测量是高动量直接光子与在其相反方向上的强子的关联。在这一测量中,直接光子标记了同样作为在初始碰撞中硬过程产生的部分子的初始能量,而强子,作为该部分子碎裂出的末态粒子,描述了穿越介质的部分子的属性。 通过比较这两种碰撞系统下的光子–强子关联测量,我们可以得到介质效应对末态运动学和喷注碎裂的修正。 然而,在碰撞中来自强子和中性介子(主要是 π^0 和 η)的衰变光子是直接光子信号提取过程中的主要背景,因此光子信号的提取在本工作中显得至关重要。

本论文着重开展如下两方面的工作。第一部分是关于光子测量,鉴别效率以及直接光子的提取研究,估计来自衰变光子误判引起的系统误差, 并研究利用光子–强子关联及强子–强子关联方法在ALICE实验中测量的可行性。 利用Monte-Carlo模拟数据,我们研究了ALICE实验中电磁量能器(PHOS和EMCAL)在探测和鉴别光子时的性能表现。 由于有限的接受度,在碰撞过程中产生的某些光子落在探测器边缘使得沉积在晶体上的能量不能获得完整的重建,这些光子将不能被正确探测到。同时,光子在穿越位于量能器之前的其它探测器时与探测器物质发生相互作用而使光子转换成正负电子对($\gamma \rightarrow e^+e^-$)。 模拟结果表明,不同探测器对光子探测效率的影响程度不一样。例如,光子在时间投影室(TPC)和内部径迹系统(ITS)的转换几率约为10%,而在跃迁辐射探测器(TRD)和时间飞行探测器(TOF)中的转换几率接近20%。 本文首先报告了在LHC能区中的质子–质子和铅–铅碰撞过程中利用ALICE实验探测器通过直接光子–强子关联测量的方法研究喷注碎裂函数和介质效应的可行性。 光子–强子关联测量在质子–质子碰撞中是必须的,因为该测量能够为我们提供有关重离子碰撞下的关联测量的基线参考。 我研究了介质可能引起的一系列效应。对于第一个相关的参数就是 k_T,即部分子层次上的有效横动量。 基于国际上已有的实验数据测量值,我们将其延伸外推到LHC能区,从而预测LHC能区上的 k_T 值。 本文估计了光子-强子关联测量对于高温热密物质的敏感度及光子–强子关联函数的重新分布,从而提取热密物质的性质。 另外,我还通过光子-喷注产生机制研究了喷注在穿越热密物质里产生的过程进行层析结构分析。

该工作的第二部分，主要聚焦在LHC于2010年首次运行的质子-质子碰撞下质心能量$\sqrt{s} = 7$ TeV下的ALICE数据分析工作。 该工作从真实数据入手，采用我们在前面已经建立的可行性研究方法，旨在测量质子-质子碰撞下的喷注碎裂函数，为铅-铅数据分析提供基线测量。 鉴于当前ALICE有限的统计量和不完整的电磁量能器接收度，本工作的测量集中在小于20GeV/c的横动量区域进行，由于在该横动量范围内大量来自衰变光子的背景贡献使得该测量在此区间特别具有难度和挑战性。 由于当前探测器的校准工作依然在进行之中，我无法利用粒子鉴别的方法来区分光子和π^0作为触发粒子，而是直接利用在量能器上形成的电磁簇射团簇和利用不变质量方法重建出的π^0作为触发粒子进行两粒子关联。而后对触发粒子进行孤立截断的判选，从而提高直接瞬时光子数据样本的机率。 双喷注结构与单光子/π^0–喷注的运动学结构通过以上研究观测到。同时，利用孤立光子–强子的方位角关联我们提取了部分子层次上的横动量k_T值，该测量值与我之前利用蒙特卡罗数据预言的k_T结果一致，更进一步，我尝试了构建 20GeV以下的喷注在质子-质子$\sqrt{s} = 7$TeV下的碎裂函数。 但展开实际数据分析的时间之短让我无法对该项研究进入到更深的地步。

对于在2010年底LHC首次运行铅-铅碰撞下的质心能量$\sqrt{s_{NN}} = 2.76$ TeV下的数据，我做了同样的数据分析，但时间之仓促不允许我将该数据分析部分纳入该论文之中。 鉴于电磁量能器覆盖范围的增加以及高横动量光子触发判选能力的实现，2011，2012年LHC运行获取的数据无疑会提供更大的统计量，让该项研究的有效测量范围达到更高，从而获得更多有趣的物理现象和物理结果。

最后， 为了论文的完整性，对于我在博士期间对于整个ALICE实验合作组中的主要贡献简要概括如下：

- 利用光子–强子关联测量的可行性研究。该项可行性研究是本人硕士论文的延续，我在硕士论文研究出的测量和分析方法基础之上，发展和延伸了该观测量对于核核碰撞下形成的热密物质的敏感度。通过各项细致研究，总结出利用光子–强子关联方法测量介质效应是敏感而且有效的，我们甚至可以通过该关联测量提取部分子层次上的运动学量k_T， 并对形成的热密物质介质本身进行层析扫描。 这些研究结果均在ALICE国际合作组中广泛讨论并得到认同，并在大型国际学术会议上报告。

- EMCal探测器校准工作。为了获得一个较好的能量和位置分辨率，我参加了在格勒诺布尔利用宇宙射线和在CERN利用高能电子束流对EMCal探测器进行校准的工作。

- EMCal在线数据质量监控(DQM)。 为了检测在数据获取过程中的探测器质量，自LHC准备运行以来，我担任了EMCal探测器数据质量检测的任务，并开发和提供了数据检测的软件工具并且保持维护和更新。还开发了数据监控的算法和质量检测的标准，并将其补充

到ALICE数据获取系统的在线数据监测框架之下。

- 电磁量能器EMCal和PHOS的离线数据监测和质量认证(QA)。我负责运行每周从LHC上取得的ALICE数据，对量能器的离线数据质量检验，并将质量检验结果在每周ALICE数据质量检验和数据分析会议上报告，为实验合作组的量能器数据物理分析提供有效数据库。

- 中性介子和光子–强子关联的数据分析工作。自2009年LHC开始采集数据以来，我一直致力于探测器的校准和实验数据的分析工作(数据分析现在依然进行之中)。其中包括π^0的重建，以及光子–强子的关联测量。我被相应的ALICE物理工作组推选为光子/π^0-强子关联测量的数据分析协调人，每周召集两次课题讨论会，并定期在ALICE合作组内报告工作进展。

关键词： 大型重离子对撞实验(ALICE)，夸克胶子等离子体(QGP)，喷注，瞬时光子，孤立截断，关联测量，碎裂函数，部分子k_T, 层析结构

Abstract

With the advent of the Large Hadron Collider (LHC)at the end of 2009, the new accelerator at CERN collides protons and heavy-ions at unprecedented high energies. ALICE , one of the major experiment installed at LHC, is dedicated to the study of nuclear matter under extreme conditions of energy density with the opportunity of creating a partonic medium called the Quark-Gluon-Plasma (QGP). This new experimental facility opens new avenues for the understanding of fundamental properties of the strong interaction and its vacuum.

To reach the objectives of this scientific program, it is required to select a set of appropriate probes carrying relevant information on the properties of the medium created in ultra-relativistic heavy-ion collisions. Based on the information delivered by all the observables and guided by modelization of the fundamental principles in action, a coherent picture will emerge to interpret the observed phenomena. In the first part of the present document I describe the context of the scientific program, the general concepts involved in heavy-ion collisions at ultra relativistic energies, and the main results obtained so far in the field.

Among the observables of interest, the production of hadrons jets is particularly attractive. Jets are the result of the hadronisation process of high transverse momentum partons and are observed in the detectors as a beam of collimated hadrons. High transverse momentum partons are created by hard scattering of partons ($2 \rightarrow 2$ type of processes) constituting the colliding projectiles. The jet structure measured, for example as the distribution of the factional jet energy carried by the individual hadrons inside the jet, is the observable of choice. In heavy ion collisions, high transverse momentum partons are created concurrently with the hot and dense medium of interest and their kinematical properties are modified as they traverse the medium. This modification, imprinted in the jet structure, is observed by comparing the jet structure measured in heavy-ion collisions (in medium jet structure) with the jet structure measured in proton-proton collisions (vacuum jet structure). Such a measurement faces however a technical difficulty: whereas jets can be easily identified and measured in proton-proton collisions, in heavy-ion collisions the large hadronic background from the underlying event (the underlying event is everything except the two hard scattered jets and is generated by the beams particle break up and by initial and final state radiation) makes the jet identification measurement quite challenging. In addition the initial momentum of the hard scattered parton is unknown since only the final jet momentum can be measured i.e. the momentum of the parton as it emerges from the medium. This complicates the

interpretation of the measurement.

To overcome these difficulties, I have selected a particular $2 \rightarrow 2$ process which creates a direct photon (direct photon at variance with decay photon) in the final state together with a high transverse momentum parton. The momentum of the photon ($\vec{p_\gamma}$), since it does not interact strongly with the medium, calibrates the momentum of the parton ($\vec{p_p} = -\vec{p_\gamma}$). Therefore the photon momentum is a measure of the parton momentum when created and the jet momentum the momentum of the parton after it has traversed the medium. In addition since the photon momentum (energy and direction) defines also the jet momentum, jet reconstruction algorithms are not required anymore. Instead of studying photon – jet correlations (where the jet is fully reconstructed), it is sufficient to study photon – hadron correlations from all the hadrons in the event. However, the relatively small cross section for the production of these particular hard scattering processes makes the measurement quite challenging. An introduction to 2 particle correlations is given in the second part of this document followed by a description of the ALICE detection systems used for this measurement.

The strategy I have followed for this study starts with a validation of the measurement. It consists first in studying with the help of Monte Carlo simulations the accuracy of the selected observable in revealing and quantifying the phenomenon under study. Second, it consists in verifying the ability to measure the observable and its robustness with the detectors setup of the ALICE experiment. The validation procedure and results are discussed in the third part of this document. I have particularly studied the possibility to extract two quantities from the 2 particle azimuthal correlation measured in proton-proton collisions: (i) the average total transverse momentum ($\langle k_T \rangle$) generated at the partonic level by the Fermi motion and initial and final state radiation, and (ii) the per trigger yield of jet hadrons as a function of the fractional jet energy (x_E) they each carry (correlation function). The same quantities have been studied from simulated heavy-ion collisions with the objective to analyze the effects due to the presence of highly dense color medium. The distribution of k_T values becomes broader in a way that can be directly related to the transport properties of the medium and the correlation function is modified so that the number of high x_E hadrons are suppressed (jet quenching) and the number of low x_E hadrons is increased (radiative gluon production) with an amplitude proportional to the transport coefficient and to distance traversed inside the medium. To finish this part of the document dedicated to Monte Carlo studies (on which I have spent most of my time as a PhD student) with another detailed study the possibility to exploit the photon – jet observable as a tomographic tool (following a suggestion by X.N.

Wang). The idea is to localize the hard scattering well inside the medium (by selecting hadrons with low x_E values) or at the surface of the medium (by selecting hadrons with large x_E values). One would therefore choose the distance in the medium through which the hard scattered parton travels and probe the medium from its densest part (center) to its less dense part (surface). I found that such a measurement will be quite challenging.

In the fourth part of the present document, I address the analysis of the data collected in 2010 for proton-proton collisions at $\sqrt{s} = 7$ TeV. During this first long data taking period at LHC, the ALICE detection system was not yet complete. In particular, the incomplete coverage of the electromagnetic calorimeters and the absence of a selective photon trigger was a severe handicap for the photon – jet measurement. The resulting event statistics available for the measurement of this observable was limited to the photon energy range below 10 GeV. This low energy domain is not well suited for the identification of direct photons because of their scarcity in the overwhelming background generated by decay photons. On top of that, the time between the availability of the data and the scheduled time for my defense was too short to perform an in-depth analysis. Most of the results presented from this analysis in the present document must therefore be considered as very preliminary, but the key features are there. The results concern the 2 jet and mono jet structure observed in the photon – jet azimuthal correlation, the measured value of $\langle k_T \rangle$ and the x_E distributions.

This very preliminary analysis of the first data collected at LHC and presented in this document is the first only toward a comprehensive study of the photon – jet observable. Since the writing of the document, the analysis has progressed and provided a few results which were considered ripe by the collaboration to be presented at the Quark Matter conference in May 2011. The data which will be collected in 2011 in proton-proton and Pb-Pb collisions will be much richer in photon – jet events thanks to the complete coverage of the ALICE electromagnetic calorimeter and thanks to a very high energy photon trigger provided by the calorimeter as well.

For completeness, I finish the present document with the description of my contribution, as being the main person in charge, to the quality assurance and monitoring tasks for the two ALICE electromagnetic calorimeters during data taking.

Keywords: ALICE, Quark-Gluon Plasma (QGP), jet, prompt photon, isolation cut, k_T, fragmentation function, tomorgraphy

Acknowledgements

smoothly.

It is my pleasure to thank all members from the Institute of Particle Physics (IOPP) and Laboratoire de Physique Subatomique & Cosmologie (LPSC) for their effort to make our institute and laboratory warm and enjoyable, just like a big family. I appreciate the help of Teacher Gao Yanmin, Teacher Wang Jianping, my colleagues like Zhu Xiangrong, Wang Mengliang, Zhu Hongsheng, Huang Meidana, Yuan Xianbao, Zhang Xiaoming, Wan Renzhuo and Yin Xuan, specially the friendship of Wu Pingping, Li Nana, Jin Dan, Xiong Juan, Zhu Lilin, Chen Jiayun and Zhang Fan.

And of course to all people that I have met, appreciates and know me and who have accompanied me physically and psychologically. Finally, last but least in my thoughts, I want to express my heartfelt gratitude to my parents and my elder sisters for their love. And I am always inspired by their belief that I can succeed in doing anything which I want to do.

To all of you,

THANK YOU !

谢谢 !

Merci Beaucoup !

Contents

List of Figures

List of Tables

Chapter 1

Introduction

During the last century, understanding the nature of matter became a long way. Atoms, thought to be indivisible at the end of 19th century, have shown a complex structure, containing a shell of electrons and a nucleus of protons and neutrons also called nucleons. These particles were soon considered as the elementary blocks of matter: the fundamental role of atoms had been taken over by electrons and nucleons.

Series of discoveries, starting with the muon in 1937 followed by pion and kaon in 1947, led to a classification of the constituents of matter in three categories: leptons, that only interact through the electromagnetic and weak forces; hadrons, that interact through the strong force, and the mediators of these three fundamental forces called gauge bosons: the photon for the electromagnetic force, the Z^0 and $W^\pm$ bosons for the weak force, and the gluons for the strong force. The group of leptons consists in the electron, the muon and the tau, the associate neutrinos and their anti-particles for a total of twelve particles, grouped into three generations (Tab. 1.1) [1]. These particles are elementary particles as they have revealed, up to now, no substructure. The large variety of hadrons, and the way they interact, has been explained by the existence of smaller constituent particles, the quarks, where no substructure has been discovered so far down to the scale of 10^{-19} m.

There are six types or flavors of quarks: up (u), down (d), charm (c), strange (s), bottom (b) and top (t), grouped into three generations, each with two quarks (Tab. 1.1). For every quark flavor there is a corresponding antiparticle, named antiquark. It differs from the quark only in that some of its properties have equal magnitude but opposite sign. Quarks have various intrinsic properties: they carry half integer spin and obey Fermi-Dirac statistics, they carry a fraction of the electron

electric charge either $+\frac{2}{3}e$ or $\frac{1}{3}e$. In addition to the electric charge, quarks carry a charge called color which is for the strong force the equivalent of the electric charge for the electromagnetic force. There are three different colors: red, blue and green, and their corresponding anti-colors. Gluons, the gauge boson of the strong interaction, are also colored objects, they carry a color and an anti-color.

Table 1.1: *Matter and interactions in the Standard Model of particles and forces [1].*

Matter particles spin = 1/2						
Generations	Leptons			Quarks		
	Flavor	Mass (GeV/c^2)	Electric Charge	Flavor	Mass (GeV/c^2)	Electric Charge
I	e	0.000511	-1	u	0.005	2/3
	ν_e	$< 7 \times 10^{\,9}$	0	d	0.01	-1/3
II	μ	0.106	-1	c	1.5	2/3
	ν_μ	< 0.0003	0	s	0.2	-1/3
III	τ	1.7771	-1	t	170	2/3
	ν_τ	< 0.03	0	b	4.7	-1/3
Force carriers spin = 1						
Force			Carrier	Mass (GeV/c^2)	Electric Charge	
Electromagnetic			γ	0	0	
Weak			$W^\pm$	80.22	± 1	
			Z^0	91.187	0	
Strong			g	0	0	

Based on their quark structure, hadrons can be divided into two subgroups: hadrons containing one quark and one anti-quark are called mesons, and hadrons consisting of three quarks are called baryons. Baryons are made of three quarks of different colors and mesons of two quarks of a color and its anti-color. Single quarks can not be observed directly as they are always confined in hadrons. This feature can be rephrased as colored objects cannot be observed free in nature, all matter is colorless, a property known as *color confinement* [2]. The confined quarks (*qqq* and

$q\bar{q}$) which determine the quantum numbers of hadrons are called valence quarks. Hadrons also contain virtual quarks called the sea quarks. They do not contribute to the quantum numbers of the hadrons but contribute to its mass. The structure function of the hadrons describes the momentum distribution of the quarks inside the hadron. A great number of hadrons are known until now, most of them differentiated by their quark content and the properties these constituent quarks confer. The existence of "exotic" hadrons with more valence quarks, such as tetraquarks ($q\bar{q}q\bar{q}$) and pentaquarks ($q\bar{q}qqq$), has been conjectured but not proven.

The Standard Model (SM) [1, 3] of elementary particles and their interactions provides a comprehensive description of the subatomic world. The SM is a theory describing the dynamics of the elementary particles under the action of the electromagnetic, weak and strong interactions. As a part of the Standard Model, Quantum Chromodynamics (QCD) [4] is the successful field theory in the sector of the strong interaction acting upon particles carrying a color charge. Since gluons carry color charges, they also interact through the strong force and couple directly to other gluons, a property which makes QCD qualitatively different in character from Quantum ElectroDynamics Theory (QED) [5] due to the fact that photons do not carry any charge. It is an important part of the Standard Model of particle physics. Exact QCD calculations that describe experimentally measurable quantities have not yet been achieved. Instead, approximate calculations are performed using perturbation techniques with expansions in the strong coupling constant α_s, which describes the strength of the strong interaction. The frame for these calculations is known as perturbative Quantum Chromodynamics (pQCD) [6]. The color confinement is described in QCD as a consequence of the dependence of α_s with the momentum transferred (Q^2) between two interacting quarks or gluons,

$$\alpha_s(Q^2) = \frac{12\pi}{(33 \quad 2n_f)\ln(Q^2/\Lambda_{QCD})} \ .$$

(1.1)

where n_f is the number of quark flavors. The characteristic scale, Λ_{QCD}, indicates the momentum beyond which $\alpha_s(Q^2)$ becomes small enough to validate perturbative calculation, typically of the order of the mass of the nucleon.

Another way to view the running character of the strong coupling constant α_s is the dependence with the distance separating the interacting quarks which is modeled by a potential between a quark -antiquark ($q\bar{q}$) pair with a short range repulsive term and a long range attractive term:

$$V_{q\bar{q}} = \quad \frac{\alpha_s(r)}{r} + Kr \ .$$

(1.2)

As r increases, the potential becomes stronger, and consequently the energy to separate quarks

becomes infinite. When this energy is about twice the rest mass of the quark, a new $q\bar{q}$ pair is created from the vacuum which materializes into new hadrons. For small r values of the order of the size of a hadron, the first term in Eq. (1.2) dominates. In the limit $r \to 0$ ($Q^2 \to \infty$), the interaction strength vanishes ($\alpha_s \to 0$): this property is known as *asymptotic freedom* [7]. Processes at small values of Q^2 cannot be calculated perturbatively.

At sufficiently high temperatures or energy densities, QCD inspired calculations predict that the elementary constituents of normal matter are not confined in nucleons anymore and roam freely over a finite volume larger than the volume of the nucleon. This state of matter is called the Quark Gluon Plasma (QGP) [8]. In this new phase mesons and baryons lose their identity and dissolve into a fluid of quarks and gluons, the quarks themselves become the basic degrees of freedom. To perform calculations in the regime where the strong coupling constant is large and to study the transition from normal hadronic matter to deconfined QCD matter, the perturbative approach does not apply. QCD can however be solved by formulating a lattice gauge theory on a grid of points in space and time. This approach is known as Lattice QCD (LQCD) [9]. LQCD calculations have been performed for two- (u, d) and three-flavor (u, d, s) quarks to establish the equation of state of nuclear matter. Fig. 1.1 shows the energy density scaled by the temperature to the fourth power ε/T^4 versus temperature T, the quantity ε/T^4 is related to, for a Boltzmann gas, in classical thermodynamics, the number of degrees of freedom. LQCD calculations have located a phase transition (sudden increase of the number of degrees of freedom while the temperature remains almost constant, and absence of phase coexistence) from normal hadronic matter to the QGP at a critical temperature of $T_C \approx 170$ MeV $\approx 10^{12}K$, and at an energy density $\varepsilon_C \approx 1$ GeV/fm^3. Fig. 1.1 indicates that the first order phase transition is a rapid crossover transition around the critical temperature of T_C. With increasing temperatures beyond the critical temperature, the equation of state reaches asymptotically the Stephan-Boltzmann value of an ideal gas corresponding to $\alpha_s \to 0$.

The schematic nuclear matter phase diagram displays the various phase boundaries: the temperature T versus baryon–chemical potential μ_B (Fig. 1.2) [10], where μ_B is related to the baryon density. Only one point in this diagram is precisely known, the one corresponding to nuclear matter inside the nucleus at $T = 0$ and $\mu_B = 1$ GeV. The critical temperature of the QGP phase transition has been calculated for $\mu_B = 0$.

Following the cosmological model of the Big Bang, the universe was created in an extremely hot and dense phase at $\mu_B = 0$, containing all kinds of quarks, leptons and their antiparticles. It
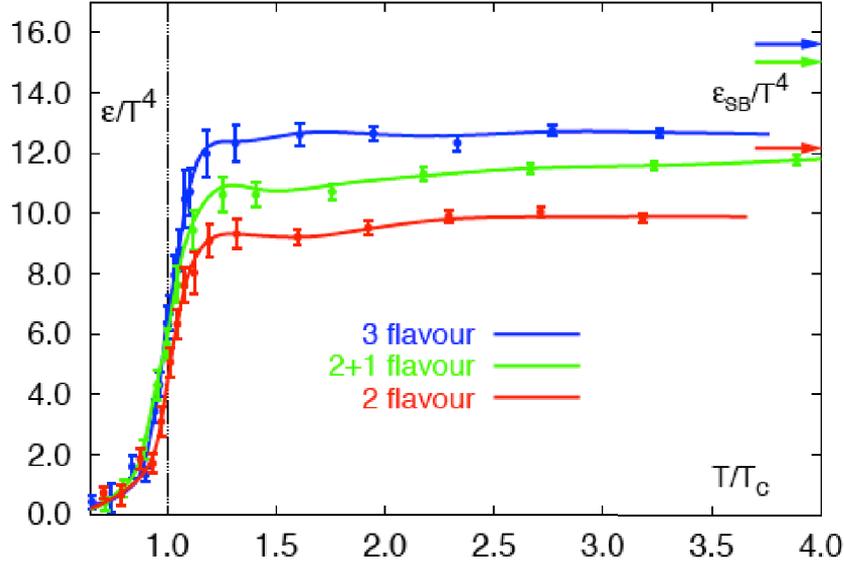
Figure 1.1: *The evolution of the energy density/T^4 as a function of temperature scaled by the critical temperature T_C resulting from Lattice QCD calculation [9]. The arrows on the right side indicating the values for the Stefan-Boltzmann limit.*

stayed in the QGP phase for a few hundred microseconds, until the expansion cooled the universe down to temperature at which the strong force combined quarks to form colorless hadrons. All visible matter in the universe is made from the first generation of matter particles, i.e. u, d and e. Particles of higher generations have greater mass and are less stable, causing them to decay into lower-generation particles by means of the weak interaction.

To explore the phase diagram and "heat up" ordinary matter beyond the phase transition (re-verting time towards the Big Bang conditions), it was suggested by Tsung-Dao Lee in 1974 [11], that collisions of heavy-ions would be the suitable tool to study collective phenomena by distributing a large amount of energy over a large volume. Ultra-relativistic heavy-ion physics was thus born with the aim of applying and extending the Standard Model to complex and dynamically evolving systems of finite size, and to explore the strongly interacting QCD matter under extreme conditions of energy density by exciting normal nuclear matter to high temperatures.

In the past three decades, the phase diagram has been explored in various regions by means of heavy-ion collisions at continuously increasing kinetic energies. Experiments performed at CERN's Super Proton Synchrotron (SPS) [12] in the 1980s and 1990s concluded in 2000 that a "new state of matter" is formed in Pb+Pb collisions at $\sqrt{s_{NN}} = 17.5$ GeV/c with energy densities surpassing the
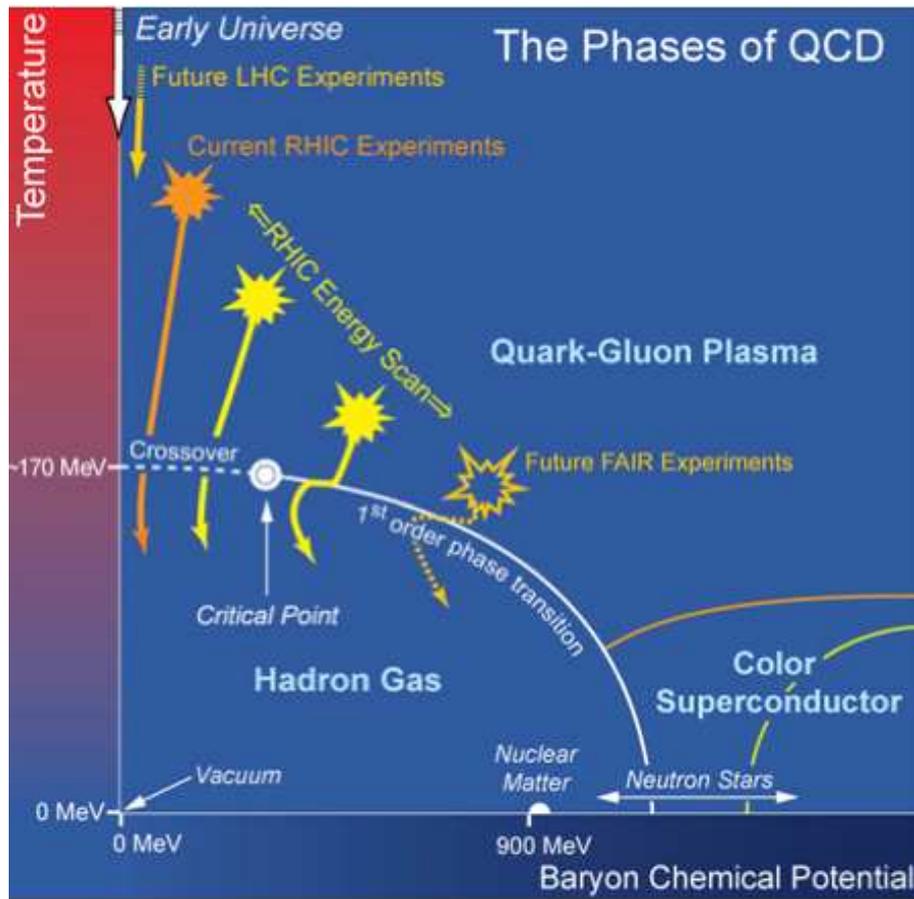
Figure 1.2: *The phase diagram of QCD [10].*

critical value. Current experiments at Brookhaven National Laboratory's Relativistic Heavy Ion Collider (RHIC) are continuing this effort. With center of mass energies up to $\sqrt{s_{NN}} = 200\,\mathrm{GeV}/c$, the deconfined phase of matter was evidenced and some of its properties have been explored quantitatively [13]. The outcome of these studies is so far quite surprising. Although RHIC has formed matter well beyond the critical temperature predicted by LQCD, measurements indicate that matter does no behave as a quasi-ideal state of free quarks and gluons, but, rather, as an almost perfect strongly interacting fluid [14]!

The new experiments, ALICE, ATLAS and CMS, operating at the CERN's Large Hadron Collider (LHC) [88], have now taken the lead in studying the properties of QGP. Thanks to the huge step in collision energy, entering the TeV scale, the largest ever in the history of heavy-ion physics, LHC opens new avenues for the exploration of matter under extreme conditions of temperature. Hot QCD matter is formed at much higher temperatures than RHIC and matter stays in the deconfined phase for a much longer duration strengthening thus the signature emerging from the collision. In addition, deeply penetrating probes or hard probes are abundantly produced in the initial stage of the collision offering the unique opportunity to scrutinize the properties of hot QCD matter.

Among the hard probes, hard scattered quarks or gluons, which materialize in the detector as a jet of hadrons and are dubbed as jets [16], provide a promising probe to investigate the properties of the hot and dense matter. They are produced in the early phase of the collision through hard scattering of the incoming quarks and gluons, and traverse the hot medium which is concurrently produced in heavy-ion collisions. As these auto generated probes are produced with energies significantly larger than the typical temperature of the medium, they decouple from the medium acting similarly to an external probe. Before reaching the detector, the hard scattered quarks or gluons (q, g) fragment into a jet of hadrons (h) with a momentum distribution defined by the jet fragmentation function (f(z) = $\frac{dN}{dz}$ with z = $\frac{p_T^h}{E_{q,g}}$). The comparison of this jet fragmentation measured in proton-proton collisions with the one measured in heavy-ion collisions provides a remarkable observable revealing the modifications inferred on the hard scattered partons by the medium and hence give access to the properties of the medium itself. Ideally, for such a measurement, one needs to know the 4-momentum of the parton as it has been produced in the hard scattering and the 4-momentum after the parton has been modified by the medium. This can be achieved by selecting particular hard processes with a photon in the final state. Since photons do not interact strongly with the medium, its 4-momentum is not modified and thus provides a measure of the

balanced hard scattered parton emitted back to back with the photon (see in Fig. 1.3). Measuring the hadrons emitted opposite to the photon as a function of the fraction of the photon energy carried by the hadrons is thus the most accurate way to measure the jet fragmentation [17] and to quantify the modifications due to the medium. This particular measurement called photon-hadron correlation constitutes the objective of my thesis.
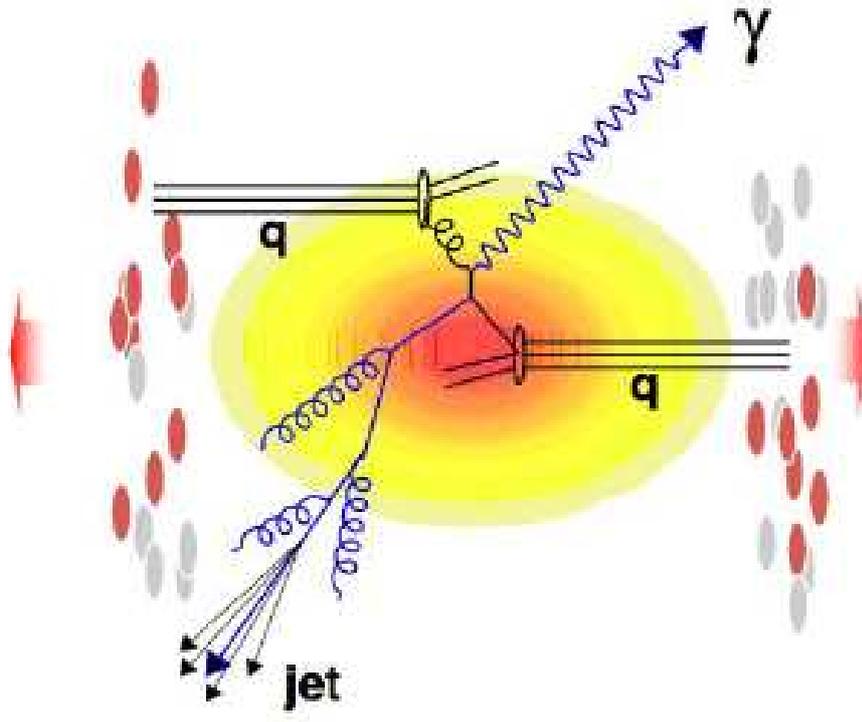
Figure 1.3: *The hard scattering of γ-jet process.*

The aim of the present analysis is to obtain information about inclusive photon-charged hadron correlation distributions in *pp* collisions at $\sqrt{s} = 7$ TeV, which serves as a baseline measurement for further studies in the more complex system of Pb+Pb collisions. I will first discuss a Monte Carlo study used to validate the photon–hadron observables in proton–proton and Pb+Pb collisions at different LHC energies based on LHC running schedule. These data are obtained using sophisticated computer algorithms including various physics generators and the transport of generated particles through a detailed simulation of the ALICE detector. This allows us to tune the reconstruction algorithms required to identify photons from the signal detected by the electromagnetic calorimeter and to calculate the detection and reconstruction efficiencies [18]. I will then present a similar analysis performed on real data from pp collisions data at $\sqrt{s} = 7$ TeV collected by ALICE

detectors with the first LHC run in 2010.

The layout of my thesis is as follows. In Chapter 2, I review the scientific background of heavy ion physics, where the experimental observables exploited so far in different experiments will be listed; Jets and two particle correlations are described in Chapter 3; the experimental apparatus especially ALICE experiment at LHC is introduced in Chap. 4; in Chap. 5, the approach for a feasibility study with ALICE detectors from Monte Carlo data is fully validated; then the two particle correlations with γ/π^0 triggers measured by ALICE within the data collected in 2010 at the first year LHC run is presented in Chap. 6; at the end, a brief summary and outlook for my PhD study is given in Chap. 7.

Chapter 2

Heavy Ion Physics Program

In this chapter, I will briefly discuss aspects of Heavy-Ion Collisions (HIC). Before introducing the anticipated properties of the QGP, I will end up by discussing the main experimental observables allowing the comprehensive study of the new state of matter and the main results obtained by experiments at SPS, RHIC and LHC.

2.1 Relativistic Heavy Ion Collisions

The study of nuclear collisions is not a new endeavor and, in fact, predates the quark model. The history of the field can be traced back to the HILAC (Heavy Ion Linear Accelerator) at Berkeley, the first dedicated heavy-ion accelerator, which entered into operation in 1957. The objectives of the field at the time were the creation of new elements by nuclear transmutation and the investigation of radiation damage to human tissue for space travel [19]. During the 1970's a new paradigm began to emerge in which heavy-ion collisions were viewed as a tool to study the equation of state of matter at high temperature and density, conditions thought to govern the behavior of matter inside neutron stars. Following the suggestion of T. D. Lee [11], the creation of the Quark Gluon Plasma (QGP), a fundamentally new state of matter, is expected to be realized in the laboratory by colliding high energy heavy-ions. However, a heavy-ion collision is a complex system with a fast thermodynamic evolution during which the system passes a fleetingly short time through the QGP phase of interest. Therefore, understanding the thermodynamic evolution of the heavy-ion colliding system is a pre-requisite before one can reliably extract from various observables effects revealing the existence and properties of QGP.

In high energy collisions of heavy-ions accelerated at ultra-relativistic high energies ($E \gg mc^2$), the two Lorentz contracted nuclei (A) appear to the fixed observer as two thin disks, traversing each other. The geometrical overlap region is parameterized by the impact parameter "b", defined as the distance between the center of nuclei in the heavy-ion collisions. In a nucleus-nucleus collision two types of nucleons are considered: the "participants" which are taking part in the primary collisions, and the "spectators" which do not take part in the collisions. The spectators go through the collision region keeping their initial velocity. Many inelastic nucleon-nucleon collisions, among the participants, with secondary particle productions and emission into all directions take place in a very short time, depositing a large amount of energy in the small region of space defined by the participants region (Figure 2.1). This energy can be converted into new degrees of freedom
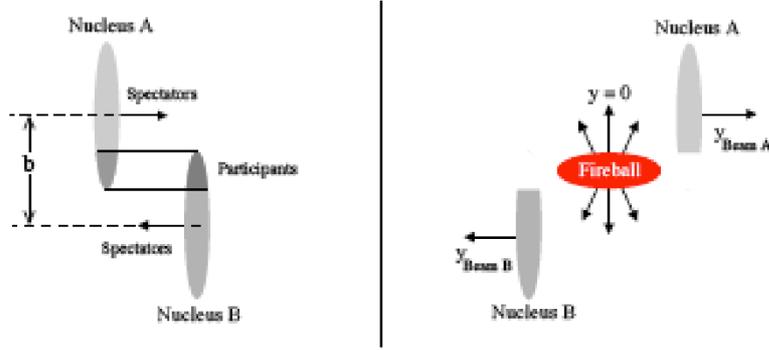
Figure 2.1: *Schematic view of two colliding nuclei in the geometrical participant-spectator model. The distance between the centers of the two Lorentz contracted nuclei is the impact parameter b.*

to produce the QGP. The amount of deposited energy depends on the thickness of the nuclei ($\propto A^{1/3}$) and on the collision energy ($\sqrt{s}$). For low collision energies, the rapidity distribution y (y is the relativistic analogue of longitudinal velocity) of the produced particle density is peaked at mid-rapidity, i.e. the center of mass of the collision, whereas for high energy collisions the particle density is constant around mid-rapidity and the net baryon density is zero with peaks near the beam rapidity. From the cartoon of Fig. 2.2, one sees that the main feature of nuclear collision changes from stopping to transparency with increasing beam energy. In other words, there is saturation of nuclear stopping, the incident nucleons do not lose all their kinetic energy, but punch through the opponent nucleus [20]. In the region between the two fast traversing nuclei, hot matter is formed with energy densities much larger (100 times larger at LHC energies) than the energy density of normal nuclear matter ($\varepsilon = 0.15$ GeV/fm^3). These high energy densities enable to excite quark-antiquark pairs out of the vacuum and to form a baryon free medium (net baryon number
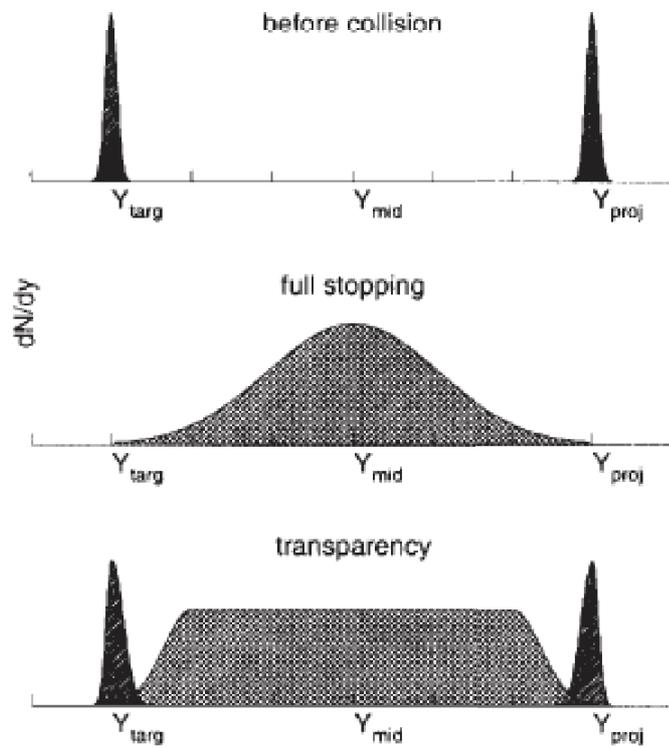
Figure 2.2: *Nuclear stopping scenarios. Th particle rapidity are given before the collision and after the collision in the case of a full stopping (Landau) and complete transparency (Bjorken).*

$\mu_B = 0$) which can evolve into an equilibrated QGP through a cascade of parton scatterings. The QGP evolves further like a fluid following the equations of hydrodynamics: it expands and cools down until the system reaches the critical temperature of the QGP phase transition and condensates into ordinary hadronic matter. The system continues to evolve hydrodynamically until interactions among the constituents cease and final state particles freely stream towards the detectors to provide the final state observables.

The Bjorken space-time evolution [21] of a relativistic heavy-ion collision is schematized in more details in Fig. 2.3 as the evolution of the longitudinal spatial coordinate z with time t. Here z is the coordinate along the collision axis, with $z = t = 0$ being the point of the collision. The following various stages can be identified:
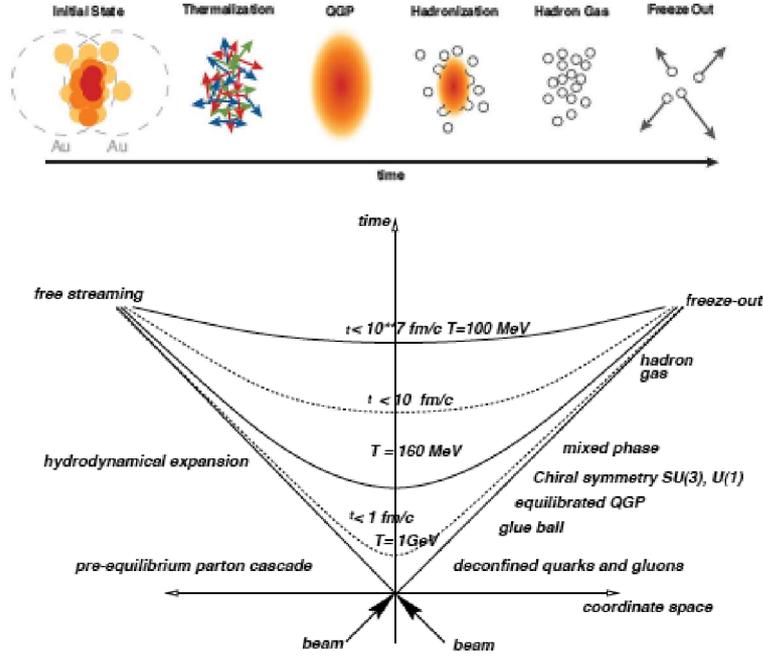
Figure 2.3: *The space-time evolution of the system in center-of momentum frame in relativistic heavy ion collisions according to Bjorken [21].*

- *Initial conditions*: The initial conditions are defined by the proper time τ_0 ($\tau = \sqrt{t^2 \quad z^2}$) starting at $z = t = 0$. The nucleons of the colliding nuclei are resolved into their parton substructure according to the measured nucleon or nucleus structure functions and yield the initial parton distribution. Because of the Lorentz contraction, the gluons inside one colliding ion appear to the other colliding ion as a gluonic wall traveling near the speed of

light and with densities increasing strongly with the collision energy or equivalently at very small values of $x = \frac{2p_T}{\sqrt{s}} \ll 0.1$ (x is the fraction of the longitudinal momentum carried by the parton).

- *Pre-equilibrium*: In the pre-equilibrium phase the dynamic of partons is described as a cascade of freely colliding partons. The space-time evolution of the partons distribution is described by a transport equation where the collision term is described by QCD processes calculated within the pertubative approximation. The main hypothesis (factorization theorem) is that the collisions during the cascade are independent of each other and that the pertubative aspects (the scattering) and the non-pertubative aspects (the structure function) can be factorized. This stage features the creation of high transverse momentum (p_T) partons, which can be used to probe the subsequent stages of the collision through their interaction with the nuclear medium.

- *Chemical and thermal equilibrium*: The subsequent multiple parton scattering brings the matter to local equilibrium. Chemical equilibrium is driven by the two-body reactions and gluon multiplication and its inverse process, gluon fusion. After the time τ_0 where the system is at thermal equilibrium, the system evolves to the law of hydrodynamics. Relativistic hydrodynamics is then used to describe the expansion of the hot and compressed central region. Until the interacting medium is thermalized, the hot and dense matter, consisting of quarks, anti-quarks and gluons (the QGP) will be formed. The average energy deposited by unit of rapidity $d<E>/dy$ reached at thermal equilibrium ($t = \tau_0$) is estimated using the rapidity y definition:

$$
\begin{aligned}
y &= \frac{1}{2}\ln\frac{E+p_z}{E-p_z}, \\
&= \frac{1}{2}\ln\frac{t+z}{t-z}(v_z = \frac{z}{t} = \frac{p_z}{E}),
\end{aligned} \tag{2.1}
$$

as well as the longitudinal thickness, $2d$, of the expanding medium and the overlap area S ($S = \pi(r_0 A^{1/3})^2$, r_0 is the nucleon radius and A is the nucleus number) as:

$$
\begin{aligned}
E &= \frac{d<E>}{dy}\Delta y, \\
&= \frac{d<E>}{dy}\frac{2d}{\tau_0},
\end{aligned} \tag{2.2}
$$

The energy density can be deduced from the measured particle density, dN/dy ,

$$
\begin{aligned}
\varepsilon_0 &= \frac{E}{2dS}, \\
&= \frac{1}{S}\frac{1}{\tau_0}\frac{d<E>}{dy}, \\
&= \frac{1}{\tau_0\pi r_0^2 A^{2/3}}\frac{d<E>}{dy}, \\
&= \frac{<E_T>}{\tau_0\pi r_0^2 A^{2/3}}\frac{dN}{dy},
\end{aligned} \tag{2.3}
$$

where, $<E_T>$ is the mean transverse energy of the produced particles. In this equation, $\frac{d<E>}{dy}|_{y=0} = <E_T> \cdot dN/dy$ is assumed at $y=0$ [22].

- *Hadronization and freeze-out*: The system continues to expand and cool down fast through strong interactions and reaches quickly the critical temperature $T_c \simeq 170$ MeV, where the hadronization takes place and a hadron gas is formed. The created hadron gas expands and cools till the distance between hadrons is large enough so that they stop interacting (freeze-out temperature, $T_f \sim 100$ MeV) and stream out of the collision region.

2.1.1　Centrality

To characterize the relativistic heavy-ion collisions and to study the nuclear phenomena in the collisions systematically, the *centrality* parameter is used. The degree of centrality C of a given subset of collisions is expressed at a given impact parameter b_C as:

$$
C = \frac{\int_0^{b_C} 2\pi\sigma_{AA}bdb}{\int_0^{b_{max}}\sigma_{AA}} . \tag{2.4}
$$

It represents the probability that the collision occurs for impact parameter $b < b_C$ [23]. Since the impact parameter is not directly measurable, experimentally one can measure C through the number of participants $N_{\mathrm{p}art}$ or the number of spectators $N_{\mathrm{s}pec}$. The number of participants $N_{\mathrm{p}art}$ is the number of nucleons contributing to the collision in the participant overlap region. The number of spectators can be deduced from measurement at zero degree with respect to the beam axis by calorimetry techniques and the number of participants through the measurement of the number of low p_T charged particles emitted in the transverse direction. It refers collectively to the soft processes producing these particles. Hard processes scale with the number of collisions N_{coll}, i.e. the number of participants which have experienced at least one scattering. In a central collision, b is equal to zero and the number of participants $N_{\mathrm{p}art}$ is equal to the total number of nucleons in both nuclei. The term *central collisions* refers to collisions with $0 < C < 0.1$ and

peripheral collisions are defined with $0.9 < C < 1$. Collisions without any selection in C are called *minimum-bias collisions*. The average number of nucleon-nucleon collisions $< N_{coll} >$ at an impact parameter b is given by $< N_{coll}(b) >= T_{AA}(b)\sigma_{pp}$, where σ_{pp} is the total proton-proton inelastic cross section.

For each centrality, the geometric parameters of nucleus-nucleus collisions (N_{part}, N_{coll}, $T_{AA}(b)$, and b) are estimated with the Glauber model [24]. $T_{AA}(b)$ is the nuclear overlapping function defined as:

$$T_{AA}(b) = \int d\mathbf{r^2}\mathbf{T_A}(\mathbf{r})\mathbf{T_A}(|\mathbf{r} - \mathbf{b}|), \tag{2.5}$$

where

$$T_A(\mathbf{r}) = \int dz\rho_A(\mathbf{r}, z). \tag{2.6}$$

The nucleon distribution inside the nucleus is assumed to follow a Woods-Saxon density profile:

$$\rho_A(r) = \frac{\rho_0}{1 + \exp\left(\frac{r - r_0}{a}\right)}, \tag{2.7}$$

where r is the distance from a given point of the nucleus to the center of the nucleus. The parameters a and r_0 are obtained empirically from electron scattering experiments. The model provides a quantitative consideration of the geometrical configuration of the nuclei when they collide, and basically describe the nucleus-nucleus interaction in terms of the elementary nucleon-nucleon cross section measured in proton–proton collisions.

2.2 Particle Production

Properties, such as phase space distribution and relative abundance of particle species, of the final state hadrons provide significant information of the heavy ion collision dynamics and reflect the properties of the colliding system at the time of freeze-out. We will discuss separately soft probes reflecting the collective dynamics of the collision at equilibrium and hard probes reflecting the dynamics at the partonic level during the pre-equilibrium phase of the collision.

2.2.1 Soft Particles Production

In high energy heavy-ion collisions, local equilibrium and collective behavior are established following multiple scatterings. The final state particle species ratio can be interpreted in terms of chemical equilibrium of the system at chemical freeze-out. These ratios can be described by thermodynamical statistical models, based for example on the grand canonical ensemble describing

the partition function. The particle density n_i of particle specie i, at the chemical freeze-out temperature T_{ch}, is described in such an approach as:

$$n_i = \frac{g_i}{2\pi^2} \int_0^\infty \frac{p_i^2 dp_i}{exp[(E_i\mu_i)/T_{ch}] \pm 1} \ . \tag{2.8}$$

where g_i is spin degeneracy factor, p_i is the momentum of particle i, E_i is its energy, and $\mu_i = \mu_B B_i \quad \mu_S S_i \quad \mu_{I_3} I_i^3$ is the chemical potential. The quantities B_i, S_i and I_i^3 denote the baryon, strangeness and third-component of the isospin quantum numbers respectively. In this model, T_{ch} and μ_B, which are independent parameters, are the free parameters used to fit the calculated n_i to the data.

Figure 2.4 shows particle ratios measured in central collisions at $\sqrt{s_{NN}} = 200$ GeV [25] compared with the particles ratio calculated with a thermal model for $T_{ch} = 177 \pm 7$ MeV and $\mu_B = 29 \pm 8$ MeV, the best fit values [26]. It is interesting to note that the resulting T_{ch} is surprisingly close to the prediced critical temperature of the QGP phase transition indicating that the chemical composition of the hadron gas is established instantaneously at the phase transition.
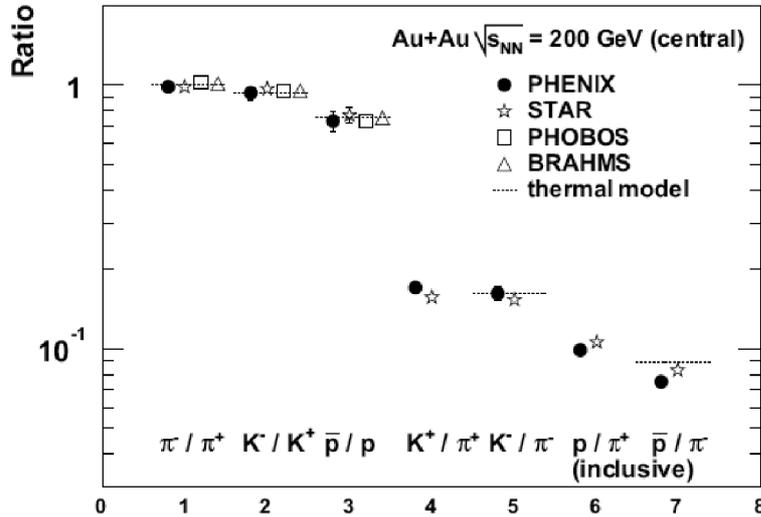
Figure 2.4: *Particle ratios [25] in central collisions at $\sqrt{s_{NN}} = 200$ GeV at mid-rapidity with thermal model prediction [26] compared with PHENIX, PHOBOS, BRAHMS, and STAR.*

Following chemical freeze-out, the relative particle abundances are fixed but hadrons continue to interact through elastic scatterings in the expanding system. When the mean free path of hadrons

becomes comparable to the size of the system, kinetic freeze-out is reached and the momentum of hadrons is frozen. Kinetic equilibration is visible predominantly in the transverse degrees of freedom and temperatures can be measured from the spectral slope of the low energy part of the transverse momentum ($p_T = \sqrt{p_x^2 + p_y^2}$, z being the beam axis) or transverse mass ($m_T = \sqrt{m_0^2 + p_T^2}$, where m_0 is the rest mass) distributions. The equation of state, the energy density ε versus temperature T, can be probed experimentally by the correlation of the mean transverse momentum $< p_T >$ of hadrons and the rapidity particle density dN/dy or the transverse energy density dN/dE_T generated in the collision. If a phase transition occurs, one expects to observe a rupture in the monotonously rise of p_T and a saturation of $< p_T >$ when the number of degrees of freedom changes.

The invariant cross section for particles with four-momentum, (E, p_x, p_y, p_z), is given by,

$$
\begin{aligned}
E\frac{d^3\sigma}{dp^3} &= E\frac{d^3\sigma}{dp_x dp_y dp_z}, \\
&= \frac{d^3\sigma}{p_T dp_T dy d\phi}, \\
&= \frac{1}{2\pi p_T}\frac{d^2\sigma}{dp_T dy},
\end{aligned} \tag{2.9}
$$

where ϕ is the azimuthal angle of the observed particles.

2.2.2 Hard Particles Production

High p_T hadrons, remnants of high p_T partons produced in the early phase of the collision through hard scattering are particularly interesting probes of the medium created concurrently in heavy-ion collisions.

The cross section for the production of these high-p_T hadrons is calculated within the factorization theorem separating pQCD calculable parton cross section (σ) and non-perturbative processes such as the parton distribution function (f) and the fragmentation function (D) (see Fig. 2.5). The production cross section of a hadron h in a nucleus-nucleus collision $A + B$ is, in this formalism, written as:

$$
\sigma^{AB \to hX} = \sum_{abcd} \int dx_a dx_b dz_c \cdot f_{a/A}(x_a, Q^2) \cdot f_{b/B}(x_b, Q^2) \cdot \sigma(ab \to cd) \cdot D_{h/cd}^0(z_{cd}, Q^2), \tag{2.10}
$$

where $f_{a/A}(x_a, Q^2)$ ($f_{b/B}(x_b, Q^2)$) is the Parton Distribution Function (PDF) of the initial parton "a" ("b") in the initial nucleus "A" ("B"), $D_{h/cd}(z_{cd}, Q^2)$ is the Fragmentation Function (FF)
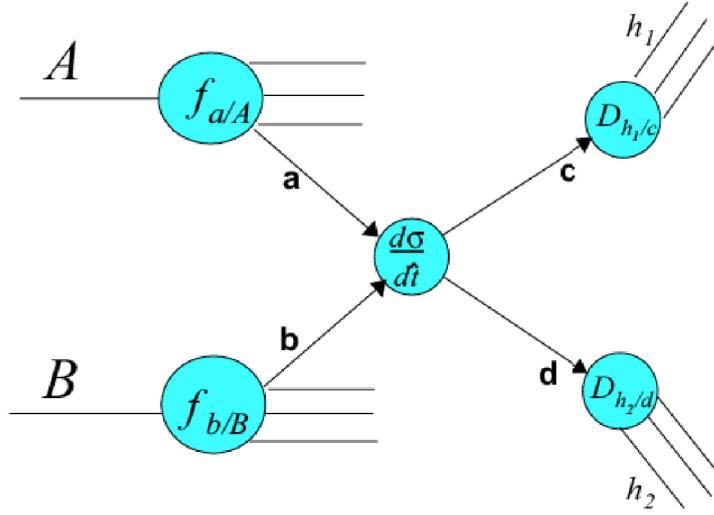
Figure 2.5: *The diagram of calculation for hard scattering.*

from the final "c" ("d") parton to the hadron h, and x is the fraction of the nucleus momentum carried by the colliding parton, and z is the fraction of the scattered parton momentum taken by hadron h.

The PDF, gives the probability that a parton of type i carries a fraction x of the particle (longitudinal) momentum. It can not be computed by perturbative methods but, PDFs are defined in a way that the momentum distributions of partons within a particle are universal, and their evolution with the factorization scale is predicted by the DGLAP equations [27]. In other words, the PDFs derived from any process at a given energy scale can be applied to other processes at any energy scale. The PDFs are obtained as a parameterization using measured nuclear structure function $F_2(x, Q^2)$ [28] in lepton deep inelastic scattering (DIS) experiments. For example, the CTEQ group [29] provides the parameterized PDF [30] as shown in Fig. 2.6.

The fragmentation function (FF), $D_{h/p}^0(z, Q^2)$, is the probability of finding a given hadron with a fraction $z = p_T^h / E_T^{parton}$ of the original parton longitudinal momentum at some fragmentation scale μ_f, which is typically related to the transverse momentum of final state hadrons (Figure 2.7).

The hard scattering cross section $\sigma(ab \to cd)$, is calculated in pQCD up to some order of α_s. Leading order (LO) and next-to-leading order (NLO) pQCD calculations succeed in describing high-p_T particle production in high-energy nucleon-nucleon collisions [32]. Figure 2.8 shows the π^0 spectra measured by ALICE in pp collisions at $\sqrt{s} = 7$ TeV (Chapter 6 for details), together
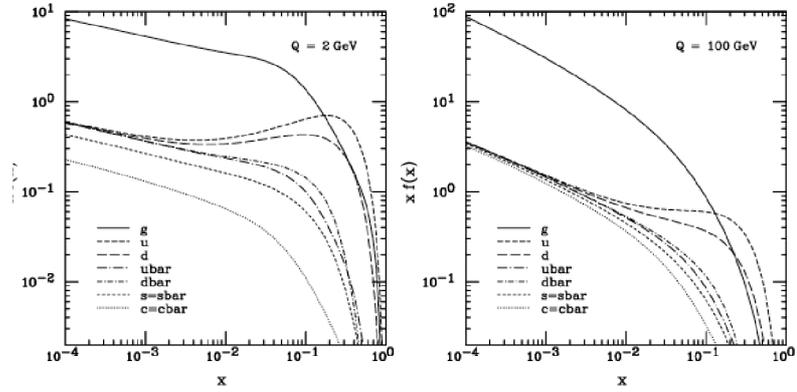
Figure 2.6: *Parton distribution function by the CTEQ group as a function of x at Q = 2 GeV (left) and 100 GeV (right) [30].*
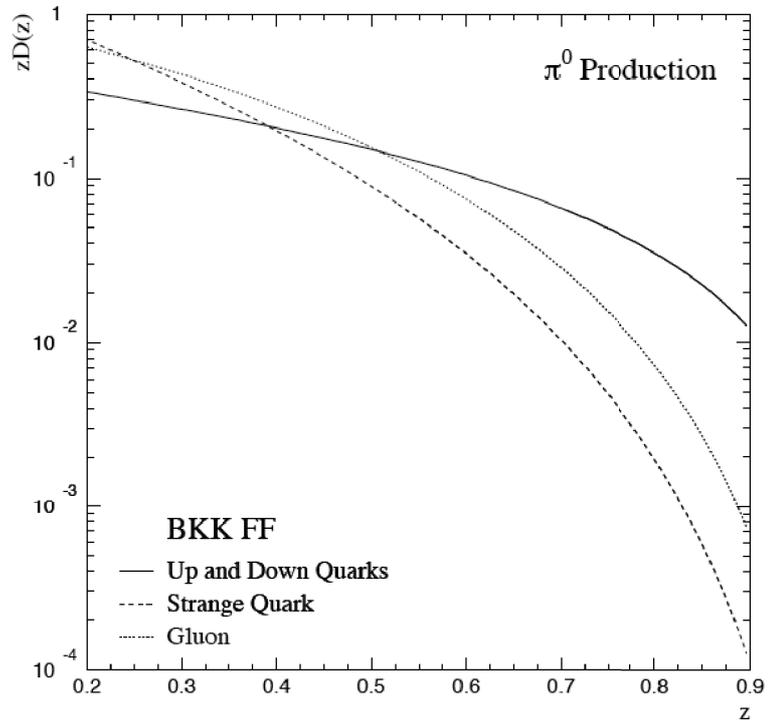
Figure 2.7: *Probability that a given parton will fragment into a π^0 as a function of the momentum fraction z of the π^0. These fragmentation functions were evaluated at $Q^2 = 10$ GeV^2 [31].*

with a NLO pQCD calculations [32]. The data are correctly described by pQCD at high-pT, which indicates that the particle production at high-p_T is dominated by the fragmentation of hard-scattered partons in this regime. The description is however not perfect (a discrepancy of the order of 20%) which reflects the need for refined pQCD calculations in the new E domain probed by LHC.
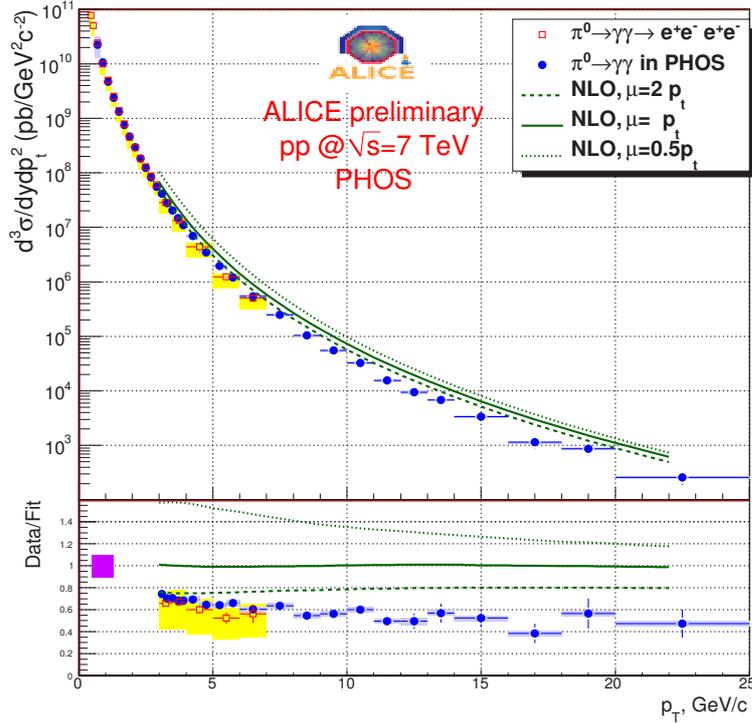
Figure 2.8: *The invariant differential cross section for inclusive π^0 production (points) and the results from NLO pQCD calculations in $\sqrt{s} = 7$ TeV pp collisions. The relative difference between the data and the theory using KKP [33] and CTEQ5M [29] sets of fragmentation functions with scales of $p_T/2$, p_T and $2p_T$ respectively.*

2.2.3 Nuclear Effects Modifying Particles Production

Assuming the absence of nuclear medium effects, a nucleus-nucleus collision can be considered as a superposition of independent nucleon-nucleon collisions. Thus, the cross section for hard processes would scale from pp to AA with the number of inelastic nucleon-nucleon collisions (N_{coll}) according to binary scaling of hard processes. The nuclear effects are usually divided in two sources: initial state or cold nuclear medium effects and final state or hot nuclear medium effects.

- *Cold nuclear medium effects*: These initial state effects modify the hadron production cross section in a way depending on the size and energy of the colliding nuclei. For instance, followings are known as initial state effects:

Cronin effect: It was observed in $p+A$ collisions [34] that the hadron production cross section instead of simply scaling with the number of nucleons A follows the functional parametrization:

$$E\frac{d^3\sigma}{dp^3}(p_T, A) = E\frac{d^3\sigma}{dp^3}(p_T, 1)A^{\alpha(p_T)} \tag{2.11}$$

to account for the observed enhancement of particle production compared to the expectation deduced by N_{coll} scaling from pp collisions. The enhancement is explained as a result of multiple scattering of the incident partons while passing through the nucleus A prior to the hard scattering. Multiple scattering smears also the axis of the hard scattering relative to the axis of the incident beam generating transverse momentum.

Nuclear shadowing: It was discovered by the EMC group that the structure function $F_2(x, Q^2)$ per nucleon in iron differs significantly from that of a free nucleon [35]. This initial state nuclear effects, are quantified by the ratio of structure functions, $F_2^A(x, Q^2)/F_2^D(x, Q^2)$, where $F_2^D(x, Q^2)$ is the deuterium structure function used as the reference. Figure 2.9 shows a collection of data for different nuclei [36], revealing clear deviations from unity. The nuclear effects in the ratio are usually divided into the following regions in Bjorken x ($\sim \frac{2p_T}{\sqrt{s_{NN}}}$): shadowing where $F_2^A(x, Q^2)/F_2^D(x, Q^2) \leq 1$ at $x \leq 0.1$; anti-shadowing where $F_2^A(x, Q^2)/F_2^D(x, Q^2) \geq 1$ at $0.1 \leq x \leq 0.3$; EMC effect with $F_2^A(x, Q^2)/F_2^D(x, Q^2) \leq 1$ at $0.3 \leq x \leq 0.7$ and Fermi motion at $x \geq 0.7$. This indicates that the parton distributions of bound protons are different from those of the free protons. The p_T region ($1 \leq p_T \leq 20$ GeV/c) of hadrons measured at mid-rapidity at LHC energies corresponds to the nuclear shadowing region ($x \leq 0.01$).

- *Hot nuclear medium effects*: These final state effects are the result of the QGP medium created at high temperature and density that modify the yields and the kinematic distributions of the produced hard scattered partons. They depend strongly on the properties of the medium (gluon density, temperature and volume). An energetic parton passing through matter looses its energy due to the interactions with the medium by the elastic scatterings with other partons (collisional energy loss) or radiating soft gluons (radiative energy loss) [37]. As the consequence, the yield of final state high p_T hadrons is suppressed while the yield of low p_T hadron yield is enhanced, this phenomenon is named *jet quenching* [38]. Theoretically,
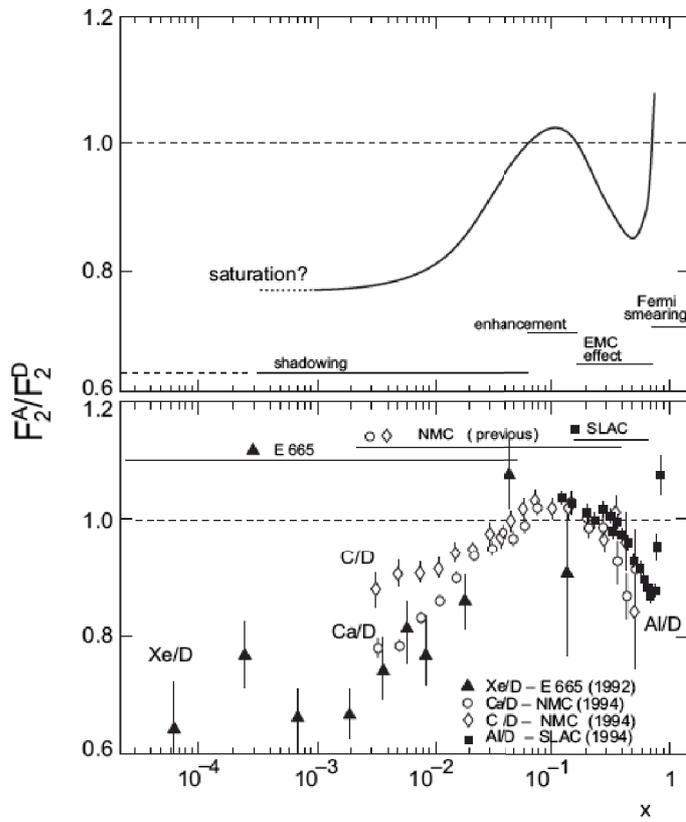
Figure 2.9: *A phenomenological curve and some experimental data for nuclear effect on structure function, F_2^A/F_2^D, from [36].*

the strength of the energy loss is quantified in terms of a single parameter, either the gluon density dN_g/dy (GLV-type models) [39] or the transport parameter $\hat{q}$, defined as the average momentum transfer squared per-unit path-length (BDMPS-type models) [40]. For a static medium [41], the energy loss depends quadrically on the path-length (L), $\Delta E \propto \hat{q}L^2$. For an expanding medium, the dependence may reduce to linear ($\Delta E \propto L$) [39].

In order to distinguish the influence of different effects, a systematic study of the effects in pp, pA and AA collisions is required. Initial state effects can be studied in pp and pA (cold nuclear effects) collisions and then reliably extrapolated to AA (hot nuclear effects). If the hot QCD medium is formed in AA collisions, the final state effects will be significantly stronger than in pA.

2.3 Probes of the QGP

In order to understand the collision dynamics and study the properties of QGP and the phase transition, experimentally one can only proceed from the measurement of final state particles. Indirect information must be inferred from the hadrons, leptons and photons produced in the collisions. Hadrons are copiously produced, but interact strongly with each other well after the transition from QGP to the hadron gas. This tends to obscure the information they carry about the system prior to the transition, but they provide information on the thermodynamic conditions at freeze out. On the other hand, leptons and photons, which are produced at all stages of the collisions and interact weakly with the rest of the system, can better reflect the properties of the system at the time they were produced. However, directly produced leptons and photons are rare in comparison to hadrons, and the information they carry can be obscured by the large background which comes from the decay of hadrons.

Many observables have been proposed to probe the high energy density of the medium created in ultra-relativistic heavy ion collisions, including the global probes to characterize the collision itself and the observables characterizing the medium produced in the collisions.

2.3.1 Global observables characterizing the collision

The measurement of global observables such as the transverse energy E_T or the rapidity distribution of charged particles allows us to determine the global properties of the collision. The first step in characterizing the system produced in the collision is the measurement of the charged-particle pseudorapidity density, which constrains the dominant particle production mechanisms

and is essential to estimate the initial energy density. The dependence of the charged-particle density on energy and system size reflects the interplay between hard parton-parton scattering processes and soft processes. The charged particle pseudorapidity density at mid-rapidity measured in Pb+Pb collisions at $\sqrt{s_{NN}} = 2.76$ TeV with ALICE is compared to similar measurements in heavy-ion and pp collisions over a wide range of collision energies [43]-[49] (Fig. 2.10 [42]). We observe that the heavy-ion value measured at LHC is significantly larger than those measured at lower energies at RHIC and that the energy dependence ($\propto s_{NN}^{0.15}$) is stronger in heavy-ion collisions than in pp collisions ($\propto s_{NN}^{0.11}$) reflecting a large nuclear amplification factor.
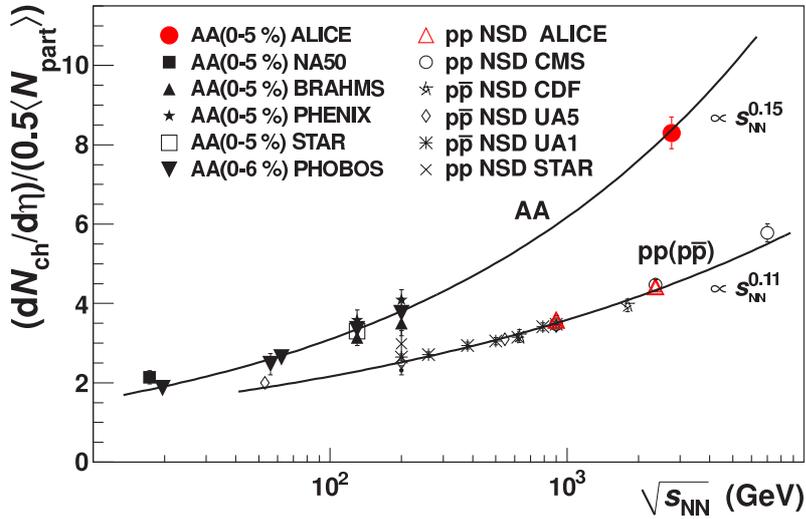
Figure 2.10: *Charged particle pseudorapidity density per participant pair for central nucleus-nucleus [43]-[47] and non-single diffractive pp (p$\bar{p}$) collisions [48]-[49], as a function of $\sqrt{s_{NN}}$. The solid lines $\propto s_{NN}^{0.15}$ and $\propto s_{NN}^{0.11}$ are superimposed on the heavy-ion and pp (p$\bar{p}$) data, respectively [42]*

Two-particle correlation measurements, known as Hanbury Brown-Twiss (HBT) interferometry measurements [50], is a precision tool to probe the dynamically generated geometry of the particles emitting system. The expansion rate and the spatial extent at decoupling (when particles cease to interact together) are accessible via such a measurement which exploits the Bose-Einstein enhancement of identical bosons emitted close in phase space. Within hydrodynamical scenarios, the decoupling time for hadrons at mid-rapidity can be estimated in the following way. The size of the homogeneity region is inversely proportional to the velocity gradient of the expanding system. The longitudinal velocity gradient in a high energy nuclear collision decreases with time as $1/\tau$ [21]. Therefore, the magnitude of the Gaussian HBT radii along the beam axis R_{long} is proportional to the total duration of the longitudinal expansion, i.e. to the decoupling time of the system [51].

The decoupling time extracted from ALICE HBT measurement in central Pb+Pb collisions at $\sqrt{s_{NN}} = 2.76$ TeV is shown in Fig. 2.11 [52], together with the results at lower energies [53]-[57]. It is found that the decoupling time τ_f scales with the cube root of the charged particle pseudorapidity density and reaches 10-11 fm/c in central Pb+Pb collisions at $\sqrt{s_{NN}} = 2.76$ TeV, which is 40% larger than at RHIC. Similarly the homogeneity volume is found to be larger by a factor of two at the LHC energy than at the RHIC highest energy. We conclude that the fireball formed in nuclear collisions at the LHC is hotter, lives longer, and expands to a larger size at freeze-out as compared to lower energies [52].
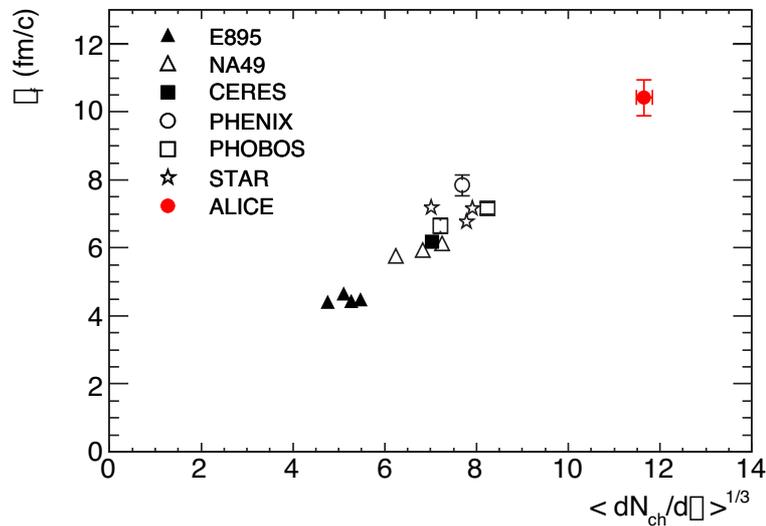
Figure 2.11: *The decoupling time extracted from R_{long} [52]. The ALICE result is compared to those obtained for central gold and lead collisions at lower energy at the AGS [53], SPS [54]-[55] and RHIC [56]-[57].*

2.3.2 Observables characterizing the medium

- Flow Measurements of the collective motion, or flow, of final state particles produced in heavy-ion collisions provide a probe of collective properties of the colliding system. It results from interactions among the soft particles in the dense medium, and thus provides information on the equation of state and the transport properties of the matter created in heavy ion collisions. If particles have a common expanding velocity β, their purely thermal transverse momentum spectrum is modified by the so called radial flow by a change of the slope parameter T so that:

$$T \approx T_f + \frac{1}{2}m\beta^2,\tag{2.12}$$

where T_f is a measure of the freeze-out temperature and m is the mass of particles. Other components of the flow are measured through the azimuthal distribution of particles with respect to the reaction plane ($\phi \quad \phi_0$, the reaction plane is defined by the impact parameter vector b and the direction of the colliding beams z). The flow components are deduced by describing this distribution as a Fourier expansion [58]:

$$\frac{dN}{d\phi} = \frac{1}{2\pi}\{1 + 2\sum_n \nu_n \cos[n(\phi \quad \phi_0)]\} \,. \tag{2.13}$$
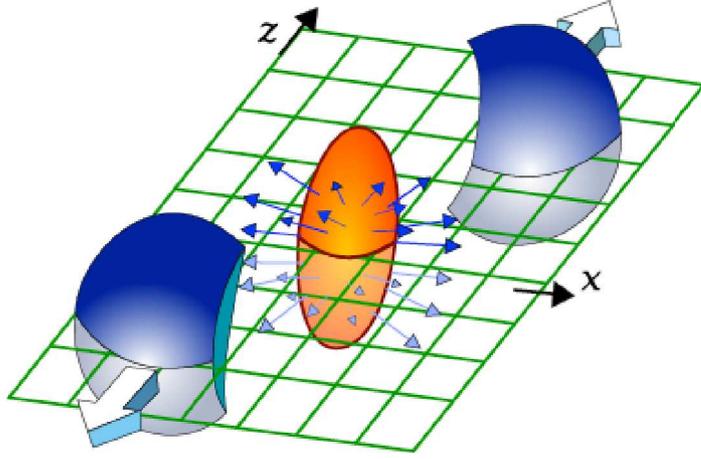
Figure 2.12: *The ellipsoidal shape of participant in non-central high energy nucleus-nucleus collisions.*

The second harmonic coefficient ν_2 of Eq. 2.13 is called *elliptic flow* and is sensitive to the geometry of the collision region in the early stage of the collisions (Fig. 2.12). The larger pressure gradient in the small axis direction of the almond shape results in a larger boost of the particles towards this direction. This causes an increase of the particle emission in the reaction plane with respect to those emitted perpendicularly to the reaction plane. Elliptic flow is a fundamental observable since it directly reflects the initial spatial anisotropy, of the nuclear overlap region in the transverse plane, directly translated into the observed momentum distribution of identified particles. Since the spatial anisotropy is largest at the beginning of the evolution, elliptic flow is especially sensitive to the early stages of system evolution. A measurement of elliptic flow thus provides access to the fundamental thermalization time scale and thermodynamics properties of the medium in the early stages of a relativistic heavy-ion collision.

The elliptic flow ν_2 for centrality 40-50% as a function of p_T in Pb+Pb collisions at $\sqrt{s_{NN}} = 2.76$ TeV has been measured by ALICE experiment (Fig. 2.13) [59]. The results from STAR measurements [60, 61] for the same centrality in Au+Au collisions at $\sqrt{s_{NN}} = 200$ GeV are very similar to the ALICE ones, which is an indication that the medium formed at RHIC and LHC have very similar characteristics.
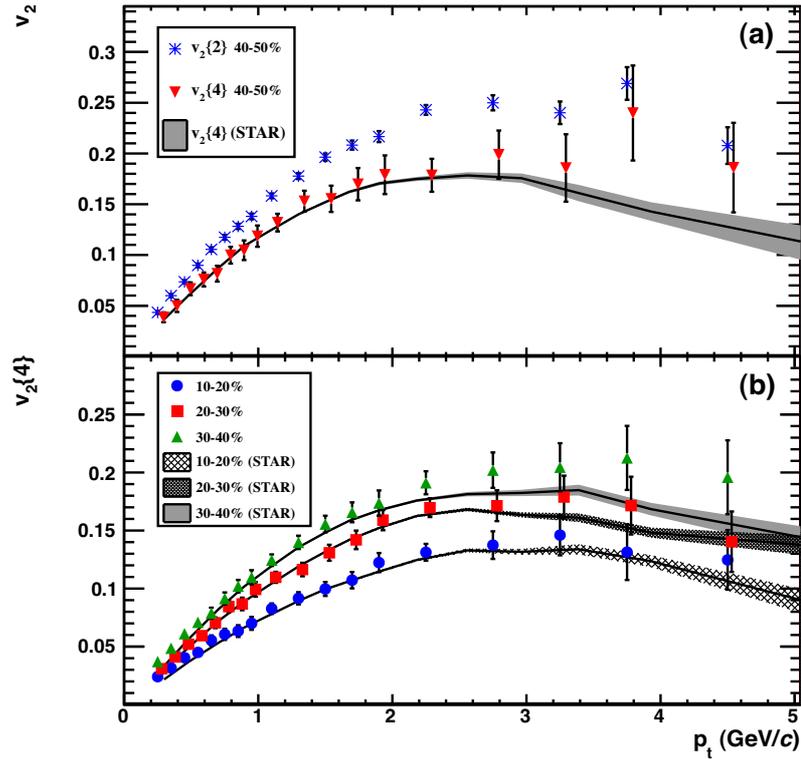
Figure 2.13: *Measured charged particle ν_2 as a function of p_T in Pb+Pb collisions at $\sqrt{s_{NN}} = 2.76$ TeV [59]. a) $\nu_2\{2\}$ for the centrality bin 40–50% from the 2- and 4-particle cumulant methods for ALICE measurement and for Au–Au collisions at $\sqrt{s_{NN}} = 200$ GeV in RHIC measurements. b) $\nu_2\{4\}$ for various centralities compared to STAR measurements. The data points in the 20–30% centrality bin are shifted in p_T for visibility.*

The partonic nature of the medium in which the elliptic flow is generated is revealed in the observation of constituent quark scaling. Figure 2.14 shows the elliptic flow for mesons and baryons in Au+Au collisions at $\sqrt{s_{NN}} = 200$ GeV measured at RHIC [62]. The baryon and meson data lie nearly perfectly on the same curve when the ν_2 values are scaled by the number of quarks and plotted as a function of the, similarly scaled, transverse kinetic energy. This observation indicates that the relevant degrees of freedom at the time of elliptic flow generation are partons [62].
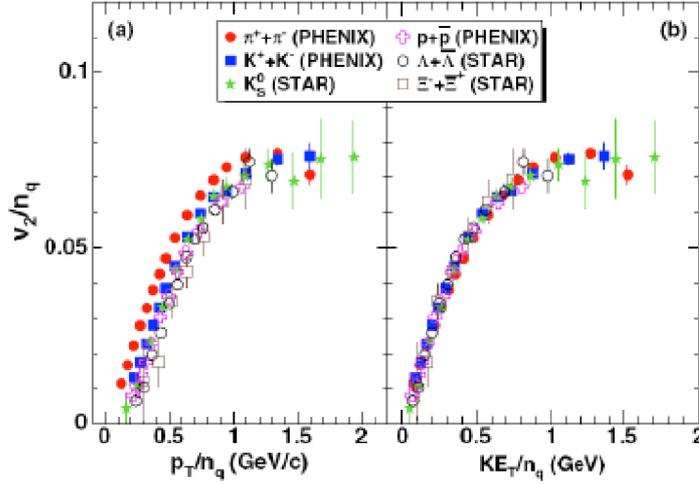
Figure 2.14: ν_2 as a function of p_T (left) and K E_T (right) scaled by the number of constituent quarks in minimum bias Au+Au collisions at $\sqrt{s_{NN}} = 200$ GeV [62].

- Strangeness: In a QGP the concentration of up and down quarks is high enough to block the creation of $u\bar{u}$ and $d\bar{d}$ pairs because of the Pauli principle. The creation of $s\bar{s}$ pairs is then favored in spite of their larger mass. This behaviour results in an enhancement of the production of strange particles in AA compared to pp collisions is observed. This enhancement could be even reinforced in case chiral symmetry is restored reducing the strange quark composite mass to its bare mass. An enhancement of the kaon (strangeness = 1) to pion (strangeness = 0) ratio production in AA collisions compared to pp collisions has been measured at mid rapidity in different experiments. Figure 2.15 shows the K/π ratio versus collision energy s_{NN} measured in pp and AA collisions. The larger ratio in AA collisions compared to pp collisions and the peak observed in AA collisions has been discussed in terms of a phase transition around $\sqrt{s_{NN}} = 7$ GeV [63] although there is no consensus on this interpretation.

- Jet quenching: An inclusive observable allowing to quantify effects of nuclear matter on particles produced in ultra-relativistic heavy ion collisions is the *Nuclear Modification Factor* R_{AA}. The latter compares the production of particles in AA collisions with the production of particles in pp collisions, under the assumption of binary scaling. Under this assumption, the yield of particle production in AA collisions is simply given by the yield in pp collisions,
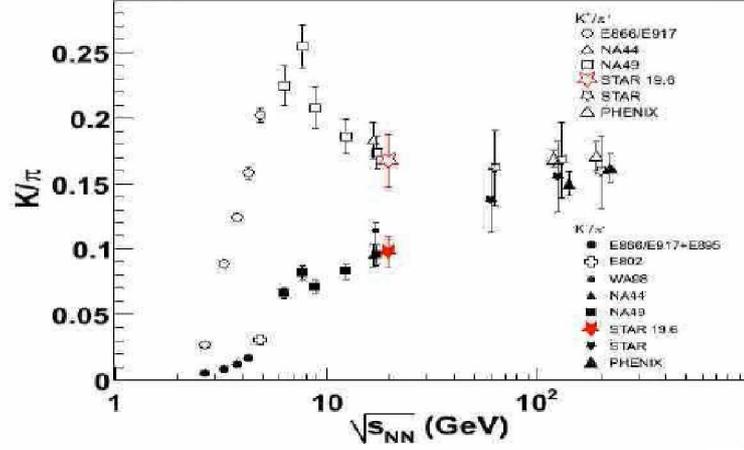
Figure 2.15: *The energy dependence of K^+/π^+ and K^-/π^- ratio at mid-rapidity* [63].

scaled with the number of binary collisions. The nuclear modification factor is written as:

$$R_{AA}(p_{\mathrm{T}}) = \frac{d^2 N_{AA}/dp_{\mathrm{T}} dy}{T_{AA}(b) d^2 \sigma_{pp}/dp_{\mathrm{T}} dy} \ , \tag{2.14}$$

where the numerator is the invariant yield per unit rapidity and the denominator is the cross section in *pp* collisions scaled by thickness function ($T_{AA}(b)$) in nucleus-nucleus collisions. In absence of nuclear effects, R_{AA} is equal to unity.

The nuclear modification factor R_{AA} of charged particles has been measured by the ALICE experiment for most central Pb+Pb collisions at $\sqrt{s_{NN}} = 2.76$ TeV (Fig. 2.16) [64]. The result is compared to R_{AA} measurements of charged hadrons from PHENIX [65] and STAR [66] experiments at $\sqrt{s_{NN}} = 200$ GeV. At low p_T, the nuclear modification factors measured at different energies are similar. The nuclear modification factor at $p_T = 6 - 7$ GeV/c is smaller at LHC than at RHIC, indicating an enhanced energy loss at LHC and therefore suggesting the formation of a denser medium.

At high p_T values, there are no comparison data. The shape of the p_T dependance of R_{AA} is a new observation that will constraint the energy loss models. In addition, RHIC has measured R_{AA} for direct photons (Figure 2.17) [65], which is equal to unity as expected since photons do not interact strongly with the medium. This experimental result, suggests that the dominant source of high p_T direct photon is coming from a hard parton scattering. The production of fragmentation photons being sensitive to the medium effects would give R_{AA} values lower than 1.
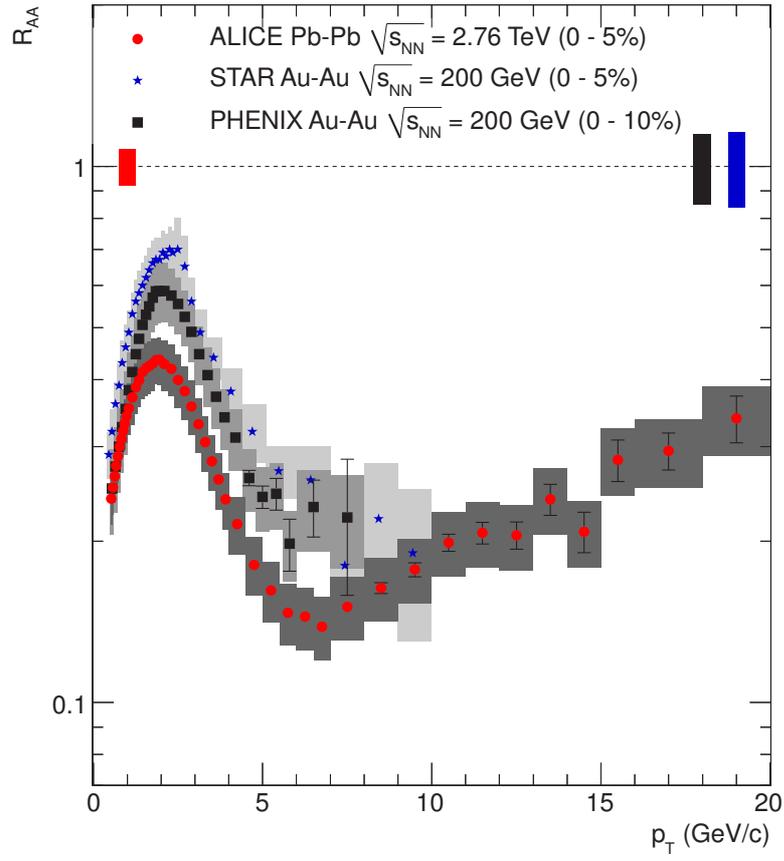
Figure 2.16: *Comparison of R_{AA} in central (0–5%) Pb+Pb collisions at $\sqrt{s_{NN}} = 2.76$ TeV at LHC to measurements at $\sqrt{s_{NN}} = 200$ GeV by the PHENIX [65] and STAR [66] experiments at RHIC. The vertical bars around $R_{AA} = 1$ show the p_T independent scaling uncertainty with $\langle N_{coll} \rangle$ [64].*

All these observations taken together can be interpreted as due to the multiple interaction of hard scattered partons with a color dense medium formed in central heavy-ion collisions by radiating soft gluons.

In addition, RHIC has measured R_{AA} for direct photons (Figure 2.17) [65], which is equal to unity as expected since photons do not interact strongly with the medium.
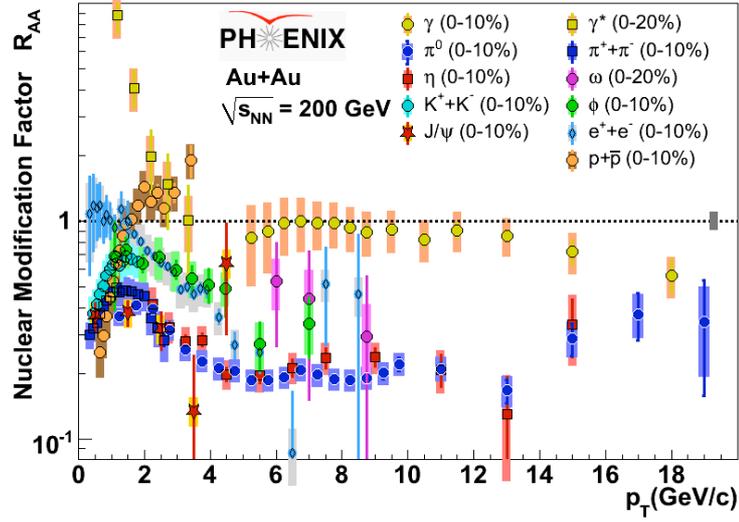
Figure 2.17: *The R_{AA} of direct photon, π^0 and η meson as a function of p_T in central Au + Au collisions at $\sqrt{s_{NN}} = 200 GeV$ [65].*

Chapter 3

Jet and Particle Correlations

The production of hadrons in heavy-ion collisions is described in QCD by the interaction of quarks and gluons. The hard QCD scattering of quarks and gluons (distance scale of $1/p_T \leq 0.1$ fm) leads to the production of jets in the final state. Jets are defined by the hadrons originating from the fragmentation of the hard scattered parton and observed in a localized spatial area. The propagation of the hard scattered parton through the hot and dense QCD medium produced in heavy-ion collisions modifies the parton transverse momentum, and generates acoplanarity and energy imbalance of the two back-to-back scattered partons due to multiple scattering and soft gluon radiation. The modifications experienced by the hard scattered partons traversing the medium is imprinted in the fragmentation of the final state high transverse momentum hadrons and can be revealed by comparing the same observables measured in proton-proton collisions and in heavy-ion collisions. Contemporary jet measurements imply jet reconstruction algorithms to determine the full energy of the jet on an event-by-event basis. However, such a reconstruction is quite challenging in heavy-ion events due to the copious production of final state particles in soft multi-scattering processes which constitute the underlying events. Particle correlations are considered as an alternative approach to study jets.

In this chapter, the two-particle correlation technique will be first discussed, then jet kinematics will be explained, and finally, the golden channel "γ+Jet" will be emphasized.

3.1 Two-Particle Correlation

Correlation techniques are powerful tools in the present quest to understand multi-particle or precisely jet production in hard scattering processes. The idea is to select a sample of high p_T particles, referred to as triggers, to obtain an enriched sample of jet events. Then one studies the correlation between the trigger particle and all other particles in the same event, called associated particles. The per-trigger yield of associated particles are usually referred to as the conditional yield. The most common example of such a measurement consists in fixing p_T ranges for the trigger and associated particles (denoted as p_T^{trig} and p_T^{assoc}) and in counting the associated yield per trigger as a function of $\Delta\phi$, the azimuthal angle between the trigger and associated particles. The per-trigger yield is given by:

$$Y(\Delta\phi) \equiv \frac{1}{N_{\text{trig}}} \frac{dN_{\text{assoc}}}{d\Delta\phi} \tag{3.1}$$

where N_{trig} is the number of triggers and N_{assoc} is the number of associated particles.

A per-trigger yield measurement using charged triggers and charged hadron correlations in pp collisions is illustrated in Fig. 3.1. The typical jet-like configuration with a near side ($\Delta\phi = 0$) and away side ($\Delta\phi = \pi$) peaks is observed. The width of the away side jet (σ_A) is much broader than the near side width (σ_N), a property related to the transverse momentum of hard scattered partons which will be explained in more details in the next section. The difference in strength of the two peaks is due to the incomplete η-coverage. The peaks sit on top of a pedestal which is due to an uncorrelated background constituted from the underlying event (UE). An example of a di-hadron correlation measured in proton-proton collision at $\sqrt{s} = $ 7 TeV with ALICE for triggers of 15 GeV/c $< p_T^{\text{trig}} <$30 GeV/c and associate particles of 1.5 GeV/c $< p_T^{\text{assoc}} < p_T^{\text{trig}}$ is shown in Fig. 3.2. A sum of two Gaussian functions centered at $\Delta\phi = 0$ and $\Delta\phi = \pi$ plus a polynom is adjusted to the data.

In the case of AA collisions, the underlying event contribution is much larger than in pp collisions as a result of the multitude of nucleon-nucleon interactions. Moreover, the flow of the soft hadrons collective motion modifies the azimuthal distribution of the underlying event. Figure. 3.3 shows the azimuthal distributions measured by STAR experiment for triggers of 4 GeV/c $< p_T^{\text{trig}} <$ 6 GeV/c and associated particles of 2 GeV/c $< p_T^{\text{assoc}} < p_T^{\text{trig}}$ for pp collisions, d+Au collisions and Au+Au collisions after subtraction of the uncorrelated background and the flow modulation. While the near side jets look very similar in the three systems, the away-side jet completely disappears in central Au+Au collisions. This is
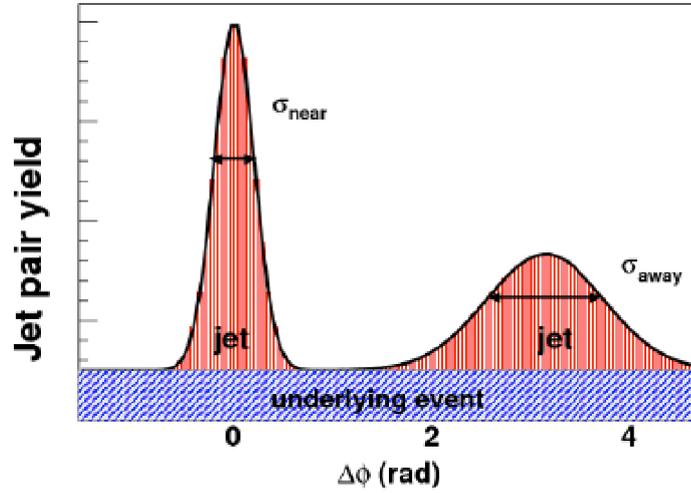
Figure 3.1: *Cartoon illustrating a measurement of two-particle correlations from jet.*
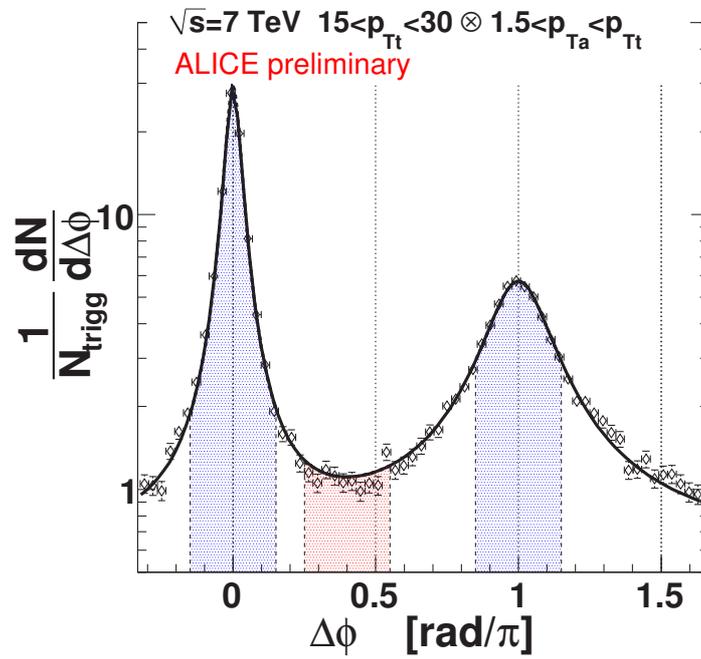
Figure 3.2: *Two particle azimuthal correlation distributions for minimum bias in proton-proton collision at $\sqrt{s} = 7\ TeV$.*

consistent with a picture in which, in AA collisions, the near-side jet is produced near the surface and the away-side jet is completely absorbed while traversing the medium along the opposite direction (Fig. 3.4). For sufficiently high energies of the trigger and the associated
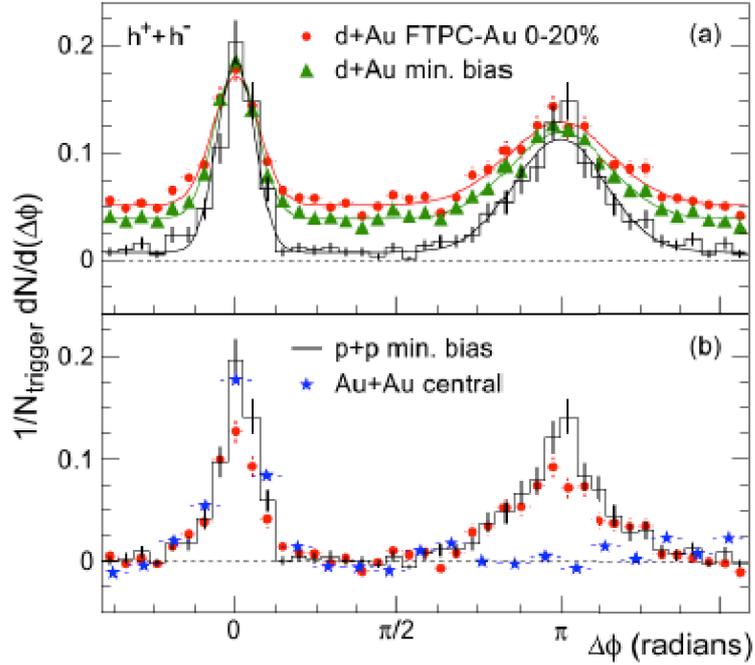
Figure 3.3: *(a) Two particle azimuthal correlation distributions for minimum bias and central d + Au collisions. (b) Comparison of two particle correlations for central Au + Au collisions to those seen in pp and central d + Au collisions [67].*

particles the away-side correlation peak reappears (Fig. 3.5) showing that the most energetic jets can still penetrate the medium. In fact, the back-to-back correlation has not disappeared but the transverse momentum of the away side hadrons is shifted by the medium to small p_T values, below the threshold imposed in the measurement [68]. Lowering the p_T^{assoc} threshold allowed also to recover the two-jet structure, but with the away side peak strongly modified by the medium. in a way reflecting how the medium responds to the energy deposited by the impinging high momentum parton. Effects such as Mach cone as shock wave effects have been invoked to interpret the data [69].
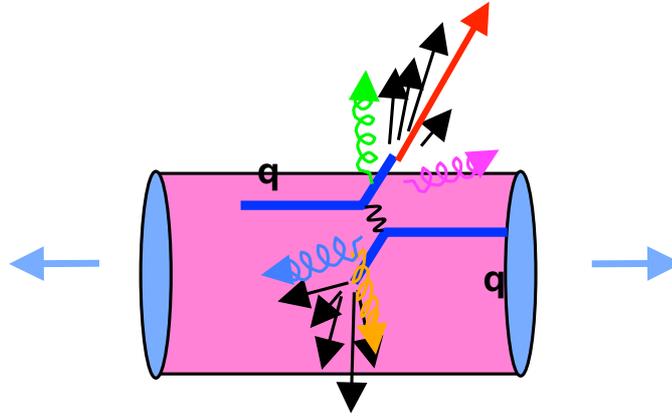
Figure 3.4: *The scheme of jet quenching in heavy-ion collisions.*
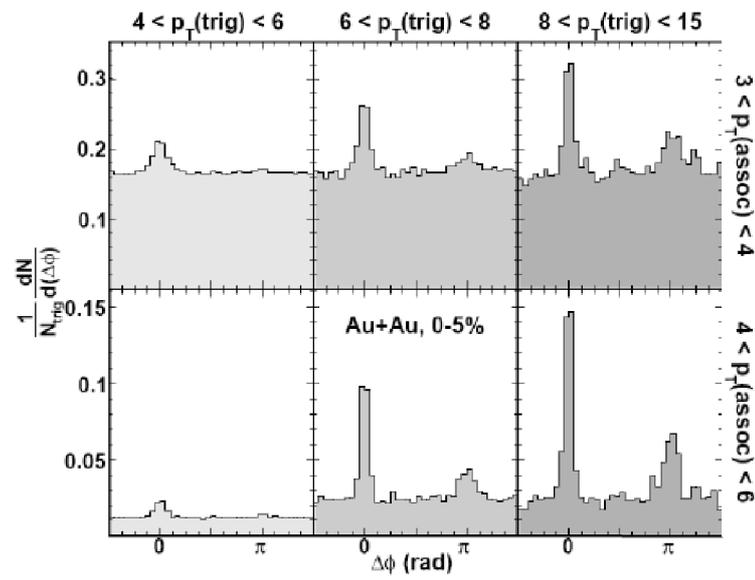
Figure 3.5: *Azimuthal correlations of high-p_T charged hadron pairs in central $Au + Au$ collisions for various p_T^{trig} and p_T^{assoc} ranges. All p_T values in this figure have GeV/c unit [68].*

3.2 Jet Properties

Knowledge of the jet fragmentation process in the vacuum (measured in pp or e^+e^- collision) is useful not only as a reference measurement for a similar analysis in heavy-ion collisions, but also to constrain pQCD calculations (the fragmentation distribution involves soft processes that cannot be calculated by pQCD and is parametrized instead). The hard scattering is treated as a $2 \rightarrow 2$ process $(1 + 2 \rightarrow 3 + 4)$ where the two incoming partons collide at center-of-mass energy $\hat{s}$ and the two outgoing partons (jets) are emitted back-to-back with equal magnitude of transverse momentum $\hat{p}_T = \hat{s}/2 \sin \theta^*$, where θ^* is the center of mass scattering angle. $\hat{s}$ is related to the total pp collision center-of-mass energy $\sqrt{s}$ as $\hat{s} = x_1 x_2 s$, where $x_{1,2}$ is the relative fraction of the proton momentum carried by the scattering partons. The distribution of the x_1 - x_2 value is quite broad, hence the proton-proton and parton-parton center-of-mass frame do not coincide.

The parameters describing the $2 \rightarrow 2$ hard scattering kinematics (Fig. 3.6) are the following:

- $\vec{p}_T^{\mathrm{trig}}$ is the trigger particle momentum;

- $\hat{\vec{p}}_T^{\mathrm{near}}$ is the jet (parton) momentum which fragments into the the trigger particle;

- $\vec{p}_T^{\mathrm{assoc}}$ is the associated particle with momentum which results either from the fragmentation of the trigger jet (near-side correlation), or from the away-side jet (parton);

- $\hat{\vec{p}}_T^{\mathrm{away}}$ is the momentum of the away side parton;

- $j_T = j_{T_y} + j_{T_z}$ is the momentum of the trigger particle with respect to the trigger parton direction, y denotes the transverse component and z the longitudinal component; p_{out} is the transverse component of the the associated particle with respect to the trigger particle momentum;

- $\Delta\hat{\phi}$ is the azimuthal angle between the trigger and the associated particle: $p_{out} = |p_T^{\mathrm{assoc}}| sin(\Delta\phi)$

At the partonic level, the back-to-back partons produced in a $2 \rightarrow 2$ hard process are balanced in momentum ($\hat{p}_T^{\mathrm{near}} = \hat{p}_T^{\mathrm{away}}$). However this ideal back-to-back azimuthal kinematics is modified in pp collisions by the finite transverse momentum (k_T) which results in an acoplanarity and momentum imbalance between the outgoing jets. This acoplanarity is quantified by the momentum of the jet pair $< p_T^2 >_{\mathrm{pair}} = 2 < k_T^2 >$ (see Fig. 3.6) [70]. The net transverse
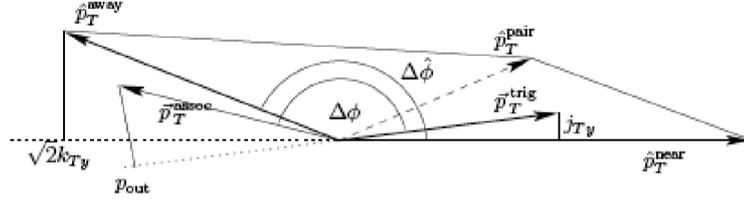
Figure 3.6: *Schematic view of a hard scattering event in the plane perpendicular to the beam.*

momentum $< k_T^2 >$ results from three contributions [71]:

$$< k_T^2 > = < k_T^2 >_{\text{intrinsic}} + < k_T^2 >_{\text{soft}} + < k_T^2 >_{\text{NLO}} \tag{3.2}$$

where

- the intrinsic component refers to the "fermi motion" of the confined quarks or gluons inside a proton,

- the soft component refers to multi-gluon radiation in the initial state (and generates a Gaussian-like distribution of the $p_{T_{\text{pair}}}$ distribution),

- and the NLO component refers to gluon radiations in the final state (and contributes to large values of $p_{T_{\text{pair}}}$ as a power law tail).

The average value of k_T can be extracted from the measurement of the two-particle azimuthal correlation using the following relation [70], the notations of Fig. 3.6 and with the approximations $j_{T_y} \ll p_T$ and $< |\vec{j_{T_y}}^{\text{assoc}}|^2 > \simeq < |\vec{j_{T_y}}^{\text{trig}}|^2 >$:

$$\frac{< z_t > \sqrt{< k_T^2 >}}{\hat{x_h}} = \frac{1}{x_h} \sqrt{< p_{\text{out}}^2 > \quad < j_{T_y}^2 > (1 + x_h)} \tag{3.3}$$

and with the additional following definitions:

- $z_t = p_T^{\text{trig}} / \hat{p_T}^{\text{near}}$ is the fragmentation variable of the trigger parton,

- $\hat{x_h} = \hat{p_T}^{\text{away}} / \hat{p_T}^{\text{near}}$ is the relative away side parton momentum with respect to the trigger parton momentum,

- $x_h = p_T^{\text{assoc}} / p_T^{\text{trig}}$ is the relative associated particle momentum with respect to the momentum of the trigger particle.

The quantities on the right-hand side of Eq. 3.3 are all measurable quantities whereas the quantities $< z_t >$ and $\hat{x_h}$ on the left-hand side of the equation are not measurable and must be evaluated from theoretical models.

41

The value of k_T has been measured from Drell-Yan, dijet and diphoton events at several energies (Fig. 3.7) [72], and was found to be of the order of few GeV/c. The data are
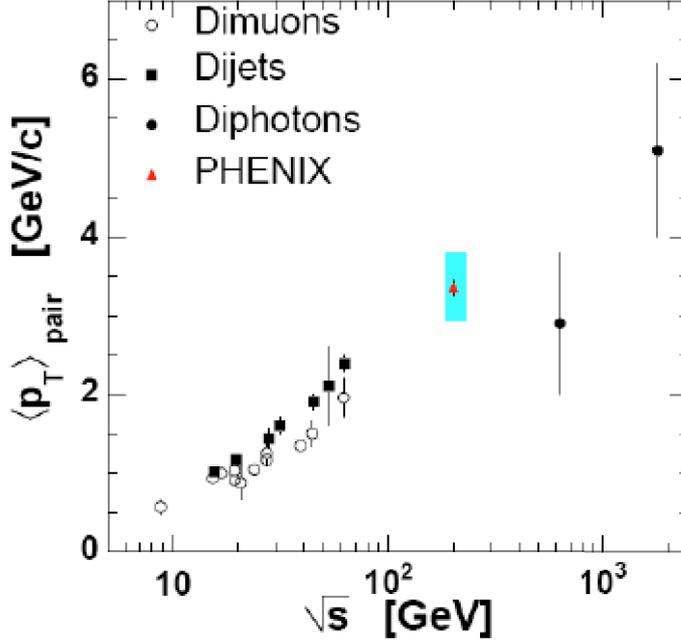
Figure 3.7: p_T^{pair} as a function of collision energy $\sqrt{s}$ from various particle correlation measurements [72].

consistent with a p_T^{pair} (or equivalently k_T 3.2) value is rising roughly logarithmically with $\sqrt{s}$ a behavior independent of the observable from which p_T^{pair} has been measured.

In heavy-ion collisions k_T measures in addition transverse momentum generated by the passage of the hard scattered parton through the medium: the jet fragmentation changes with an increased value of $< j_T >$ (jet heating) and multiple scatterings adding an additional misalignment between the two jets with respect to pp. A broadening $< \triangle k_T^2 >$ of the k_T distribution is anticipated and can be related to the transport parameter $\hat{q}$ of the medium, which describes the averaged medium-induced transverse momentum transfer squared per unit path length [73]:

$$< \triangle k_T^2 >= \int dy \ \hat{q}(E, y) \tag{3.4}$$

3.3 $\gamma+$ Jet

The inclusive photon spectrum is defined as the unbiased photon spectrum observed in a collision. It is made of two main contributions: decay photons and direct photons. Direct photons emerge directly from a parton collision, whereas decay photons are the decay product of hadrons such as π^0, η, emerging at the end of the thermal evolution of the system produced in the collisions. Because of their short lifetime, the decay from neutral mesons occurs close to the collision vertex (hundreds of nanometers for $E_\pi > 1$ GeV). These decay photons constitute the main background to direct photon measurements and dominate the inclusive photon spectrum.

In heavy-ion collisions, the production of direct photons is complex and can be categorized into three possible production mechanisms:

– *prompt photons:* These photons are produced during the pre-equilibrium stage of the collision in hard interactions of partons from the colliding nuclei. At leading order in α_s, direct photons are produced through $2 \rightarrow 2$ QCD hard processes such as Compton scattering ($g+q \rightarrow \gamma+q$, "a" in Fig. 3.8) or quark-antiquark annihilation ($q+\bar{q} \rightarrow \gamma+g$, "b" in Fig. 3.8). Prompt photons are a valuable probe of both proton-proton and heavy ion collisions since they are not complicated by final state interactions in contrast to hadronic observables. Their rate can be calculated by perturbative QCD techniques and their spectrum follows a power law distribution at large transverse momentum [74]. The Compton process ($g + q \rightarrow \gamma + q$) dominates the prompt photon production cross section as a result of the scarcity of quarks in the low x domain probed by LHC energies. Therefore their production depends strongly on the gluon distribution function of hadrons in the initial state. A quark can also radiate photons ("c" in Fig. 3.8) after its initial hard scattering as part of the jet fragmentation process. This process enters the pQCD calculations as a next-to-leading order process. At LHC energies they represent up to 50% of the prompt photon production, depending on their energy. These three subprocesses are all the relevant processes for direct photon production in elementary hadron-hadron and nuclear-nuclear collisions.

– *Thermal Photons:* The thermal emission of real, energetic photons from the fireball created in relativistic heavy-ion collisions has been suggested as the most direct signature of the QGP formation. To the lowest order, thermal photons are produced

43
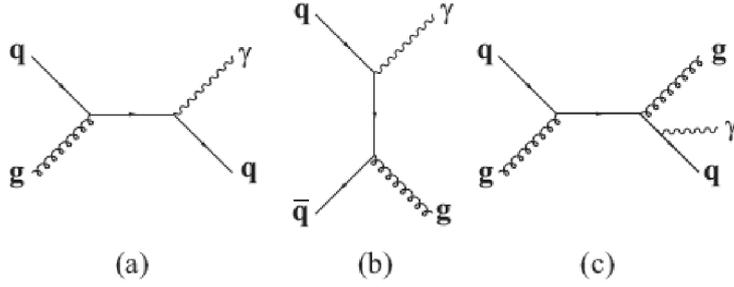
Figure 3.8: *Feynman diagrams of the main production processes for direct photons in initial hard scatterings as well as in a thermalized quark-gluon plasma phase: (a) quark-gluon Compton scattering of order α_s; (b) quark-antiquark annihilation of order α_s; (c) fragmentation photons of order α_s^2.*

from quark-antiquark annihilation or Compton scattering (Fig. 3.8) among the thermalized QGP constituents. Thermal photons are coupling to the medium and thus serve as a thermometer of the QGP. Calculation of the production of these photons from an hydrodynamically evolving system and including a phase transition predict that thermal photons populate mainly the soft region of the spectrum up to energies of several GeV [75].

– *Jet Conversion Photon:* The presence of a dense strongly interacting medium allows for new mechanism of direct photon production. A hard scattered parton, traveling and fragmenting in a space-time co-occupied by the medium, can generate photons by interactions with soft partons from the medium. Their energy spectrum is predicted to be damped exponentially and contributes mainly to the intermediate p_{T} range [76].

In order to extract the signal from the direct photons produced in heavy-ion collisions from the measured inclusive photons, one needs to subtract the dominant contribution from decay photons. It is therefore necessary to measure the main sources of the decay photons, i.e. measure the production of π^0, η, and other resonances in a transverse momentum range as wide as possible. Fig. 3.9 illustrates the accurancy with which the measurement can be done. The excess above unity represents the direct photon signal, it must be larger than 6% to be observable.

Experimentally, the direct photons spectrum has been measured by the WA98 experiment at CERN SPS by subtracting the contribution of decay photons from the measured inclusive photon spectrum. in $Pb + Pb$ collisions at $\sqrt{s}$=17 GeV (Figure 3.10) [78]. Calculations including prompt photons and thermal contributions from the QGP and the hadron phase are
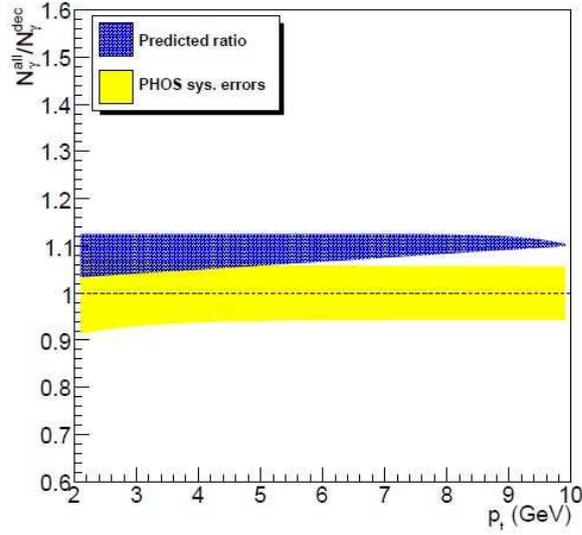
Figure 3.9: *Error band, including systematic uncertainties, for the ratio of all photons to decay photons as a function of p_T [77].*

also shown [79]. While they yield a reasonable description of direct photon spectrum at high p_T, the calculations can not account for the yield at low p_T. The direct photon spectra measured by the PHENIX experiment [80] at RHIC (Fig. 3.11) shows a good agreement at high p_T with predictions of pQCD calculations [81]. The contribution from low energy thermal photons could only be measured at RHIC through the $\gamma > e^+e^-$ conversion pairs [82].

γ+jet events are often referred to as the "golden channel" for jet studies. The point-like nature of the photon coupling turns out to be an extremely useful property of the γ+jet channel if one wants to measure the fragmentation function, or effective modifications to the fragmentation function in nuclear collisions. The dominant processes are $g+q \rightarrow \gamma+q$ (Compton) and $q + \bar{q} \rightarrow \gamma + g$ (Annihilation) (Fig. 3.8), where photons emerge almost unaltered from the dense strongly-interaction medium. In contrast to dihadron measurements, where the initial parton energy cannot be known, $\gamma + jet$ measurements provide thus a calibrated measurement since jets recoiling from direct photon exactly balance the photon momentum at Leading Order and in absence of k_T.

Then $\gamma - h$ correlations provide the momentum and angular distribution of hadrons emitted by the known recoil parton without the need to reconstruct the jet. The reconstruction of jets at moderate p_T (< 50 GeV) being quite challenging in heavy-ion collisions because of
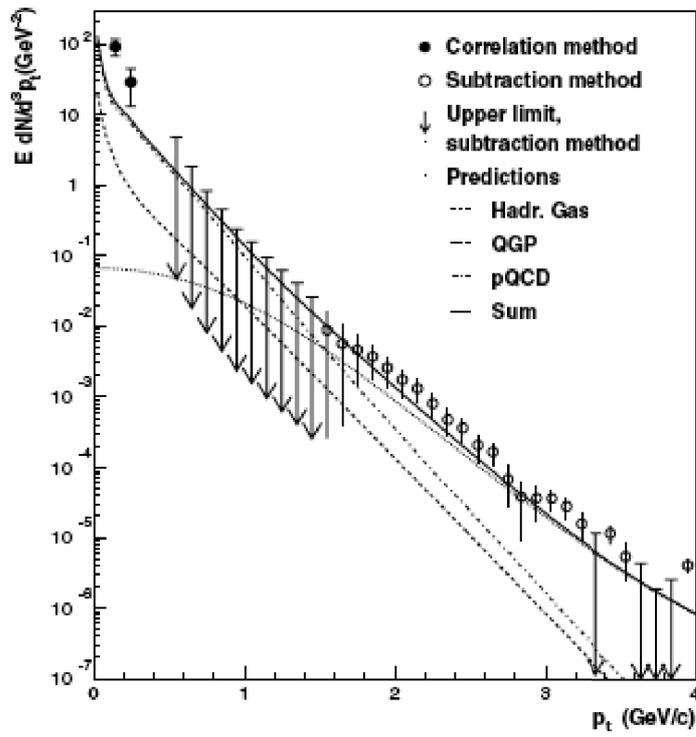
Figure 3.10: *The photon spectrum for central Pb + Pb collisions at the SPS including recent interferometry results from WA98 [78]. For comparison, results from theoretical calculation are included [79].*
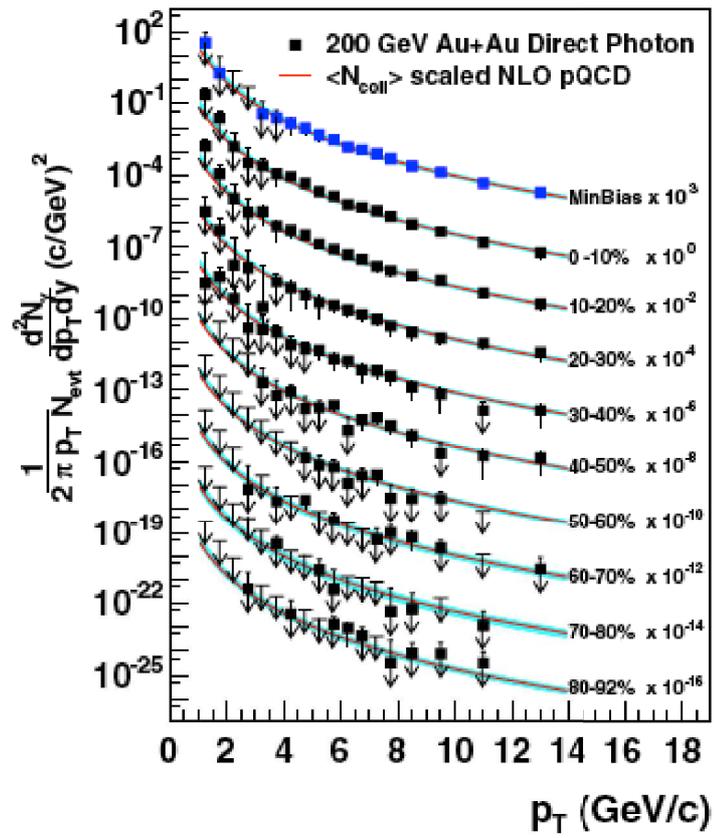
Figure 3.11: *Direct photon spectra for different centralities in Au + Au collisions at RHIC [80].*

the high multiplicity environment, such measurement allows to extend jet studies toward low p_T where the medium effects should be relatively the largest. Medium effects will be better identified through modification of the fragmentation function, i.e., the redistribution of the jet energy. The use of the $\gamma+$ jet channel to study jet topology was first advocated by Xin-Nian Wang and collaborators in a pair of seminal articles on the subject more than 10 years ago [83].

The γ–hadron correlation method suggested in Ref. [84] rests on the fact that under given kinematical conditions, the imbalance parameter x_E:

$$x_E = \frac{\vec{p}_{T_h} \cdot \vec{p}_{T_\gamma}}{\left|p_{T_\gamma}\right|^2} , \tag{3.5}$$

between a hard photon trigger and hadrons produced in collisions may allow the determination of the jet fragmentation function $D_i^h(z \simeq x_E)$. At least this two-body kinematics may be a valid picture when higher order corrections remain small. In order to probe efficiently the jet fragmentation function through γ–hadron correlations, the kinematical conditions which verify this equivalence are the following:

– The hadrons must be produced from the fragmentation of a hard scattered parton, excluding hadrons from the soft underlying event by the cut, $p_{T_h} > p_{T_h}^{cut} \gg \Lambda_{QCD}, T$.

– The photon must be produced directly from a hard partonic process, i.e., $p_{T_\gamma} > p_{T_\gamma}^{cut} \gg \Lambda_{QCD}, T$, and it must not be produced in a jet fragmentation.

– The range over which the equivalence is verified is given by $p_{T_h}^{cut}/p_{T_\gamma}^{cut} \leq z_{h\gamma} \leq 1$, therefore to probe the broadest range the photon and hadron momenta cuts must be very asymmetric, $p_{T_\gamma}^{cut} \gg p_{T_h}^{cut}$.

Indeed, the measurable quantity, p_T^{assoc}/p_T^γ is nothing but the fragmentation variable z ($= p_T^{assoc}/p_T^{jet}$) since the photon balances the opposite jet from a $2 \to 2$ hard scattering. This is clearly demonstrated in Fig. 3.12 which compares x_E distribution to prediction using quark and gluon fragmentation based on parameterizations of the LEP data [71]. It is shown that the sample of jets selected depends strongly on p_T^{trig} due to the steeply falling cross section of the jets. Despite the fact that the two fragmentation functions were taken to be quite dissimilar, $D_g \propto e^{-11z}$ and $D_q \propto e^{-8z}$, they only result in a slight difference in the x_E distributions.
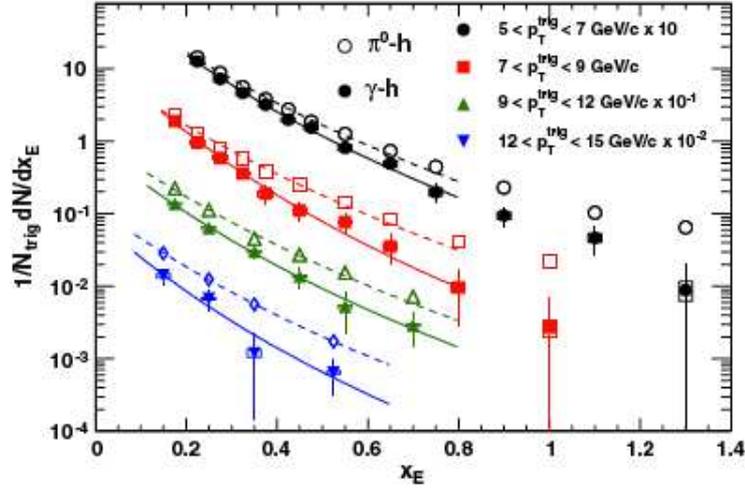
Figure 3.12: x_E distributions for several ranges of p_T^{trig} compared to calculations using quark (solid) and gluon (dashed) fragmentation functions as parameterized by the LEP data [71].

The PHENIX experiment has measured photon triggered jets correlation measurements to study the jet fragmentation in both pp and central Au + Au collisions at $\sqrt{s} = 200$ GeV. Fig. 3.13 shows the per-trigger yields of associated charged hadrons after the flow and combinatorial background subtraction as a function of $\Delta\phi$. The triggers were either an inclusive photon, a decay photon or a direct photon with $7 < p_T^{trig} < 9$ GeV/c and the condition on the associated particles was $3 < p_T^{assoc} < 5$ GeV/c, where the decay photon trigger is identified by 'tagging' from the reconstructed π^0 and η, and the direct photons are sampled by applying an isolation criterion (more details see Sec. 5.2). The strong near-side correlation for inclusive and decay photons is largely absent for direct photon triggers as expected from a sample dominated by photons produced directly in the hard scattering. Comparing the inclusive and decay photon near side correlations for pp (top) and Au + Au (middle) the larger direct photon signal-to-background in Au + Au is evident. The absence of the direct photon triggered near-side correlation is apparent in the Au + Au data, as well as in pp. The disappearance of the away-side correlation in Au + Au can be seen by comparing to the pp correlations [85].

The modification of jet fragmentation function is evidenced by comparing the direct photon triggered away-side yields as a function of $z_T = p_T^{assoc}/p_T^{\gamma}$ in pp and AA collisions. A suppression has been observed in central Au + Au collisions with respect to pp (Fig. 3.14): the slope of the correlation distribution in Au + Au collision is steeper than the one in pp
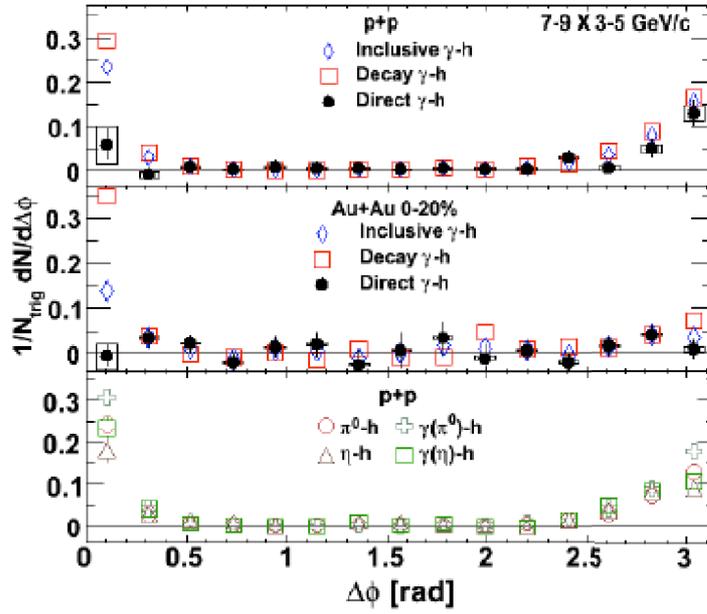
Figure 3.13: *Azimuthal correlation distribution of charged hadrons with various trigger particle types with 7 GeV/c <* p_T^{trig} *< 9 GeV/c and 3 GeV/c <* p_T^{assoc} *< 5 GeV/c for pp and central Au + Au (0-20%) collisions. Top: Inclusive, decay and direct jet function in pp collisions. Middle: Inclusive, decay and direct jet function is central Au + Au collisions. Bottom:* π^0, η, $\gamma(\pi^0)$ *and* $\gamma(\eta)$ *associated yields in pp. [85].*

collisions as anticipated [86].
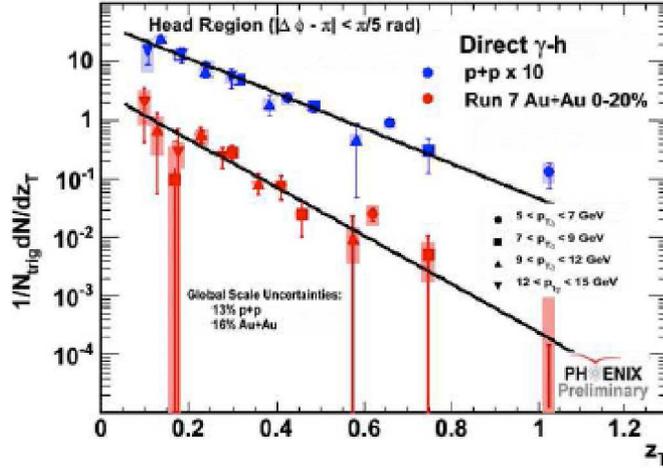
Figure 3.14: *The direct γ h correlation distribution for pp collisions multiplied by a factor of 10 and Au + Au [86].*

Since the Compton process dominates the cross section by roughly an order of magnitude over annihilation, the production of direct photon production probes the gluon distribution function in the initial state and the opposite jet probes the quark fragmentation function in the final state and the quark propagation in the medium. Unlike identified baryon and meson spectra which have only a very tenuous connection to the parton flavor, the correspondence of γ triggered jets to their quark progenitors may be readily verified. Since there are two valence up quarks in a proton, each with a charge $\frac{2}{3}$, compared to only 1 valence down quark of charge $\frac{1}{3}$, then the probability to be a recoil jet initiated by an up quark a $2(\frac{2/3}{1/3})^2 = 8$ times larger than a down quark. As a result, one expects to see more positive charged hadrons than negative on the away-side jets. Figure 3.15 shows the ratio of positive to negative charged hadrons $(R(+/\ ))$ on the away-side of both π^0 and isolated direct photon triggers as a function of p_T^{assoc} [85]. Several p_T^{trig} selections are shown along with in PHENIX, along with the corresponding Monte-Carlo. For a given p_T selection the available statistics do not permit a strong statement about the charge asymmetry, however, when considering data without p_T selection, an excess of the positive charge is evident in the direct photon triggered yield. The π^0 triggered data, which is dominated by gluon production, shows an $R\pm$ close to unity for nearly all of the data points.

The use of γ-h correlations offers the additional advantage of the tomographic tool enabling
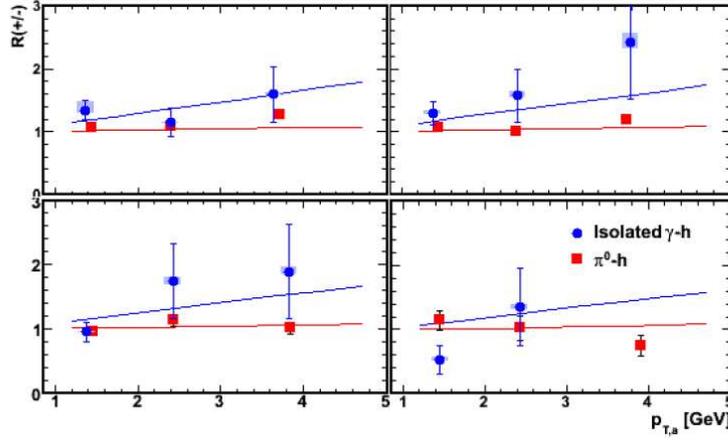
Figure 3.15: $R(+/-)$ for isolated photons (blue) and π^0 (red) triggers as a function of associated particles p_T^{assoc} for several selections of p_T^{trig}. The lines are calculated using DSS fragmentation functions [85].

to disentangle the properties of the dense medium from the nuclear geometry and space-time evolution of the system. Contrast to hadronic observables, which are strongly biased towards surface production (by selecting a high p_T trigger hadron, one samples the hadrons which have lost no or a small fraction of their energy in the medium or equivalently the hadrons which have traversed small distances inside the medium), photons sample the entire collision including the core of the overlap zone where the density is greatest. The use of the $\gamma+$ jet channel as a tomographic tools was first advocated by H. Zhang and collaborators using NLO pQCD parton model [87]. They concluded that one can effectively control hadron emission from different regions of the dense medium by selecting γ-h pairs with different values of x_E, and therefore extract the corresponding jet quenching parameters. The results demonstrates that hard scattering occurring mostly at the surface of the medium can be selected with large values of x_E, while the volume emission dominates the $\gamma+$ jet events for small values of x_E due to the large path length the jet traversed through the medium (Fig. 3.16). Therefore, the average path-length of the away-side parton may then be varied in a well controlled manner by selecting events of various momentum differences between the γ-h pair, and one can extract jet quenching parameters from different regions of the dense medium by measuring the nuclear modification factor of the γ-triggered jet fragmentation function in the kinetic region, achieving a true tomographic study of the dense medium.
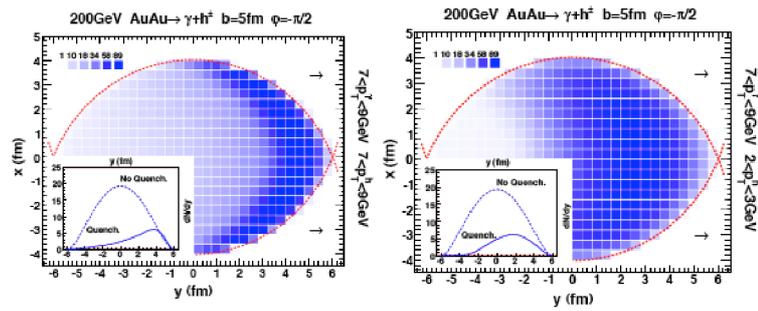
Figure 3.16: *Transverse distributions of the initial γ jet production vertices that contribute to the final observed γ hadron pairs along a given direction (arrows) with $x_E \approx 0.9$ (left plot) and $x_E \approx 0.3$ (right plot) [87].*

Chapter 4

Experimental Facility

The Large Hadron Collider (LHC) at CERN near Geneva is the world newest and most powerful tool for Particle Physics research. This chapter is devoted to the description of the ALICE experiment at LHC. First, a brief description of the LHC and some relevant parameters are given. Then, the ALICE detector layout is described, and finally, the software currently being developed to simulate, reconstruct and analyze ALICE data is briefly discussed.

4.1 The Large hadron Collider: LHC

The Large Hadron Collider is a two-ring-superconducting-hadron accelerator and collider installed in the existing 26.7 km tunnel that was constructed between 1984 and 1989 for the CERN LEP (Large Electron-Positron Collider) machine [88]. There are two transfer tunnels, each approximately 2.5 km in length, linking the LHC to the CERN accelerator complex that acts as injector. The chain of accelerators, sketched in Fig. 4.1, includes the Linac2 injector for proton beams (until 50 MeV) or the Linac4 injector for heavy-ion beams (up to 160 MeV/c), Proton Synchrotron (PS) and the Super Proton Synchrotron (SPS) (up to 450 GeV/v) and finally the LHC rings.

The LHC will ultimately deliver proton–proton collisions at center of mass energy $\sqrt{s} = 14$ TeV and Pb–Pb collisions at $\sqrt{s_{NN}} = 5.5$ TeV with maximum luminosities of $L = 10^{34}\ cm^{-2}s^{-1}$ and $L = 10^{27}\ cm^{-2}s^{-1}$ respectively.
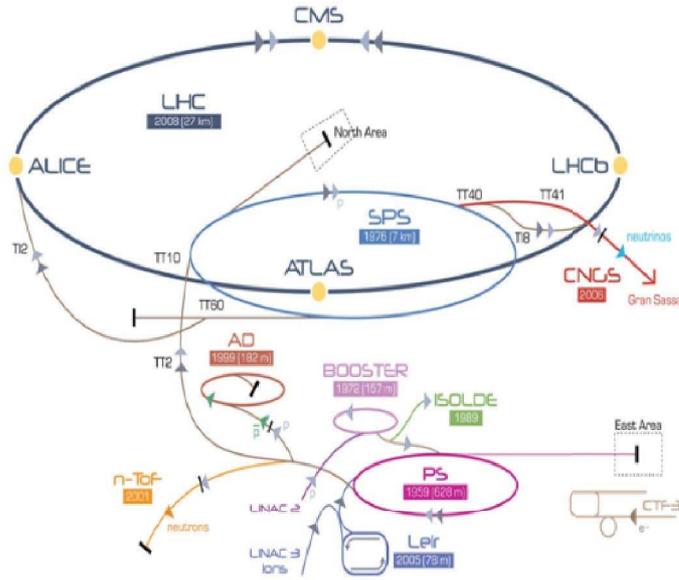
Figure 4.1: *The LHC injector complex [88].*

In the starting phase, LHC has operated at energies below the nominal values. In 2009, it has delivered proton-proton collisions at $\sqrt{s} = 900$ GeV, i.e. at the injection energy (2×450 GeV, no acceleration by LHC). In 2010, LHC has delivered proton-proton collisions at $\sqrt{s} = 7$ TeV and Pb+Pb collisions at $\sqrt{s_{NN}} = 2.76$ TeV (this has happened in March), the highest collision energies ever achieved by an accelerator. Until 2013 the LHC will operate at the same energies with an intermezzo for a short operation to deliver proton-proton collisions at $\sqrt{s} = 2.76$ TeV [1]. The data from this lower energy proton-proton collisions are essential as a reference for several observables to be compared in proton-proton and Pb+Pb collisions.

LHC realizes collisions in the center of four large experiments distributed around the LHC ring. In a broad scope, the four experiments have in common similar fundamental scientific objectives by trying to answer the questions on the origin of mass, broken symmetries and search of new physics beyond the standard model. The ATLAS [2] and CMS [3] experiments address the fundamental questions on how elementary particles acquire their mass and why elementary particles span such a wide range of masses from the electron to the top quark. The Higgs mechanism is so far the theoretical answer to these questions and the discovery

---

[1] This run has taken place in April 2011.

[2] http://atlas.web.cern.ch/Atlas/Collaboration/

[3] http://cms.web.cern.ch/cms/index.html

of the Higgs boson will be the experimental prove of this theory. The ALICE experiment addresses the equally fundamental question on how composite particles such as nucleons acquire their mass, knowing that the mass of u and d quarks (of a few MeV) represents only a small fraction of the total mass of the nucleon (~ 1 GeV). This "swelling" of quarks "glued" inside the nucleon is thought to originate from the interaction of the valence quarks with the sea quarks from the QCD medium. By creating the Quark Gluon Plasma, where quarks are not "glued" anymore, ALICE will shed light on the properties of the true QCD vacuum.

Understanding the role of symmetries and how they are broken in our universe is the second set of common questions the LHC experiments aim to answer. ATLAS and CMS will explore the concept of Super Symmetry which makes an equivalence between matter particles and the force particles, LHCb [4] will explore the Charge-Parity (CP) symmetry which is broken in the matter–anti-matter symmetry and ALICE will explore the concept of Chiral Symmetry which is broken during the phase transition from the QGP phase of matter toward its normal phase. To answer these common questions, the four experiments adapt different empirical approaches which can be described in the following shortcut: ATLAS and CMS by colliding protons concentrate energy to form new high mass particles (Higgs boson, supersymmetric particles), LHCb also collides protons to borrow energy to create particle–anti-particle pairs ($B\bar{B}$) and study differences in their decay, and ALICE by colliding heavy-ion distributes the energy over large volumes (the size of a nucleus) to heat up and melt matter.

4.2 ALICE: A Large Ion Collider Experiment

ALICE is a general-purpose experiment designed for a comprehensive study of the production of hadrons, electrons, muons and photons produced in the collision of heavy nuclei at LHC energies. The ALICE detection systems are optimized to measure these particles in a high multiplicity environment, with charged particles rapidity densities ($dN/d\eta$) of the order of 4000 but they can operate with sufficient good performances up to values as high as 8000 (at the time the ALICE experiments was designed, extrapolating the measured particles density to the values at LHC energies was quite uncertain). The experiment design also offers excellent and in some aspects unique performances to measure the reaction products in proton-proton collisions. On one hand, these data allow us to address a number of specific

[4]http://lhcb.web.cern.ch/lhcb/

strong interaction topics for which ALICE is complementary to the other LHC experiments. On the other hand, these data provide the necessary reference data to which heavy-ion data are compared to in order to reveal effects related to the formation of a hot and dense nuclear medium.

The ALICE detector has been designed, built and is now operated by a collaboration including currently over 1000 physicists and engineers from 105 institutes in 30 countries. Its overall dimensions are $16 \times 16 \times 26\ m^3$ for a total weight of approximately 10000 t. The ALICE experiment (Fig. 4.2) consists of a central barrel detection system, covering the mid-rapidity region ($\eta \leq 0.9$; polar angles from $45°$ to $135°$) over the full azimuth, to measure and identify charged hadrons and electrons, and several detectors at forward/backward rapidity [89]. The central barrel is installed inside the large L3 [90] [5] solenoid magnet which generates an
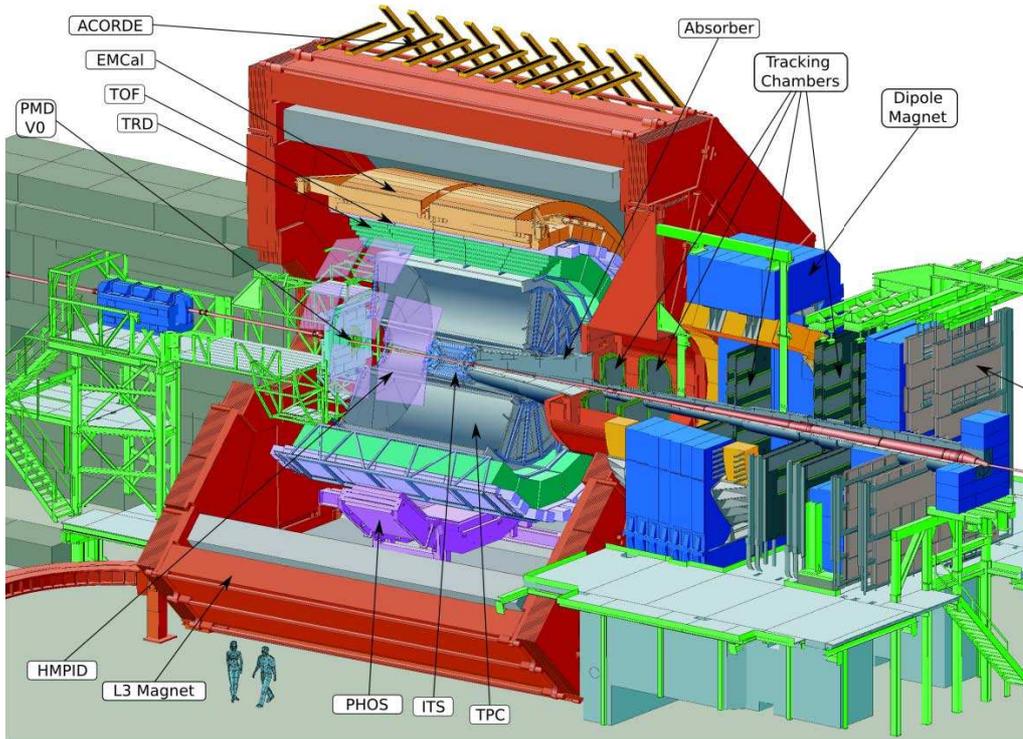
Figure 4.2: *Longitudinal view of the ALICE detector [89].*

uniform magnetic field of up to 0.5 T and oriented along the beam axis. It is composed, from the interaction vertex outwards, of the following detectors:

---

[5]L3 [90] is the former experiment operated at the LEP accelerator which infrastructure has been reused by ALICE

- six cylindrical layers of high-resolution silicon pixel (SPD), drift (SDD) and strip (SSD) detectors, forming the Inner Tracking System (ITS), for secondary vertex identification of short lived particles and the tracking and identification of low transverse momentum charged particles down to 100 MeV/c;

- a cylindrical Time Projection Chamber (TPC) for the high resolution tracking and particle identification;

- a Time of Flight (TOF) detector to optimize charged hadrons identification;

- and a Transition Radiation Detector (TRD) for electron identification.

A ring imaging Cerenkov detector (HMPID) extending the useful range for the identification of p/K and K/p, on a track-by-track basis, up to 3 GeV/c and 5 GeV/c respectively, covers a limited acceptance ($\eta < 0.6$, $\Delta\phi = 58°$). Two electomagnetic calorimeters (EMCAL and PHOS), covering also a limited acceptance ($|\eta| < 0.7$ for EMCAL and $|\eta| < 0.12$ for PHOS, and for both $\Delta\phi = 100°$), for the detection and identification of photons and neutral mesons and for providing a trigger on high-p_T photons and jets, complete the central barrel systems.

Outside the central magnetic field and at very forward rapidity ($4.0 < \eta < 2.5$), the forward muon arm consists of a complex arrangement including hadron absorbers, a large dipole magnet, and fourteen planes of tracking and triggering chambers, to detect and identify with high momentum-resolution and low background muons from heavy quarks and quarkonia decay. Opposite to the muon spectrometer ($2.3 \leq \eta \leq 3.7$), a Photon Multiplicity Detector (PMD) measures the inclusive-photon multiplicity.

Additional detectors located at large rapidity complete the ALICE setup to characterize the global event and to provide the interaction trigger:

- an ensemble of Si strip detectors, the Forward Multiplicity Detectors (FMD), covering acceptance at large rapidities ($3.4 \leq \eta \leq 1.7$, $1.7 \leq \eta \leq 5.0$) to measure the charge particles multiplicity in very forward directions;

- a Zero Degree Calorimeter (ZDC), consisting of two sets of neutron and hadron calorimeters located at 90 m from the interaction vertex, to measure the impact parameter of the collision;

- a system of scintillation and quartz counters, V0 and T0, to provide fast trigger signals.

The detectors used for my study and their performance will be described in more details next.

4.2.1 Central Tracking System

Tracking in the central barrel is performed by the ITS and the TPC. The need for efficient and robust tracking has led to the choice of a TPC as the main tracking detector. Together with the other central barrel detectors, TPC provides charged-particle momentum measurements with excellent two-track separation, particle identification and vertex determination. The main tasks of the ITS are to localize the primary vertex with a resolution better than 100 μm (longitudinal spatial precision is 100 μm and the radial spatial precision is 12 μm), to reconstruct the secondary vertices from the decays of strange baryons and D and B mesons, to track and identify particles with momentum below 200 MeV/c which can not reach the TPC, and to improve the momentum and angle resolution for particles reconstructed by the TPC.

4.2.1.1 Layout

The ITS surrounds the beam pipe, a 800 μm-thick beryllium cylinder of 6 cm outer diameter, coaxial with the ITS detector layers. The layers are located at radii ranging between 4 and 43 cm and cover the rapidity range of $\eta \leq 0.9$ for all vertices located within the length of the interaction diamond ($\pm 1\sigma$, i.e. ± 5.3 cm along the beam direction). Because of the high particle density expected in heavy-ion collisions, and in order to achieve the required impact parameter resolution, the innermost four layers (SPD and SDD) are truly two-dimensional devices. The two outer layers (SSD) are equipped with double-sided silicon micro-strip detectors. The four outer layers have analog readout for independent particle identification via dE/dx in the non-relativistic ($1/\beta^2$) region, which provides the ITS with stand-alone capability as a low-p_T particle spectrometer [91]. The number, position and segmentation of the layers are optimized for efficient track finding and high impact-parameter resolution. In particular, the outer radius of ITS, $r_{\max} = 43$ cm, is determined by the track matching with the TPC and the inner radius ($r_{\min} = 4$ cm) is the minimum allowed by the size of the beam pipe (3 cm). The first layer has a more extended coverage ($|\eta| < 1.98$), in order to provide, together with the FMD, a continuous coverage in rapidity for the measurement of

the charged particle multiplicity.

The TPC design is optimized to provide the largest possible acceptance for full-length, high-p_T tracks, in order to ensure significant statistics and good momentum resolution for high-mass and high-p_T electron pairs, high tracking efficiency and good performance even at as high multiplicities as $dN/d\eta \sim 8000$.

The TPC has an inner radius of $r_{min} = 80$ cm, an outer radius of $r_{max} = 250$ cm, and an overall length along the beam direction of $l = 500$ cm. The inner radius of the TPC is determined by the maximum acceptable hit density, the outer radius by the length required for achieving dE/dx resolution of better than 5-7 %. Particle identification is performed for low momentum particles with dE/dx measurement in the $1/\beta^2$ region (below the particle mass). For high momentum particle, up to momenta of the order of several tens of GeV/c, accurate particle identification can be performed thanks to the relativistic rise of the dE/dx. The TPC is filled with a gas mixture of 90% of Ne and 10% of CO_2. Ionisation electrons drift in a longitudinal electric field toward the end-plate of the cylinders where they are detected by multi-wire proportional chambers [92].

4.2.1.2 Performances

One of the most challenging tasks for ALICE is that of track finding in an unprecedented high particle multiplicity density environment. Track finding begins with the reconstruction of the primary vertex using the correlation of the *hits* position in the innermost detector (SPD). Pairs of reconstructed points close in azimuthal angle in the transverse plane are selected in the two layers. The z position of the primary vertex is estimated from their z-coordinates using a linear extrapolation. The same procedure is repeated in the transverse plane. The resulting position of the primary vertex position is used as an input for the tracking.

The basic method for track finding depends critically on the determination, for each track, of a set of initial seed values for the track parameters and their covariance matrix. This seeding is done using the *space points* reconstructed in the TPC. To start, a few outermost *space points* from pad rows are used to build track seeds and the track is propagated inwards. The procedure is repeated several times, choosing a set of *space points* closer and closer to the centre of the TPC. After this step, the tracks are propagated to the outer layers of the ITS. The combined track reconstruction accumulates the information from the different detectors

in order to optimize the track reconstruction performance. The overall physical track-finding efficiency (including geometrical acceptance and reconstruction efficiency) is above 85% over the whole p_T range in proton–proton as well as in heavy-ion collisions. For TPC and TPC-ITS track finding the efficiency is 90% at very high momenta (Fig. 4.3); this value is essentially determined by the size of the TPC dead zones, which cover about 10% of the azimuthal angle. The large drop after inclusion of the TRD in the tracking procedure is due to interactions in the material and decays as well as additional dead zones. However, TRD is essential for
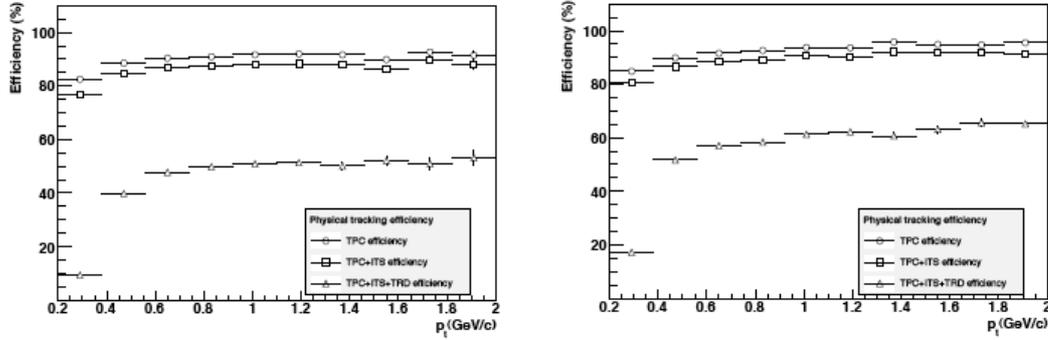
Figure 4.3: *Physical track-finding efficiency for different combinations of the tracking detectors in central Pb+Pb collisions ($dN_{ch}/d\eta = 6000$) (left) and proton–proton collisions (right)* [77].

electron identification and improves the overall momentum resolution, especially at higher momenta (Fig. 4.4). For both track-finding efficiency and the momentum precision, only a slight deterioration is seen when going from low to high charged-high density.
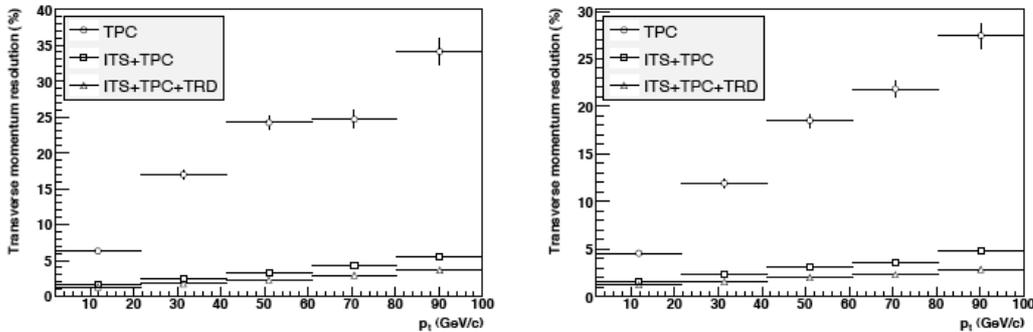
Figure 4.4: *Transverse-momentum resolution for different combinations of the tracking detectors in central Pb+Pb collisions ($dN_{ch}/d\eta = 6000$) (left) and proton–proton collisions (right)* [77].

Several detectors (ITS, TPC, TRD, TOF and HMPID) contribute to the charged Particle IDentification (PID), each with a different momentum-dependent performance. Four layers of ITS (two silicon-drift and two silicon-strip detector layers) provide signal amplitude information, which can be used for PID in the low momentum range by measuring ionization energy loss dE/dx. The resolution of the ITS dE/dx measurement is about 11%, which allows for a good π/K separation up to 450 MeV/c and for good p/K separation up to about 1 GeV/c. The dE/dx measurement in the TPC is treated in a similar way, using the truncated mean of the 65% lowest amplitude pad-row samples. The resolution of dE/dx measurement depends slightly on the charged particle density: it changes from 5.5% for pp events to 6.5% for central Pb+Pb events. The measurement of dE/dx in the TRD contributes to charged particle PID in the same momentum range as for the TPC. The TOF detector is able to measure a particle arrival time with a precision of about 80 ps, which allows to extend, on a track-by-track basis, the K/π separation up to 2.5-3 GeV/c and provide p/K separation up to 3.4-4 GeV/c. Finally, HMPID provides a particle identification deduced from the characteristic Cerenkov light pattern. The various PID measurements are translated into probabilities for each track to belong to the different particle types. Such "a priori" probabilities are taken into account at the combined PID stage, using an iterative procedure.

The measurements of dE/dx in the TPC and ITS with real data taking by ALICE during the LHC first year confirm the excellent particle identification capability (Fig. 4.5), and the same particle species identified by different detectors using the approach mentioned above show consistent results (Fig. 4.6).
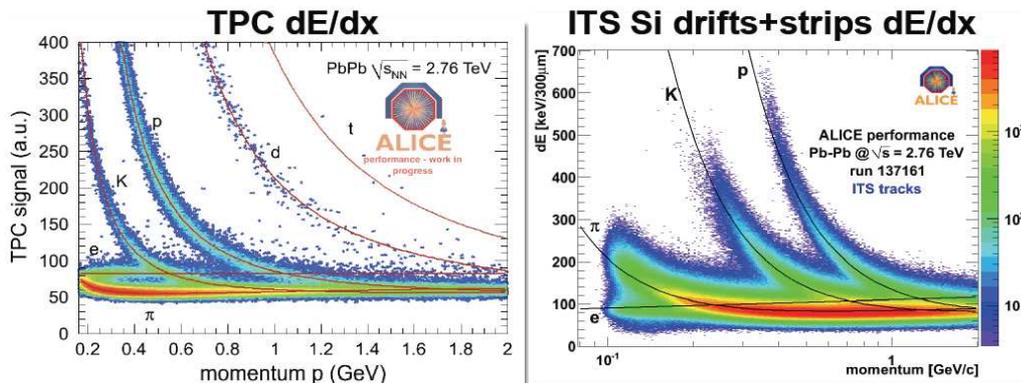
Figure 4.5: *dE/dx measurements performed by TPC and ITS with ALICE in proton-proton collisions at $\sqrt{s} = 7$ TeV.*
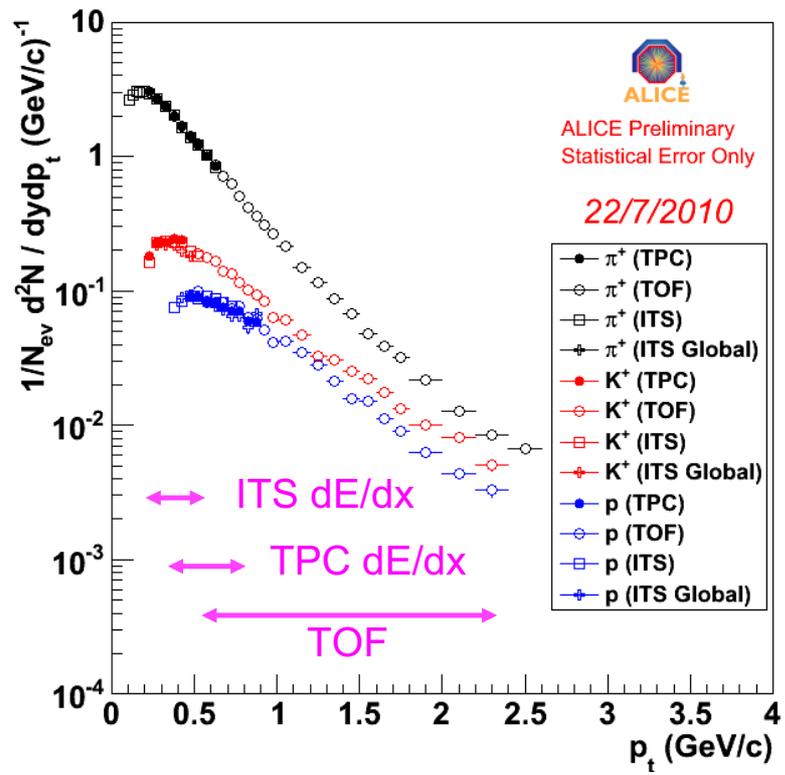
Figure 4.6: *Identified particle transverse momentum distribution measured by ALICE detectors in proton-proton collisions at $\sqrt{s} = 7$ TeV.*

4.2.2 Electromagnetic Calorimeters

Photons, spanning the energy range from thermal photons (a few hundred MeV to a few GeV) to hard QCD photons (up to hundred GeV), as well as decay photons from neutral mesons are detected and identified in a small single-arm, high-resolution and high-granularity (PHOS) and in a large acceptance (EMCal) electromagnetic calorimeter.

4.2.2.1 Layout

The high photon multiplicity generated by nuclear collisions requires a dense and highly segmented calorimeter with small Molire radius at a large distance from the interaction point in order to keep the cell occupancy at a manageable level of about 10-20%. Therefore, PHOS or EMCAL, are located far away from the interaction vertex ($\sim$ 4.6 m).

– PHOS, thanks to its high granularity and high energy resolution, is optimized for high resolution measurement of the low energy thermal part of the photon spectrum and of π^0 and η and other electromagnetically decaying mesons in the energy range up to $\sim$ 50 GeV. It is made of dense scintillating crystals ($PbWO_4$), subdivided into five independent calorimeter units, named modules. Each module consists of 64 $\times$ 56 (across and along the beam direction, respectively) $PbWO_4$ scintillator crystals. Each crystal is a 18 cm long parallelepiped, equivalent to 20 radiation length units ($X_0[PbWO_4]$=0.89 cm). A module covers approximately a quarter of a unit in pseudo-rapidity, $\quad 0.12 \leq \eta \leq 0.12$, and 100° in azimuthal angle, and its total area is $\quad$ 8 m^2. Only 3 modules have been installed at P2 for the first operational period at LHC, the remaining 2 will be sampled and installed in the next 2 years. The technical data of the PHOS electromagnetic calorimeter are listed in Tab. 4.1 [93].

– EMCAL, the second calorimeter has been designed to enhance the ALICE capabilities for measuring jet properties over a large kinematic range. It is less segmented and provides a worse energy resolution than PHOS. It is a large-acceptance, moderate-resolution electromagnetic calorimeter providing a fast and efficient trigger for hard jets, photons and electrons. The scope and basic design parameters of the calorimeter are chosen to match the physics performance requirements of the high-p_T physics goals. The EMCAL is integrated within a cylindrical volume approximately 110 cm deep in the radial direction sandwiched between the frame which supports the entire ALICE central

Table 4.1: Technical data of the PHOS electromagnetic calorimeter [93].

Coverage in pseudorapidity	$0.12 \leq \eta \leq 0.12$
Coverage in azimuthal angle	$\Delta\phi = 100°$
Distance to IP	4.6 m
Material	Lead tungstate crystals (PbWO$_4$)
Crystal dimensions	$2.2 \times 2.2 \times 18$ cm^3
Depth in radiation length	20
Effective moliere radius R_M	2 cm
Number of crystals	17920
Granularity	5 modules of 3584 crystals each
Total area	8 m^2
Crystal volume	1.5 m^3
Total crystal weight	12.5 t
Operating temperature	25°C

detector and the ALICE solenoid magnet coils. It covers $|\eta| < 0.7$ and $\Delta\phi = 100°$, and is positioned approximately opposite to PHOS at a radius of about 4.5 meters from the beam line. It is divided into 10 units, named supermodule, each supermodule spanning 20 degrees in azimuth. The chosen detection technology is a layered Pb-scintillator sampling calorimeter with a longitudinal pitch of 1.44 mm Pb and 1.76 mm scintillator traversed by wavelength shifting fibers for the light collection. Each full size super module is assembled from $12 \times 24 = 288$ modules arranged in 24 strip modules of 12×1 modules each. A module is a single self-contained detector unit, each module is made out of four independently read-out towers, each spanning $\Delta\eta \times \Delta\phi = 0.014 \times 0.014$, with a fixed width in the ϕ direction and a tapered width in the η direction with a full taper of 1.5°. The physical characteristics of the EMCAL are summarized in table 4.2 [94].

Additional calorimeter modules, DCAL for Di-jet calorimeter, are presently under construction. They will installed adjacent to PHOS and provide an extended acceptance coverage for back-to-back measurements with EMCAL.

Table 4.2: The EMCAL physical parameters [94].

Quantity	Value
Tower Size (at $\eta = 0$)	$6.0 \times 6.0 \times 24.6 \ cm^3$ active
Tower Size	$\Delta\phi \times \Delta\eta = 0.0143 \times 0.0143$
Sampling ratio	1.44 mm Pb / 1.76 mm scintillator
Number of layers	77
Effective radiation length X_0	12.3 mm
Effective moliere radius R_M	3.2 cm
Effective density	$5.68 g/cm^3$
Sampling fraction	10.5
Number of radiation length	20.1
Number of towers	12672
Number of modules	3168
Number of super modules	10
Weight of super modules	7.7 metric tones (full size)
Total coverage	$\Delta\Phi = 100°, \quad 0.7 \leq \eta \leq 0.7$

4.2.2.2 Performances

Photon detection performance is provided by the PHOS and EMCal. The experimental energy resolution can be parameterized as (E in GeV):

$$\frac{\sigma_E}{E} = \sqrt{\frac{a^2}{E^2} + \frac{b^2}{E} + c^2} \, , \tag{4.1}$$

where a is determined by the electromagnetic noise, which includes contributions from preamplifier noise and digitization noise, b is the stochastic term, which takes into account the fluctuations in the electromagnetic showers and the variations due to photon statistics, and the constant term c is due to detector and readout inhomogeneity and to the calibration error.

The energy resolution calculated from simulated data and the one measured in beam test (mono energetic electrons) [95] is shown in Fig. 4.7 as a function of energy. The three
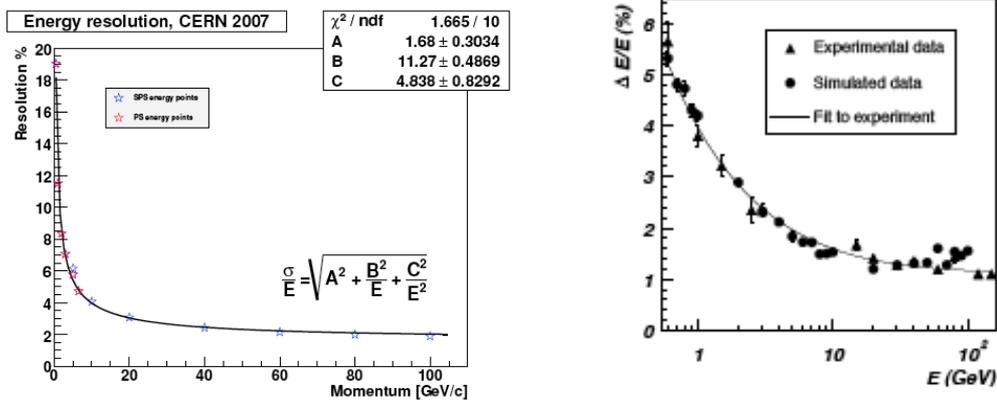
Figure 4.7: *Energy resolution in EMCal (left) and PHOS (right) for electrons as a function of incident beam momentum. The continuous line represents the result of the fit of Eq. (4.1) to the experimental data [77].*

parameters of the energy resolution (in %) are found to be

$$a = 3.0, \ b = 3.0, \ c = 1.0 \ for \ \text{PHOS} \, ,$$

$$a = 4.8, \ b = 11.3, \ c = 1.7 \ for \ \text{EMCal} \, .$$

respectively.

4.3 ALICE Offline Computing

Offline Computing provides the framework for data processing [96], including simulation, reconstruction, calibration, alignment, visualization and analysis. The layout of the ALICE offline framework AliRoot [97], is shown schematically in Figure 4.8. Its implementation
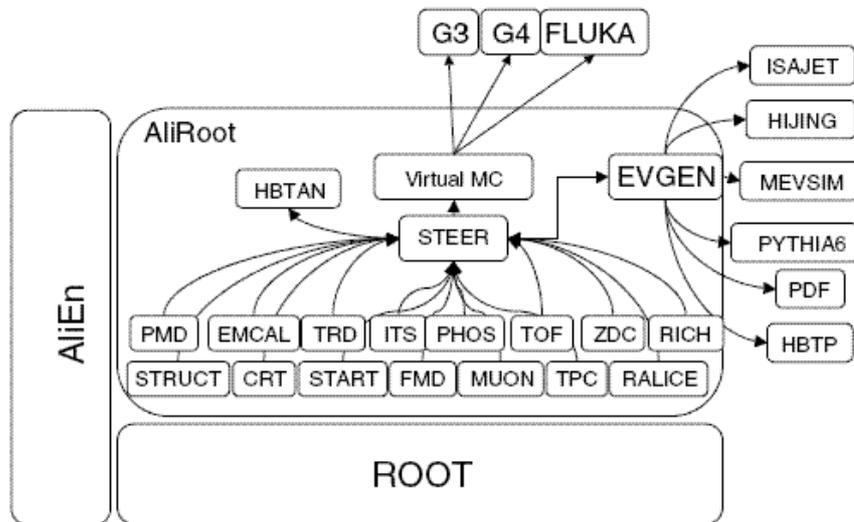
Figure 4.8: *Schematic view of the AliRoot framework [97].*

is based on the object oriented techniques for programming and C++ as a language. It is associated to a supporting framework, the C++ environment ROOT [98], complemented by the AliEn system which provides the interface to the computing Grid.

The simulation framework is used to evaluate the physcis performance including the detectors response with respect to the physics requirements:

1. Event generators: Different generators are employed depending on the physics studies to be performed; for example, PYTHIA [99] is used to generate proton–proton collision events and HIJING [100] to generate heavy-ion collisions events. Produced particles are stored in a root container (a TTree) called the kinematics tree which contains the full information about the generated particles: type, momentum, charge, and mother-daughter relationship.

2. Particle transport model: The transport of the generated particles through the detector material is performed by the Monte Carlo codes GEANT3 [101], GEANT4 [102]

69

or FLUKA [103]. The energy deposited by the generated particles in the detector is stored in the form of *hits*. It consists of a deposited energy per tracking step (the minimum propagation distance for which the deposited energy is calculated by the transport model), the volume in which the energy is deposited, the time at which the energy is deposited and the identification of the primary particle. A primary particle can generate several *hits* in different volumes and there can be several *hits* in a single volume originating from different primary particles. The *hits* are stored separately for each detector. The information is complemented by the so called "track references" corresponding to the location where the particles are crossing user defined reference planes.

3. Digitalization: The deposited energy, stored in the *hits*, is then modified for various effects (adding the response of the front-end electronics, noise, digitization) to yield the amplitude of the signal simulating the one delivered delivered by the detectors electronics. It is stored as *digits*. Finally, pseudo *raw data* are produced from these simulated *digits* in a format identical to the one used for real data.

The next steps are common to the processing of simulated data and real raw data.

4. Reconstruction: As an input, the reconstruction uses the *digits* together with some additional information like the detector geometry. The reconstruction can use both *digits* stored in the ROOT format and *digits* extracted from real raw data acquired by the detectors. At this point, the reconstruction algorithms [96] reconstruct the full information about the particles trajectory and mass. For *digits* found in the central tracking detectors, reconstruction produces first *clusters*, a set of adjacent (in space and/or in time) *digits* that were presumably generated by the same particle crossing the sensitive element of a detector. It then calculates *space points* which provides an estimation of the position where a particle crossed the sensitive element of a detector (often, this is done by calculating the center of gravity of the *cluster*). After that, *tracks* are reconstructed by combining clusters and consist of five parameters (such as the curvature and the angles with respect to the coordinate axes) of the particle's trajectory together with the corresponding covariance matrix (used to calculate the probability that the reconstructed track represents a real track) the estimated at a given *space point*. Finally, with the reconstructed vertices and tracks, particles types are identified.

For the calorimeters, the reconstruction algorithm produces *clusters* of hit cells and

calculates various parameters such as, the position in the reference frame local to the calorimeter (super)module, the local deposited energy, shape parameters of the *cluster*, and store them into a *RecPoint* in which the list of *digits* at the origin of the *cluster* is stored as well. This list is important to recalibrate the calorimeter without need to repeat the entire reconstruction process. The output of the reconstruction is stored as the Event Summary Data (ESD).

Chapter 5

Validation of γ -hadron observable: A Monte-Carlo Study

In this chapter, I will present my work while ALICE was waiting for the start of the LHC operation. I describe first the generators for the Monte-Carlo studies. The methods to identify direct photons among inclusive photons and to identify π^0 will be explained next. Finally, the results from a feasibility study demonstrating that the ALICE experiment is well suited for photon-hadron correlation measurements in proton–proton and heavy-ion collisions at LHC energies are discussed.

5.1 Monte Carlo Event Generator

As discussed earlier, two processes are involved for the prompt photon production at leading-order (LO). The elementary $2 \to 2$ hard processes contributing at the parton-level are gluon Compton scattering and quark annihilation (Fig. 3.8),

$$g + q \to \gamma + q \, ,$$
$$q + \bar{q} \to \gamma + g \, . \tag{5.1}$$

These two processes generate prompt direct photons in what we will call γ–jet events.

As main background, we considered the following $2 \to 2$ hard QCD processes at LO:

$$q + q \to g + g \,,$$
$$q + q^{'} \to q + q^{'} \,,$$
$$q + \bar{q} \to q + \bar{q} \,,$$
$$q + g \to q + g \,, \qquad\qquad (5.2)$$
$$g + g \to g + g \,,$$
$$g + g \to q + q^{'} \,.$$

These processes contribute to the photon production through the decay photons from neutral mesons, originating from the fragmentation of the hard scattered partons. These processes generate what we will call the *jet–jet events*.

We have used the event generator of leading order processes of the Standard Model PYTHIA 6.214 [99] to simulate proton–proton collisions. This event generator is a Monte Carlo type of generator and can be used to generate high-energy-physics "events", i.e., sets of outgoing particles produced in the interactions between two incoming particles. The PYTHIA event generator provides an accurate (provided adequate tuning) representation of the event properties in a wide range of reactions, within and beyond the Standard Model, with emphasis on those where strong interaction plays a role, directly or indirectly, including multiple soft scattering that constitutes the underlying event of the multi-hadronic final state. Due to the Fermi motion of partons inside the colliding hadrons, the initial state partons have an intrinsic transverse momentum motion, $k_{T_{intric}}$. Soft gluons radiation occurring in the initial and final state of the hard scattering contribute also to the overall transverse momentum $< k_T >$ observed in the final state measurable particles (see Sec. 3.2). PYTHIA provides switches for these initial- and final-state radiation (ISR/FSR) processes. The processes of interest for the present study are those leading to the production of prompt photons, they are treated as the *signal* while those leading to the production of neutral pions are treated as the *background*.

Proton–proton events triggered either by the γ–jet (from Eq. 5.1) or jet–jet (from Eq. 5.2) processes were generated with the default parton distribution function CTEQ4L [104]. Initial and final state radiation were switched on and the intrinsic transverse momentum of the colliding partons was set to the default value $k_{T_{intric}} = 1$ GeV/c. Fragmentation photons

are produced during the parton shower evolution, as final state radiation to mimic NLO contributions to the photon production. From INCNLO [105] calculations (Fig. 5.1), we have estimated that the next to leading contribution is 1.65 times larger than the LO contribution at $p_T = 5$ GeV and 1.4 times above 20 GeV.
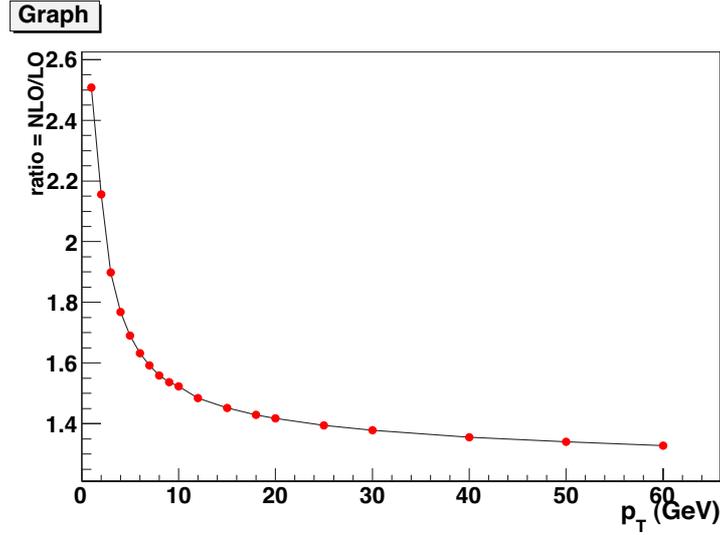
Figure 5.1: *The ratio of NLO contribution to LO contribution for direct photon production.*

Since the momentum spectra of the final state particles follows a steeply falling power law, the events have been generated in bins of p_T^{hard}, where p_T^{hard} refers to the transverse momentum of the outgoing hard scattered parton. The number of events generated for each p_T^{hard} bin were normalized to the cross section calculated by PYTHIA. The events of interest for the present study were obtained by selecting prompt photons (in the case of γ–jet events) or π^0 (in the case of jet–jet events) produced in the laboratory system inside an acceptance slightly larger than the geometrical acceptance of two PHOS modules ($\Delta\eta = 0.26$, $\Delta\phi = 42°$) or slightly larger than the full EMCAL super modules ($\Delta\eta = 0.701$, $\Delta\phi = 112°$). Jet–jet events were triggered by π^0 with p_T larger than 1 GeV/c entering the acceptance of PHOS or EMCAL. This trigger considerably reduces the computing time needed to generate a statistically significant sample of decay photons detected in the calorimeters.

The generated particles from the accepted events were stored for later analysis and are referred to as the *kinematics* in the following. The photon p_T spectra (Fig. 5.2) obtained for proton– proton collisions at $\sqrt{s} = 7$ TeV follow a power law distribution $p_T{}^n$ with $n = 3.9 \pm 1.0$ for γ–jet photons in the p_T range from 10 to 90 GeV/c and $n = 5.1 \pm 0.6$ for jet–jet photons

in the p_T range from 10 to 50 GeV/c. The achieved Monte-Carlo counting statistics are obviously much lower for the decay photon spectrum than for the prompt photon spectrum. This is a result, of the fact that the π^0 meson and hence the decay photons carry only a fraction of the jet energy from where they fragment and therefore copulate mainly the low p_T region of the spectrum. To reach a significantly larger sample of decay photons at high p_T would require unaffordable computing resources.
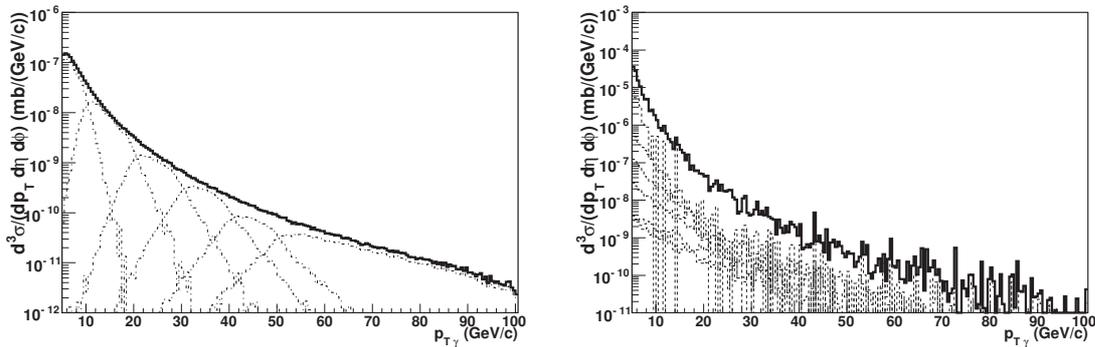
Figure 5.2: *Monte Carlo (PYTHIA) γ–jet photon spectrum (left) and jet–jet photon spectrum (right) p_T spectra in proton–proton collisions at $\sqrt{s} = 14$ TeV. γ–jet photons are produced in $qg \rightarrow \gamma q$ and $q\bar{q} \rightarrow \gamma g$ hard processes and jet–jet photons in final state radiation during the parton shower evolution or in the decay of neutral pions fragmenting jets from $2 \rightarrow 2$ hard processes. Simulation bins in p_T^{hard} normalized to the cross section are also displayed.*

5.2 Direct photon identification

To measure photon-hadron correlations, events with a leading photon trigger are tagged and the distribution of hadrons from the same event associated to this leading trigger is constructed. Such a measurement requires on one hand an excellent photon and π^0 identification and on the other hand the measurement of charged hadrons with high p_T resolution.

In ALICE, the electromagnetic calorimeters, PHOS and EMCAL, are able to measure photons with high efficiency and resolution. In the calorimeters, electromagnetic particles are detected as clusters of neighboring hit cells. Two cells are considered as neighbors if they have a common side or a common edge. Any cell with an energy above a chosen threshold larger than the energy deposited by minimum ionizing particles ($E_{MIP} \simeq 260$ MeV) is taken as a seed of a new cluster. The energy E and the position of the clusters in the (x, z) plane of the

module reference frame, are calculated respectively, as the sum of the individual cell energies e_i, and the center of gravity with a logarithmic energy weight,

$$\bar{s} = \frac{\sum_{digits} s_i w_i}{\sum_{digits} w_i} \ , \tag{5.3}$$

where $\bar{s}$, standing either for $\bar{x}$ or $\bar{z}$, is the coordinate of the cluster center of gravity, and s_i, denoting either x_i or z_i, is the coordinate of the individual cells; the sum extends over all the cells forming the cluster. The weight w_i is defined by,

$$w_i = \max[0, p + \log(\frac{e_i}{E})] \ , \tag{5.4}$$

where p is a parameter empirically determined (4.5 for PHOS and 0.35 for EMCAL). Since the edges of the cells in a module are not parallel to the momentum of particles emerging from the interaction point, the center of gravity of electromagnetic clusters with energy E is further corrected for the incidence direction (θ, ϕ) of the primary particle in calorimeters [106]:

$$
\begin{aligned}
x^{'} &= x \quad (A + B \log E) \sin \phi \ , \\
z^{'} &= z \quad (A + B \log E) \cos \theta \ ,
\end{aligned}
\tag{5.5}
$$

where the parameters A and B were determined empirically by simulations.

At low energy, photon and π^0 can be discriminated by invariant mass analysis since the two clusters created by the decay photons are spacially well separated. With increasing π^0 energy, the two clusters merge into a single cluster (for $E_{\pi^0} \geq 25$ GeV for PHOS and $E_{\pi^0} \geq 6$ GeV for EMCAL). Such events can however be still identified as π^0 with a cluster shape analysis. To select further the direct photons, an isolation criteria is applied to reject very high energy π^0 background. In the following we will briefly describe the three procedures for trigger selection.

5.2.1 Invariant Mass Analysis: IMA

The dominating decay mode of π^0 meson occurs via the electromagnetic process $\pi^0 \rightarrow \gamma\gamma$, which has a mean life time $\tau_{\pi^0} \sim 8.4 \times 10^{17}$ s. With a large relativistic boost, the two decay photons are seen to originating directly from the interaction point. Low energy π^0 are identified by an invariant mass analysis of their two decaying photons as long as the two clusters in the calorimeters are well separated (Fig. 5.3). The invariant mass m_{ij} spectrum
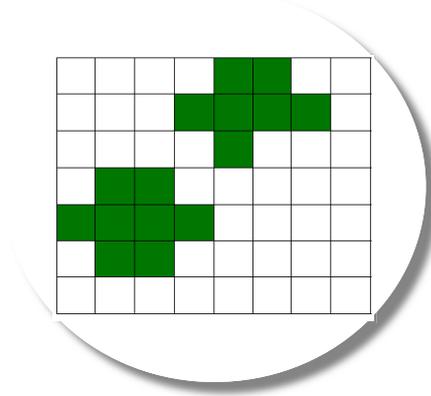
Figure 5.3: *Example of the two decay photon clusters from π^0.*

is constructed from all possible cluster pair combinations, using the measured energy E_i, E_j and the opening space angle θ_{ij}

$$m_{ij} = \sqrt{2E_iE_j(1 - \cos\theta_{ij})}\,, \tag{5.6}$$

The probability of reconstructing π^0 by invariant mass analysis was evaluated from events generated with a π^0 of energy uniformly distributed between 0.5 and 30 GeV and entering the calorimeters. The reconstruction probability was studied in three different cases allowing also to study the influence of the materials in front of the calorimeters reducing π^0 identification because of photon conversion:

i) the detector is not filled and no materials from other detectors in front of calorimeter;

ii) the detector is filled but no materials in front;

iii) the real ALICE detector frame with the materials in calorimeters and other detectors in front. The invariant mass spectra for different π^0 energy shows a Gaussian peak around π^0 mass, and a sum of Gaussian and linear fitting function is used to count the number of reconstructed π^0 from the fittings. The efficiency is then calculated by comparing the reconstructed and generated π^0 spectrum. We found a constant efficiency for PHOS of about 65% below 25 GeV and it drops because the two decay clusters merge into a single one making the invariant mass impossible [18]. Due to much larger cell size for EMCAL, the two decay clusters start to merge much earlier which shows a drop of the efficiency happened at 6 GeV. One can then switch to the shower shape analysis for π^0 identification.

5.2.2 Shower Shape Analysis: SSA

The shape of the clusters is defined by the intersection of the cone containing the shower with the front plane of the calorimeter (Fig. 5.4). This surface can be expressed in terms of the covariance matrix,

$$S = \begin{pmatrix} s_{xx} & s_{zx} \\ s_{xz} & s_{zz} \end{pmatrix} , \tag{5.7}$$

where,

$$s_{xx} = < (x \quad \bar{x})^2 > = \frac{\sum_{digits} w_i x_i^2}{\sum_{digits} w_i} \quad \left(\frac{\sum_{digits} w_i x_i}{\sum_{digits} w_i} \right)^2 , \tag{5.8}$$

with similar definitions for s_{zz} and s_{zx}. Here $<>$ denotes averaging with the logarithmic weights w_i defined by Eq. (5.4), $\bar{x}$ and $\bar{z}$ are the coordinates of the center of gravity of the cluster [Eq. (5.3)],(x_i, z_i) are the coordinate positions of crystal i. The core energy is the sum of the energies of the crystal with the largest energy and the neighbor crystals. The principal axes of the shower surface are the eigenvectors (e_1, e_2) of the covariance matrix, with eigenvalues λ_0 and λ_1. The geometrical meaning of the principal axes is illustrated in Fig. 5.4. The lateral dispersion d of the clusters in the (x, z) plane, measured on the surface
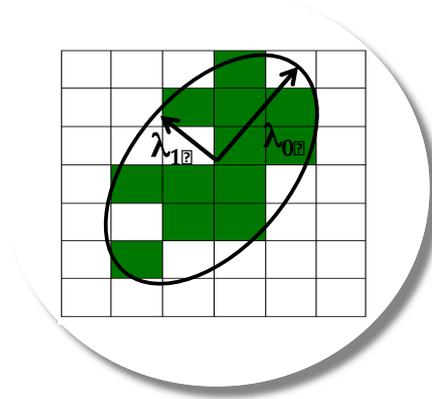
Figure 5.4: *Example of a shower profile and its principal axes e_1 and e_2 [93].*

of electromagnetic calorimeters,

$$d = \frac{\sum_{digits} w_i [(x_i \quad x)^2 + (z_i \quad z)^2]}{\sum_{digits} w_i} . \tag{5.9}$$

Using shower shape analysis, the particles detected with calorimeters relies on three independent identification parameters derived from the data collected by the detector. For high

energy π^0 ($p_{\mathrm{T}} > 25$ GeV/c for PHOS, and $p_{\mathrm{T}} > 6$ GeV/c for EMCAL), the Lorentz boost contracts the relative angle between π^0 decay photons to small values ($\Delta\gamma_1\gamma_2 < 0.8°$ for a symmetric decay) and the two showers developing in calorimeters overlap and are reconstructed as one single photon. This configuration provides, however, the opportunity to discriminate photons from overlapped decay photons based on an analysis of the cluster shape: a cluster with axial symmetry in (x,z) signs a photon, whereas an asymmetric cluster signs overlapped decay photons [107]. Particle identification weights, which represent the probability that the detected particle is of a given type, among photon (γ), electron ($e^\pm$), charged hadron ($h^\pm$), neutral hadron (h^0) and high–p_{T} π^0, are assigned to each reconstructed particle following a Bayesian approach [108]. For the Monte-Carlo study, we considered a particle to be a photon when the probability weight is larger than 0.5. With this selection criteria, we find an efficiency to reconstruct and identify direct photons, calculated as the ratio of reconstructed and identified photons to γ–jet generated photons, equal to 70% at 10 GeV and about 55% at 80 GeV. This efficiency includes a 10% loss due to γ-conversion in the material in front of PHOS and an additional loss of 10% due to border effects. In jet-jet events, we observe a decrease in the ratio identified to generated photons from the same value as the one obtained for γ–jet events, below 20 GeV/c, to a value of 0.2 at 45 GeV/c, demonstrating the excellent rejection provided by the shower shape analysis [109].

We therefore conclude that the shower shape analysis, for distinguishing direct photons and decay photons merging into a single cluster, allows us to enrich substantially the data sample with direct photons. However the ratio of direct photon to decay photon, of about 0.2 at p_{T} of 20 GeV/c [109], remains too low. The method is not selective enough to reduce the contribution of decay photons to a negligible low level. We then consider the isolation techniques to enhance the significance of signal to background level.

5.2.3 Isolation Cut: IC

Prompt photons are produced from Compton Scattering and Annihilation (Eq. 5.1) in which the final state photon and parton are emitted back-to-back. As there is no hadron from the parton jet flying in the same direction as the photon, the latter should appear as isolated photons. One can take benefit of this kinematics and apply isolation selection to identify prompt photons and obtain a sufficiently clean sample of prompt photons [107]. The isolation

criteria defines the level of hadronic activity in a cone axed on the direction of the trigger candidate, which searches for hadrons inside a cone center around the direction (η_0, ϕ_0) of high-p_T trigger candidates (Fig. 5.5). The cone size is given by:
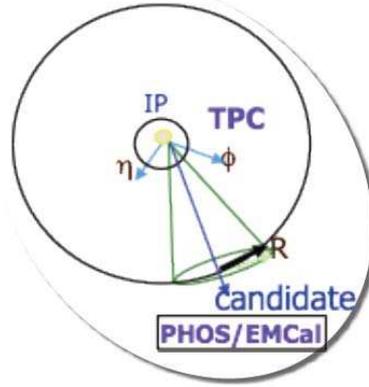
Figure 5.5: *The scheme of isolation criteria.*

$$R = \sqrt{(\phi - \phi_0)^2 + (\eta - \eta_0)^2} \ . \tag{5.10}$$

The hadron multiplicity depends on the cone size and on the event type, thus, applying p_T cuts to the particles in a cone around the photon cluster candidate helps to distinguish prompt photons and non-isolated photons. Three different selection criteria can be used:

1. No hadron with p_T above a given threshold (p_T^{thres}) is found in the cone.

2. The sum of the transverse momentum of all hadrons inside the cone is smaller than a given threshold ($\sum p_T^{\text{thres}}$). This method is based on the value of the sum of the transverse momentum ($\sum p_T$) of all particles found in a given cone around the photon candidate.

3. The sum of the transverse momentum of all hadrons inside the cone is smaller than a given fraction (ε) of the transverse momentum of the trigger candidate. For low energy photon candidate, the sum of the transverse momentum ($\sum p_T$) of all particles inside the cone is smaller than the mean transverse momentum of hadrons (p_T^{thres}) from the underlying events at forward region to take into account the background hadrons surrounding the photon candidate.

A set of parameters defining the phase space in which the hadronic activity is calculated and thresholds on the hadronic activity have been deduced to optimize the isolated photon

identification efficiency and minimize the contamination level from decay photons. From previous studies [106, 109], we conclude that in the case of proton–proton collisions, a threshold on $\sum p_{\mathrm{T}}$ is more efficient than a simple threshold on p_{T}. For γ–jet events, most of the hadronic activity stays below a few GeV/c due to the few hadrons coming from the underlying proton–proton events. The high-p_{T} activity observed in the reconstructed events is interpreted as due to photons which have been converted before reaching calorimeters, the converted electron triggers are taken while in the meantime the two electron tracks contribute to the hadronic activity. For jet–jet events the hadronic activity is distributed over several tens of GeV/c [109].

Considering the incomplete EMCAL geometry at the time of the first data taking, only charged hadrons activity is taken for isolation cut study. Choosing the isolation cut parameters of $R = 0.4$, $\varepsilon = 0.1$ and $p_{\mathrm{T}}^{thres} = 1$ GeV/c on the photon clusters from generated γ-jet and jet-jet events with jet energy $E_{jet} > 5$ GeV, the distribution below 5 GeV for γ-jet events is not trustable due to the trigger energy threshold, and the isolation removes a large fraction of decay photon clusters while most of direct photons from γ-jet events remains (Fig. 5.6).
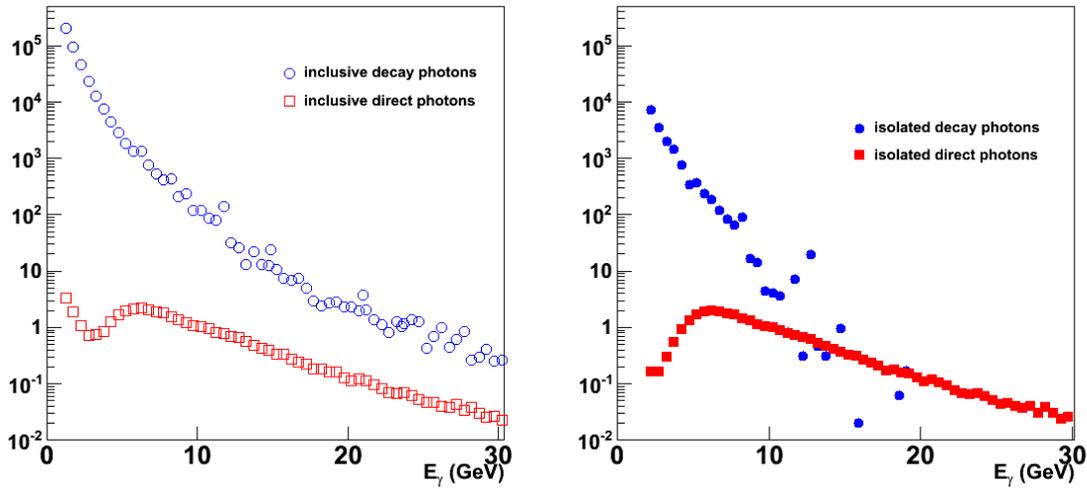
Figure 5.6: *Number of photons from PYTHIA generated (left) γ-jet and jet-jet events with jet energy $E_{jet} > 5$ GeV and the isolated photons after applying the isolation cut parameters of $R = 0.4$, $\varepsilon = 0.1$ and $p_{\mathrm{T}}^{thres} = 1$ GeV/c on the photon clusters from generated ones (right).*

The identified prompt photon sample which can be accumulated with the two PHOS modules during the first year of LHC running ($\mathcal{L} = 10^{30}$ cm^{-2}s^{-1} and $t = 10^7$ s) in proton–proton

collisions at $\sqrt{s} = 14$ TeV will be sufficient to measure the prompt photon spectrum over a large p_T range between 20 and 80 GeV/c. Counting rates will limit the measurement, but not systematic errors which are dominated by the remaining decay photon and fragmentation photon background (the systematic errors have been arbitrarily multiplied by two to take into account additional source of photons in jet–jet events not considered in our simulation).

The larger acceptance calorimeter EMCal allows to improve the quality of the measurements, where the direct prompt photon p_T range could reach up to 120 GeV/c with the full EMCAL super modules during the LHC running ($\mathcal{L}_{int} = 0.5 \times 10^6$ mb $^{-1}$) in proton–proton collisions at $\sqrt{s} = 5.5$ TeV.

5.3   Correlation distributions in pp collisions

Jets are usually produced in pairs, that are back-to-back in the transverse plane, and are separated by an azimuthal distance $\Delta\phi \approx \pi$. They can be revealed by studying azimuthal correlations as a function of $\Delta\phi$ ($= \phi_{trig} - \phi_h$) between a trigger particle with high transverse momentum in calorimeters, i.e. prompt photon clusters from γ–jets events or decay clusters from jet–jet events, and associated particles from the same event. For jet–jet events, the correlation shows a near ($\Delta\phi = 0$) and an away side ($\Delta\phi = \pi$) peak, and in γ−jet events there are no hadrons surrounding the prompt photons as selected trigger therefore no near side correlations is observed (Fig. 5.7, left). The difference between the generated MC distribution and reconstructed ESD distribution results from the detector response loss. In jet-jet events the away side peak is shifted with respect to π and is broader than the far side peak in γ–jet events, because the tagged decay cluster from π^0 in jet–jet events carries only a fraction of the jet and is not necessarily the leading particle of the jet fragments hadrons. (Fig. 5.7, right).

To construct the photon-hadrons correlation distribution, events where photons and charged hadron are emitted in different hemispheres ($\pi/2 < \Delta\phi < 3\pi/2$) are selected. The contribution from the underlying proton–proton events was estimated by correlating the trigger photon with the charged hadrons emitted on the same side ($-\pi/2 < \Delta\phi < \pi/2$). We define our signal (S) as the opposite side correlated charged hadrons minus the same side correlated charged hadrons (B) and compare their p_T spectra (Fig. 5.8) to the one of the opposite side correlated charged hadrons (S+B). At p_T larger than 5 GeV/c, the contri-
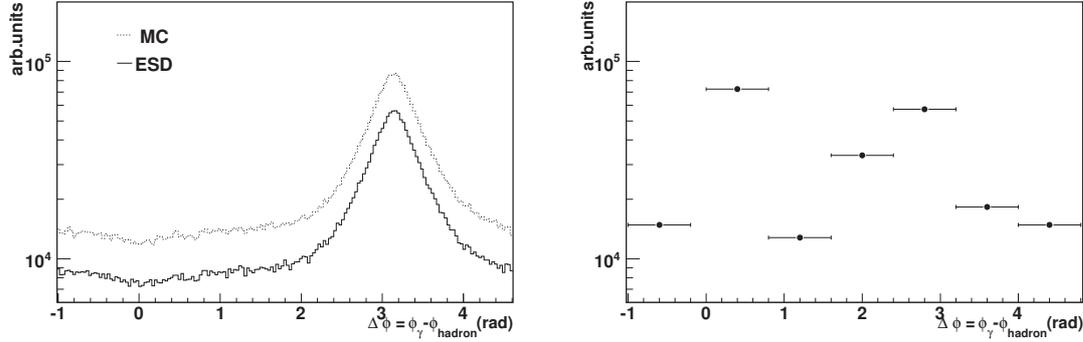
Figure 5.7: *Relative azimuthal angle distribution* $\Delta\phi = \phi_\gamma - \phi_{hadron}$ *in proton–proton collisions at* $\sqrt{s} = 14$ *TeV for isolated photons with* $p_{T_\gamma} > 20$ *GeV/c: from Monte Carlo events (dashed line) and from events reconstructed by ALICE (solid line) for* γ*–jet events (left) and jet–jet events (right). In jet–jet events the* π^0 *trigger is not necessarily the leading particle.*

bution from the underlying event (UE) is small and stays constant, at the level of 2%. Therefore we conclude that in the $x_E > 0.2$ range, this UE contribution remains negligible. The photon tagged hadrons distribution, and the underlying event contribution normalized to the number of triggers measured by 10 EMCal super modules are shown as the MLLA variable [110] $\xi \equiv \ln(1/z) \approx \ln(1/x_E)$, i.e. the number of isolated photons $(1/N_{trigger}dN_{hadrons}/d(\ln(1/x_E)))$ (Fig. 5.9 [111]). It is shown that the UE contribution is negligible.

The jet fragmentation function from γ–jet events is calculated at the generator level in the following way. Starting from the generated events, the jet in each event was reconstructed (E_T^{jet}, η_0, ϕ_0) using the UA1 jet finder algorithm [112] implemented in the PYTHIA PYCELL cluster finding routine. The true jet fragmentation function was then constructed from all particles (p_T, η, ϕ) within a cone of $R = \sqrt{(\eta - \eta_0)^2 + (\phi - \phi_0)^2} = 1$ around the jet direction as a function of $z = p_T/E_T^{jet}$. We have compared the shape of the jet fragmentation function and the photon tagged hadrons distribution as a function of x_E for $p_{T_\gamma}^{cut} = 20$ GeV/c, $p_{T_h}^{cut} = 2$ GeV/c constructed from the same sample of events (Fig. 5.10). The two distributions are in agreement in the x_E range between 0.12 and 0.65 and differ slightly at higher x_E values by about 10% at $x_E = 0.7$ and by about 20% at $x_E = 0.9$. The difference below $x_E = 0.12$ is a consequence of the kinematical cut applied in the construction of the photon tagged hadrons distribution and the difference above $x_E = 0.7$ is due to the finite energy resolution of the photon measurement and k_T effect (see Sec. 5.4). The resulting photon tagged hadrons
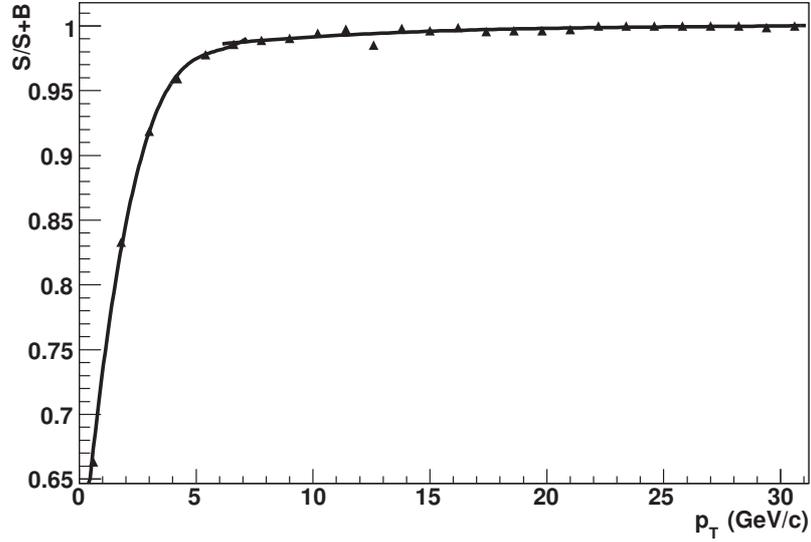
Figure 5.8: *The ratio of reconstructed signal hadrons from jet fragmentation to background hadrons from underlying events in γ–jet events. The solid line is a fit to the data points.*

distribution indicates that the uncertainty in such kind of measurement is dominated by the counting rate but not systematic errors. The systematical errors could be reduced by selecting a sufficiently high photon, but measurements with higher $p_{\mathrm{T}\gamma}^{\mathrm{cut}}$ values are limited by the available counting rate.

We conclude that the photon tagged hadrons distribution can, under these conditions be constructed in proton-proton collisions between $x_E \sim 0.2$ and ~ 0.8 with an accuracy sufficient to measure jet fragmentation functions.

Obviously, in heavy-ion collisions because of the high multiplicity underlying events, the identification of direct photons through isolation selection is less efficient but remains an excellent means to enrich the data sample with prompt photons since high-p_{T} π^0 production is quenched by the medium. The isolation selection has the additional advantage to reject as well fragmentation photons (NLO photons) or bremsstrahlung photons which could be present in heavy-ion collisions. These two contributions would alter the equivalence between the photon-hadrons correlation distribution and the jet fragmentation function.
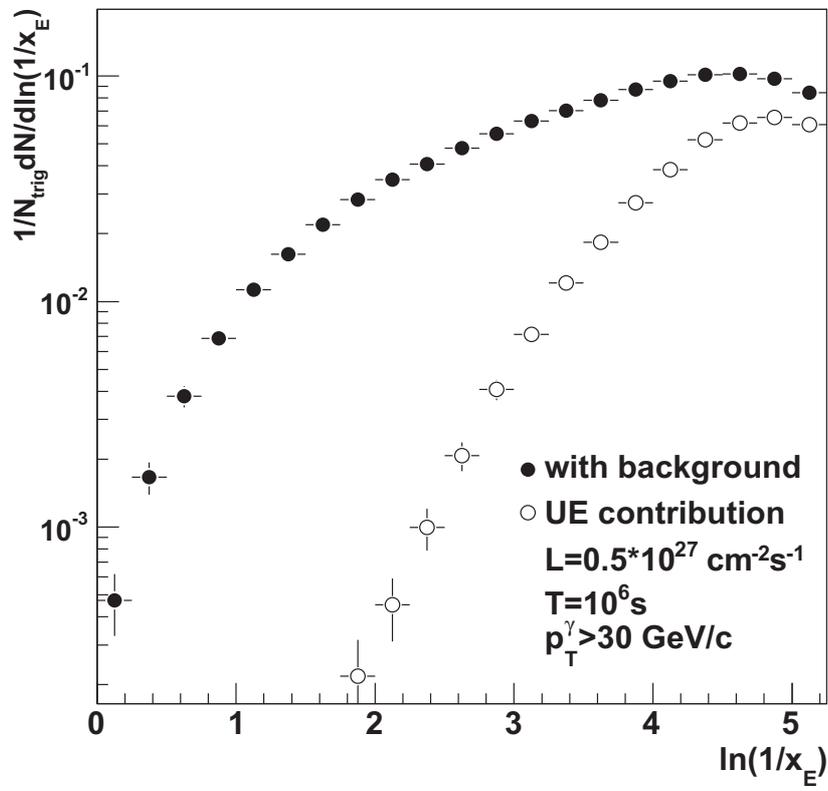
Figure 5.9: Photon-charged hadron correlation spectrum and the contribution from underlying event using photons identified by EMCal in pp collisions at $\sqrt{s} = 5.5$ TeV [111].
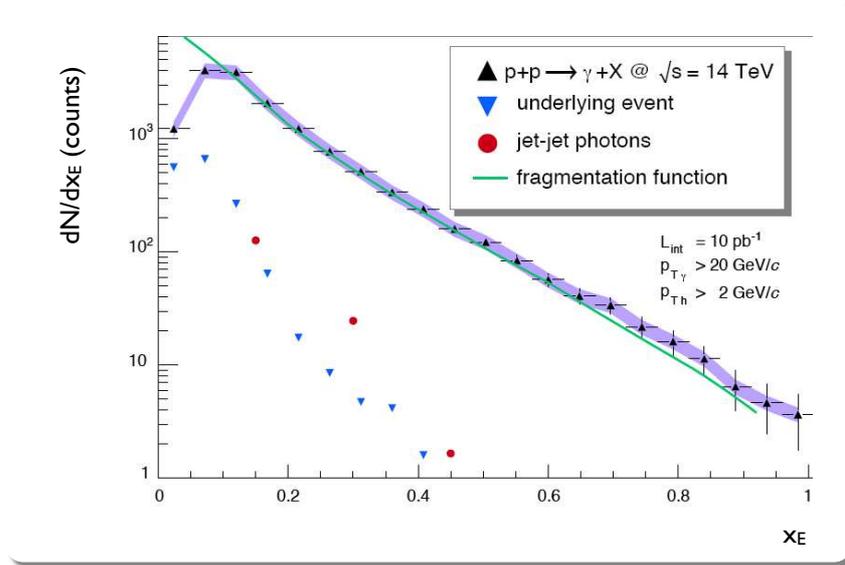
Figure 5.10: *Photon–charged hadrons correlation distribution with $p_{T_\gamma} > 20$ GeV/c, $p_{T_h} > 2$ GeV/c calculated in proton–proton collisions at $\sqrt{s} = 14$ TeV from PYTHIA generated Monte-Carlo data. The data points with error bars represents the total spectrum (γ–jet plus jet–jet events) as it will be measured, the errors bars represent the statistical errors of the measurement and the area around the data points represents the systematic errors due to the jet–jet photons not properly identified. The contribution from jet–jet photons (closed circles) and from the underlying event (downwards triangles) are displayed as well. The ideal jet fragmentation function are calculated from the PYTHIA generated Monte-Carlo γ–jet events is also shown (green line) [17].*

5.4 k_T smearing

The effect of $\vec{k_T}$ smearing results from the original back-to-back pair is modified by the finite transverse momentum present in the initial state of the hard scattering, which will misalign the back-to-back azimuthal correlations and distort the photon-tagged hadrons distribution for jet fragmentation study. In order to estimate how the k_T smearing affect the correlation study, first we have predicted the k_T values at LHC energies starting from different experimental measurements on the average $< k_T >$ (Fig. 3.7) from two particle correlations. Then we have reproduced the measured $< k_T >$ values from the existing worldwide experimental data by tuning the PYTHIA parameter (intrinsic k_T).

PYTHIA provides three parameters to add transverse momentum to the $2 \rightarrow 2$ pQCD processes: $k_{T_{intrinsic}}$ for the intrinsic transverse momentum (Fermi motion) in the initial state, the initial state gluon radiation (ISR) and final state gluon radiation (FSR) switch. The k_T parameter was tuned with ISR and FSR switched on to reproduce the measured $< k_T >$ (on Fig. 3.7) in γ jet events produced in proton-proton collisions at energies ranging from $\sqrt{s} = 23.6$ GeV to 1.96 TeV with the PYTHIA generated events. k_T was calculated from $< p_T >_{pair}$ ($< p_T^2 >_{pair} = 2 < k_T^2 >$), where $< p_T >_{pair}$ is the average sum value of the transverse momentum between γ and jets. The function $< p_T >_{pair} = A \cdot \log(B \cdot \sqrt{s})$ was fitted to the evolution of the $< p_T >_{pair}$ with $\sqrt{s}$ and extrapolated to the LHC energies. Doing so we predict a k_T value equal to 4.5 ± 0.5 GeV/c at $\sqrt{s} = 7$ TeV (Fig. 5.11) with the fitting parameters of $A = 2.064 \pm 0.171$ and $B = 0.164 \pm 0.045$ correspondingly.

The presence of a finite value of k_T modifies the ideal kinematics of $2 \rightarrow 2$ processes and hence the two particle correlations and measurement of jet fragmentation. We focus now on these modifications.

To that purpose, γ-jet events have been generated with PYTHIA in pp collisions at $\sqrt{s} = 10$ TeV according to the initial plan at LHC, the k_T setting are taken from Fig. 5.11 including the uncertainties on the extrapolated values, and ISR/FSR switched alternatively on and off. The jet is reconstructed by the PYTHIA jet finder with cone size $R = 1$. The γ tagged hadrons distribution (CF) obtained for various combination of the parameters (k_T values, ISR/FSR) is compared to the jet fragmentation function (FF) calculated with the same parameters settings (Fig. 5.12). As expected, CF and FF have an identical distribution when k_T and ISR/FSR are set off. On the other hand, finite values of k_T generate a tail in CF
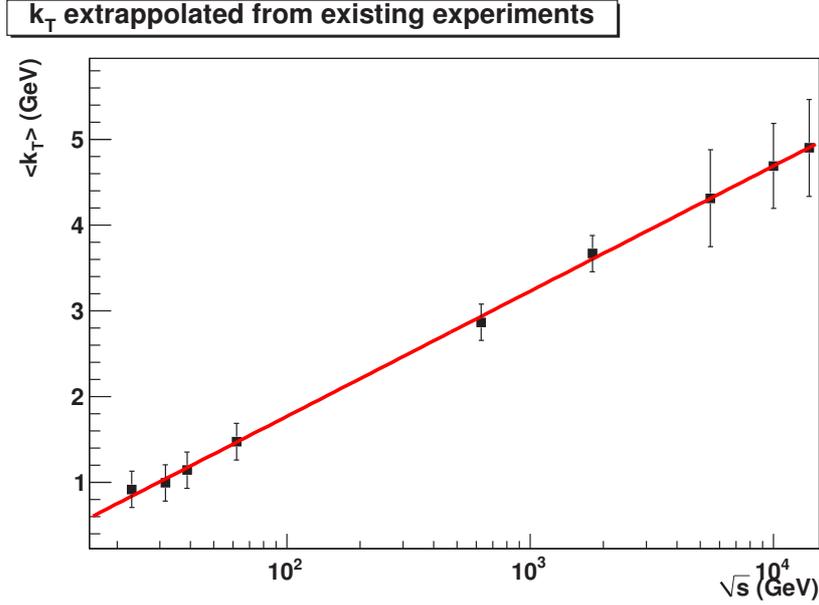
Figure 5.11: k_T reproduced by PYTHIA generated γ-jet events and extrapolated to LHC energies.

beyond $x_E = 1$. Switching ISR and FSR on depletes both CF and FF at $x_E \leq 1$ and increases the strength at small values of x_E. This effect is similar to the effect due to jet quenching. All the effects can been seen in the ratio of CF and FF for ISR/FSR on and off together with various k_T settings for the generation (Fig. 5.13). We then conclude that initial state k_T will distort the correlation distribution from jet fragmentation, on the other hand, it implies the photon-hadrons correlation observable is quite sensitive to the k_T and the initial and final state radiation as we anticipated on jet fragmentation.

5.5 Measurements of Nuclear Effect via Photon-Hadron Correlations

In the heavy-ion environment, jets with energy below 50 GeV cannot be reconstructed with standard jet finder algorithms. These low energy jets are however interesting because they will be very sensitive to the medium as they loose a large fraction of their energy, of the order of 20 GeV. Such large energy loss can be identified in the fragmentation function of these low energy jets by measuring the correlations between direct photon and charged hadrons. The observable is the photon-tagged hadrons distribution, where the hard scattering parton
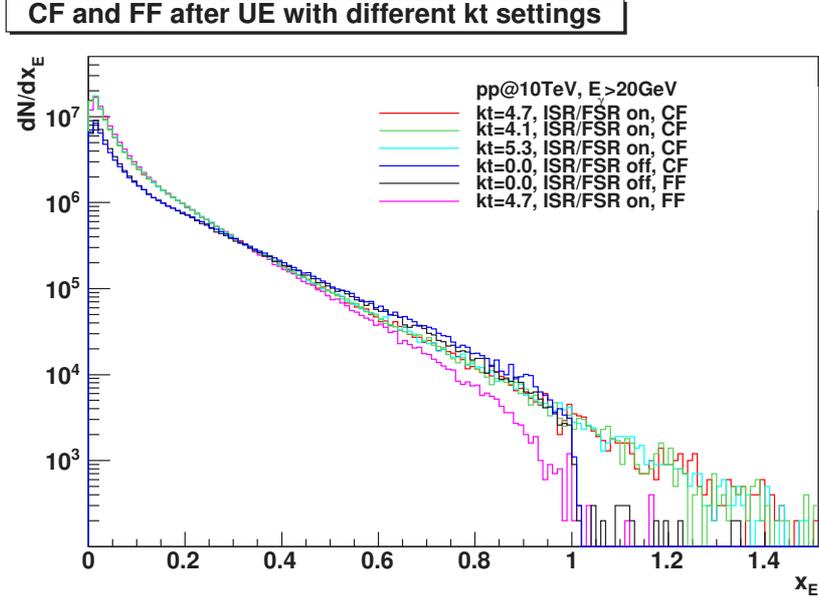
Figure 5.12: *Comparison of fragmentation function with imbalance distribution from Monte Carlo generated γ-jet events with jet energy larger than $20GeV$ in pp@10TeV by tuned parameters in PYTHIA, the uncertainty of k_T from the estimation are shown as well.*
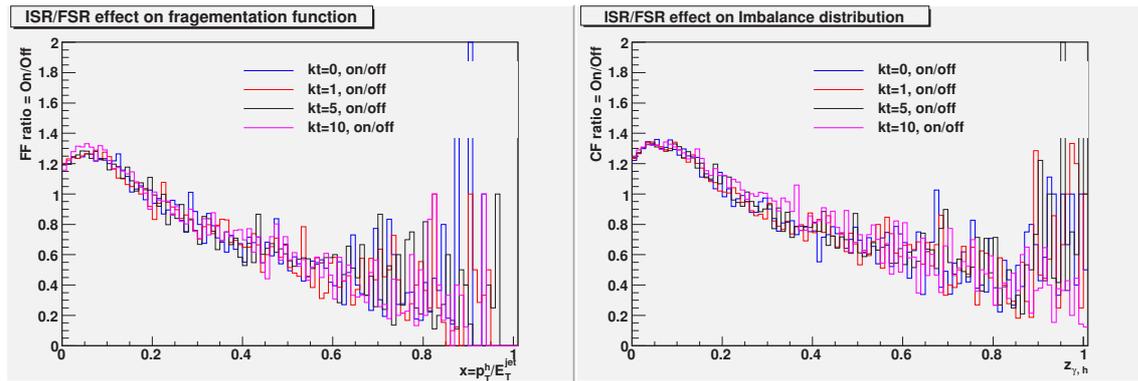
Figure 5.13: *Ratio of fragmentation function (left) and correlation function (right) distribution when ISR/FSR radiation on and off from Monte Carlo generated γ-jet events with jet energy larger than $20GeV$ in pp@10TeV by PYTHIA.*

opposite to photon will experience medium induced energy loss in AA collision compared to pp collision.

To quantify this medium modification of γ-hadrons correlation distribution in heavy ion collisions relative to pp collisions, one defines the medium modification factor I_{AA},

$$I_{AA}(x_E) = \frac{CF_{AA}}{CF_{pp}} \; , \tag{5.11}$$

for γ-hadrons correlation distribution.

5.5.1 Energy Loss via $\gamma+$ Jets

To study this medium induced energy loss, we have used a simple quenching model (QPYTHIA) [113] implemented into PYTHIA. Such a quenching model combines the calculation of energy loss [114] and a realistic description of the collision geometry [24], which plays an important role for studying medium induced energy loss and the possibility for a tomographic study in heavy-ion collisions, where a HIJING [100] event generator is taken for heavy-ion collisions. Within these generators, three samples of γ-jet events with energy larger than 20 GeV have been generated:

- The first sample is composed of γ-jet events generated in pp collisions at 5.5 TeV, using PYTHIA under the AliRoot framework. No quenching is considered. This sample is representative of a baseline of quenching study.

- The second sample, consists in merging quenched γ-jet events from QPYTHIA, and the underlying events of central heavy-ion collisions from the HIJING generator.

- The last sample, is similar to the previous one but without quenching and the underlying events of peripheral heavy ion collisions.

In the Figure 5.14, which shows the p_T spectrum of hadrons with and without quenching effect, the suppression at high p_T can be clearly observed, as well as an enhancement at low p_T.

In the γ-hadrons correlation distribution (Fig. 5.15), the large contribution from the UE of heavy-ion collisions is clearly visible. It can be subtracted by evaluating its contribution from emitted hadrons in the same azimuthal directions as the photon trigger. After UE subtraction, the modification when going from peripheral to central collisions become visible.
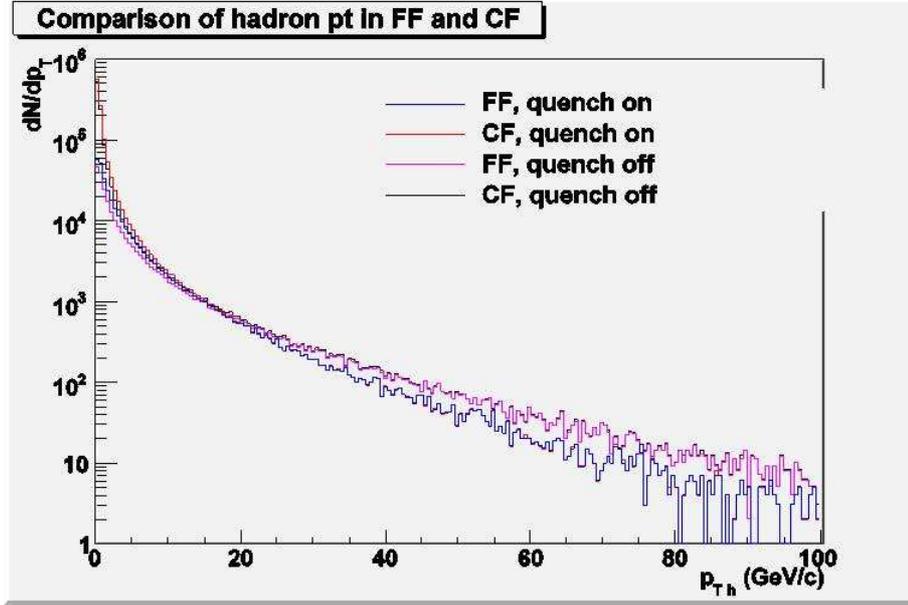
Figure 5.14: *Comparison of hadrons transverse momentum spectrum with and without quenching in jet fragmentation function and correlation distribution from Monte Carlo generated γ-jet events with jet energy larger than 20GeV in pp@5.5TeV by tuned parameters in PYTHIA.*

The effect of the medium modification is better seen in the medium modification factor I_{AA} (Eq. 5.11) as shown in Fig. 5.16. The enhancement at low x_E and the suppression at high x_E can be seen nicely for central collision, whereas, I_{AA} is equal to 1 for peripheral collisions as expected.

This purely Monte-Carlo study has been further constrained to take into account the finite acceptance of ALICE calorimeter EMCal for the detection of the trigger photons, We proceed as follows. First, an isolated photon is identified in EMCal with p_T larger than 30 GeV/c; then the distribution as a function of x_E or the relative azimuth angle $\Delta\phi = \phi_\gamma \quad \phi_h$ is accumulated. Hadrons are selected within $\pi/2 < \Delta\phi < 3\pi/2$ and minimum p_T threshold of 200 MeV/c to reduce the background influence.

We have studied the nuclear modification factor R_{AA} (Fig. 5.17) for charged hadrons produced in γ-jet events and I_{AA} (Fig. 5.18) for γ-hadrons correlation function. Different values of the transport coefficient $\hat{q}$ have been considered. We observed that R_{AA} and I_{AA} behave similarly, the larger values of $\hat{q}$ generate a stronger suppression at high p_T (or x_E) and enhancement at low p_T (or x_E) as expected.
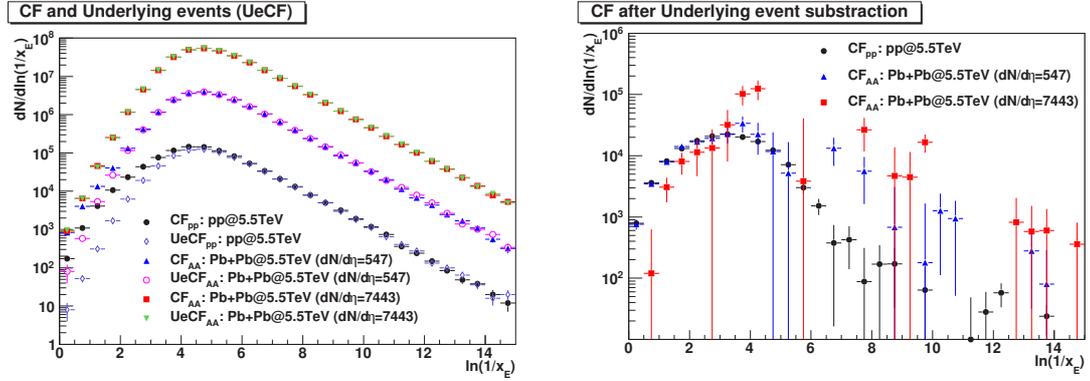
Figure 5.15: *γ-hadrons correlation distribution in heavy ion collisions, the underlying events distribution is correlated photons with the hadrons at the same side of photons. On the right is the γ-hadrons correlation distribution after the underlying subtraction.*
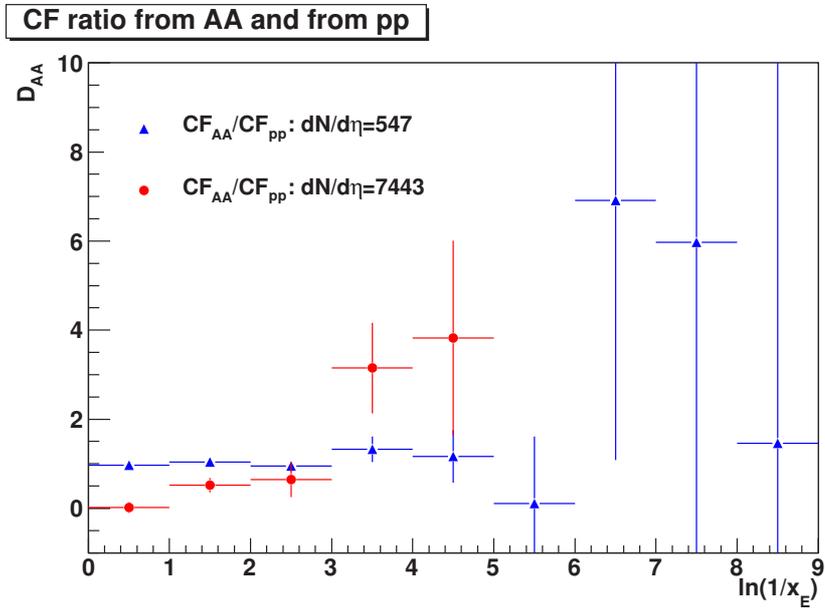
Figure 5.16: *The nuclear modification factor I_{AA} for γ-hadrons correlation distribution in central and perpgeral Pb+Pb collisions at LHC energy.*
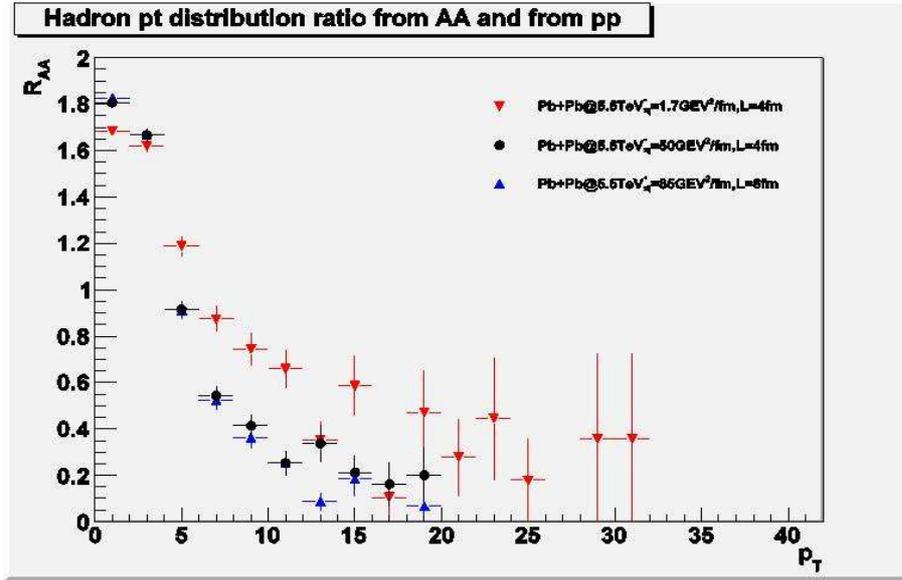
Figure 5.17: *The nuclear modification factor R_{AA} for charged hadrons in γ-jet events at LHC energy, different transport coefficient $\hat{q}$ are used for different production.*
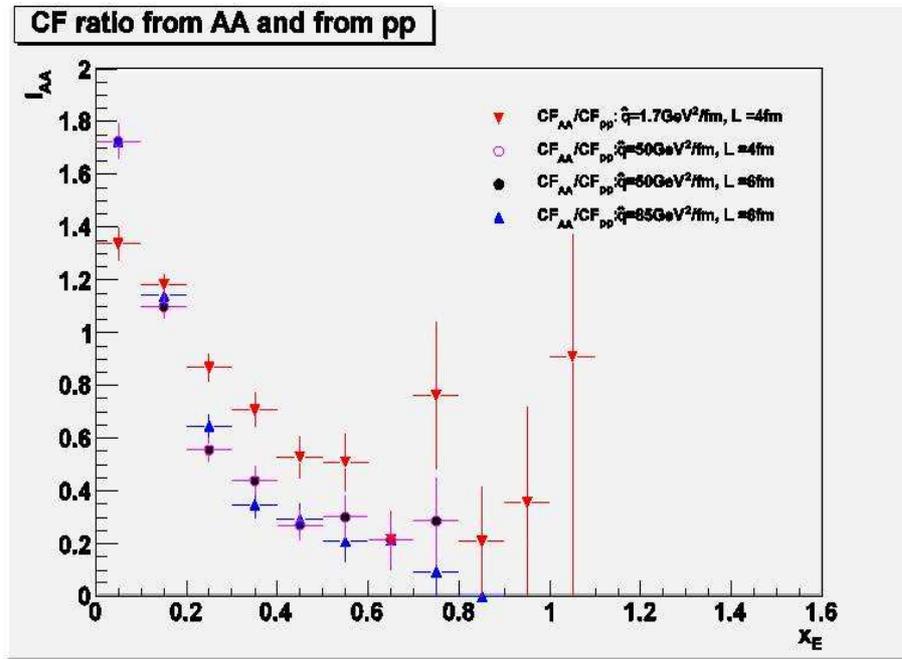
Figure 5.18: *The nuclear modification factor I_{AA} for γ-hadrons correlation distribution at LHC energy, different transport coefficient $\hat{q}$ are used for different γ-jet production.*

Fig. 5.19 shows the relative azimuthal angle distribution between the direct photon and charged hadrons with and without quenching ($\hat{q} = 50$ GeV/fm). The width of the away side peak ($\Delta\phi = \pi$) distribution becomes wider when medium effect is included. This broadening width is related to the k_T value as we explained in the previous chapter, by measuring such a broadening will serve as a realistic probe of the medium and its characteristic parameters $\hat{q}$ since $< \Delta k_T^2 > \propto \int \hat{q}(y)dy$.
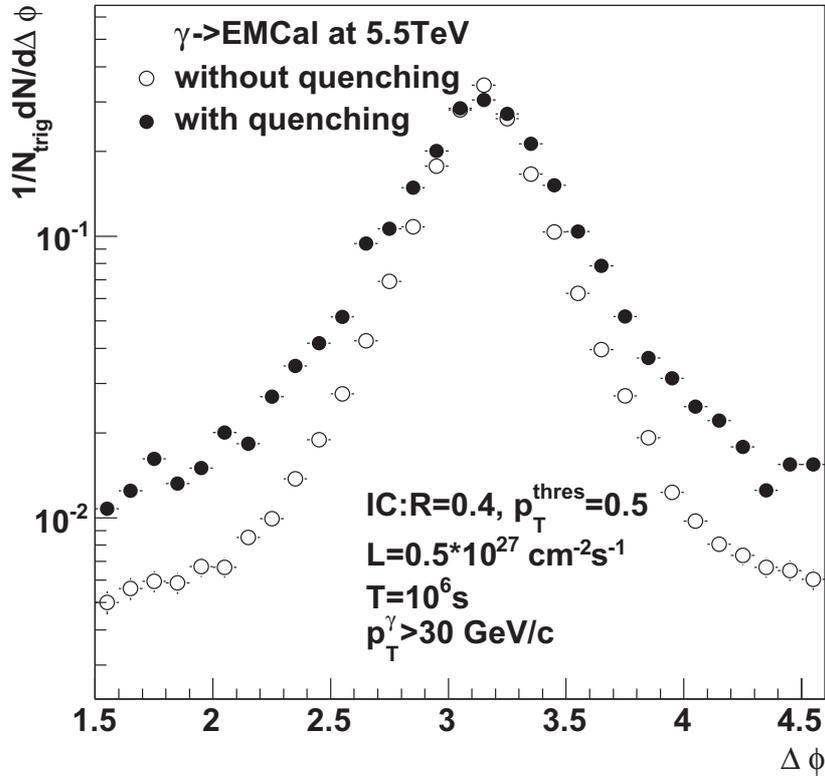
Figure 5.19: Relative azimuthal angle distribution $\Delta\phi = \phi_\gamma \quad \phi_{hadron}$ for γ-jet events in pp collisions at $\sqrt{s} = 5.5$ TeV. Photons with $p_{T,\gamma} > 30$ GeV/c are measured and isolated in EMCAL. Associated hadrons have $p_{T,hadron} > 2$ GeV/c. Full circles indicate quenched events and empty circles indicate unquenched events by PYTHIA generator. Distributions are normalized to the total number of isolated photons.

The resulting photon-tagged hadrons spectra after the underlying event subtraction with photon triggers measured in EMCAL are shown in Fig. 5.20-left. Each distribution is normalized to the number of triggers and plotted as the MLLA variable [110] $\xi \equiv \ln(1/z) \approx \ln(1/x_E)$. The ratio of the quenched over unquenched distributions, labeled R_{CY}, is shown in Fig. 5.20-

right. The statistical errors are based on the achievable annual yield of hadrons correlated with photons with p_T larger than 30 GeV. An enhancement at low x_E and a suppression at high x_E are clearly observed.
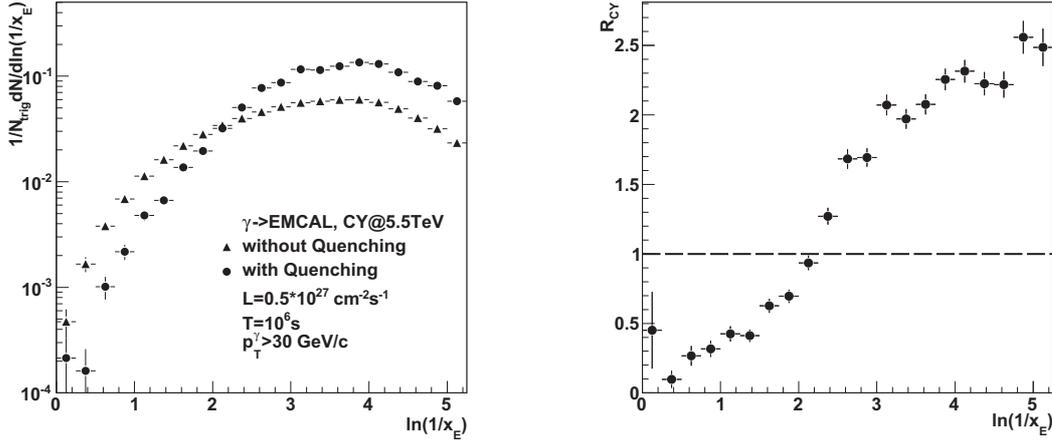
Figure 5.20: Left: γ-hadron correlation distributions in quenched and unquenched PYTHIA events as a function of ξ. Right: The ratio of the photon-triggered conditional hadron yields R_{CY} for PYTHIA and qPYTHIA events.

5.5.2 Tomography with $\gamma+$ Jet events

An energetic parton produced in a hard collision undergoes multiple scattering along its path in the dense medium. In this multiple scattering process, the gluons in the parton wave function pick up transverse momentum k_T with respect to the direction and may eventually decohere and be radiated. The scale of the energy loss is set by the characteristic energy of the radiated gluons [115]

$$\omega_c = \hat{q}\, L^2/2 \;, \tag{5.12}$$

which depends on the in-medium path length L of the parton and on the BDMPS transport coefficient of the medium, $\hat{q}$ [40]. The transport coefficient is defined as: $\hat{q} = < k_T^2 >_{medium} /\lambda$, where λ is the mean free path [114]. Moreover, the suppression of the opposite jet is averaged over all path-lengths given by the distribution of hard scattering vertices. Since photons do not carry color charge and hence do not interact strongly when traversing the medium, the distribution of hard scattering vertices sampled by photon tagged hadrons is thus unbiased by the trigger condition.

By selecting γ-h pairs with different values of x_E, one can effectively control hadron emission from different regions of the dense medium and therefore extract the corresponding jet quenching parameters [87]. In this way, the average path-length of the away-side parton may then be varied in a well controlled manner by selecting events of various momentum differences between the γ-h pair.

To illustrate the picture of volume and surface emission of γ-hadrons correlation, a Monte-Carlo simulation based on QPYTHIA and the fast Glauber model [24] has been performed to study medium length L dependence. The medium length along which the hard scattered parton travels inside the medium is calculated according to its kinematics information and the nuclear geometry. The distribution of fraction of the trigger photon energy carried by the leading hadron (with highest transverse momentum) emitted opposite to the trigger photon is first calculated (Fig. 5.21). In presence of quenching effects, the distribution is shifted to lower values of x when compared to the distribution without quenching.
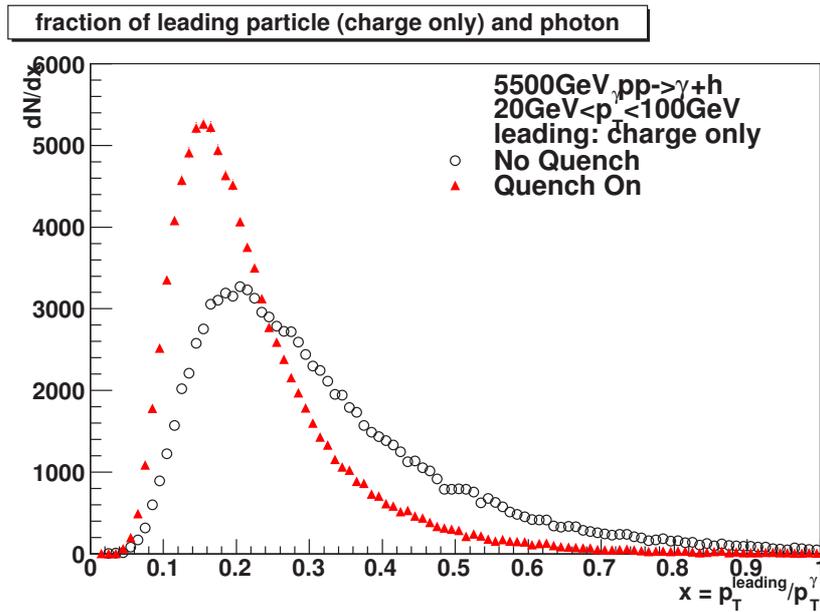
Figure 5.21: *The ratio of the leading particles p_T over the photons p_T with and without quenching effect is taken into account.*

The dependence of the momentum carried by the leading hadrons (x) with its azimuthal correlation with the photon ($\Delta\phi$) is shown in Fig. 5.22, and with the distance inside the medium in Fig. 5.23. They indicate that the highest p_T leading particles are preferably originating from hard scattering occurring at the surface of the medium (small L), while the

low p_T leading particles are generated inside the volume.
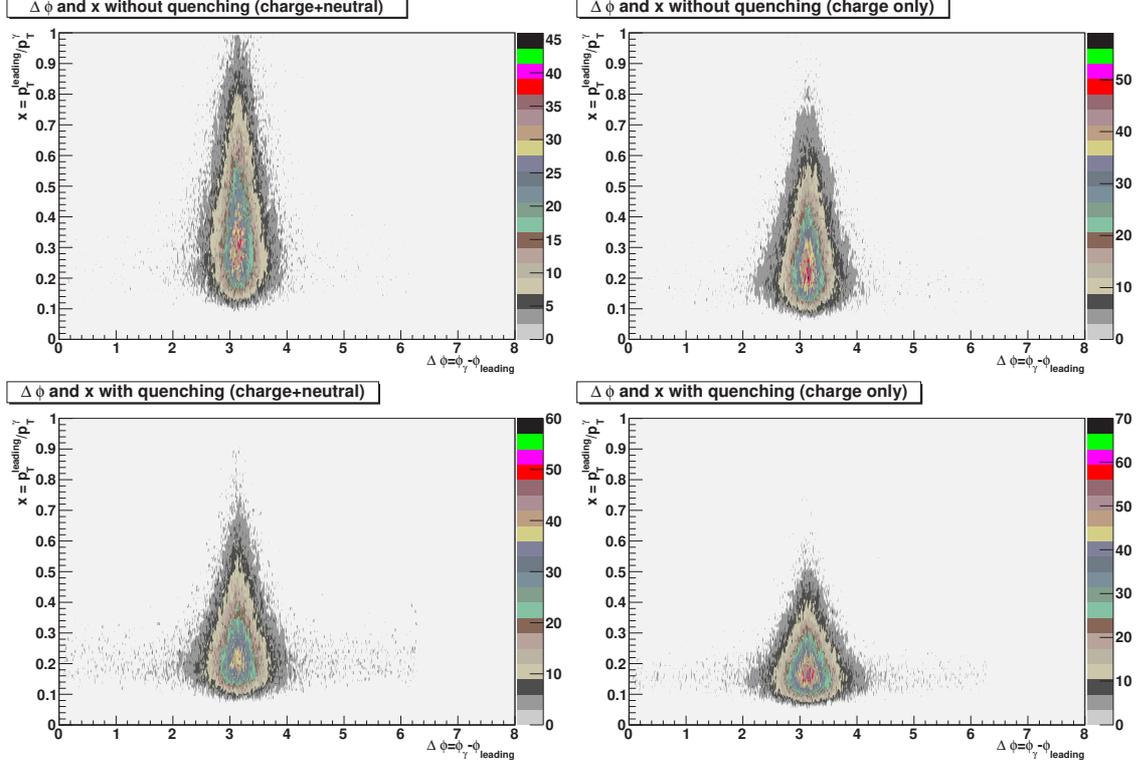
Figure 5.22: *The correlation between the leading particle ratio and the $\Delta\phi$ distribution of leading particles and photons, with (low) and without (up) quenching effect is taken into account respectively. The left panel is selecting leading particles inside all the generated particles (ideal case), the right one just took final state particles which could be measured in the experiment.*

This observation can be confirmed by studying the distribution of leading particle versus the path length L (the distance traversed by the hard scattered parton inside the medium) with two different values of x (Fig. 5.24). One again observes that low x_E hadrons originated mainly from partons that have traversed larger distance inside the medium (see also Fig. 5.25). We have also verified that there is no L dependence in absence of quenching (Fig. 5.24 and Fig. 5.25). The probability to find high p_T particles at the surface is much higher than inside the medium when the quenching is presenting (Fig. 5.25).

Finally, the quenching effect can be studied as a function of the in medium length (Fig. 5.26). An obvious suppression for large x leading particles is observed while an enhancement is seen for low x particles, and the larger suppression or enhancement with the in medium length L increases. By selecting different x_E regions on CF, different behaviors of medium modification
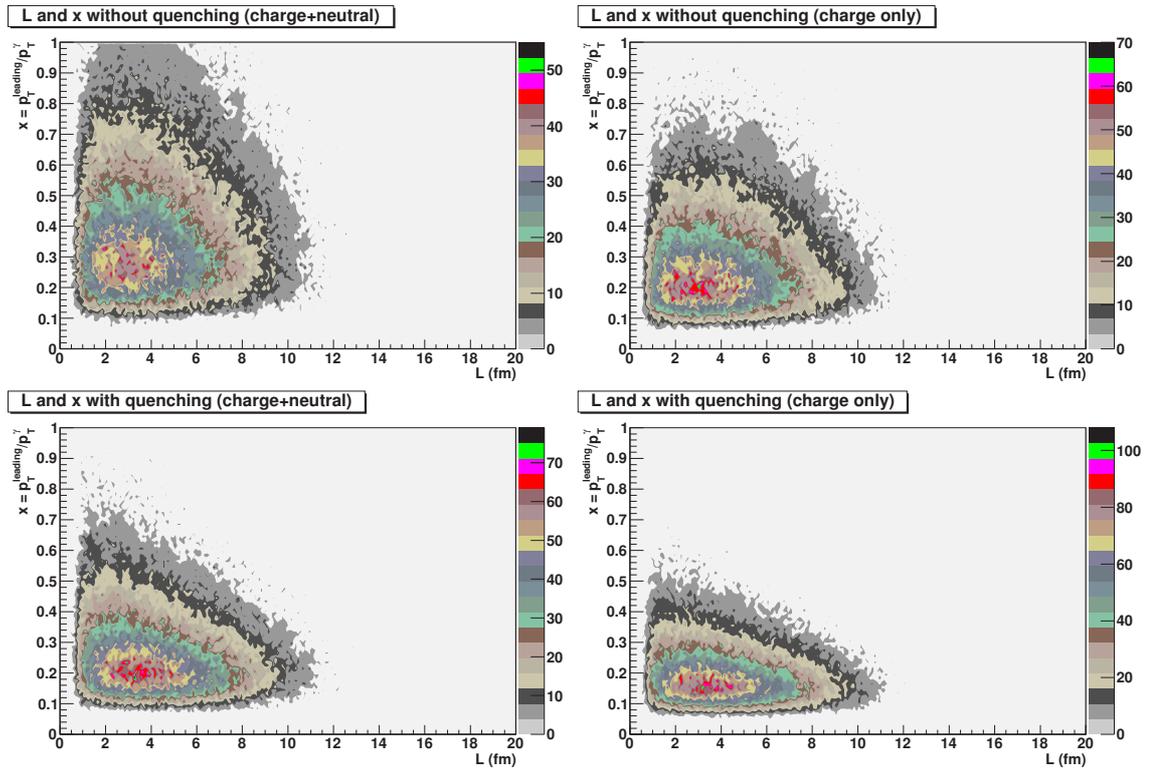
Figure 5.23: *The correlation between the leading particle ratio and the medium length distribution of leading particles, with (low) and without quenching effect (up) is taken into account respectively. The left panel is selecting leading particles inside all the generated particles (ideal case), the right one just took final state particles which could be measured in the experiment.*

factor I_{AA} depending on the medium length L can be found (Fig. 5.27), which verifies that γ-hadrons correlation could probe volume (surface) emission of heavy ion collisions by selecting imbalance variable x_E at different range, for small values of x_E, the γ-hadrons correlation yield is dominated by volume emission while surface emission is the dominate production mechanism for large x_E. Such kind of study will enable us to extract jet quenching parameters from different regions of the dense medium via measurement of the nuclear modification of γ-hadrons correlation in the whole kinetic region, achieving a true tomographic study of the dense medium.
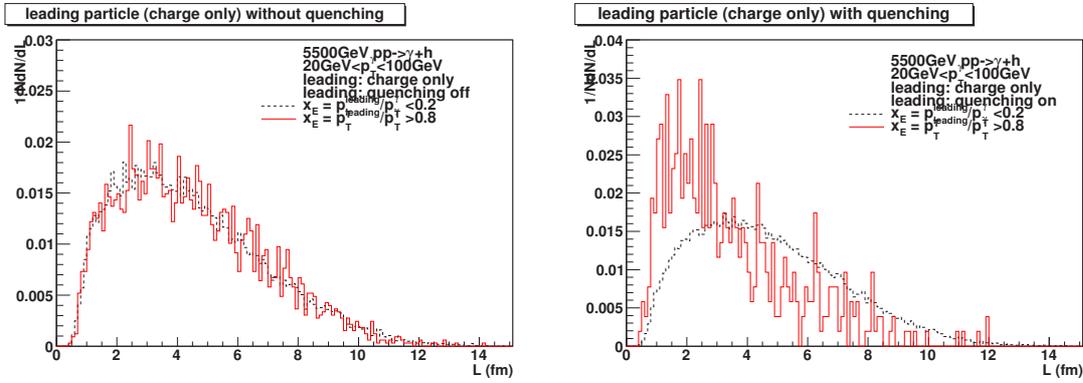
Figure 5.24: *The probability of the leading particles production as a function of medium length L, with (right) and without (left) quenching effect is taken into account.*
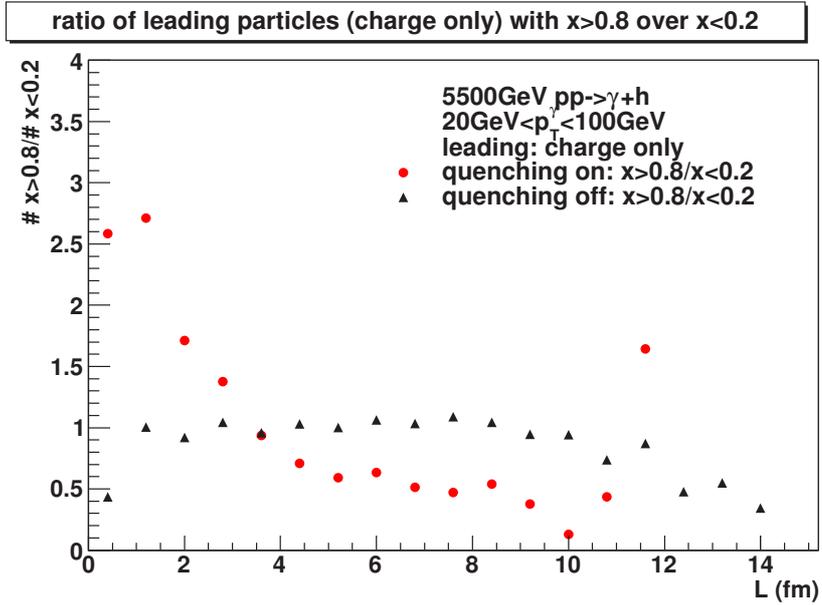
Figure 5.25: *The ratio of the probability for leading particles with large x over small x as a function of medium length L.*
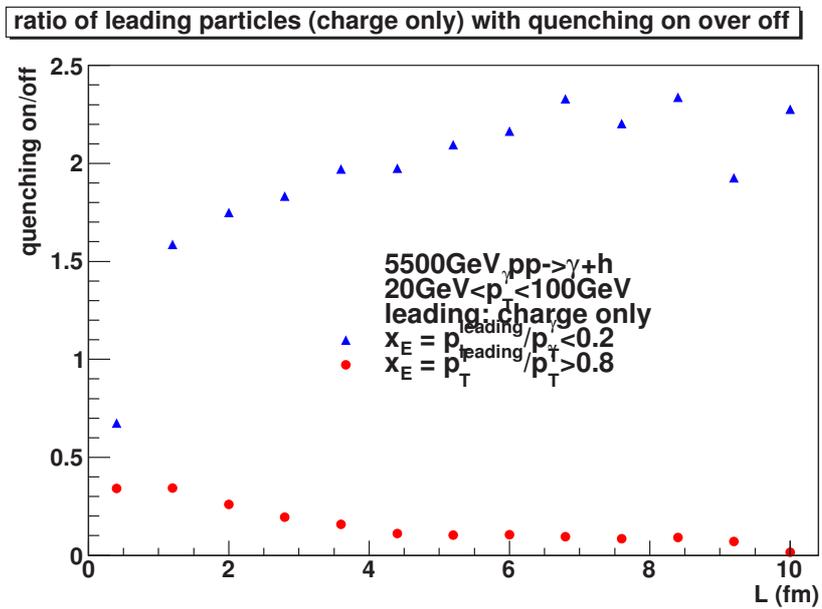
Figure 5.26: *The ratio with quenching over without quenching for leading particles with large x and small x as a function of medium length L.*
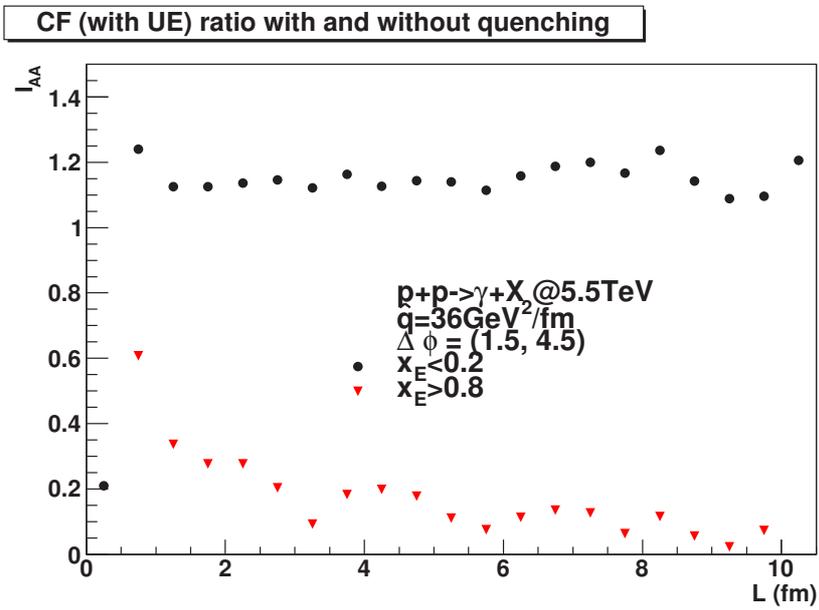
Figure 5.27: *The nuclear modification factor I_{AA} distribution as a function of medium length L by selecting different regions of x_E correlation distribution.*

Chapter 6

Analysis of ALICE Data

In this chapter I present the status (March 2011) of my analysis of the data collected for proton-proton collisions at $\sqrt{s} = 7$ TeV during the first LHC run in 2010. The goal of this analysis is to construct the direct photon-charged hadron correlations. This analysis will provide a reference for a data analysis of heavy-ion data. The results to be shown here are obtained by analyzing about 160 million minimum bias events. The preliminary result include inclusive photon-charged hadrons and π^0-charged hadrons correlation all showing the characteristic di-jet pattern from where the momentum imbalance k_T is extracted. Results on direct photons are not convincing because of the limited statistics accumulated during this time.

6.1 Data Sample

The definition of an interaction, the basis of the minimum bias trigger, is based on a logical mix of different detector inputs, two detectors have been used for triggering [116]:

- The Silicon Pixel Detector (SPD) provides trigger signals, which can be set up in a programmable way to run with the main multiplicity-based trigger selections.

- The scintillator hodoscopes V0 provide four basic signals, corresponding to hits on either side of the interaction region in the time windows for incoming beam-gas and outgoing colliding-beam interactions, the latter classified according to multiplicity.

The trigger used to record the events for the present analysis is defined by requiring a hit in the SPD or a hit in one of the two planes of the V0, in coincidence with the two beam pick-up counters indicating the presence of two passing proton bunches. This minimum bias trigger requires essentially at least one charged particle in a detector anywhere in the 8 units of pseudorapidity.

The position of the interaction vertex is reconstructed by correlating hits in the two SPD layers to obtain tracklets. The achieved resolution depends on the tracklet multiplicity and is approximately 0.1-0.3 mm in the longitudinal direction and 0.2-0.5 mm in the transverse direction. The distribution of the vertex position in the longitudinal direction (z-axis) has a gaussian shape in the range $|z| < 10$ cm (Fig. 6.1). Events with vertices within $|z| > 10$ cm were rejected for the present study. For events with only one charged tracklet, the vertex
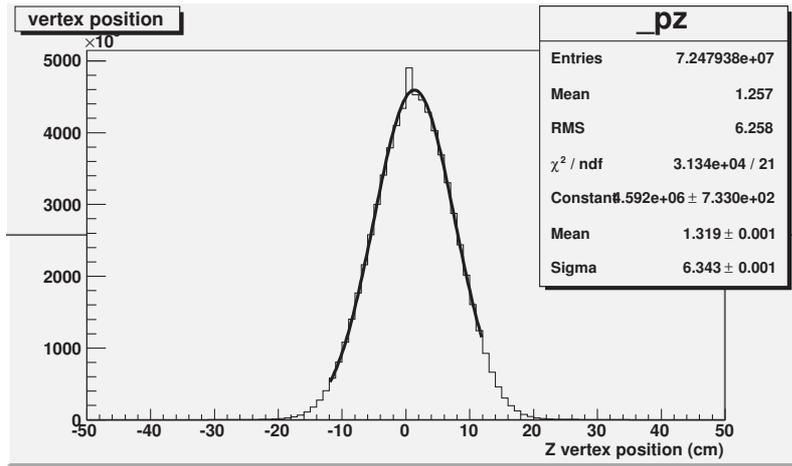
Figure 6.1: *Longitudinal vertex distribution from hit correlations in the two pixel layers of the ALICE inner tracking system. A Gauss fit with an estimated r.m.s of about 6 cm to the central part is also shown.*

position is determined by intersecting the SPD tracklet with the mean beam axis determined from the vertex positions of other events in the sample.

The beam-gas and beam halo background events were removed by the use of timing information from the V0 detectors. The timing information is recorded in a time window of ± 25 nsec around the normal beam crossing time with a resolution better than 1 ns [116]. Particles hitting one of the detectors before the beam crossing have negative arrival times (Fig. 6.2) and are typically due to interactions taking place outside the central region of ALICE such as beam-gas interaction. These events were rejected from the data analysis.
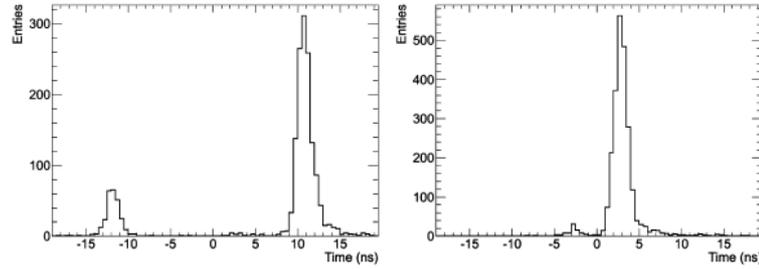
Figure 6.2: *Arrival time of particles in the V0 detectors relative to the beam crossing time (time zero). A number of beam-halo or beam-gas events are visibles as secondary peaks in V0A (left panel) and V0C (right panel) [116]. This is because particles produced in background interactions arrive at earlier times in one or the other of the two counters. The majority of the signals have the correct arrival time expected for collisions around the nominal vertex.*

To monitor the quality of the data collected by the ALICE detectors, a set of physics histograms are defined for each detector. During the data taking, the data quality is monitored online at the Data Quality Monitor (DQM) station. Details on the EMCal DQM are reported in the Appendix C [117].

After reconstruction, sets of data with sufficient good quality and to be used for the analysis are selected based on several criteria adopted for the physics observables relevant for an analysis. We use several parameters to provide the basic quality check of the events recorded by the calorimeters. The data quality analysis consists in making trending plots for each parameter and removing runs with large deviation from the mean value on the trending [118]. These parameters are:

– the cell multiplicity;

– the cluster multiplicity, which is less sensitive to noise than the cell multiplicity (Fig 6.3);

– the cluster with $E_{cluster} > 0.3$ GeV, in order to eliminate the detector hardware noise and the hadronic background due to the energy deposited by minimum ionizing hadrons in a single calorimeter cell;

– the mean energy per event of all clusters with energy above $E_{cluster} > 0.5$ GeV (Fig. 6.4);

– the slope of the cluster energy spectrum: in this case a power law function $f(E) = (a + b * E)^n$ is fitted to the data between $0.5 \leq E_{cluster} \leq 4.5$ GeV (Fig. 6.5);

– the position and width of the π^0 invariant mass peak; to monitor the energy scale, a gaussian plus a 2nd order polynomial function is fitted to the 2-cluster invariant mass

spectrum for clusters with $1 < p_T < 15 \ GeVc$ (Fig. 6.6 and Fig. 6.7);

– the mean number of reconstructed π^0 per event, to monitor the trigger quality and to identify pileup events;

– the ratio between the number of π^0 (N_{π^0}) and the number of cluster pairs ($N_{\gamma\gamma}$), in order to monitor the significance of the π^0 signal (Fig. 6.8);
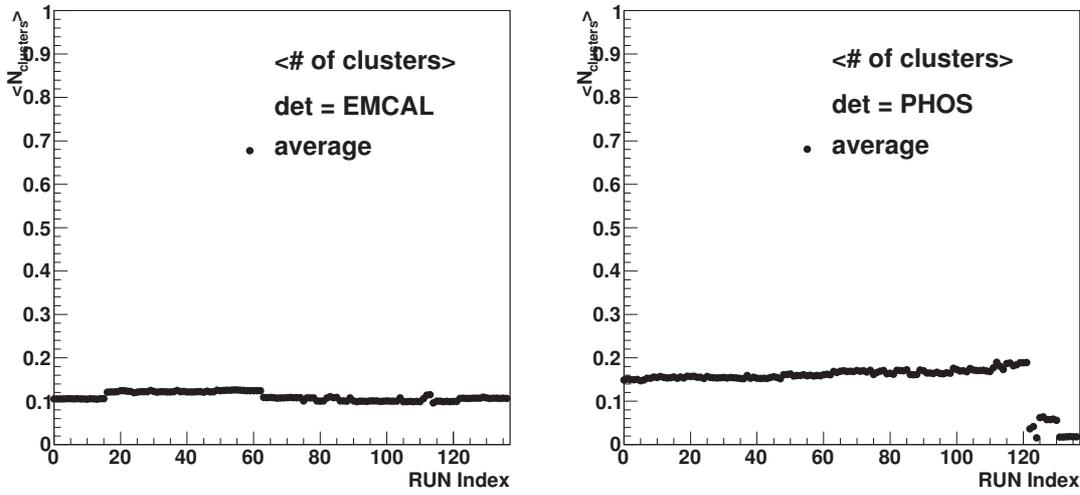
Figure 6.3: *Run quality criteria for pp data at $\sqrt{s} = 7 \ TeV$: the mean cluster multiplicity distribution for EMCAL (left) and PHOS (right) as a function of run numbers. The run index and run number correspondence is in Appendix.*

For the correlation analysis, a charged track quality selection is performed to filter out fake reconstructed tracks. A set of standard track selection criteria has been defined by the experts of the tracking algorithms [119]. They are listed in Tab. 6.1.

6.2 Calorimeter Calibration

To reach the design energy resolution of the electromagnetic calorimeters, a channel-by-channel relative energy calibration better than 1% must be achieved. A calibration system, in which all cells view a calibrated pulsed LED light source, has been successfully tested to track and adjust for the temperature dependence of the APD gains during operation. The absolute energy calibration is obtained using monoenergetic electron beams and the cosmic
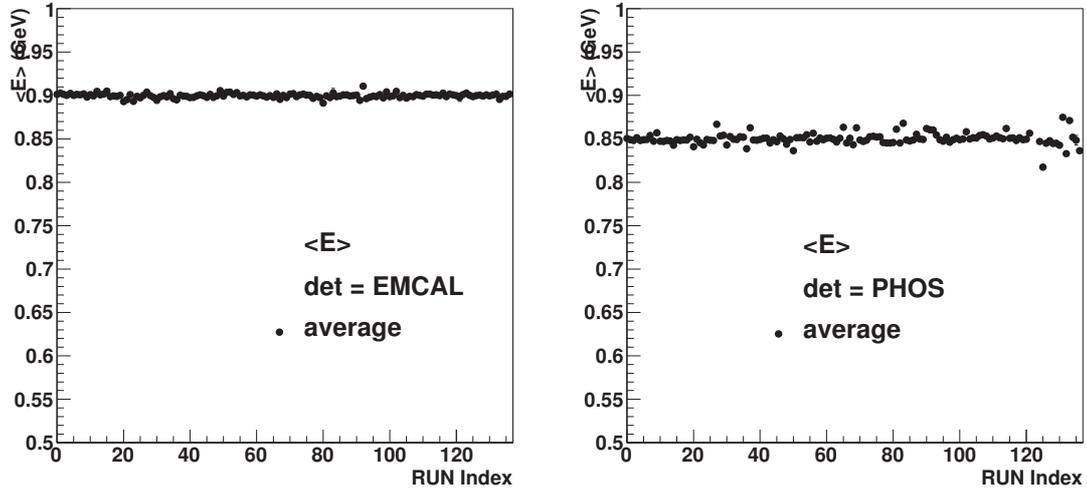
Figure 6.4: *Run quality criteria for pp data at $\sqrt{s} = 7$ TeV: the mean total energy ($< E >= \frac{\sum E * N_{cluster}(E)}{\sum N_{cluster}(E)}$) deposited on EMCAL (left) and PHOS (right) with cluster energy larger than 0.5 GeV per event. The different colors on the same canvas represent single (Super) Modules check from each run.*
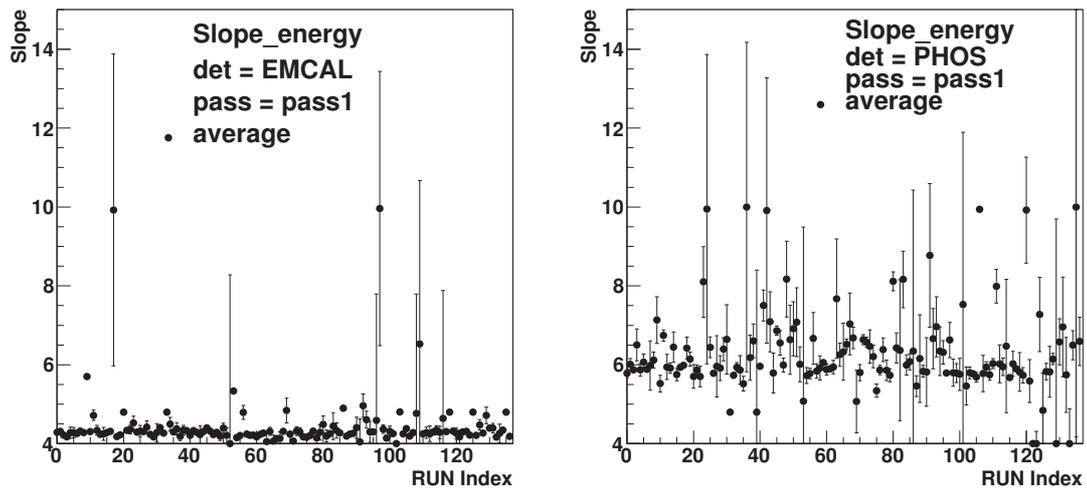
Figure 6.5: *Run quality criteria for pp data at $\sqrt{s} = 7$ TeV: the slope of the cluster energy spectrum from power law function fitting ($f(E) = (a + b * E)^{n}$) for EMCAL (left) and PHOS (right).*
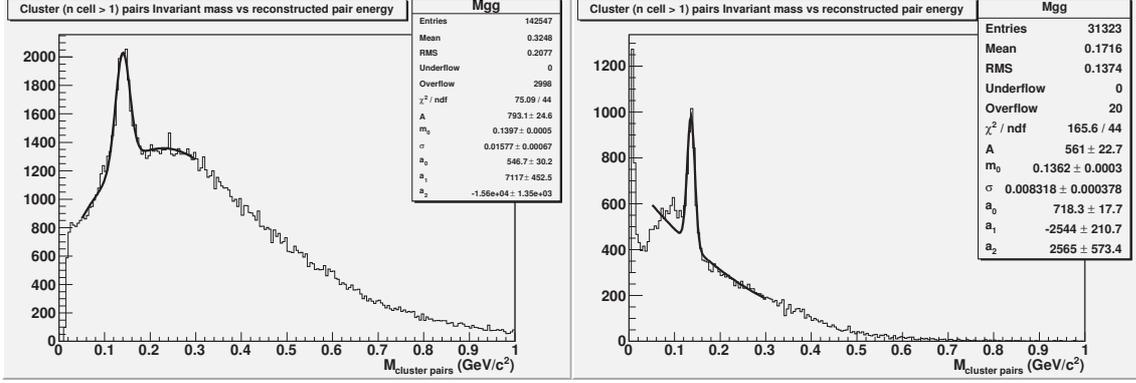
Figure 6.6: *Invariant mass analysis for pp data at $\sqrt{s} = 7$ TeV for EMCAL (left) and PHOS (right). A Gauss + Polynoimal function $(A * e^{\frac{(x - m_0)^2}{2 * \sigma^2}} + a_0 + a_1 * x + a_2 * x^2)$ is fitted on the invariant mass spectrum at the mass range $110 < M_{\gamma\gamma} < 160$ MeV/c^2 as the black solid curve.*

Accepted pseudorapidity range	$|\eta| < 0.8$
Accepted z vertex range (cm)	$10 < |z_{vertex}| < 10$
Maximal DCA to vertex in xy	3.2 cm
Maximal DCA to vertex in z	2.4 cm
Minimal number of TPC clusters	70
Maximal χ^2 per TPC cluster	4.0
Accept kink TPC daughters	NO
Require TPC refit	YES
Require ITS refit	NO
Require SPD vertex constrain	YES

Table 6.1: Track quality cuts used in the analysis.
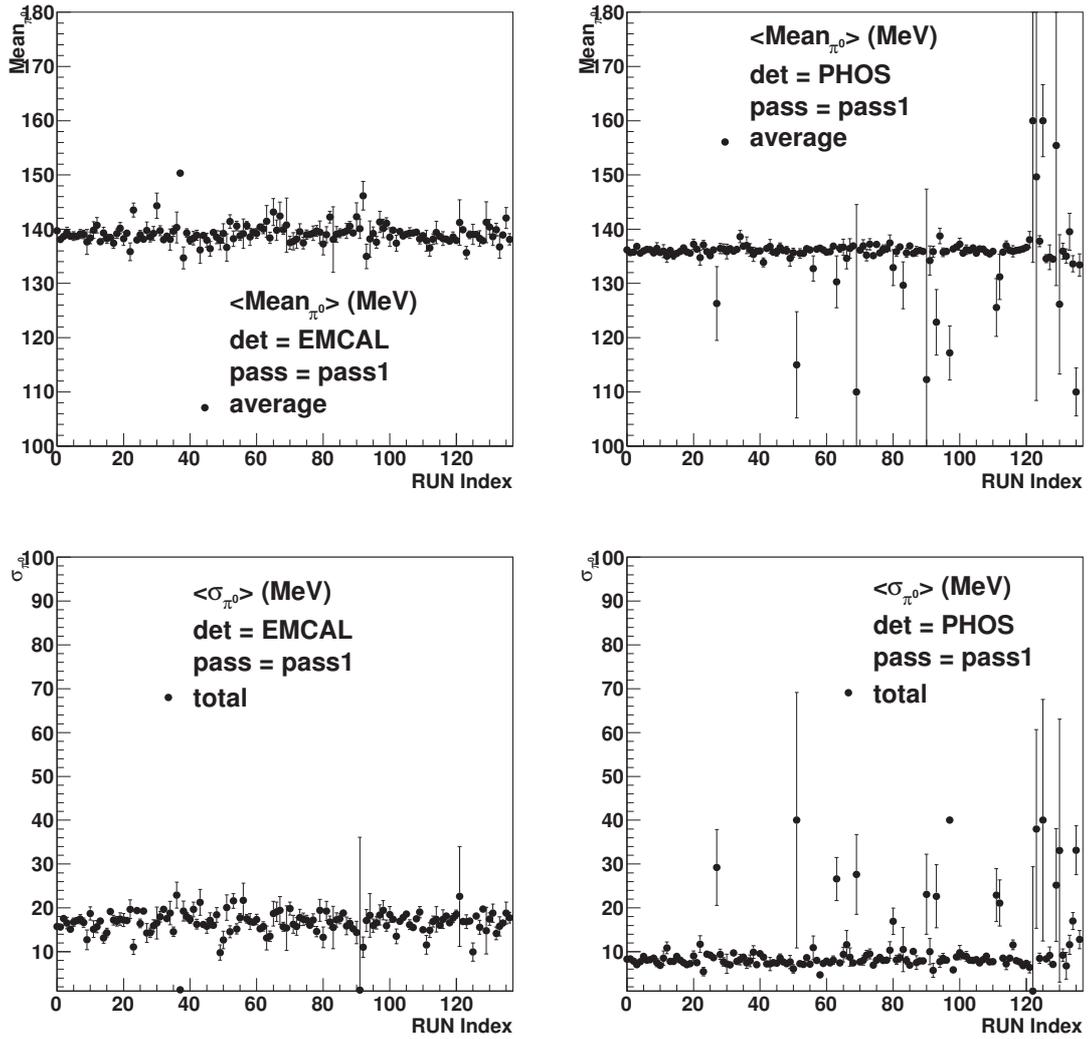
Figure 6.7: *Run quality criteria for π^0 analysis in pp collisions at $\sqrt{s} = 7$ TeV: the mean position of the π^0 peak (upper panel) and width (bottom panel) obtained from the fitting on Fig. 6.14 for EMCAL (left) and PHOS (right).*
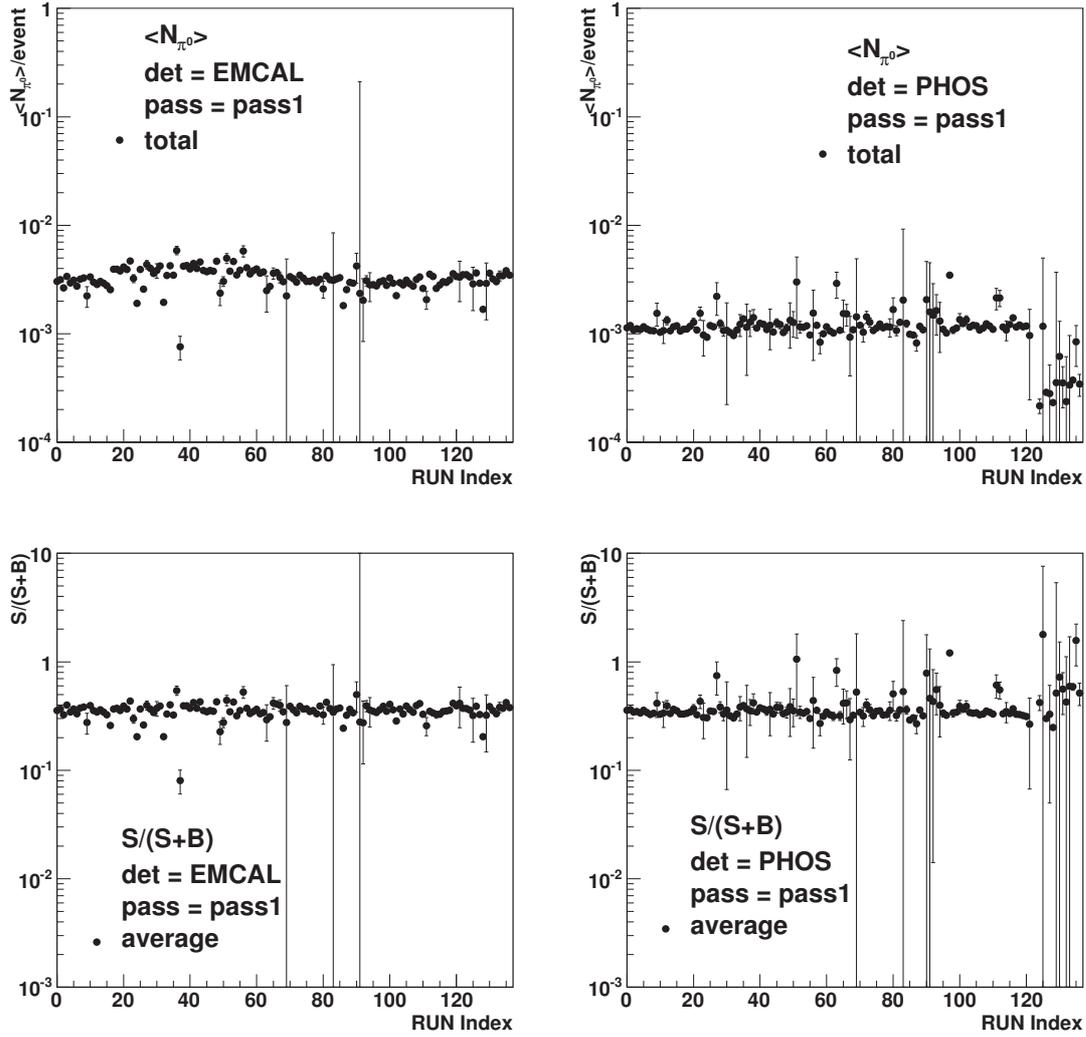
Figure 6.8: *Run quality criteria for π^0 analysis in pp collisions at $\sqrt{s} = 7$ TeV: the mean number of reconstructed π^0 (upper panel) and the significance ($\frac{S}{S+B} = \frac{N_{pi0}}{N_{\gamma\gamma}}$) of the signal over the signal plus background (bottom panel) obtained from the fitting on Fig. 6.14 for EMCAL (left) and PHOS (right).*

muons. Final tuning of the calibration is achieved with the collision data by adjusting the position of the π^0 peak in the 2-clusters invariant mass distribution.

6.2.1 Cosmic muons calibration

High statistics MIP data enable us to adjust the relative gain factors between EMCAL towers. The muon signal measured in each tower is obtained by the use of an isolation procedure applied offline. For each event, the maximum amplitude is chosen and for all neighboring towers a signal smaller than a threshold value is required. This threshold is limited by the electronic noise (set to 3 ADC counts for the present study). The muons, passing the towers along their length, are selected using scintillator paddles. Each paddle covers 12 modules grouped into a "*strip module*", and is read out at both extremities by photomultiplier tubes (PMT). The time of flight between both PMTs allows one to select vertical muons with a spatial accuracy of a few centimeters. The isolation procedure then ensures that no energy was deposited in the neighboring towers. The amplitude of the signal is extracted by fitting a Gamma-2 function ($F = A * t^N * e^{N*(1-t)}$, where A is the amplitude value, N is the order of Gamma function) to the time dependent electronic signal delivered by a tower.

A 24-h run allows the accumulation of about 500 muons per towers, which is sufficient to exact the MIP peak with an accuracy of about 1% (Fig. 6.9). An individual gain calibration is performed for each tower by aligning the MIP peak for all towers. The tower gains, which are controlled through the tower high voltage power, are tuned iteratively. The mean amplitude signal from all towers are clearly peaked around 16 ADC counts after the isolation selection, and other additional cuts only change slightly the mean and the width of the relative calibration (see Fig 6.9). Fig. 6.10 shows the dispersion of the MIP peak position for 384 towers before and after several iterations done (thin and bold lines, respectively), A final relative dispersion < 3% is reached [120].

6.2.2 π^0 mass calibration

With high statistics pp collision data, two photon invariant mass spectra are accumulated for each tower. The position of the observed π^0 peak is used to improve the channel by channel absolute energy calibration. In the ideal case, the reconstructed two photon invariant mass shows a sharp peak at the π^0 mass with a width corresponding to the intrinsic resolution of
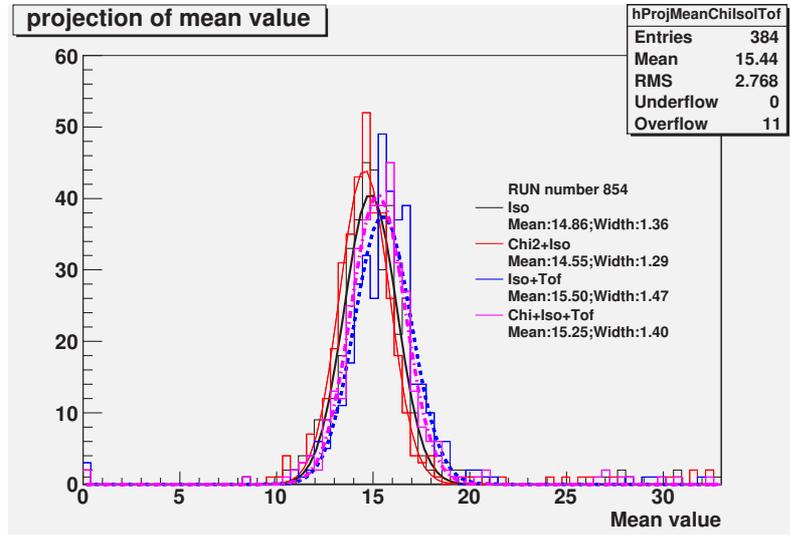
Figure 6.9: *Mean value of MIP position in ADC counts from all the towers calibration.*
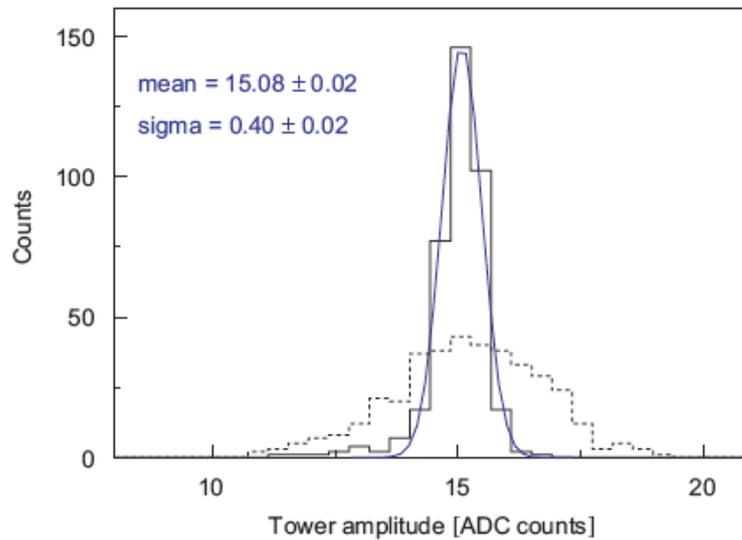
Figure 6.10: *Response of 384 towers of the EMCAL to cosmic muons before (dashed histogram) and after (full histogram) individual gain calibration. The curve represents a fit of a Gaussian to the full histogram with fit results as given together [120].*

112

the electromagnetic calorimeter. When the detector is de-calibrated, the position of the π^0 mass peak deviates from the ideal mass ($m_{\pi^0} = 134.98$ MeV). For each channel i, photon pairs are selected only if one of the clusters deposits at least 50% of its energy in a single tower. The resulting two-photon invariant mass distribution is fitted and the extracted mean π^0 peak position m_i is used to correct each channel calibration coefficient cc_i using:

$$cc_i^{corr} = cc_i(1 + k_i^2)/2 \; . \tag{6.1}$$

where $k_i = m_{\pi^0}/m_i$. These procedure is repeated several times until the invariant mass distribution is centered at the π^0 mass for all channels. Fig. 6.11 shows a comparison of the π^0 mass position and width between Monte-Carlo (MC) and real data in PHOS and EMCal. A de-calibration factor is needed to apply on the channel calibration to fit the p_T dependence obtained with data (6.5% for PHOS and 2 % for EMCal).

6.3 Photon and π^0 measurements

Photon clusters are identified by applying several selection criteria.

– First a minimum cluster energy is required ($E_{cluster} > 0.3$ GeV) to remove hadronic clusters due to minimum ionization energy deposition by charge hadrons;

– second, to reduce the effects of noisy channels, a number of cells per cluster larger than 1 is required for EMCal and larger than 2 for PHOS (this takes into account the different size of the two calorimeters);

– hot cells identified following the QA analysis are ignored during the analysis;

– to minimimize edge effects, clusters located at the border of EMCal (one cell) or PHOS (two cells) are ignored;

– for EMCal, a time of flight cut ($550 < T < 750$ ns) is applied to remove clusters generated by non-physical signal with too small or too large arrival time (Fig. 6.12).

The resulting inclusive cluster energy spectra (Fig. 6.13) obtained for the EMCAL and PHOS from $\sim 160,000,000$ minimum bias events after all the selections are identical.

Decay photons are identified through their characteristic kinematics. Depending on the electromagnetic calorimeter geometry and on the neutral meson energy, the two decay photons
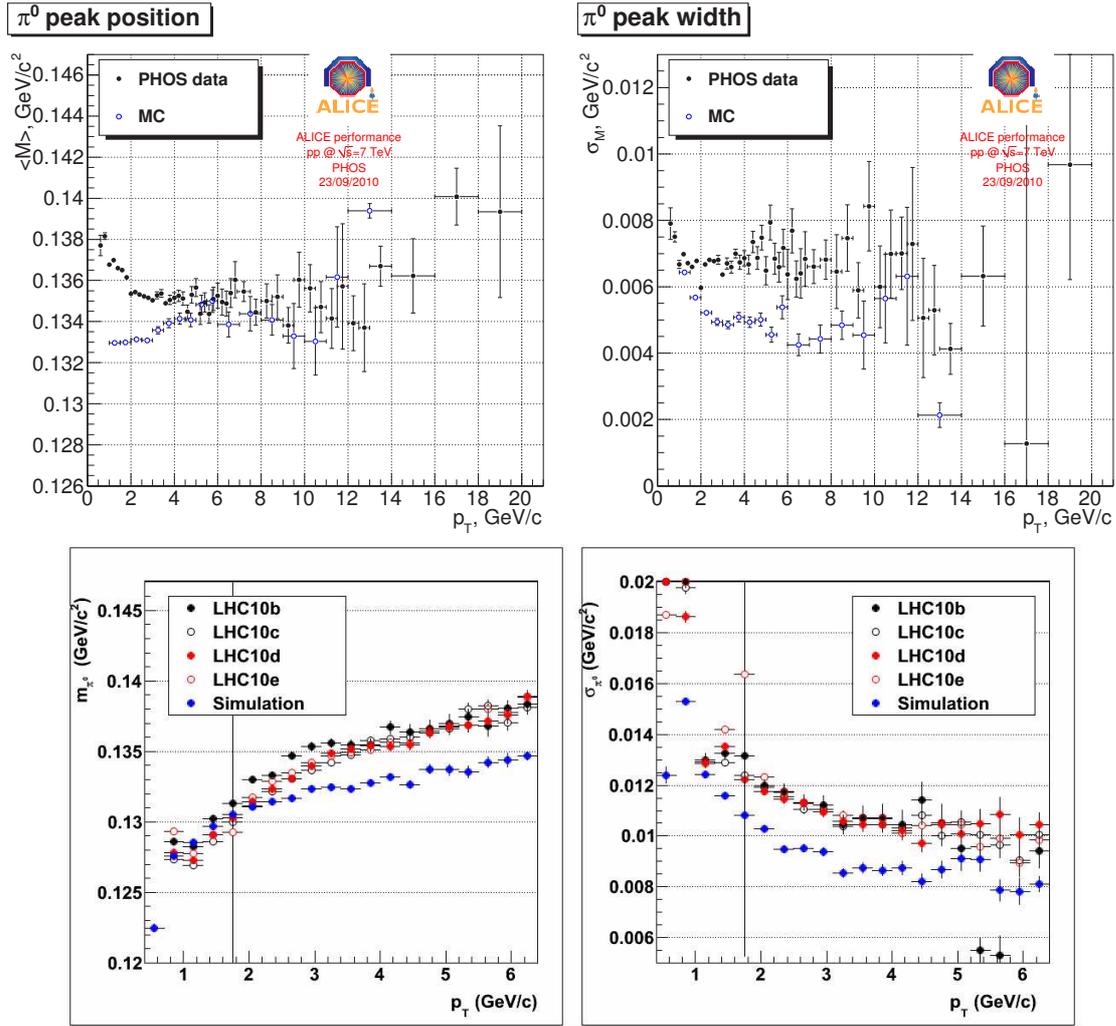
Figure 6.11: *The π^0 mass position and width from decalibrate Monte-Carlo (MC) and real data in PHOS (upper) and EMCal (bottom).*
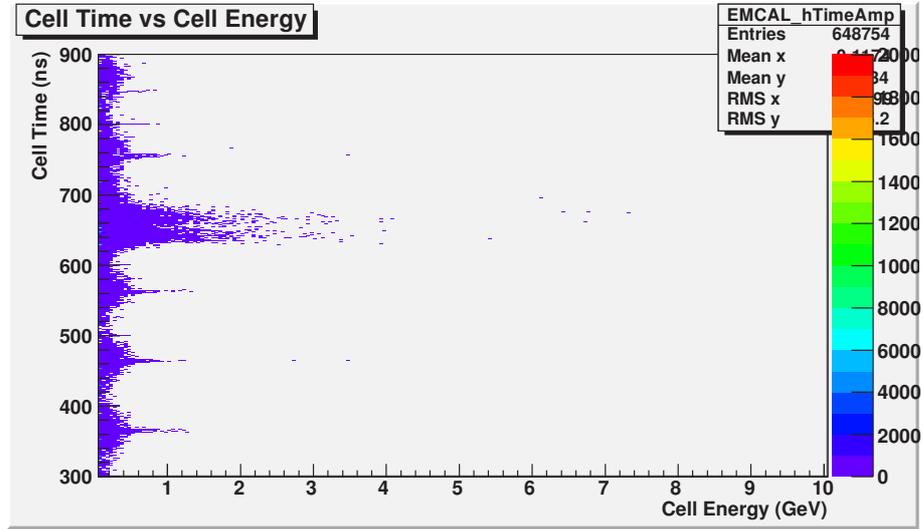
Figure 6.12: *The EMCal time vs. cell energy distribution.*
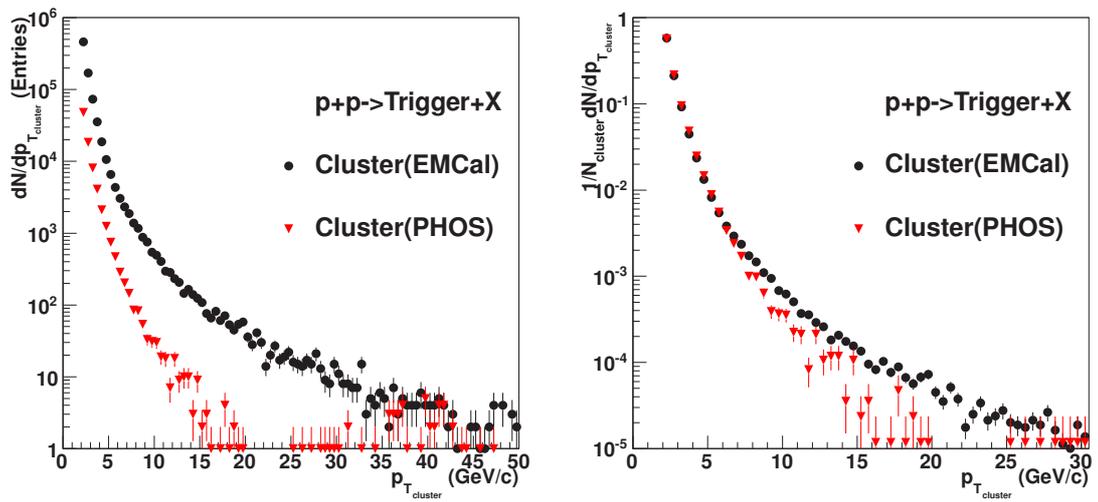
Figure 6.13: *The raw inclusive cluster energy spectrum (left) and the normalized spectrum from different calorimeters.*

will be detected as two distinct clusters or as a single cluster when the calorimeter resolution does not allow to resolve anymore the two decay photons.

The π^0 meson is identified from a two cluster invariant mass analysis. Examples of the invariant mass spectrum for several p_T bins are shown in Fig. 6.14. The background under the π^0 peak, mainly due to combinational is calculated using a second order polynomial function plus a gaussian distribution Fig. 6.14). Position and width of the π^0 peak are
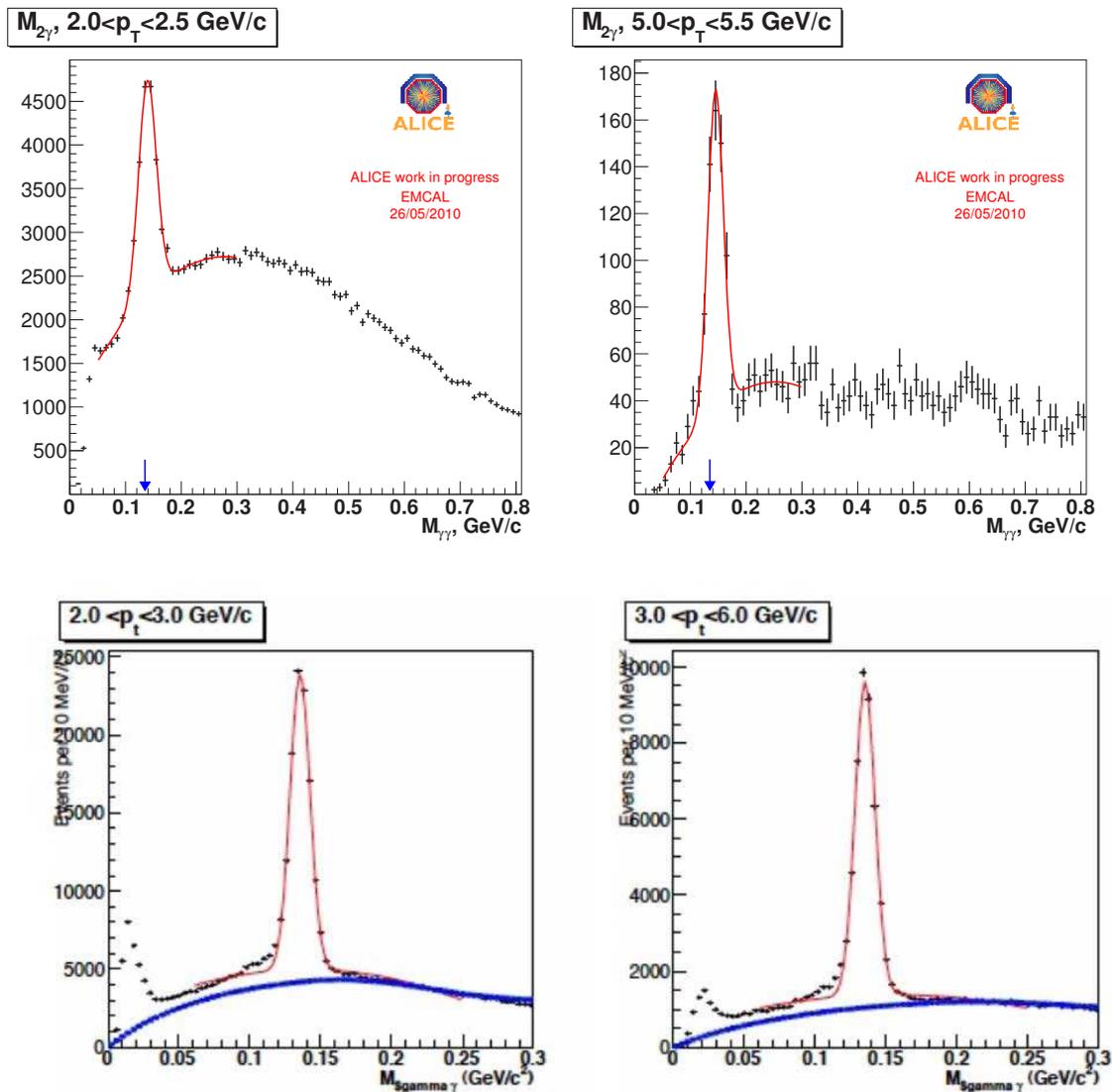
Figure 6.14: *The invariant mass spectrum of cluster pairs in pp@7TeV from EMCal (top) and PHOS (bottom) detector.*

116

extracted from the fit on the invariant mass distributions (Fig. 6.14) for $\sqrt{s} = 7$ TeV. It was found some dependence of the π^0 peak position and width with the momentum p_T as shown in Fig. 6.15. With the decalibration factor discussed above, the data and MC approaches to each other quite well. The number of reconstructed π^0 is then calculated as the integral
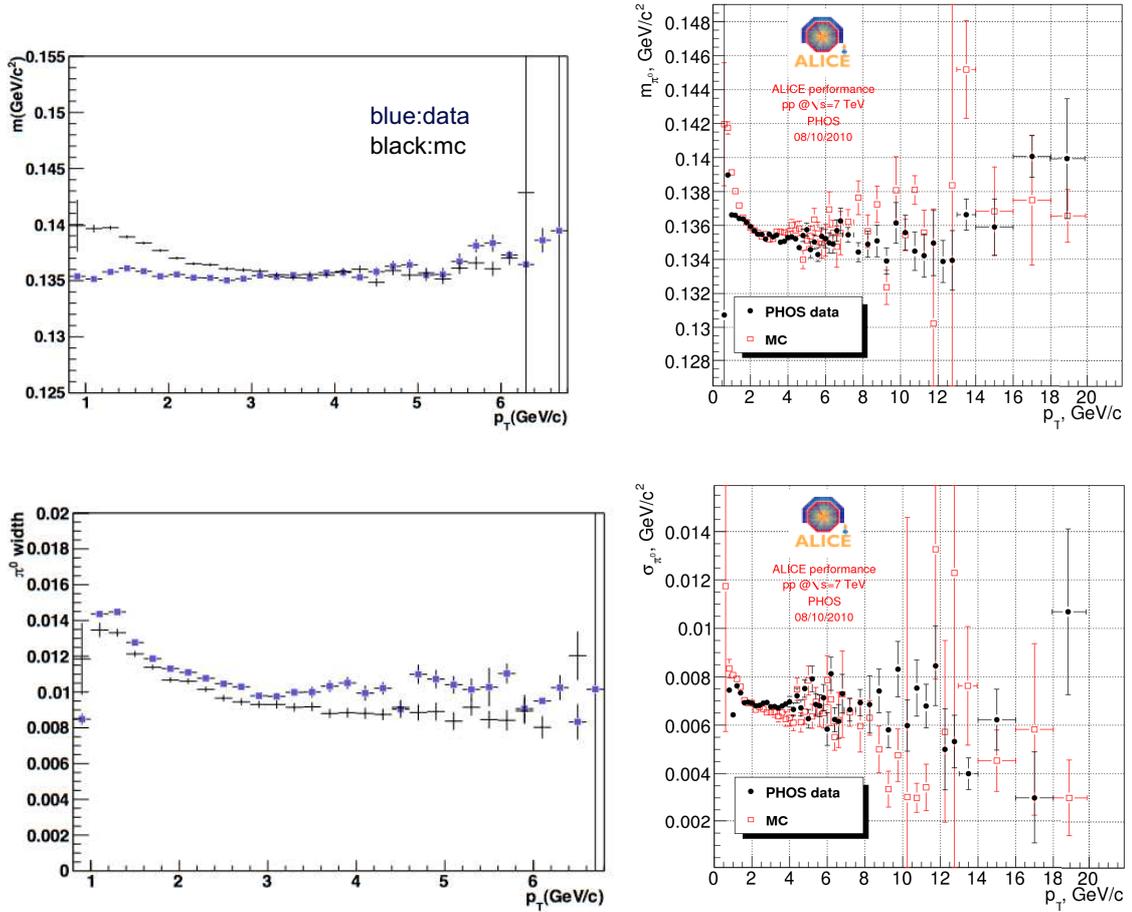
Figure 6.15: *Dependence of the π^0 peak position (upper) and width (bottom) on p_T for EMCal (left) and PHOS (right) in pp collisions at $\sqrt{s} = 7$ TeV.*

of the Gaussian function. The resulting raw π^0 spectrum of the number of reconstructed π^0 mesons versus p_T is obtained from the invariant mass spectra (Fig. 6.14) and are shown in Fig. 6.16. The final spectrum measured in pp at $\sqrt{s} = 7$ TeV with all the correction factors applied is shown in Fig. 2.8.
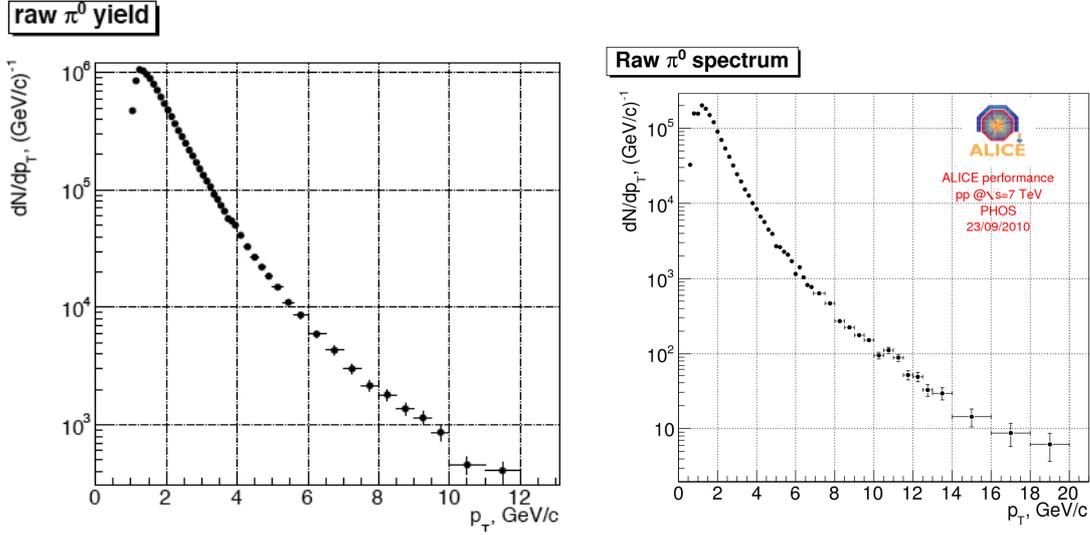
Figure 6.16: *Raw spectra of π^0 vs p_T measured by EMCal (left) and PHOS (right) detector in pp collisions at $\sqrt{s} = 7$ TeV.*

6.4 Two particle correlations with photon and π^0 triggers

The study of the two-particle correlations consists in studying the relative azimuthal and transverse momentum distribution of charged particles associated to a high energy photon or π^0 selected as a trigger. The relevant variable is the number of associated particles per trigger, also referred to as the conditional or per-trigger yield:

$$Y \equiv \frac{N^{pair}}{N_{trig}} \ . \tag{6.2}$$

This quantity is typically studied as a function of the relative azimuthal angle of the associated particle with respect to the trigger, $\Delta\phi$, to evidence the particular hard $2 \rightarrow 2$ processes kinematics or final state di-jet events.

The trigger particle is selected starting from the clusters detected in the calorimeters, we consider:

– any cluster is identified as an inclusive photon candidate (no particle identification has been applied, therefore this cluster sample contains clusters from charged particles which develop a shower or clusters from the merging of the two decay photon of high-p_T π^0),

    – π^0 candidates are identified as a pair of clusters with an invariant mass between 110 and 160 MeV/c^2.

The central tracking system (ITS and TPC) provides the charged track measurements and contributes to the direct photon identification through the isolation technique.

For the correlation analysis, the trigger particle is selected on an event by event basis. Three different trigger particles have been selected:

1. the charged trigger is the track with the highest transverse momentum among all charged tracks in the event;

2. the photon cluster trigger is the calorimeter cluster with the highest energy among all clusters and all charged track in the event;

3. the π^0 trigger is identified by the cluster pair within the appropriate invariant mass range and with the highest transverse momentum among all particles in the event.

The trigger multiplicity spectra are shown in Fig. 6.17. The photon cluster trigger distribution in EMCal deviates from the one in PHOS for $p_T > 6$GeV/c due to the merging of the two π^0 decay photons into a single cluster. In PHOS the merging occurs only for $p_T > 25$GeV/c.

6.4.1 Azimuthal Correlation

The azimuthal correlation distribution is constructed by correlating the selected trigger particle with all charged tracks in the event with $p_T > 1$ GeV/c as a function of the relative azimuthal angle ($\Delta\phi = \phi_{trig} - \phi_{h^\pm}$) between the trigger and the charged track. Various p_T thresholds are applied on the trigger (Fig. 6.18). The main feature of this distribution is the 2-jets structure with a near side ($\Delta\phi = 0$) and away side ($\Delta\phi = \pi$) peak. This structure becomes stronger when triggers with larger p_T values are selected reflecting the larger multiplicity of fragmented hadrons from high energy jets. The 2-jet structure is on top on an approximately constant background which originates from the random correlation of the trigger with hadrons from the underlying event. To estimate the strength and the azimuthal distribution of this uncorrelated background, we use the mixed event technique. The "mixed" azimuthal correlation is constructed by correlating trigger from one event with
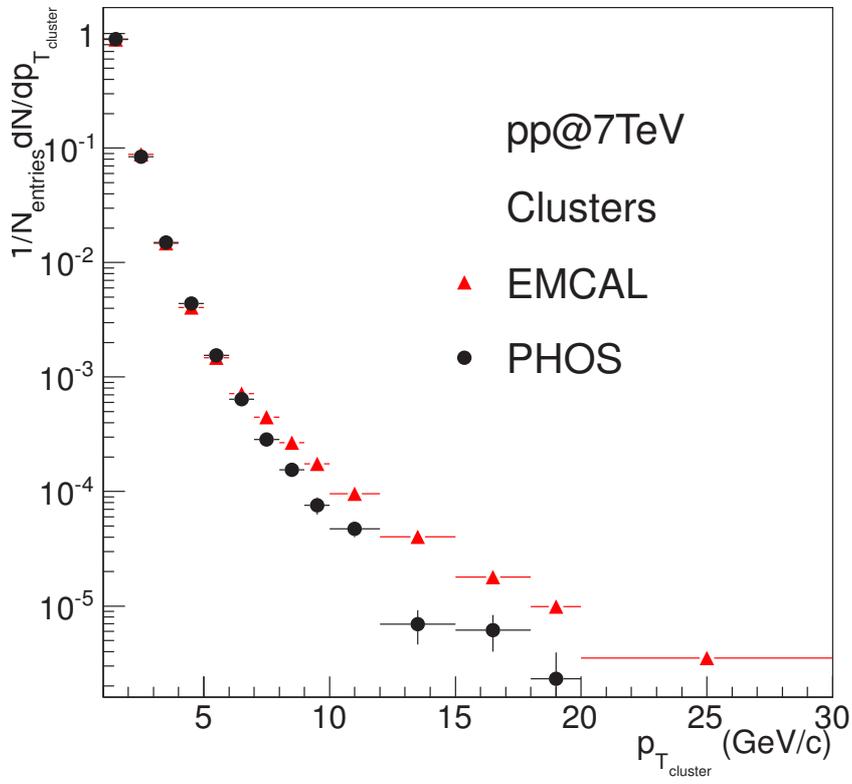
Figure 6.17: *Different trigger transverse momentum distribution from different detector measurements.*
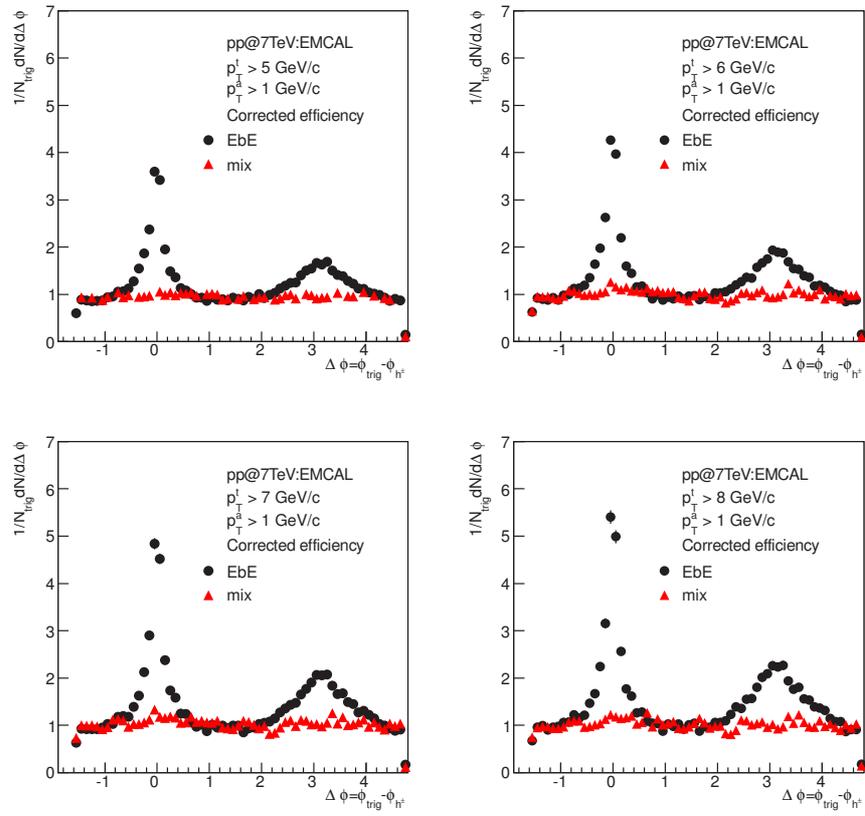
Figure 6.18: *Relative azimuthal angle distribution* $\Delta\phi = \phi_{trig} - \phi_{h^\pm}$ *for different* p_T *cluster triggers in EMCal and charged tracks with* $p_T^{h^\pm} > 1$ *GeV/c in central tracking system in pp collisions at* $\sqrt{s} = 7$ *TeV.*

hadrons from different events. The resulting distribution (Fig. 6.18) provides quite well the shape the uncorrelated background.

The azimuthal correlation for charged track triggers and cluster triggers are compared in Fig. 6.19. For cluster triggers the stronger di-jet structure reflects the fact that the neutral trigger selection enhances the probability that the trigger is the real leading particle of the jet fragmentation compared to the less restrictive charged trigger selection.
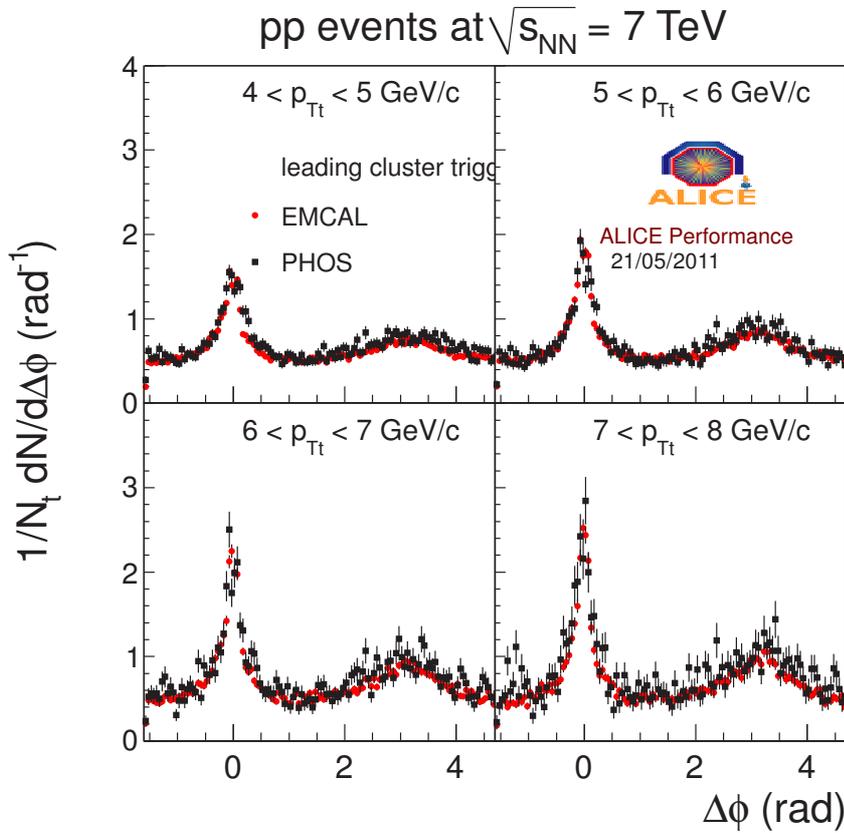
Figure 6.19: *Relative azimuthal angle distribution* $\Delta\phi = \phi_{trig} - \phi_{h^\pm}$ *for charged track triggers and cluster triggers with* $p_T^{h^\pm} > 1$ *GeV/c in pp collisions at* $\sqrt{s} = 7$ *TeV.*

The next step of the analysis is to select isolated trigger with the goal to enrich the trigger sample with prompt photons or single hadron jets. This is obtained by applying an isolation cut. The sum of the transverse momentum of the hadrons inside a cone with radius $R = 0.4$ around the trigger is calculated. If the sum is less than 10 % of the trigger transverse momentum the trigger is tagged as isolated. From the comparison of the trigger distribution
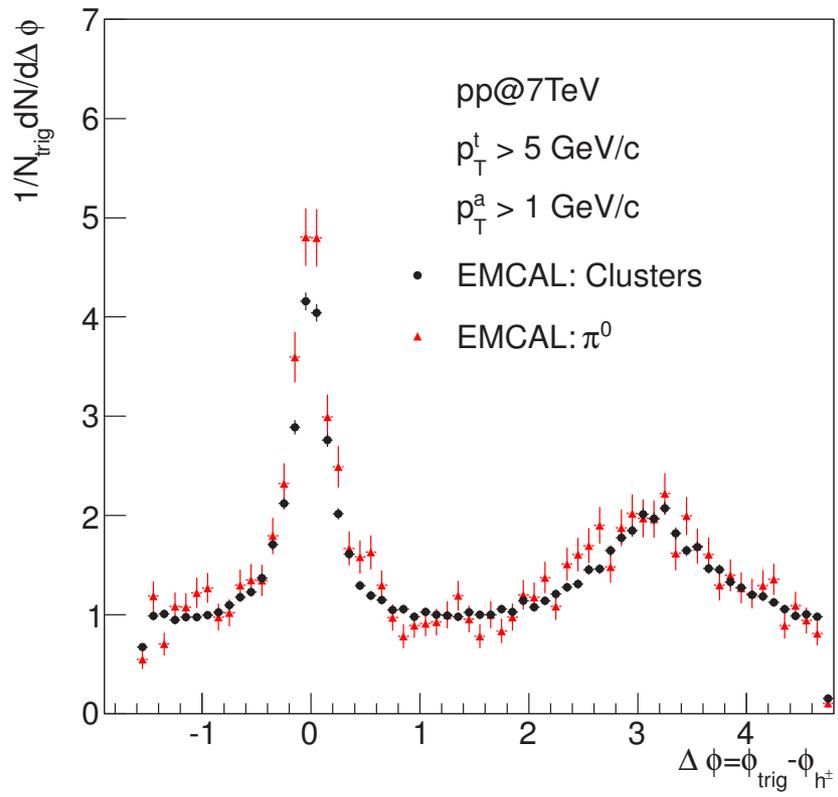
Figure 6.20: *Relative azimuthal angle distribution* $\Delta\phi = \phi_{trig} \quad \phi_{h\pm}$ *for inclusive cluster triggers and* π^0 *triggers in EMCal with* $p_T^{trig} > 5$ *GeV/c and* $p_T^{h^\pm} > 1$ *GeV/c in pp collisions at* $\sqrt{s} = 7$ *TeV.*

(Fig. 6.21) with and without isolation selection, we find that 20% of the inclusive clusters are isolated. As seen in Fig. 6.22, the near side peak in the isolated trigger azimuthal correlation
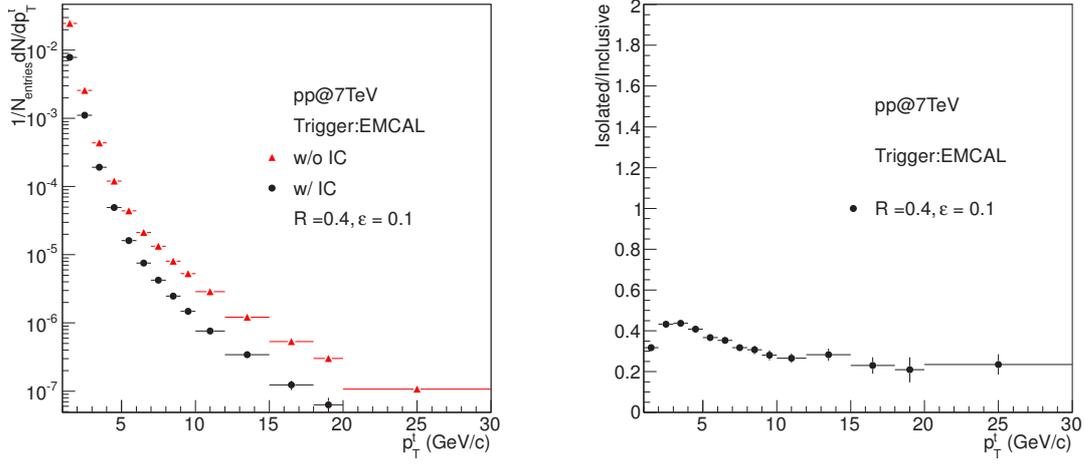
Figure 6.21: *Energy distribution of cluster triggers (left) from EMCAL before and after the isolation selection* ($R = 0.4$, $\varepsilon = 0.1$) *in pp collisisons at* $\sqrt{s} = 7$ *TeV. The right hand figure shows the isolation efficiency on the inclusive cluster triggers.*

distribution (Fig. 6.22) is suppressed by construction, whereas some strength remains in the away side peak. Whereas this would be the typical structure for a direct-photon – jet event, this structure is most likely due to an isolated π^0 or charged hadron which fragments from a jet of lower energy than does an non-isolated π^0 or charged hadron with the same p_T value. The observation of less strength in the away side peak when compared to the non-isolated cluster or charged track triggered azimuthal correlation (Fig. 6.22) is consistent with this last interpretation.

The slightly difference on the away side peak before and after isolation can be explained by the z_t bias with and without isolation, from the previous study we conclude that the non-isolated trigger takes $\sim 50\%$ of the jet energy while for an isolated trigger this fraction is about 80%. Therefore the same p_T isolated trigger will select lower energy jets. This interpretation is verified by a scaling factor $(\frac{0.5}{0.8})$ multiplied on the non-isolated trigger azimuthal correlation from Fig. 6.22 and compared the azimuthal correlation with isolated trigger (Figure. 6.23). By such a simple scaling factor, the away side peak agrees quite well.

124
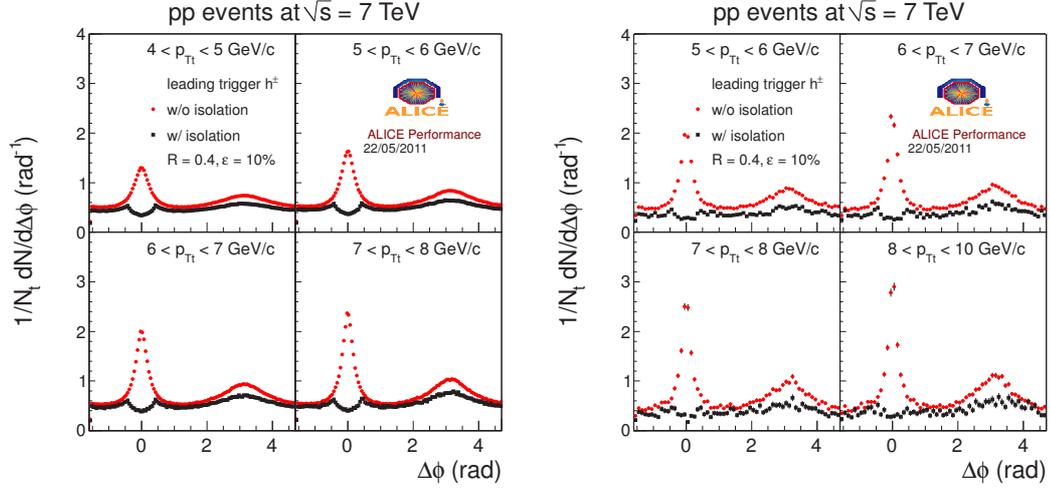
Figure 6.22: *Relative azimuthal angle distribution $\Delta\phi = \phi_{trig} - \phi_{h\pm}$ for inclusive charged and cluster triggers with different p_T bins and $p_T^{h\pm} > 1$ GeV/c in pp collisions at $\sqrt{s} = 7$ TeV before and after isolation cut (IC) selection: $R = 0.4$, $\varepsilon = 0.1$.*

6.4.2 k_T extraction

Because of the hadronization, we do not have direct access to the parton kinematics and therefore can measure neither the fragmentation function nor the magnitude of partonic transverse momentum k_T which modifies the ideal $2 \to 2$ kinematics. The transverse momentum of the parton pair is related to $\vec{k}_T$ by $\vec{p}_{T,pair} = \sqrt{2}\vec{k}_T$. The vector $\vec{p}_{out}$, measured between the trigger and the associated hadrons, has its origin in the parton pair imbalance due to the transverse momentum present in the intial and final state of the hard process and quantified by k_T effect (see Sec. 3.2 for details). To measure k_T value, one needs to choose a set of hadronic observables that maximizes the sensitivity to this parameter. $\vec{p}_{out}$ measures the same out-of-plane momentum ($p_{out} = p_{T_h} \sin(\Delta\phi)$), but uses the axis of the trigger particle instead of the parton, as a reference. Fig. 6.24 shows the p_{out} distribution for inclusive cluster triggers from EMCal with $p_T^{h\pm} > 1$ GeV/c in pp collisions at $\sqrt{s} = 7$ TeV for different $p_{T_{trig}}$ ranges. The p_{out} distributions are fitted with a Gaussian function or a Kaplan function ($C(1 + p_{out}^2/b)^{-n}$, where C, n and b are free parameters). The tail of the $\vec{p}_{out}$ distributions exhibits a small deviation from the best Gaussian fit describing the data at small p_{out} values to a power-law behaviors as p_{out} becomes large. This may point out the transition from a regime dominated by multiple soft gluon emission to one dominated by radiation of a single hard gluon.
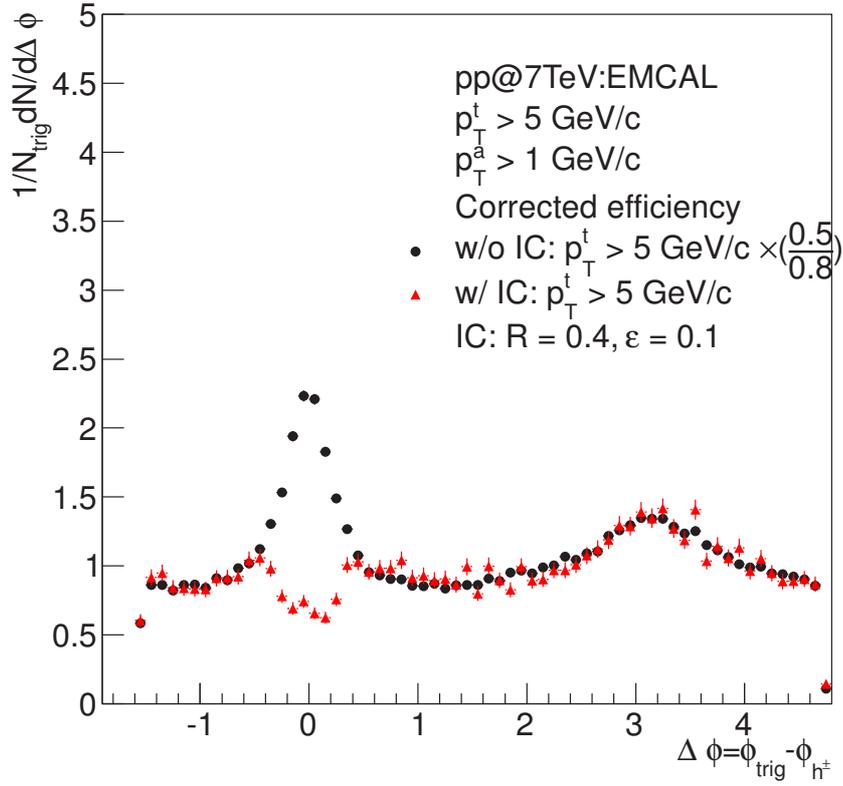
Figure 6.23: *Two-particle correlation distribution as a function of the relative azimuthal angle between trigger particles and associate particles $\Delta\phi = \phi_t - \phi_a$. Trigger particles are selected as the isolated trigger ($R = 0.4$, $\varepsilon = 0.1$ red triangle symbols) with $p_T > 5$ GeV/c or non-isolated trigger (black dot symbols) with $p_T > 5 \times \frac{0.5}{0.8}$ GeV/c detected in EMCAL. Associated particles are selected as tracks detected by the central tracking system with $p_T > 1$ GeV/c. The data have been obtained in proton-proton collisions at $\sqrt{s} = 7$ TeV.*
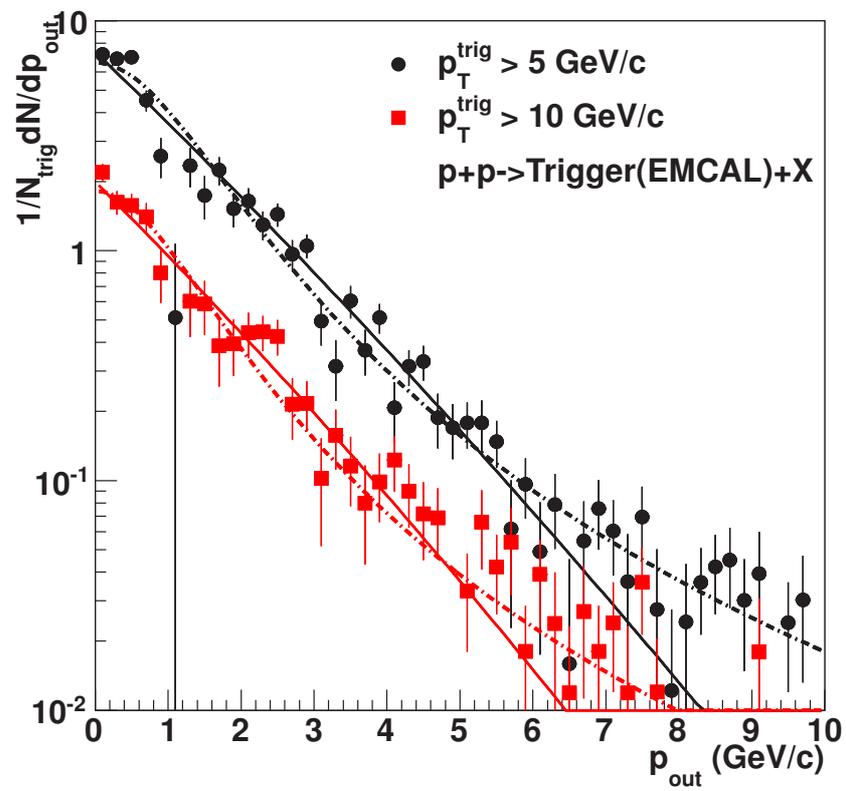
Figure 6.24: p_{out} distributions for inclusive cluster triggers from EMCal with $p_T^{h^{\pm}} > 1$ GeV/c in pp collisions at $\sqrt{s} = 7$ TeV for different $p_{T_{trig}}$ ranges. The distributions have been fitted with both Gaussian (solid lines) and Kaplan (dashed lines) functions.

Since the soft multiple scattering background is included in the p_{out} distribution, rather than extracting the value of $\sqrt{<|p_{out}|^2>}$ directly from the p_{out} distribution, it is extracted from the width of the away side peak in the azimuthal correlation, following the procedure described in [71, 121]. The following fit function is used to determine the magnitude of p_{out} from the away-side jet width:

$$\frac{1}{N_{trig}}\frac{dN_{real}}{d\Delta\phi} = \frac{1}{N}\frac{dN_{mix}}{d\Delta\phi}\cdot(C_0 + C_1\cdot\frac{dN_{near}}{d\Delta\phi}|_{\pi/2}^{\pi/2} + C_2\cdot\frac{dN_{away}}{d\Delta\phi}|_{\pi/2}^{3\pi/2}) \qquad (6.3)$$

where

$$\frac{dN_{near}}{d\Delta\phi}|_{\pi/2}^{\pi/2} = (1 - (1 - q)\frac{\Delta\phi^2}{\sigma_{near}^2})^{1/(1-q)} \qquad (6.4)$$

and

$$\frac{dN_{away}}{d\Delta\phi}|_{\pi/2}^{3\pi/2}) = \frac{p_{T_a}\cos\Delta\phi}{\sqrt{2\pi<p_{out}^2>}Erf(\sqrt{2}p_{T_a}/\sqrt{<p_{out}^2>})}e^{\frac{p_{T_a}^2\sin^2\Delta\phi}{2<p_{out}^2>}} \qquad (6.5)$$

The near and away-side amplitudes C_1 and C_2 and $\sqrt{<p_{out}^2>}$ are free parameters. The fits to the azimuthal correlations are shown in Fig. 6.25. C_0 is determined from the mixed
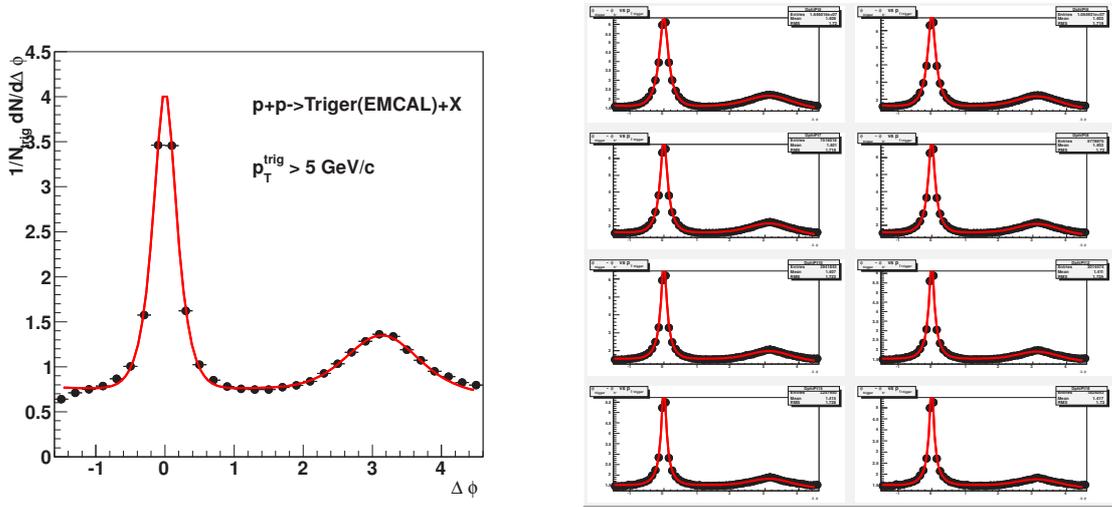
Figure 6.25: *Yield per trigger of charged tracks associated with cluster triggers in EMCal (left) and charged track triggers in CTS (right) as a function of $\Delta\phi$ in pp collisisons at $\sqrt{s} = 7$ TeV. The lines correspond to fits which are described in the text.*

azimuthal correlation and treated as constant. The $\sqrt{<p_{out}^2>}$ values obtained from these fits on the azimuthal correlations with non-isolated triggers are shown in Fig. 6.26. The width of the away side peak is found to be independent on the triggers.

128
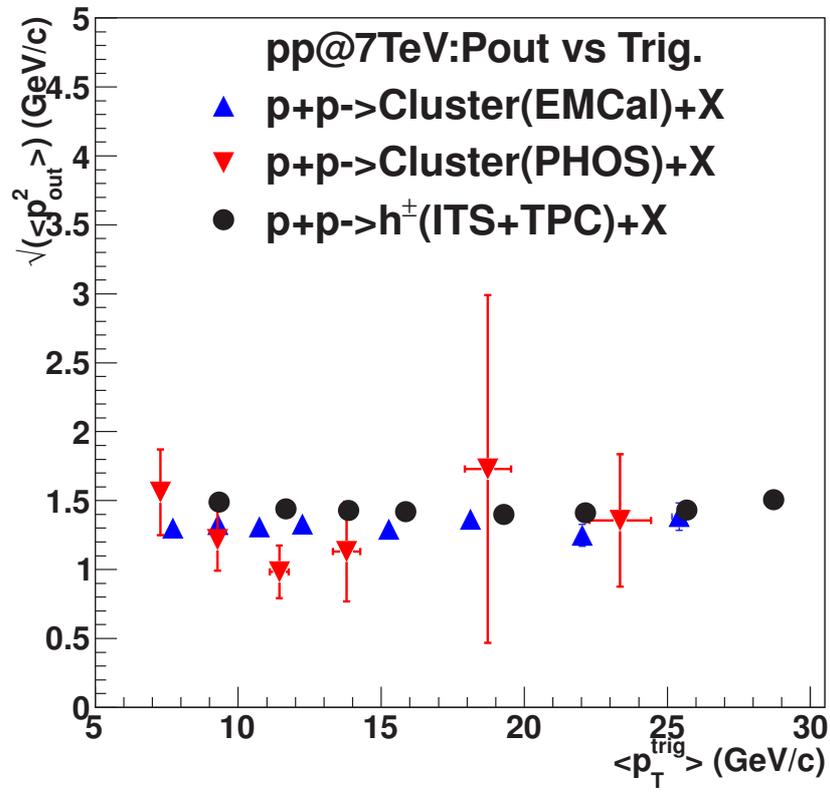
Figure 6.26: $\sqrt{<p_{out}^2>}$ values obtained from the fits for different triggers with $p_T^{trig} > 5\ GeV/c$ and $p_T^{h^\pm} > 1\ GeV/c$ in pp collisions at $\sqrt{s} = 7\ TeV$.

In order to interpret two particle correlations of final state particles in terms of properties of the hard scattered partons, as was shown in Eq. 3.3, the right hand side of the equation is a measurable quantity once $< p_{out}^2 >$ and $< j_{T_y}^2 >$ are determined. In particular, the isolated trigger represents the hard scattered parton direction approximately, which $\hat{p}_T^{trig} \simeq p_T^{trig}$, $z_t \approx 1$ and $j_{T_y} \approx 0$, and then Eq. 3.3 reduces to:

$$\frac{1}{\hat{x}_h}\sqrt{< k_T^2 >} = \frac{1}{x_h}\sqrt{< p_{out}^2 >} \tag{6.6}$$

where $x_h \equiv \frac{p_{T_a}}{p_{T_{trig}}}$ is obtained from the charged track transverse momentum distribution by projecting to different trigger p_T ranges. $\hat{x}_h = \frac{\hat{p}_T^a}{\hat{p}_T^{trig}}$, the same ratio at the partonic level, is taken from a Monte-Carlo model using the Born level pQCD cross sections and with a Gaussian k_T smearing [121]. By applying the same fitting procedure on the away side peak
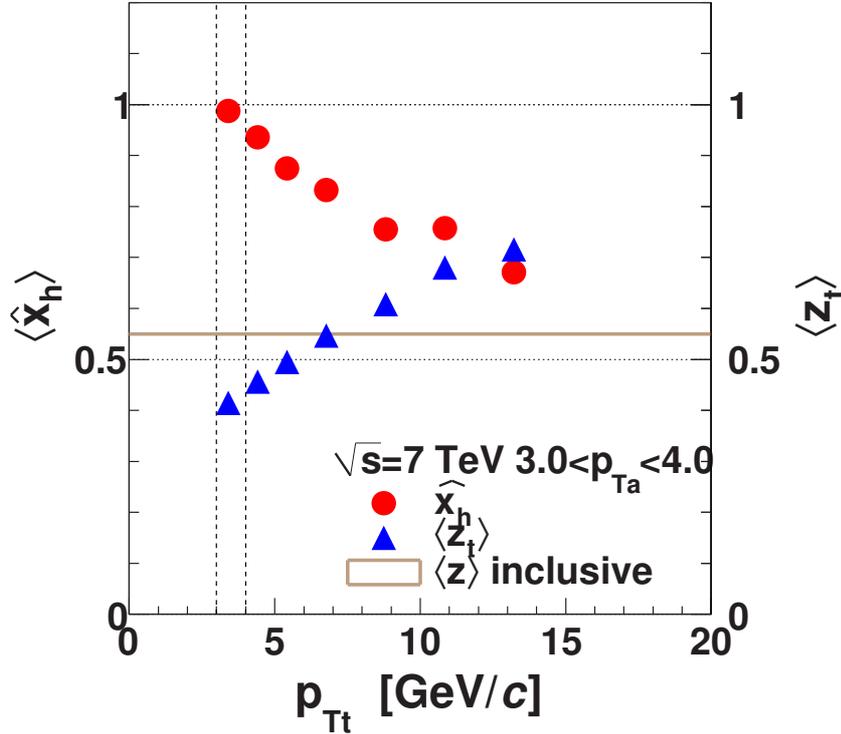
Figure 6.27: z_t and $\hat{x}_h$ calculated by a Monte-Carlo model using the Born level pQCD cross sections plus a Gaussian k_T smearing in pp collisions at $\sqrt{s} = 7$ TeV.

of the azimuthal correlation with isolated triggers, we are able to measure the value of the

width of the away side peak $\sqrt{<p_{out}^2>}$ (Fig. 6.28), where the value of $\sqrt{<p_{out}^2>}$ changed slightly after applying the isolation cut on the triggers.

In summary the measurement of $\sqrt{<p_{out}^2>}$ and x_h are used to extract the k_T dependence with the isolated trigger p_T^{trig}. Results shown in Fig. 6.29 in in agreement with the value at LHC energy extrapolated from worldwide data (Fig. 5.11) [122].
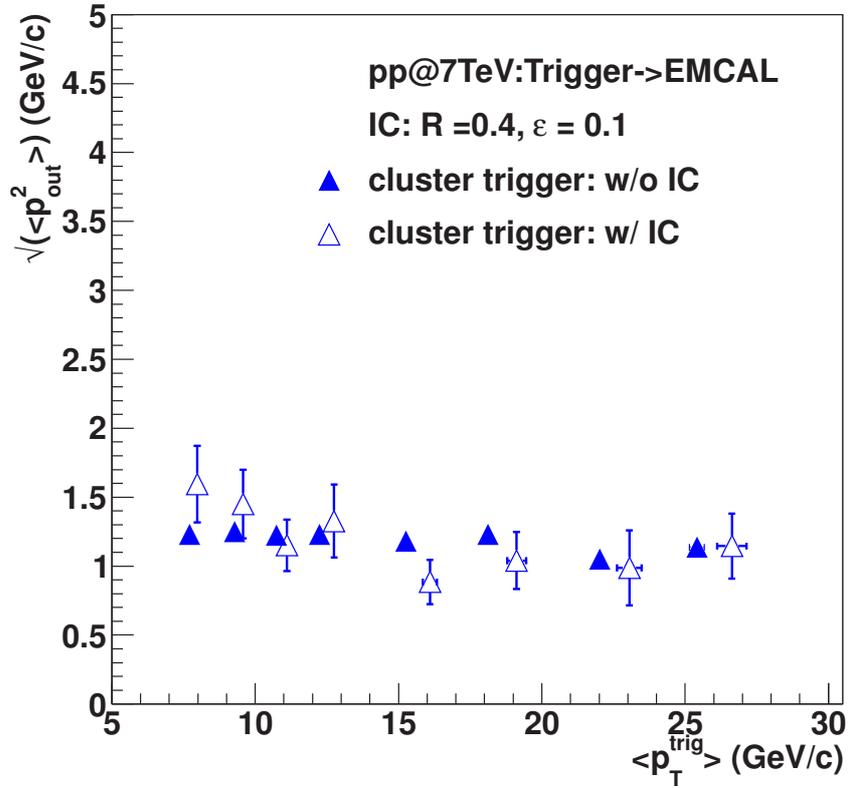
Figure 6.28: $\sqrt{<p_{out}^2>}$ values obtained from the fits for inclusive and isolated cluster triggers from EMCal with $p_T^{trig} > 5$ GeV/c and $p_T^{h^\pm} > 1$ GeV/c in pp collisions at $\sqrt{s} = 7$ TeV.

6.4.3 Per-trigger conditional yield

The per-trigger conditional yield is a representation of the associated hadron distribution in the away side peak as a function of the variable x_E,

$$x_E = \frac{\vec{p}_{T_h} \cdot \vec{p}_{T_{trig}}}{\left|p_{T_{trig}}\right|^2} \ , \tag{6.7}$$
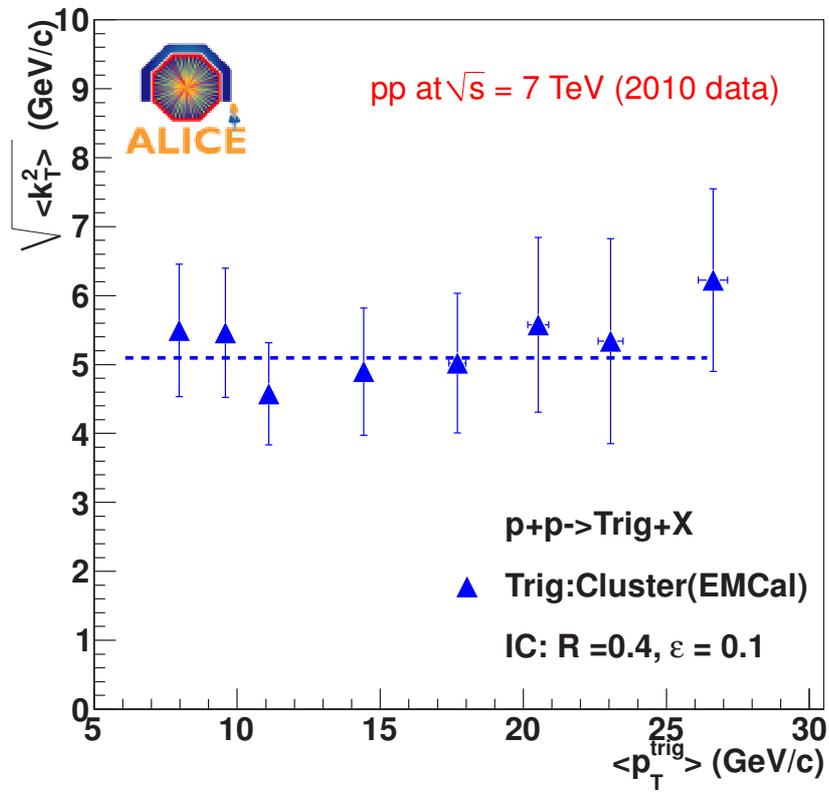
Figure 6.29: $\sqrt{<k_T^2>}$ values euvalated from Eq. 6.6 by obtaining the $\sqrt{<p_{out}^2>}$ values from the fits for isolated cluster triggers from EMCal with $p_T^{trig} > 5$ GeV/c and $p_T^{h^{\pm}} > 1$ GeV/c in pp collisions at $\sqrt{s} = 7$ TeV.

In case that the trigger particle is a direct prompt photon ($2 \rightarrow 2$ process), the x_{E} distribution is equivalent to the parton fragmentation function $D^{\mathrm{h}}_{\mathrm{q}/g}(z)$. Indeed, the measurable quantity, $p^{\mathrm{a}}_{\mathrm{T}}/p^{\mathrm{t}}_{\mathrm{T}}$ is nothing but the fragmentation variable $z = p^{\mathrm{a}}_{\mathrm{T}}/p^{\mathrm{jet}}_{T})$ when the isolated trigger particle is a direct prompt photon or a single hadron jet, since the isolated trigger energy balances the opposite jet energy. The equivalence is only approximate when, as in our case, the isolated trigger sample consists mostly of isolated π^0, but x_{E} remains a good approximation of z since the isolated hadron carries a large fraction of the jet energy.

As discussed above, a large part of the associated particle yield is composed of particles which are uncorrelated with the trigger. This contribution can be estimated by selecting associate particles in an azimuthal region relative to the trigger particle where the jet contribution is minimum. To that purpose, we have studied the transverse momentum spectra of associate particles contributing to different $\Delta\phi$ regions: (i) the near side peak $\pi/3 < \Delta\phi < \pi/3$; (ii) the away side peak $2\pi/3 < \Delta\phi < 4\pi/3$ and (iii) three regions where the azimuthal correlations strength is minimum $\pi/3 < \Delta\phi < \pi/2$ (transverse region in the near side hemisphere), $\pi/2 < \Delta\phi < 2\pi/3$ and $4\pi/3 < \Delta\phi < 3\pi/2$ (transverse region in the away side hemisphere). The uncorrelated background contribution is estimated from these last three regions. The spectrum of the underlying event is estimated from the particles which contribute in the azimuthal correlation distribution in regions transverse to the trigger particle (Fig. 6.30). One observes that independent of the trigger selection, non-isolated or isolated cluster, the p_{T} spectra for particles in the two away-side transverse regions are identical. The near-side transverse region cannot be considered for an estimation of the underlying-event contribution because of the way the trigger is selected which forces the associated particles in the near-side hemisphere to have a softer spectrum (Fig. 6.30) than the corresponding spectrum in the away-side hemisphere.

The p_{T}-spectra of the associate particles (Fig. 6.31) belonging to the jet are constructed from the particles with azimuthal directions with respect to the trigger around particle $\Delta\phi = 0$ (toward region) and around $\Delta\phi = \pi$ (away region). One observes that the toward-associate p_{T} spectrum is harder than the away-associate spectrum as a result of the trigger bias. Indeed, adding the trigger particle to the toward-associate particle spectrum, one recovers a spectrum identical to the away-associate particle spectrum (Fig. 6.31). The similarity of the away-associate spectrum (jet contribution) with the away-transverse spectrum (mainly underlying contribution) reflects both the weak contribution of the jet on top of the underlying event and
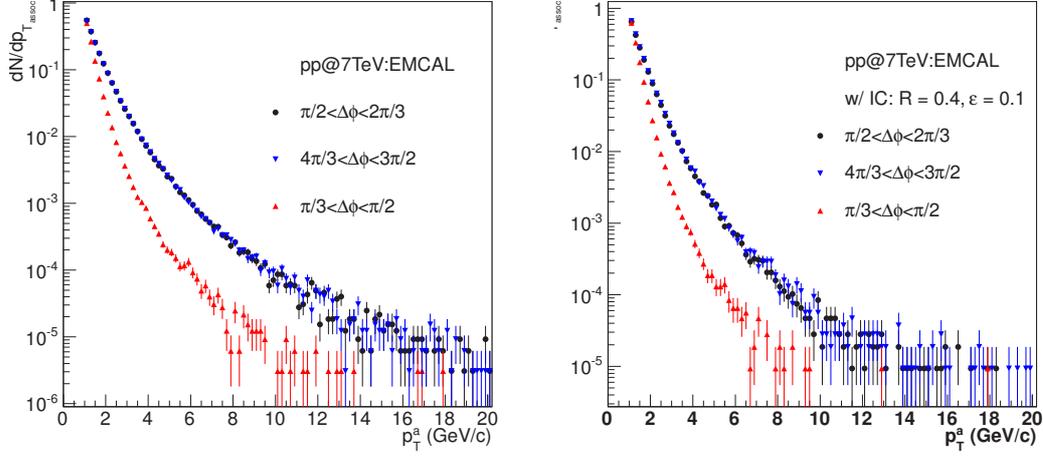
Figure 6.30: *Associate particles spectra selected in the transverse azimuthal regions with respect to the trigger particle: $\pi/2 < \Delta\phi < 2\pi/3$ and $4\pi/3 < \Delta\phi < 3\pi/2$ (away-side hemisphere) and $\pi/3 < \Delta\phi < \pi/2$ (near-side hemisphere) for non-isolated (top left) and isolated (top right) cluster triggers detected in EMCal. Ratio of the the spectra from the two different away-side transverse regions for non-isolated and isolated triggers detected in EMCAL (bottom). Data have been taken in pp collisions at $\sqrt{s} = 7$ TeV.*

possibly a "leak" of the jet in the transverse region (k_T generates a mis-alignment between the two back-to-back jets). When selecting isolated triggers, the toward and away spectra become softer as a result of the isolation selection which selects fragmentation particles from jets with lower energy than those sampled by the non-isolated particles.

The contribution of the underlying event to the x_E distribution was calculated from the associate particles spectrum under the $\Delta\phi$ window $\pi/2 < \Delta\phi < 2\pi/3$, where we assume the particle distribution from underlying events is isotropic in the full azimuth range. The x_E is calculated by randomly choosing one p_T from the associate particle transverse momentum spectra from $\pi/2 < \Delta\phi < 3\pi/2$ and the trigger distribution. The resulting x_E distribution was normalized to the height of the uncorrelated background on the $\Delta\phi$ distribution determined by fitting a gaussian plus a constant function to the measured azimuthal correlation distribution in the away-hemisphere. The contribution of the underlying event to the x_E distribution is displayed on Fig. 6.32 together with the measured isolated cluster (left) or charge (right) particle triggered x_E distribution. Because of the trigger selection algorithm, different for cluster triggers and charged particle triggers, the x_E distribution for charged triggers is limited to $x_E \leq 1$ (the charged trigger is the leading charged particle among all

134
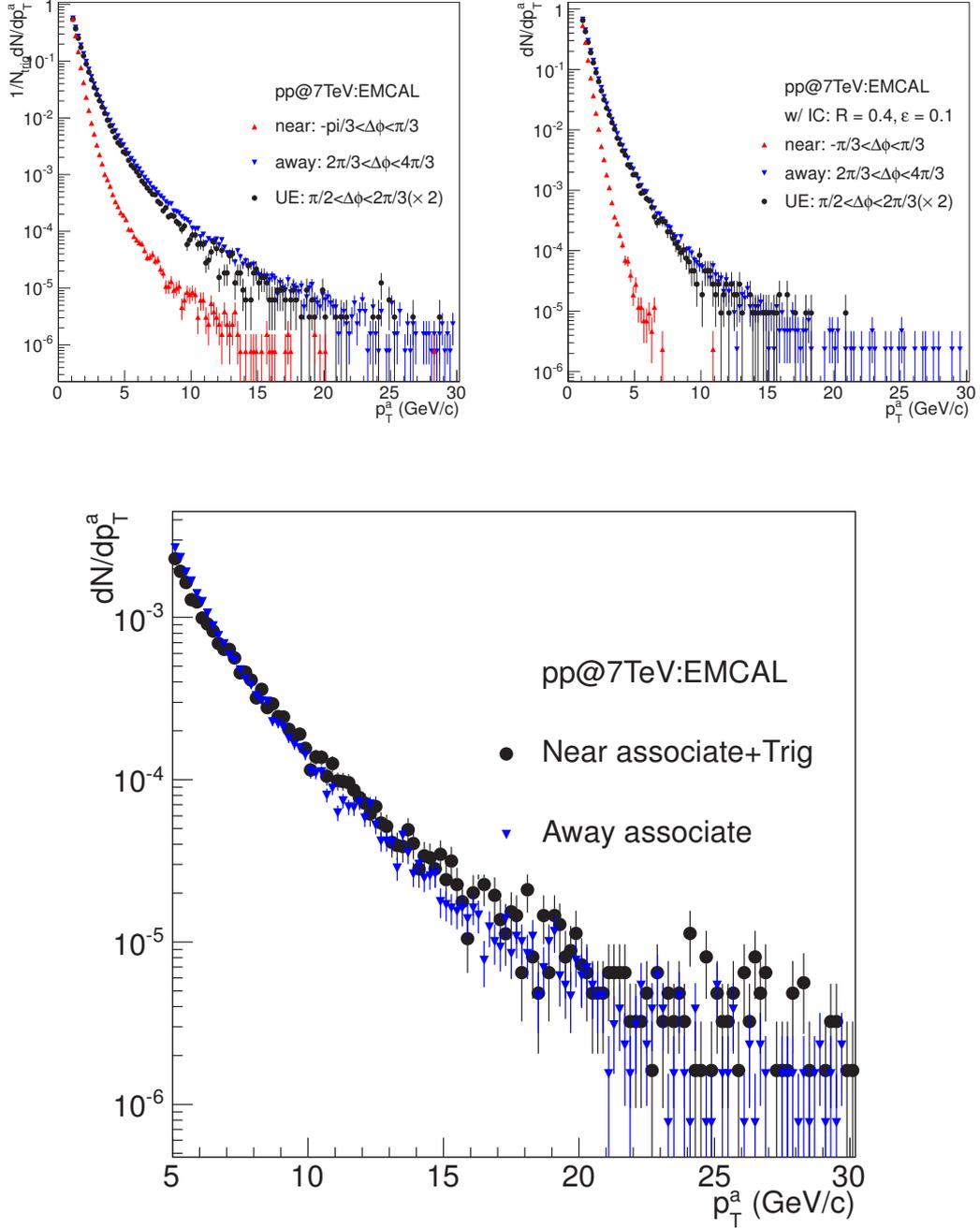
Figure 6.31: *Associate particle spectra selected in various azimuthal regions with respect to non-isolated (top let) or isolated (top right) cluster triggers detected in EMCAL: $\pi/3 < \Delta\phi < \pi/3$ (toward region), $2\pi/3 < \Delta\phi < 4\pi/3$ (away region) and $\pi/2 < \Delta\phi < 2\pi/3$ (away-side transverse region, same as Fig. 6.30). Toward-associate particle spectrum including the trigger particle compared to the away-associate particle spectrum (bottom). Data have been taken in proton-proton collisions at $\sqrt{s}$= 7 TeV.*
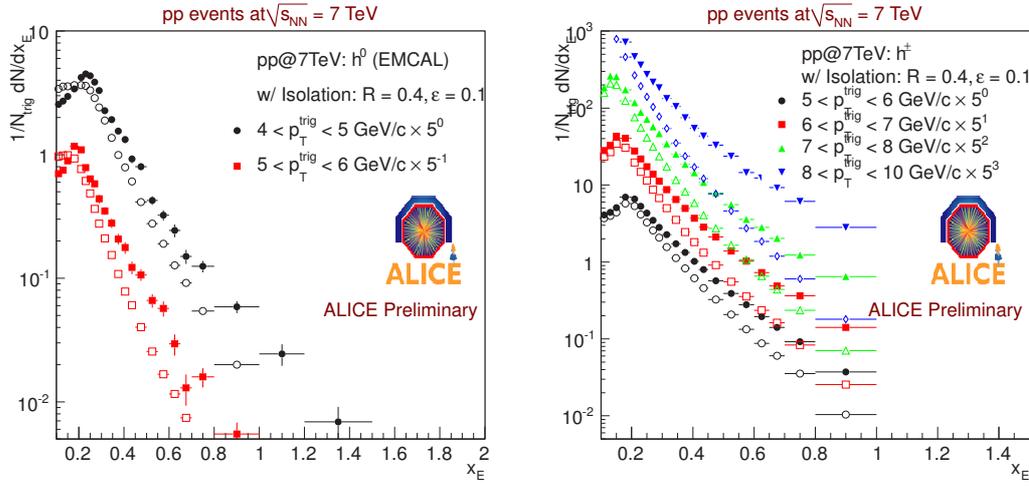
Figure 6.32: *Associate away-side charged hadrons ($p_T^a > 1$ GeV/c) per trigger ($p_T^t > 5$ GeV/c) yield as a function of x_E for isolated cluster triggers detected in EMCal (left) and charged particle triggers (right) detected in the central tracking system. Data have been taken in pp collisions at $\sqrt{s}$= 7 TeV.*

the charge particles in the event). For small x_E values, the contribution of the underlying event is important. Data are suppressed at $x_E = 0.2$ as a result of the selected kinematic cuts, $p_T^a > 1$ GeV/c and $p_T^t > 5$ GeV/c for triggers.

The charged hadron yield per trigger as a function of x_E (Fig. 6.33) has been constructed for associate hadrons ($p_T^a > 1$ GeV/c) emitted in the away region ($\pi/2 < \Delta\phi < 3\pi/2$) with respect to non-isolated and isolated cluster or charged triggers ($p_T^t > 5$ GeV/c). One observes that the x_E distribution for isolated cluster triggers is significantly steeper than the distribution for non-isolated clusters reflecting the fact that for isolated triggers the z_t value is closer to one (see Chapter **??**). The resulting x_E signal distributions after underlying event background subtraction for different p_T bins exhibits remarkable uniformity of the slope. In order to quantity this feature, an exponential function ($f(x_E) = Ce^{-n \cdot x_E}$) is fitted to the x_E distribution in the range $0.4 < x_E < 0.8$, the fitting parameter n stands for the *inverse x_E slope*. Fig. 6.34 shows the evolution of the inverse x_E slope as a function of the mean trigger p_T from ALICE measurements. The slope agrees quite well for charged and neutral triggers which is explained by the fact that neutral cluster triggers are dominated by neutral pions. The difference between charged and cluster triggers in the low p_{Tt} range is explained by the composition of clusters dominated by single decay photon clusters. From di-hadron correlation measurements performed at LEP [**?**], it was concluded that the x_E distribution is

136
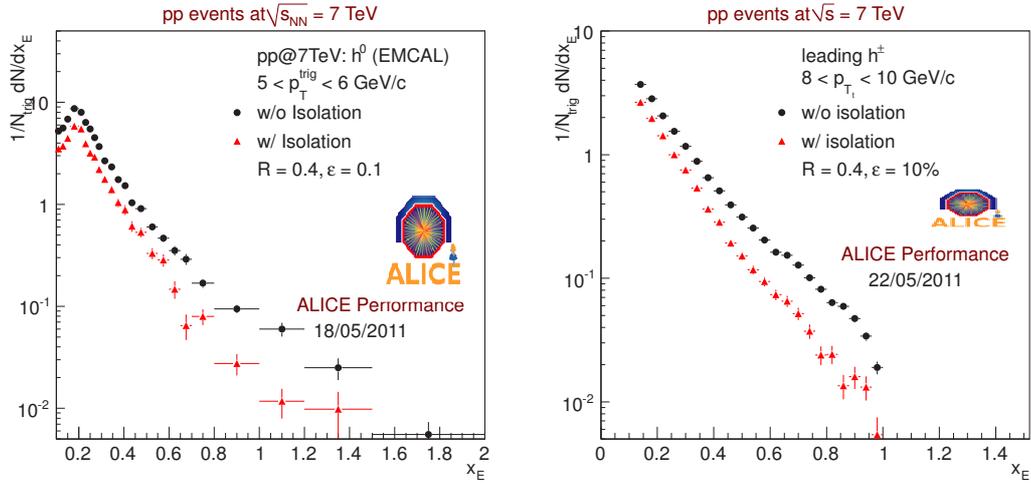
Figure 6.33: *Away-side associate charged hadron ($p_T^a > 1$ GeV/c) yield per trigger ($p_T^t > 5$ GeV/c) as a function of x_E for non-isolated (dot symbols) and isolated (triangle symbols) triggers detected in EMCal (left) and central tracking system (right). Data have been taken in pp collisions at $\sqrt{s} = 7$ TeV.*

not sensitive to the away side jet fragmentation function because the trigger particle carries only a small fraction of the full jet energy ($z_t = \frac{p_{T_t}}{p_{T_{jet}}} < 1$). This conclusion is confirmed by our measurement where the measured inverse slope is in the region where one expects (blue band) the x_E slope when the trigger particle samples the jet momentum at $z_t \sim 0.5$. The same fit performed to the isolated clusters and charged particles triggered x_E distributions leads to n-values displayed in Fig. 6.35. One observes that the n-value is generally higher for the isolated triggers than for the non-isolated triggers and is increasing with p_{Tt}, faster for the isolated triggers. The slope approaches the region where one expects n to represent the slope of the true fragmentation function for quarks and gluons (blue band defined by $z_t = 1$). The same behavior as for charged particle triggers is observed of the n values extracted from cluster triggered x_E distributions. The colored bands on the same figure indicated the range expected for fragmentation function of quarks (lower limit) and gluons (upper limit) of the x_E slope parameter when for $<z_t> = 0.5$ (yellow band) and for $<z_t> = 1$ (grey band). The x_E slope parameters measured for isolated triggers enter the grey band indicating that the x_E distribution probes the fragmentation function.

This last observation can be further visualized by comparing (Fig. 6.36) the measured x_E distribution for isolated clusters with the fragmentation function calculated from PYTHIA generated γ+jet events (initial and final state radiation were switched on and the PYTHIA
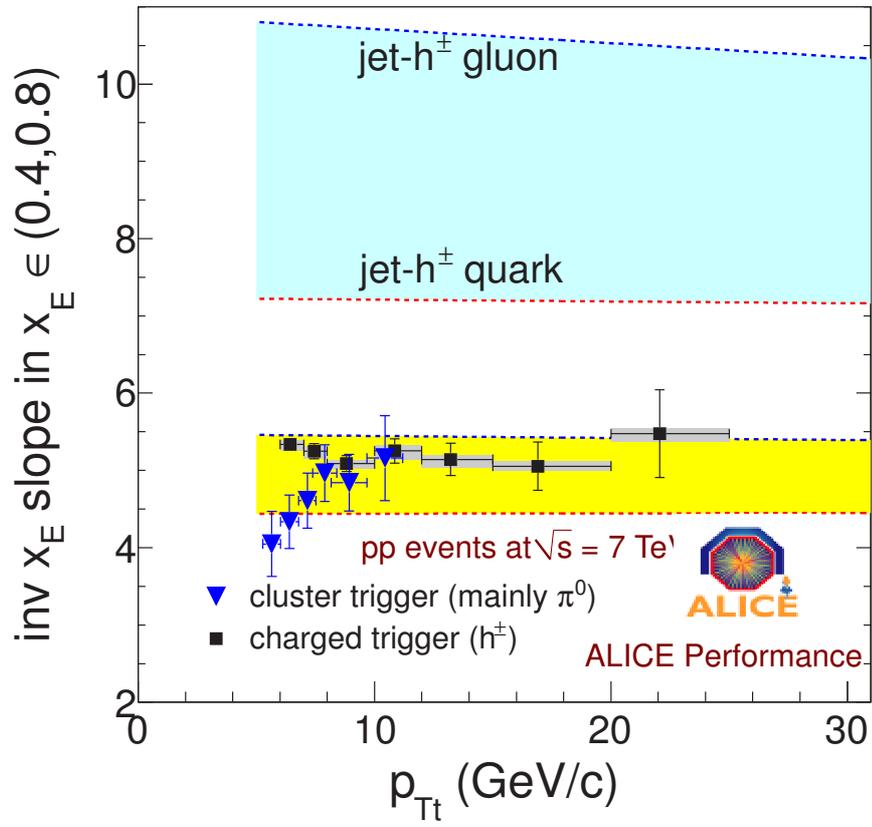
Figure 6.34: *Extracted inverse x_E slope as a function of the mean trigger p_{Tt} for charged (red) and neutral triggers (blue) in pp collisions at $\sqrt{s} = 7$ TeV. The contribution of the underlying event has been subtracted.*
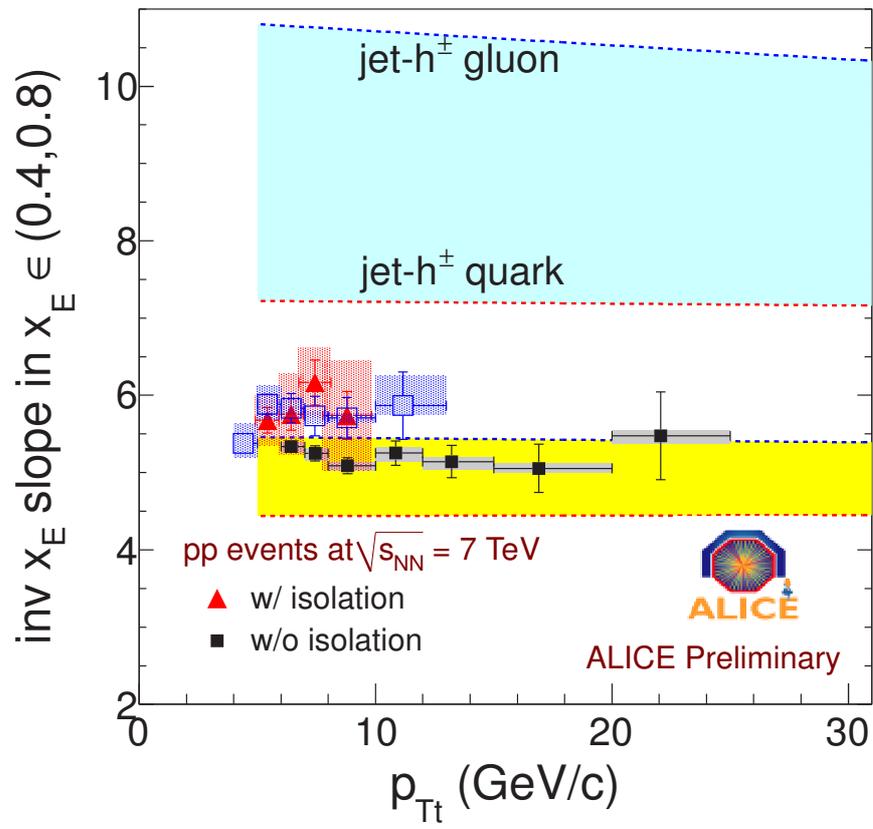
Figure 6.35: *Extracted inverse x_E slope as a function of the mean trigger p_{Tt} for non-isolated and isolated triggers in pp collisions at $\sqrt{s} = 7$ TeV.*

k_T value vas set equal to 4.5 GeV/c. The slope parameters of the two distributions are identical between $x_E = 0.2$ and 0.6. The discrepancy at large x_E values is mainly due to finite detectors (EMCAL and central tracking system) resolution effects and to the fact that our z_t is not equal to 1 a variance with the z_t value of the prompt direct photon from the PYTHIA γ+jet events.
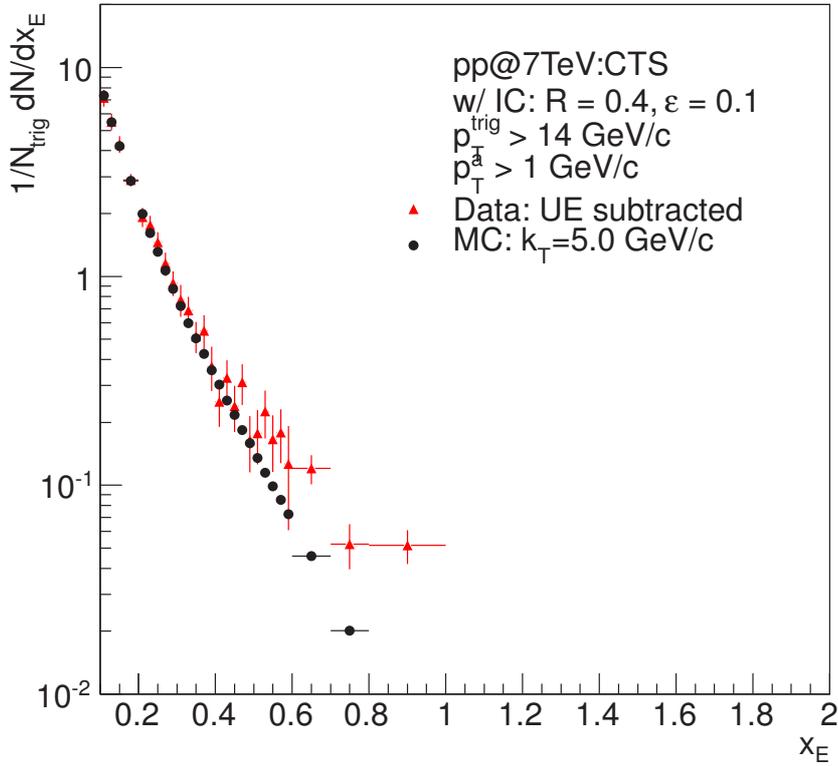
Figure 6.36: *Associate away-side charged hadron ($p_T^a > 1$ GeV/c) yield per trigger ($p_T^t > 14$ GeV/c) (triangle symbols) as a function of x_E for isolated cluster triggers detected in central tracking system in pp collisions at $\sqrt{s} = 7$ TeV compared to the same distribution calculated from PYTHIA generated γ+jet events (initial state and final state radiation switched on and PYTHIA k_T value set equal to 5.5 GeV/c.*

Chapter 7

Summary and Outlook

The ultimate objective of the work partly presented in this thesis is to study the properties of the hot and dense QCD (Quantum Chromo Dynamics) matter in the deconfined QGP (Quark Gluon Plasma) phase through the measurement of direct photon tagged charged hadrons correlations. This study is part of the scientific program of the ALICE experiment designed and optimized for the detection and identification of a complete set of probes generated in heavy-ion collisions at LHC energies. The QGP is the fundamental state of QCD matter and is, according to the Big Bang cosmological model, the primordial state of matter that prevailed during the first hundreds of micro seconds of existence of the Universe. Recreating this state of matter and studying its properties will shed light on fundamental still unanswered questions, such as the origin of the constituent mass of matter (the constituent mass of quarks contributes to 99% of the mass of the nucleon whereas the bare mass, supposedly generated through the Higgs mechanism, contributes to the remaining 1%) and the Chiral symmetry breaking (which could be at the origin of the difference in quark masses). LHC has already provided heavy-ion collisions at the unprecedented high energies of $\sqrt{s_{NN}} = 2.76$ TeV and ALICE was quickly able to establish the global properties of the collision and to have a glimpse on the properties of the created medium. So, from the measurement of charged particle densities, we deduced that the energy density of the medium is 15 GeV/fm^3 (three times larger that the density reached at RHIC) and the temperature is 30% larger than the one reached at RHIC. The volume and lifetime of the collisions was deduced, from identical particles interferometry measurement, to be two times larger and 40% longer, respectively,

than the ones at RHIC. Collective flow measurements indicate that the medium produced at LHC has the properties of an ideal liquid (almost zero viscosity) and has a very high color density able to absorb completely high energy partons (jet quenching measurement). It is precisely this last effect which drives my study.

Partons with high $p_{\rm T}$ (transverse momentum) are produced in hard pQCD (perturbative QCD) scattering between constituent partons inside the colliding nuclei and are observed in the detectors as a collimated jet of hadrons. The 4-momentum of the hard scattered parton is modified through soft gluons radiation while traversing the color dense and deconfined medium created concurrently in the collision. The modification, which depends on the color density of the medium and on the distance traversed inside the medium, is imprinted in the fragmenting hadrons in a way that modifies dynamically the fragmentation function of the jet (he fragmentation function measures the hadrons distribution inside a jet as a function of the jet fractional momentum carried by each hadron). The medium modification is evidenced in the jet fragmentation function by a suppression of high $p_{\rm T}$ hadrons (jet quenching effect) and a simultaneous enhancement of low $p_{\rm T}$ hadrons originating from the fragmentation of the soft radiated gluons. The suppression and enhancement in heavy ion collisions are defined with respect to the fragmentation function measured under similar conditions in proton-proton collisions. Hence the importance of the proton-proton measurements to provide the reference data. For the measurement itself one needs to measure, on one hand, the total energy of the jet (i.e., the energy of the primary hard scattered parton), and on the other hand, the momentum of the hadrons which make up the jet. Whereas measuring with high resolution the momentum of charged partons (the central tracking system of ALICE was designed with this objective) is relatively straightforward, identifying jets is challenging because of the high particle density from the underlying heavy-ion event that limits these measurements. Jets with energies below 50 GeV cannot be reconstructed with standard jet algorithms (the jet particles do not stand out sufficiently on top of the background). These low jet energies are however particularly interesting since energy loss models predict that the medium effect will be the most dramatic, they will loose a large fraction of their energy. One can advocate however an alternative approach by selecting the often considered as the golden channel, i.e., the particular hard scattering QCD processes which produce in the final state a direct photon (direct characterizes photons not coming from the decay of hadrons such as π^0) and a parton, the so called γ - jet events. Since photons do not interact through the strong

interaction with the color charges of the medium, they traverse the medium unscathed and can therefore be detected with the energy with which they emerged from the hard scattering process. By momentum balance in a $2 \rightarrow 2$ process, the photon provides therefore also the direction (opposite in azimuth, the correlation in polar angle or rapidity is smeared out by the Fermi motion of partons inside nucleons) and the energy of the parton/jet emerging from the same process: we say that we tag the jet with a direct photon. We therefore have at hand the measure of the parton energy as it has been produced (measure the photon energy) and the the parton energy after it has traversed the medium (measure the final state jet energy). The measurement can still be simplified. Following a suggestion by X. N. Wang, F. Arleo *et al.*, I have demonstrated in this thesis, though a detailed Monte-Carlo study, that instead of identifying a jet detected opposite in azimuth to a direct photon, measuring the correlation of all the hadrons emitted opposite to a direct photon provides a sufficiently good approximation and enables to construct a quasi fragmentation function (we call it per-trigger conditional yield) in which the medium effects can be identified and quantified. The measurement can be perfected further making the γ - jet observable a real tomographic tool. Following an idea by H. Zhang, X.N. Wang *et al.*, I have demonstrated that by selecting adequately the fraction z of the photon energy carried by the hadrons emitted opposite to the photon, one can select the distance the hard scattered parton travels through the medium (z values close to 1 select hard processes at the surface of the medium and z values much smaller than one select hard processes in the interior of the medium) and hence the location of the hard scattering inside the medium. One can thus probe the medium throughout its volume, however, with less sensitivity as anticipated by a pure theoretical model.

A key requirement for this study is the proper identification of direct photons among the very larger amount of decay photons and fragmentation photons (photons radiated from a quark in the final state of a hard scattering or Next to Leading Order $2 \rightarrow 3$ process). The method retained presently (the shower shape analysis is an additional possibility) is the isolation selection which requires the absence of hadronic activity around the photon candidate. I have discussed the efficiency and remaining contamination of this selection and applied in the Monte-Carlo study and real data analysis.

In ALICE the measurement of γ-jet events is achieved by combining the ALICE calorimeters, for the detection and the identification of photons, with the ALICE central tracking detectors for the detection of charged particles. My feasibility study has been performed for both

proton–proton and Leas–Lead collisions simulated by Monte-Carlo techniques. Anticipated effects due to the formation of a quark gluon plasma can indeed be observed by comparing the same measurement performed in proton–proton collisions and in heavy-ion collisions. I have shown that the measurement is feasible, based on statistical and systematic errors arguments, the correlation distribution can be measured with sufficient counting rate, the systematic errors, due to improperly identified π^0 decay photons and fragmentation photons and, at small values of z, to the underlying event contribution, remaining low enough for a meaningful measurement.

The analysis of data acquired in real proton–proton collisions during 2010 constitutes the last part of my doctoral study. This study must be considered as preliminary: the statistics was limited during this first year of LHC operation, the calorimeters coverage was incomplete (less than 50% of the final coverage), absence of photon triggers and at last but not at least the time left (a few months) for the final analysis was to short because of the quite long time needed a priori to understand the various detectors. Consequently, the results are limited to a quite low p_T range, the most unfavorable for the identification of direct photons and jets. It was however a very useful exercise with some valid results for the preparation of the analysis of the data to be collected under much more favorable conditions.

After the raw data have been properly corrected for detector calibrations and reconstructed, I have performed the final analysis. Photons are detected in the calorimeters as clusters of hit elementary detection cells. I have considered three cases to trigger the analysis: single clusters (mainly decay photons), identified π^0 and charged tracks (for a control measurement). The azimuthal correlation of these three type of trigger "particles" with the remainder charged hadrons in the event shows the expected 2 jets structure and the structure is similar with the three kind of triggers again as anticipated. This comparison validates the use of calorimeter clusters as a trigger of jet events (such a trigger has now been implemented in the hardware of the calorimeters). I have also demonstrated that calorimeters allow us a much sharper selection of the jet trigger selection enhancing the 2 jet structure in the azimuthal correlation. I have also constructed the correlation starting from isolated clusters where the structure due to jet emitted in the direction opposite to the isolated cluster remains present. Such events are presently interpreted as hard fragmenting partons into a single π^0 or direct photons. The production of these events is now being quantified to confirm the interpretation of their origin.

A detailed analysis of the opposite jet structure has been performed to estimate the total transverse momentum k_T involved in the hard process. This transverse momentum is generated by the convolution of the Fermi motion of partons in nuclei, the multi-gluon radiation of the quarks in the initial state (before the hard scattering) and the single gluon radiation of the quarks in the final state (after the hard scattering). Prior to this analysis, I have performed a Monte-Carlo study to extrapolate from the world wide data the value of k_T at LHC energies. The value obtained from my real data analysis, equal to 5 GeV/c, reproduces well my prediction.

Finally, I have constructed the per-trigger conditional yield of charged hadrons as a function of $x_E = \frac{\vec{p}_T^{assoc} \cdot \vec{p}_T^{trig}}{|p_T^{trig}|^2}$. When isolated cluster are selected as photon candidate, the conditional yield comes very close to the fragmentation function. Detectors effect have still to be understood before final conclusions can be drawn.

To conclude, I can say that I had a very long training with Monte-Carlo studies (thanks or because of the delayed start of LHC). When data became available I was confronted with "real life" and with the hard work until the detector was sufficiently understood to proceed with the data analysis. I have learned in all aspects of the experiment and feel confident enough to reach the original objectives of my study with the new data to be collected soon.

Bibliography

[1] M. J. Herrero, The standard model (1998). hep-ph/9812242. Lectures presented at the NATO ASI 98 School, Techniques and Concepts of High Energy Physics; St. Croix, Virgin Islands, USA, June 18-29.

[2] V. Barger, R. Phillips Collider Physics (1997) ISBN 0201149451.

[3] S. F. Novaes, standard model: An introduction (2000). hep-ph/0001283. Published in "Particle and Fields".

[4] G. Dissertori, I. Knowles, and M. Schmelling, Quantum Chromodynamics - High Energy Experiments and Theory. Oxford University Press, 2003.

[5] R. P. Feynman (1998). Quantum Electrodynamics. Westview Press; New Ed edition. ISBN 978-0201360752.

[6] B. Jager, A. Schafer et al., Phys. Rev. D67 (2003) 054005.

[7] D. J. Gross and F. Wilczek, Phys. Rev. Lett. 30 (1973) 1343.

[8] E. V. Shuryak, Phys. Rep. 61 (1980) 71.

[9] S. Hands, Contemp. Phys. 42 (2001) 209.

[10] R. J. Fries and B. Müller, Eur. Phys. J. C34 (2004) S279.

[11] T. D. Lee, in Proceedings of the $XVII$ International Conference on High Energy Physics, 1974.

[12] U. W. Heinz and M. Jacob, arXiv:nucl-th/0002042.

[13] RHIC, URL http://www.bnl.gov/rhic.
BNL, URL http://www.bnl.gov/.

[14] http://www.bnl.gov/rhic/news2/news.asp?a=05-38&t=pr.

[15] L. Evans and P. Bryant, JINST 3 (2008) S08001.

[16] S. Grinstein, PhD thesis: The Inclusive Jet Cross Section using the k_T Algorithm (2003).

[17] Y. X. Mao et al., ALICE-INT-2007-021, Euro. Phys. J. C 57 (2008) 613.

[18] Y. X. Mao et al., ALICE-INT-2007-017, Chinese Physics C 32(07) (2008).

[19] Time Magazine (1957), http://www.lbl.gov/Science-Articles/Research-Review/Magazine/1997-fall/contents.html.

[20] U. Yves, http://www-subatech.in2p3.fr/ photons/subatech/physics/potpourri/physics.html.

[21] J. D. Bjorken, Phys. Rev. D27 (1983) 140.

[22] K. Miki, PhD thesis: Azimuthal Anisotropy Measurement of Neutral Pion and Direct Photon in $\sqrt{s_{NN}} = 200$ GeV Au+Au collisions at RHIC-PHENIX (2009).

[23] Z. Yin, Ph. D. Thesis: High p_T physics in heavy ion collisions at $\sqrt{s_{NN}} = 200$ GeV (2004).

[24] R. Glauber and G. Matthias, Nucl. Phys. B21 (1970) 135.
T. Wibig and D. Sobezynska, J. Phys. G: Nucl. Part. Phys. 24 (1998) 2037.

[25] A. Kiyomichi, PhD thesis: Study of identified hadron spectra and yields at mid-rapidity in Au+Au collisions at $\sqrt{s} = 200$ GeV (2005).

[26] P. Braun-Munzinger, D. Magestro, K. Redlich and J. Stahel, Phys. Lett. B 518 (2001) 41.

[27] Yu. L. Dokshitzer, Sov. Phys. JETP 46 (1977) 416;
V. N. Gribov and L. P. Lipatov, Sov. J. Nucl. Phys. 15 (1972) 438;
G. Altarelli and G. Parisi, Nucl. Phys. B 126 (1977) 298.

[28] M. Gluck, E. Reya and A. Vogt, Z. Phys. C 67 (1995) 433.

[29] G. Sterman et al., CTEQ Collaboration, Rev. Mod. Phys. 67 (1995) 157.

[30] J. Pumplin et al., JHEP, 07 (2002) 012.

[31] J. Binnewies, B. A. Kniehl and G. Kramer, Phys. Rev. D 52 (1995) 4947.

[32] P. Aurenche et al., Euro. Phys. J. C 13 (2000) 347.

[33] B. A. Knirhl, G. Kramer and B. Potter, Nucl. Phys. B 597 (2001) 337.

[34] J. W. Cronin et al., Phys. Rev. D11 (1975) 3105.

[35] J. J. Aubert et al., Phys. Lett. B123 (1983) 275.

[36] M. Arneodo et al., Nucl. Phys. B441 (1995) 12-30.

[37] Y. X. Mao, W. C. Xiang and D. C. Zhou, International Journal Modern Physics E, Vol.16, Nos. 7-8 (2007) 2130.
J. Liu, Y. X. Mao, W. C. Xiang and D. C. Zhou, Chinese Science Bulletin Vol.51,No.2 (2006) 139.
D. C. Zhou, W. C. Xiang and Y. X. Mao, Journal of Central China Normal University (Natural Sciences) 39 (2005) 482.

[38] X. N. Wang and M. Gyulassy, Phys. Rev. Lett 68 (1992) 1480.
M. Gyulassy and X. N. Wang, Nucl. Phys. B420 (1994) 583.
X. N. Wang, Phys. Lett. B579 (2004) 299 nucl-th/0307036.

[39] M. Gyulassy, P. Levai and I. Vitev, Phys. Lett. B 538 (2002) 282.

[40] R. Baier, Y. L. Dokshitzer, S. Peigne and D. Schiff, Phys. Lett. B 345 (1995) 277.

[41] R. Baier, D. Schiff and B. G. Zakharov, Ann. Rev. Nucl. Part. Sci 50 (2000) 37.

[42] K. Aamodt et al., ALICE Collaboration, Phys. Rev. Lett. 105 (2010) 252301.

[43] M. C. Abreu et al., NA50 Collaboration, Phys. Lett. B 530 (2002) 43.

[44] C. Adler et al., STAR Collaboration, Phys. Rev. Lett 87 (2001) 112303.

[45] I. G. Bearden et al., BRAHMS Collaboration, Phys. Rev. Lett. 88 (2002) 202301.

[46] K. Adcox et al., PHENIX Collaboration, Phys. Rev. Lett. 88 (2001) 3500.

[47] B.B.Back et al., PHOBOS Collaboration, Phys. Rev. Lett. 87 (2001) 102303.

[48] K. Aamodt et al., ALICE Collaboration, Euro. Phys. J. C 68 (2010) 89.

[49] V. Khachatryan et al., CMS Collaboration, JHEP 02 (2010) 041.

[50] R. Hanbury Brown and R. Q. Twiss, Nature (London) 178 (1956) 1046.

[51] A.N. Makhlin, Y. M. Sinyukov, Z. Phys. C 39 (1988) 69.

[52] K. Aamodt et al., ALICE Collaboration, Phys. Lett. B 696 (2011) 328.

[53] M. A. Lisa, et. al., E895 Collaboration, Phys. Rev. Lett. 84 (2000) 2798.

[54] C. Alt, et. al., NA49 Collaboration, Phys. Rev. C 66 (2008) 064908.

[55] D. Adamova, et .al., CERES Collaboration, Nucl. Phys. A 714 (2003) 124.

[56] B.I. Abelev et al., STAR Collaboration, Phys. Rev. C 80 (2009) 024905.

[57] B.B.Back et al., PHOBOS Collaboration, Phys. Rev. C. 73 (2006) 031901.

[58] H. Sorge, Phys. Rev. Lett. 82 (1999) 2048.

[59] K. Aamodt et al., ALICE Collaboration, Phys. Rev. Lett. 105 (2010) 252302.

[60] Y. Bai, PhD thesis, Nikhef and Utrecht University (2007).

[61] B. I. Abelev et al., STAR Collaboration, Phys. Rev. C 77 (2008) 054901.

[62] A. Adare et al., PHENIX Collaboration, Phys. Rev. Lett. 98 (2007) 162301.

[63] S. M. Dogra, PhD thesis: Particle Production and Correlations in Ultrarrelativeistic Nucleus-Nucleus Collisions (2008).

[64] K. Aamodt et al., ALICE Collaboration, Phys. Lett. B 696 (2011) 30.

[65] S.S. Adler et al., PHENIX Collaboration, Phys. Rev. C. 69 (2004) 034910.

[66] J. Adams et al., STAR Collaboration, Phys. Rev. Lett. 91 (2003) 172302.

[67] J. Adams et al., STAR Collaboration, Phys. Rev. Lett. 91 (2003) 072302.

[68] D. Magestro, Nucl. Phys. A 774 (2006) 573.

[69] http://xxx.lanl.gov/pdf/nucl-th/0610051.

[70] R. Feynman, R. Field and G. Fox, Nucl. Phys. B128 (1977) 1.

[71] S. S. Adler et al., PHENIX Collaboration, Phys. Rev. D74 (2006) 072002.

[72] L. Apanasevich, et. al., Phys. Rev. D 59 (1999) 074007.

[73] R. Baier, Y. L. Dokshitzer, S. Peigne and D. Schiff, Phys. Lett. B 345 (1995) 277.

[74] T. Horaguchi, Ph. D. Thesis: Prompt Photon Production in Proton–Proton Collisions at $\sqrt{s} = 200$ GeV (2005).

[75] E. V. Shuryak, Sov. J. Nucl. Phys. 28 (1978) 408.

[76] R. J. Fries, B. Muller and D. K. Srivastava, Phys. Rev. Lett. 90 (2003) 132301.

[77] ALICE Collaboration, J. Phys. G: Nucl. Part. Phys., 32 (2006) 1295.

[78] M. M. Aggarwal et al., (WA98 Collaboration), Phys. Rev. Lett. 85 (2000) 3595.

[79] S. Turbide, R. Rapp and C. Gale, Phys. Rev. D56 (2004) 014903.

[80] S. S. Adler et al., (PHENIX Collaboration), Phys. Rev. Lett. 94 (2005) 232301.

[81] L. E. Gordon and W. Vogelsang, Phys. Rev. D (1993) 3136.

[82] A. Adare et al., PHENIX Collaboration, Phys. Rev. Lett. 104 (2010) 132301.

[83] X. N. Wang, Z. Huang and I. Sarcevic, Phys. Rev. Lett. 77 (1996) 231.

[84] F. Arleo, J. Phys. G: Nuclear and Particle Physics, 34, 8 (2007) S1037.
F. Arleo, P. Aurenche, Z, Belghobsi, J.-P. Guillet, JHEP 11 (2004) 009.
F. Arleo, JHEP 09 (2006) 015.

[85] M. Nguyen, PhD thesis: Two particle correlations with direct photon and π^0 triggers in 200 GeV p+p and Au+Au collisions (2009).

[86] M. Connors, PHENIX Collaboration, nucl-ex/0907.4571v2 (2009).

[87] H. Zhang, J. F. Owens, E. Wang and X. N. Wang, hep-ph/0907.4816v2 (2009).

[88] L. Evans and P. Bryant, JINST 3 (2008) S08001.

[89] K. Aamodt et al., ALICE Collaboration, JINST 3 (2008) S08002.
ALICE, URL http://aliceinfo.cern.ch/.

[90] http://l3.web.cern.ch/l3/.

[91] ALICE Collaboration, ALICE TDR 4 (1999).

[92] ALICE Collaboration, ALICE TDR 7 (2000).

[93] ALICE Collaboration, CERN/LHCC 99-4, http://alice.web.cern.ch/Alice/TDR/.

[94] T. M. Cormier, Eur. Phys. J C34 (2004) s333.

[95] Test Beam, URL http://aliceinfo.cern.ch/Collaboration.

[96] offline, URL http://aliceinfo.cern.ch/Offline/.

[97] AliRoot, URL http://pcaliweb02.cern.ch/Offline/AliRoot/.

[98] Root, URL http://root.cern.ch.

[99] T. Sjostrand, L. Loonnblad and S. Mrenna, hep-ph/0108264 (2001).
     T. Sjostrand et al., Comput. Phys. Commun. 135 (2001) 238.

[100] M. Gyulassy and X. N. Wang, Comput. Phys. Commun. 83 (1994) 307.

[101] R. Brun et al., GEANT3 User Guide, (1985) CERN Data Handling Division
      DD/EE/84-1. GEANT3, URL http://wwwasd.web.cern.ch/wwasd/geant/.

[102] GEANT4, URL http://wwasd.web.cern.ch/wwasd/geant4/geant4.html.

[103] A. Fassò et al., FLUKA: Status and Prospective for Hadronic Applications (Springer-
      Verlag Berlin, 2001)955.

[104] H. L. Lai et al., Phys. Rev. D55 (1997) 1280-1296. e-Print Archive: hep-ph/9606399.

[105] P. Aurenche et al., arXiv: hep-ph/9811382 (1998).

[106] G. Conesa, Ph. D. Thesis: Identification of particles and hard processes with the spec-
      trometer PHOS of the ALICE experiment (2005).

[107] G. Conesa et al., Nucl. Instr. and Meth. Nucl. Res. A580 (2007) 1446.

[108] G. Conesa et al., ALICE-INT-2005-16.

[109] Y. Mao, Master thesis: Study of jet fragmentation with ALICE at LHC through
      γ hadron correlation measurement.

[110] Y. L. Dokshitzer, V. A. Khoze and S. I. Troian, Z. Phys. C55 (1992) 107.

[111] U. Abeysekara et al., ALICE/EMCAL Collaboration, arXiv: hep-ph/10080413v1 (2010).

[112] C. Albajar et al., UA1 Collaboration, Nucl. Phys. B309 (1988) 405.

[113] N. Armesto, L. Cunqueiro and C. A. Salgado, arXiv:hep-ph/0907.1014.

[114] C. A. Salgado and U. A. Wiedemann, Phys. Rev. D68 (2003) 014008, hep -ph/0302184.

[115] A. Dainese, C. Loizides and G. Paic, hep-ph/0406201v3 (2004).

[116] K. Aamodt et al., ALICE Collaboration, Euro. Phys. J. C 65 (2010) 111.

[117] https://twiki.cern.ch/twiki/bin/viewauth/AliceEVE/EVEEMC.

[118] https://twiki.cern.ch/twiki/bin/viewauth/ALICE/CaloQA.

[119] K. Aamodt et al., ALICE Collaboration, Phys. Lett. B 693 (2011) 53.

[120] J. Allen et al., ALICE/EMCAL Collaboration, Nucl. Instr. and Meth. Nucl. Res. A615 (2010) 6.

[121] S. S. Adler et al., PHENIX Collaboration, Phys. Rev. D81 (2010) 072001.

[122] http://qm09.phys.utk.edu/indico/getFile.py/ access?contribId=745&sessionId=44&resId=0&materialId=poster&confId=1

[123] F. Poukoutakis et al., Proceedings of the Computing in High Energy Physics (CHEP 2007), http://cdsweb.cern.ch/record/1066450.

Publications

– **Y. Mao**, for the ALICE Collaboration, Two Particle Correlations with Photon and π^0 triggers in ALICE, arXiv:hep-ex/1102.2116v1, will be published on Nuclear Physics A.

– **Y. Mao**, G. C. Balbastre, Y. Schutz, D. Zhou, Direct isolated photons and jets to probe the LHC medium: A feasibility Study, will be published on India Journal of Physics.

– **Y. Mao**, for the ALICE Collaboration, Two Particle Correlations: a probe of the LHC QCD medium, arXiv:hep-ex/1102.2119v1, Journal of Physics: Conference Series 270 (2011) 012032.

– **Y. Mao**, Yves Schutz, Daicui Zhou, Christophe Furget, Gustavo Conesa Balbastre, QG-P tomography with photon tagged jets in ALICE, arXiv:hep-ex/1102.2123v1, Chinese Physics C 34 (2010) 9.

– D. C. Zhou, **Y. Mao** et al., Potential physics measurement with ALICE electromagnetic calorimeters, Nuclear Physics A 834 (2010) 291c-294c.

– D. C. Zhou, R. Wan, **Y. Mao** et al., High Pt and photon physics with ALICE at LHC, Chinese Physics C Vol 34, No.9 (2010) 1383.

– **Y. Mao**, G. C. Balbastre, M. Sano, Y. Schutz, D. C. Zhou, γ–hadron correlation measurements to study jets fragmentation with ALICE at LHC, ALICE-INT-2007-021, Eur. Phys. J. C 57 (2008) 613.

– **Y. Mao**, Zhou Daicui, Xu Chuncheng, Yin Zhongbao, Study of Photon Identification Efficiency with ALICE Photon Spectrum, ALICE-INT-2007-017, Chinese Physics C, 32(07) (2008).

– 周代翠，万仁卓，**毛亚显**等，"LHC/ALICE及其光子探测"，原子能科学技术，第42卷第7期(2008)655.

– **Y. Mao**, W. C. Xiang, D. C. Zhou, Charm Quark Energy Loss in Dense Matter within the Light–Cone Path Integral Approach, International Journal Modern Physics E, Vol. 16, No. 7-8 (2007) 2130.

– J. Liu, **Y. Mao**, W. C. Xiang, D. C. Zhou, Parton energy loss in hot and dense QCD matter, Chinese Science Bulletin Vol. 51, No. 2 (2006) 139.

– 刘杰，**毛亚显**等，"热密QCD介质中部分子能量损失"，科学通报，51(2006)13.

– D. C. Zhou, W. C. Xiang, **Y. Mao**, Heavy quark energy loss in dense medium, Journal of Central China Normal University (Natural Sciences) 39 (2005) 482.

ALICE Collaboration Publications

– ALICE Collaboration, Two-pion Bose-Einstein correlations in central PbPb collisions at $\sqrt{s_{NN}}$ = 2.76 TeV, Phys. Lett. B 696 (2011) 328.

– ALICE Collaboration, Centrality dependence of the charged-particle multiplicity density at mid-rapidity in Pb-Pb collisions at $\sqrt{s_{NN}}$ = 2.76 TeV, Phys. Rev. Lett. 106 (2011) 032301.

– ALICE Collaboration, Suppression of Charged Particle Production at Large Transverse Momentum in Central Pb-Pb Collisions at $\sqrt{s_{NN}}$ = 2.76 TeV, Phys. Lett. B 696 (2011) 30.

– ALICE Collaboration, Elliptic flow of charged particles in Pb-Pb collisions at $\sqrt{s_{NN}}$ = 2.76 TeV, Phys. Rev. Lett. 105 (2010) 252302.

– ALICE Collaboration, Charged-particle multiplicity density at mid-rapidity in central Pb-Pb collisions at $\sqrt{s_{NN}}$ = 2.76 TeV, Phys. Rev. Lett. 105 (2010) 252301.

– ALICE Collaboration, Transverse momentum spectra of charged particles in proton-proton collisions at $\sqrt{s}$ = 900 GeV with ALICE at the LHC, Phys. Lett. B 693(2010)53.

– ALICE Collaboration, Two-pion Bose-Einstein correlations in pp collisions at $\sqrt{s}$ = 900 GeV, Phys. Rev. D 82 (2010) 052001.

– ALICE Collaboration, Midrapidity Antiproton-to-Proton Ratio in pp Collisons at $\sqrt{s}$= 0.9 and 7 TeV Measured by the ALICE Experiment, Phys. Rev. Lett. Vol 105 No. 7 (2010).

– ALICE Collaboration, Charged-particle multiplicity measurement in proton-proton collisions at $\sqrt{s}$ = 7 TeV with ALICE at LHC, Eur. Phys. J. C 68 (2010) 345.

– ALICE Collaboration, Charged-particle multiplicity measurement in proton-proton collisions at $\sqrt{s}$ = 0.9 and 2.36 TeV with ALICE at LHC, Eur. Phys. J. C 68 (2010) 89.

– ALICE Collaboration, Alignment of the ALICE Inner Tracking System with cosmic-ray tracks, JINST 5 (2010) P03003.

– ALICE Collaboration, First proton-proton collisions at the LHC as observed with the ALICE detector: measurement of charged-particle pseudorapidity density at $\sqrt{s} = 900$ GeV, Eur. Phys. J. C 65 (2010) 111.

– ALICE Collaboration, The ALICE experiment at CERN LHC, JINST 3 (2008) S08002.

– ALICE/PHOS Collaboration, Solving a Deconvolution Problem in Photon Spectrometry, NIMA 620 (2010) 526.

Appendix A: 2-Dimension kinematical quantities

Let x be a 1-dimensional variable with normal (Gaussian) distribution and $r = \sqrt{x^2 + y^2}$ is a 2-dimensional variable with x and y of normal distribution. Then the following relations can be easily be derived

$$
\begin{aligned}
< x > = 0 \quad < r > &= \sqrt{\frac{\pi}{2}} \, \sigma \\
< |x| > = \sqrt{\frac{2}{\pi}} \, \sigma \quad < |r| > &= < r > \\
< x^2 > = \sigma^2 \quad < r^2 > &= 2 \, \sigma^2
\end{aligned} \tag{7.1}
$$

Both $\vec{j}_T$ and $\vec{k}_T$ are 2-dimensional vectors. If x and y components are Gaussian distributed, the mean value $< k_{T_x} >$ and $< k_{T_y} >$ is equal to zero. The non-zero components of the two-dimensional Gaussian distribution are the root mean squares $\sqrt{< j_T^2 >}$ and $\sqrt{< k_T^2 >}$ or the mean absolute values of the $\vec{j}_T$, $\vec{k}_T$ projections into the perpendicular plane to the jet axes $< j_{T_y} >$ and $< k_{T_y} >$. There is a trivial correspondence

$$
\sqrt{< k_T^2 >} = \frac{2}{\sqrt{\pi}} \; < k_T > = \sqrt{\pi} \; < k_{T_y} > . \tag{7.2}
$$

Appendix B: k_T dependence on transverse momentum study

To study how final k_T (or $< p_T >_{pair}$) differs by the transverse momentum, we generated few γ-jet and jet-jet events by PYTHIA generator in different p_T bins, within k_T setting predicted on Fig. **??** and ISR/FSR on. The hard scattered *gamma*-parton (or parton-parton) p_T pair from γ-jet (or jet-jet) events are taken as the reference for later study respectively. A Landau function is used to do the fitting on p_T^{pair} distribution to get the averaged value $< p_T >_{pair}$, the width of the fitting is shown as the vertical line on each point corresponding to each p_T bin (Fig. 5.11), the fitting lines are shown on the same plot as well by assuming the transverse momentum dependence is linear. The fitting parameters are given in Table. 7.1 by the function $< p_T >_{pair}$=A+B*p_T.
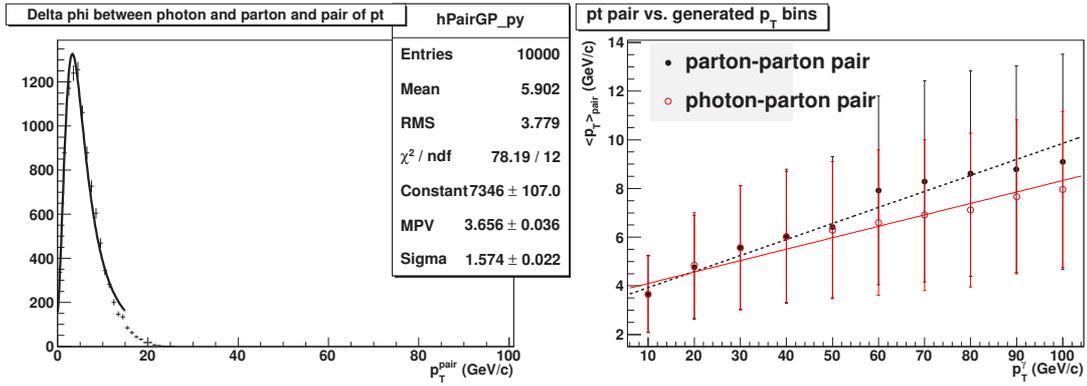
Figure 7.1: *p_T^{pair} distribution (left) and the averaged value $< p_T >_{pair}$ from each p_T bin (right). The p_T dependence is interpreted by a linear function (lines).*

	A (GeV)	B (GeV/c) [1]
parton-parton	3.27 ± 1.46	0.07 ± 0.03
photon-parton	3.63 ± 1.40	0.05 ± 0.03

Table 7.1: *Parameters fitted on averaged parton-parton p_T pair and photon-parton p_T pair by a linear function respectively.*

The jets are reconstructed (E_T^{jet}, η_0, ϕ_0) within a cone of $R = \sqrt{(\eta - \eta_0)^2 + (\phi - \phi_0)^2}$ in each event by UA1 jet finder algorithm [112] implemented in the PYTHIA PYCELL cluster finding routine. Within the jets opposite to each other, we calculate the p_T^{pair} from hard

159

scattering, then a Landau fitting is used to extract the mean value of $< p_T >_{pair}$. By different cone size (R =1, 0.7, 0.4, 0.2), a similar linear p_T is seen from the Fig. 7.2, however, the slope (see Tab. 7.2) is strongly dependent on jet reconstruction.
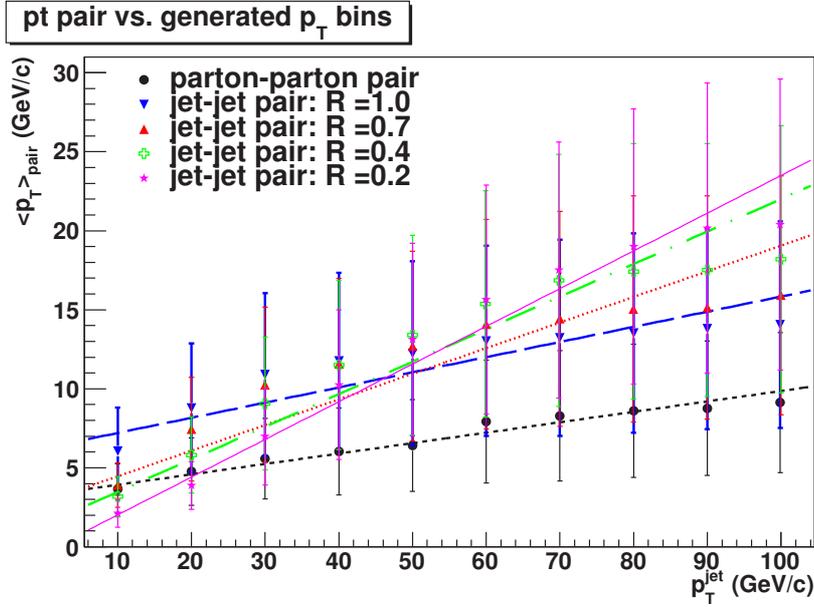
Figure 7.2: *The averaged $< p_T >_{pair}$ as a function of jet p_T from jet-jet events. The p_T dependence is interpreted by a linear function (lines)*

.

	A (GeV)	B (GeV/c) [1]
R = 1	6.25 ± 2.56	0.10 ± 0.05
R = 0.7	2.84 ± 1.56	0.16 ± 0.05
R = 0.4	1.42 ± 1.45	0.21 ± 0.05
R = 0.2	-0.36 ± 1.08	0.24 ± 0.05

Table 7.2: *Parameters fitted on averaged jet-jet p_T pair by the linear function.*

Dijet pairs provide an ambiguous measurement of the k_T since the jet is a product of parton fragmentation and therefore it is not possible to determine, event-by-event, the final k_T precisely in heavy ion collisions considering both jets will lose energy inside the hot medium and hence modify the kinematics. Direct photon-jet pairs offer two major advantages in

studying k_T as compared to dijets because of the nature of the photon. The distribution of hard scattering vertices sampled by direct photon-triggered correlations is thus unbiased by the trigger condition. At the LO level, direct photon production in pp and AA collisions is dominated by the QCD Compton scattering process, and the photons momentum in the center-of-mass frame is exactly balanced by that of the parton, then it will become more reliable to see how k_T modify final jets. Therefore the same study is done with the same sample of γ-jet events, where the jet is found by jet finder which is opposite to the photon, the γ and jet pair with different cone size are shown in Fig. 7.3, the fitting parameters are shown in Tab. 7.3.
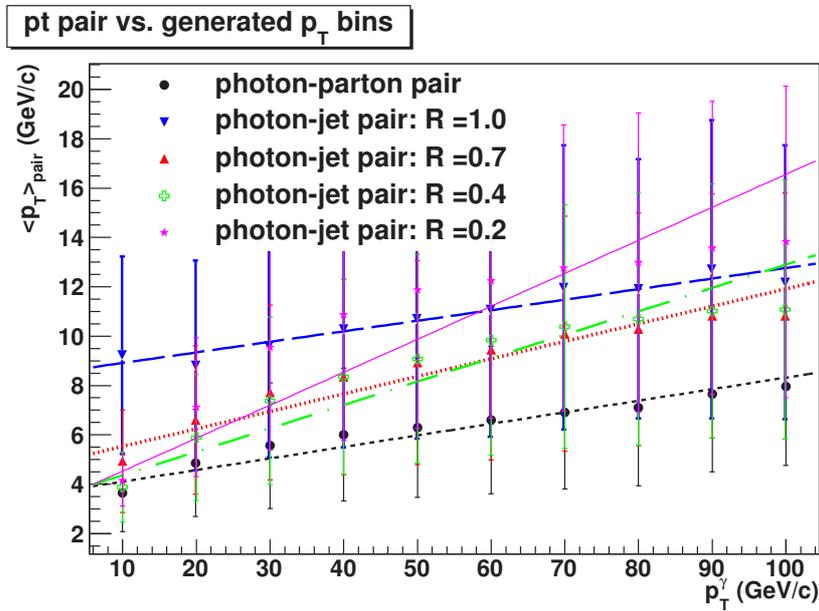

Figure 7.3: *The averaged $< p_T >_{pair}$ as a function of photon p_T from γ-jet events. The p_T dependence is interpreted by a linear function (lines)*

.

However, the cross section of the direct photons are quite small, which makes the measurement in real life more difficult. Instead of waiting a long time in order to collect enough statistics, a high p_T leading hadron-jet pair is used to measure final k_T approximatively, even though it is not exactly equivalently since the leading hadron only carry a small fraction of jet p_T and thus poorly define the jet axis. The leading particle is defined as the highest p_T particle inside the jet, after leading is found, a jet is searched by jet finder at the opposite, the leading and jet pair is shown in Fig. 7.4, the fitting parameters are shown in Tab. 7.4.

	A (GeV)	B (GeV/c) [1]
R = 1	8.49 ± 3.01	0.04 ± 0.05
R = 0.7	4.82 ± 1.91	0.07 ± 0.04
R = 0.4	3.42 ± 1.45	0.10 ± 0.04
R = 0.2	3.19 ± 1.19	0.13 ± 0.04

Table 7.3: *Parameters fitted on averaged γ-jet p_T pair by the linear function.*
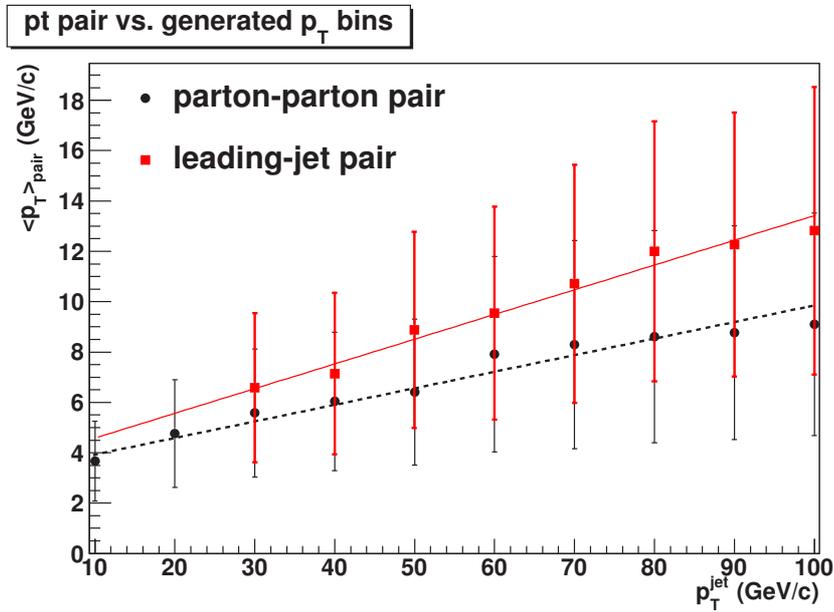


Figure 7.4: *The averaged $< p_T >_{pair}$ as a function of jet p_T from jet-jet events. The p_T dependence is interpreted by a linear function (lines)*

.

	A (GeV)	B (GeV/c) [1]
parton-parton	3.27 ± 1.46	0.07 ± 0.03
leading-jet	3.60 ± 3.84	0.10 ± 0.07

Table 7.4: *Parameters fitted on averaged jet-jet p_T pair by the linear function.*

162

A more efficient way is using leading-leading hadron pair instead of leading-jet pair since no jet reconstruction is needed anymore, which make the measurement in AA collisions possible. Again, two highest p_T hadrons are searched almost back to back, and then the pair p_T of the two leading particles are calculated as well, which is shown in Fig. 7.5, and the fitting parameters are shown in Tab. 7.5, the slop on the figure indicates a good approximation by leading-leading pair measuring k_T, a constant scaling might be necessary corrected after the final measurement.
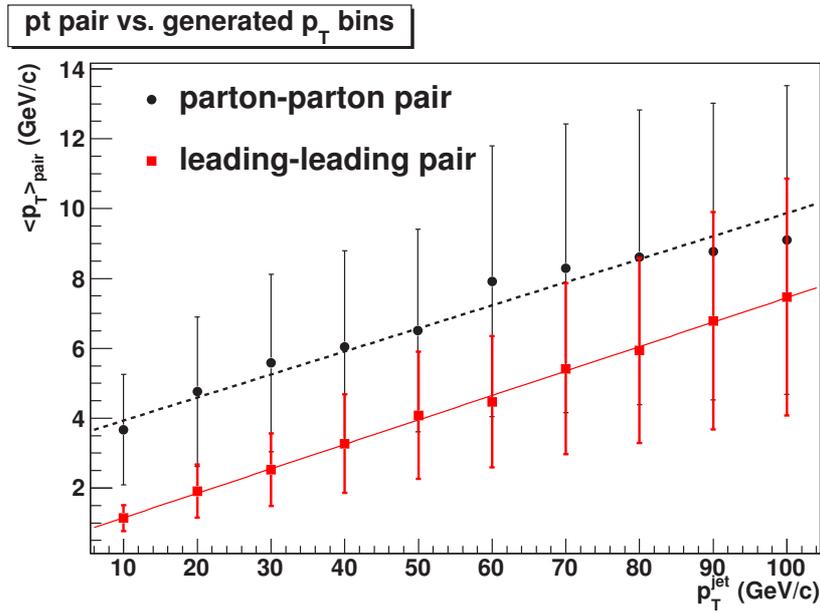

Figure 7.5: *The averaged $< p_T >_{pair}$ as a function of jet p_T from jet-jet events. The p_T dependence is interpreted by a linear function (lines)*

.

	A (GeV)	B (GeV/c) [1]
parton-parton	3.27 ± 1.46	0.07 ± 0.03
leading-leading	0.45 ± 0.44	0.07 ± 0.02

Table 7.5: *Parameters fitted on averaged leading-leading p_T pair by the linear function.*

Appendix C: EMCal Data Quality Monitoring (DQM)

To monitor the quality of the data stream created by any of the ALICE detectors, each detector defines a set of physics plots which have to be continuously filled and checked against reference ones. The AMORE framework [123] includes three components: the client part which collects the data, the server part which accumulates the plots and archives them, and the display program which provides an interactive distributed access to the plots archives. In addition, alarms are raised as soon as collected plots do not conform any more to the expected reference.

Normal physics data taken for EMCAL includes a low frequency of calibration events, some of which are EMCal LED triggers. A Light-Emitting Diode (LED) is a semiconductor light source, which is continuously monitored the performance of the EMCAL to track and correct for gain variations of the Photomultiplier Tubes (PMTs). The goal of the LED system is to provide time-dependent calibrations, together with the Embedded Local Monitor Board (ELMB) temperature sensors. The LED system, combined with muon measurements taken during the experiment, was crucial in the calibration of the EMCAL. The EMCal Data Quality Monitoring (DQM) is based mostly on LED calibration events. It was read out between spills of the proton beam. The light from a single LED is distributed via fiber to the 48 (2 columns x 24 rows) towers of a so-called EMCal strip module. Thus there are 24 LEDs used to monitor each EMCal Super Module, with the light from each LED monitored in the LED monitoring system. Each EMCal Super Module is readout with 36 FEE cards where each FEE card reads out 32 (4 columns x 8 rows) EMCal towers. The LED signals are measured not only by the APDs/towers, but also a monitoring/reference system (using a stable Si photodiode) is used, called LEDMon below. This way we can divide out any instabilities in the LED itself. At the moment there are 4 histograms for EMCAL DQM, there are ratio plots of LED calibration events from current LED signal amplitudes relative to those of an earlier reference run on EMCal towers, as well as for the so-called LED monitoring system which checks the stability of the LED system.

- *Tower Amplitude over Reference run (2D Location)*: The figure 7.6 shows the activity of each cell on different SMs (x-column(eta direction); y-row(phi direction)) from one run during the data taking. The ratio (z-axis in plot) should be around 1 on all the SMs (give the same color for all towers). There was several issues with EMCal illustrated
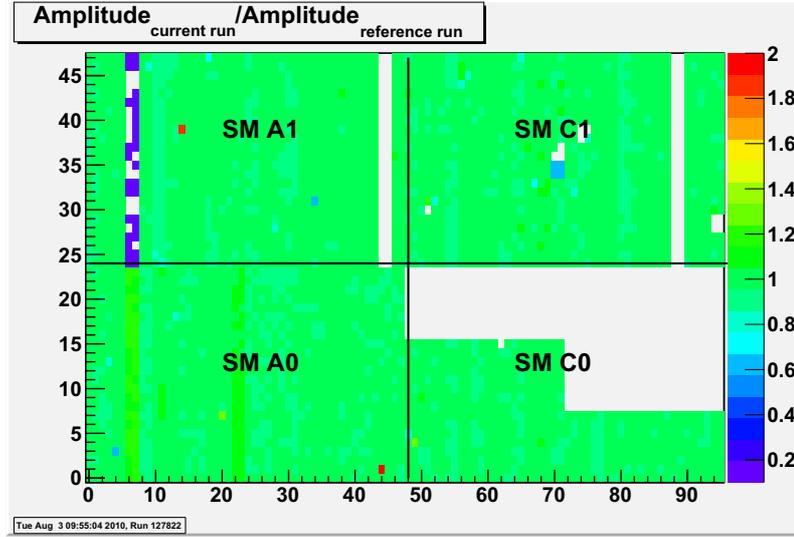
Figure 7.6: *The ratio of the tower amplitude over Reference data as a function of cell eta and phi for different SMs (x-column(eta direction); y-row(phi direction)) from one run during the data taking.*

in this plot: The LED signals in SMA1 (top left) for this run shows 2 strips have a bit lower value, also SMC1 (top right) one strip modules have 0 value due to LEDs partially missing (check the lower right histogram for LED Monitor Ratio in DQM plots) , 1 missing FEE on SMC0 (bottom right), few towers deviating from 1 (indicating for example, an HV problem for the towers or noisy).

– *Towers Amplitude over Reference run (1D ratio check)*: The projection of the 2D histogram, for Quality Assurance (QA) checker usage (Fig. 7.7). If the ratio is between 0.8 and 1.2 and more than 90% of towers are inside this range, EMCAL is with status OK, otherwise it indicates some problem. The box on top displays the checker results. A green box shows everything is fine, otherwise you should call On-Call EXPERTS and the color becomes red, this data taking should be labeled specially by experts and should be careful for analysis usage purpose. Sometimes the red box indicates the missing readout for one branch on SMC0, as also seen for the first plot. The total entries on this plot is the total channels for EMCAL 4 supper modules (4608 totally).

– *LEDMon channels - LED Monitor System readout for current run over Reference run (profile ratio plot)*: The profile ratio plot shows the ratio of LED Monitor system readout during the data taking for each LEDs channel (at moment we have 24 * 4 = 96 for 4 SMs). In principal the distribution should be rather flat and the ratio should be around
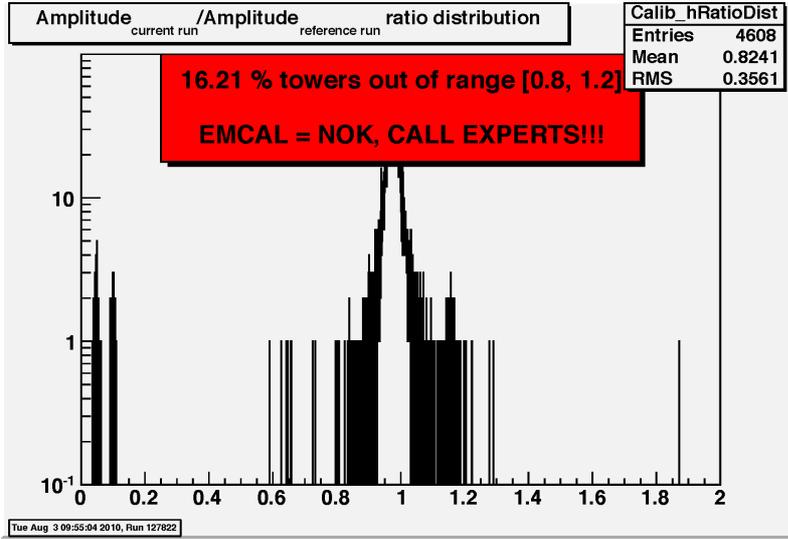
Figure 7.7: *The projection of the 2D figure 7.6, for data Quality Assurance (QA) checker usage.*

1 since we expect LED system is rather stable. However, with the time going on, the environment change (for example temperature) may result the light signal changes then it is not flatted at 1 as it should. For that the best way is to update our QA reference data since our checker rely on the LED system.

– *LEDMon channels - LED Monitor Amplitude over Reference run (1D ratio plot)*: The projection of third histogram (lower left in DQM). As explained on that plot, we should see the distribution peaked at 1 with 96 entries. This two plots (lower part) are for LED monitor system check.

Finally, the AMORE canvas for EMCAL at P2 DQM station during the data taking is shown on Fig. 7.8, where all the 4 plots explained above are shown together from different running period with good data quality (left) and problemable data (right). Since the EMCal data quality is checked within LED calibration events, the different collision system (no matter pp or PbPb) has no impact on EMCal DQM display since they look the same during the proton-proton and Pb+Pb data taking in 2010.
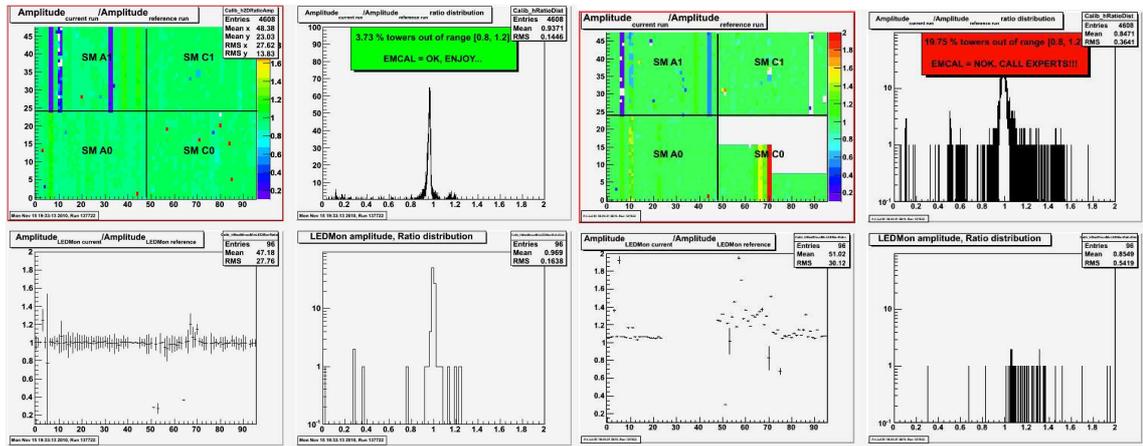
Figure 7.8: *the AMORE canvas for EMCAL at P2 DQM station during the data taking from different running period with good data quality (left) and problemable data (right).*

Table 7.6: *Run Number and Run Index: LHC10e period*

0	127719	1	127724	2	127729	3	127730	4	127814
5	127815	6	127817	7	127822	8	127931	9	127932
10	127933	11	127935	12	127936	13	127937	14	127941
15	127942	16	128175	17	128180	18	128182	19	128185
20	128186	21	128189	22	128191	23	128192	24	128257
25	128260	26	128452	27	128483	28	128486	29	128494
30	128495	31	128498	32	128503	33	128504	34	128505
35	128506	36	128507	37	128581	38	128582	39	128590
40	128592	41	128594	42	128596	43	128605	44	128609
45	128611	46	128615	47	128621	48	128678	49	128777
50	128813	51	128819	52	128820	53	128823	54	128824
55	128833	56	128835	57	128836	58	128843	59	128850
60	128853	61	128855	62	128913	63	129513	64	129514
65	129515	66	129516	67	129519	68	129520	69	129521
70	129523	71	129524	72	129525	73	129527	74	129528
75	129536	76	129540	77	129586	78	129587	79	129599
80	129639	81	129641	82	129647	83	129650	84	129652
85	129653	86	129654	87	129659	88	129666	89	129667
90	129723	91	129725	92	129726	93	129729	94	129735
95	129736	96	129738	97	129742	98	129744	99	129959
100	129960	101	129961	102	129962	103	129966	104	129983
105	130149	106	130151	107	130157	108	130158	109	130172
110	130178	111	130179	112	130342	113	130343	114	130479
115	130480	116	130481	117	130517	118	130519	119	130520
120	130524	121	130526	122	130601	123	130608	124	130628
125	130696	126	130704	127	130793	128	130795	129	130798
130	130799	131	130834	132	130840	133	130842	134	130844
135	130847	136	130848						